ABSTRACT

Quantitative Characterization of Steady and Time-Varying, Sooting,
Laminar Diffusion Flames using Optical Techniques

Blair C. Connelly
2009

In order to reduce the emission of pollutants such as soot and NO_x from combustion systems, a detailed understanding of pollutant formation is required. In addition to environmental concerns, this is important for a fundamental understanding of flame behavior as significant quantities of soot lower local flame temperatures, increase overall flame length and affect the formation of such temperature-dependent species as NO_x. This problem is investigated by carrying out coupled computational and experimental studies of steady and time-varying sooting, coflow diffusion flames.

Optical diagnostic techniques are a powerful tool for characterizing combustion systems, as they provide a noninvasive method of probing the environment. Laser diagnostic techniques have added advantages, as systems can be probed with high spectral, temporal and spatial resolution, and with species selectivity. Experimental soot volume fractions were determined by using two-dimensional laser-induced incandescence (LII), calibrated with an on-line extinction measurement, and soot pyrometry. Measurements of soot particle size distributions are made using time-resolved LII (TR-LII). Laser-induced fluorescence measurements are made of NO and formaldehyde. These experimental measurements, and others, are compared with computational results in an effort to understand and model soot formation and to examine the coupled relationship of soot and NO_x formation.

Quantitative Characterization of Steady and Time-Varying, Sooting, Laminar Diffusion Flames using Optical Techniques

A Dissertation

Presented to the Faculty of the Graduate School

of

Yale University

in Candidacy for the Degree of

Doctor of Philosophy

by

Blair C. Connelly

Dissertation Director: Professor Marshall B. Long

December 2009

ACKNOWLEDGEMENTS

TABLE OF CONTENTS

LIST OF FIGURES

CHAPTER 1

1 Introduction

Combustion systems produce a large majority of the energy used in the world today. The emission of pollutants, such as soot, NO_x and SO_x, from these systems is recognized as a considerable problem, causing adverse effects to the environment [Schumann 1996; Penner 1999; Menon 2002] and to personal health [Dockery 1982; Schwartz 1993]. As emission legislation becomes more restrictive, a detailed understanding of pollutant formation in flames will become even more critical for the design of pollutant abatement strategies and for the preservation of the competitiveness of combustion related industries. It is also necessary to reduce the emissions of greenhouse gases. One approach to this problem involves carbon sequestration, which involves storing carbon dioxide emissions through injection into depleted oil and gas reservoirs. In order to take full advantage of this strategy, the combustion process must be properly modeled. Further, it is now known that particulate size is an indicator as to the adverse health and environmental effects that are caused from combustion-generated soot. Particles in the size of 10 μm and smaller (PM_{10}) are known to produce clouds in the upper atmosphere and adversely affect the climate. Regulations have been passed for particles in the $PM_{2.5}$ range, as smaller particles have been observed lodged in respiratory

tissue, and recent evidence suggests that even smaller particles ($PM_{1.0}$) should be of concern.

It is clear that there will be continuing pressure to lower both NO_x emission indices and soot volume fractions in practical combustion devices. In an effort to reduce these emissions, a better understanding of the processes responsible for the creation of the pollutants is required. In addition to health and environmental effects, combustion-generated soot causes a decrease in flame temperature due to radiative losses, which can affect flame length and other temperature-dependent processes such as the formation of NO_x. As a result, a deeper understanding of these systems is desired. Fundamental combustion research often considers simplified systems as a test of the basic understanding of chemically and thermally reacting fluid systems. Numerical simulations of these simplified systems can be replicated and tested experimentally. Comparison between numerical calculations and experimental measurements provides guidance for the development of more accurate simulations.

Practical combustion systems, however, generally operate under unsteady and often turbulent conditions. As the simplified systems become better understood, research applications can move towards more complex configurations by increasing the flow complexity and the detail of the chemical model. Transitional diffusion flames – those flames that mark the boundary between fully laminar and fully turbulent diffusion flames – play an important role in the stability and structure of diffusion flames. A periodic perturbation can be applied to well-characterized steady flames in order to study transitional flames systematically. Also, studies of well-modeled laminar diffusion flames can be expanded to include an investigation into the characteristics of more complex, real

fuels such as JP-8 (and surrogates), gasoline, dodecane, etc. As our need for fuels

evolves, it is important to be able to predict the behavior of a wide range of fuels. To

study this case, computational and experimental approaches will have to be adapted to

study the larger molecules that can be found in realistic combustion systems. Ultimately,

a better understanding of both of these problems can be applied to realistic combustion

systems in an effort to minimize pollutants and greenhouse gases and to improve fuel

efficiencies even as the fuels themselves become more diverse and complex.

Experimentally, optical diagnostic techniques are a powerful tool for

characterizing combustion systems as they provide a noninvasive method of probing the

combustion environment. Laser diagnostic techniques have added advantages, as systems

can be probed with high spectral, temporal and spatial resolution, and with species

selectivity [Eckbreth 1996]. As systems become more complex and move from steady

laminar environments to turbulent systems, and as the level of simulations become more

detailed, the ability of a laser to resolve better the system becomes even more essential.

My dissertation research has been performed in Professor Marshall Long's group

at Yale University. The work focuses on the study of pollutant formation in steady and

time-varying sooting diffusion flames using laser diagnostic techniques. Experimental

work is done in collaboration with computational efforts in Professor Mitchell Smooke's

group. Comparisons are made between computational and experimental results for such

quantities as temperature, gaseous species, soot volume fraction and fluorescence signals

using two-dimensional images.

For continuity, these studies have been carried out on a burner geometry that was

used in previous studies. David Marran [Marran 1996] investigated major species and

NO concentrations in steady methane flames. Kevin Walsh [Walsh 2000a] examined methane diffusion flames under both normal and microgravity conditions. Soot concentrations, OH and CH structures, and extinction limits were investigated. Andrew Schaffer [Schaffer 2001] studied sooting, temperature, and major species in steady and time-varying methane and ethylene diffusion flames.

As the target flames studied have moved towards more heavily sooting flames common light scattering techniques, such as Rayleigh and Raman scattering, can no longer be used as the soot provides an overwhelming amount of interference. As a result, experimental techniques that concentrate on probing soot characteristics, such as laser-induced incandescence and soot pyrometry, are of value. Further, fluorescence measurements of minor species, where the laser can be tuned to a resonant transition to target the molecule of interest and then tuned off of a resonance peak for a background correction, can also provide additional information to the study. The goal is to add experimental information to the existing data, and to provide further comparisons for the numerical calculations.

Chapter 2 reviews the diagnostic techniques used in this study. Measurement techniques that take advantage of luminous species in the flame, such as imaging of chemiluminescence and soot pyrometry, are discussed. Also discussed are laser-based measurements such as laser-induced incandescence (LII) and laser-induced fluorescence.

Chapter 3 presents results from investigations on steady flames. Experimental soot volume fractions were determined using two-dimensional laser-induced incandescence (LII), calibrated using an on-line extinction technique, and soot pyrometry. Measurements of soot particle size distributions are made using time-resolved

LII (TR-LII). Laser-induced fluorescence measurements are made of NO and formaldehyde.

Chapter 4 presents results from investigations on forced, time-varying flames.

Chapter 5 explores the approach of comparing measured signals with simulated signals from computational results as an alternative to the traditional approach of comparing fundamental quantities such as temperature and mole fractions.

Finally, Chapter 6 provides some concluding remarks regarding the scope of this work.

Overall, this work provides a coupled experimental and computational study for a series of nonsooting and sooting, steady and time-varying, laminar coflow diffusion flames. The goal of the investigation presented here is to improve our understanding of combustion systems, and the specific processes responsible for the production of pollutants such as soot and NO_x. Ultimately, this work should build upon the work done for previous dissertations in Professor Marshall Long and Professor Mitchell Smooke's groups, and to provide a foundation for future studies that will help to understand the combustion process better.

CHAPTER 2

2 Optical Diagnostic Techniques

2.1 Introduction

Optical diagnostics are a useful tool for studying a wide variety of problems. Optical techniques provide non-intrusive measurements with high spatial and temporal resolution. This is particularly important in the harsh environment of combustion, where the high temperatures and small spatial and temporal scales make many measurements inaccessible to other techniques. Techniques that rely on probe sampling suffer from poor spatial resolution and irreversibly perturb the environment that they seek to measure.

Proper experimental design permits the measurement of a wide variety of flame parameters. Luminous species in the flame can be investigated using simple imaging techniques to provide information on flame phenomena. For laser-based techniques, appropriate selection of excitation and detection wavelengths allows for measurements that are sensitive to composition. Non-resonant laser measurements can be used to measure flame temperature and major species concentrations through Rayleigh and Raman scattering; soot characteristics can be measured through scattering and incandescence measurements. If the laser is tuned to a resonant wavelength, information on minor species can be gained. When combined with off-resonant measurements it becomes possible to remove unwanted interferences from the measurement. The ability to correct for background interferences is particularly important for sooting flames.

6

2.2   Luminosity Techniques

2.2.1   Chemiluminescence

Chemiluminescence is the emission of a photon by a molecule that is chemically produced in an electronically-excited state. Molecule, M, is formed in an electronically-excited state, M*, due to a reaction with molecules A and B

$$A + B \rightarrow M*.$$
(2.2.1)

Once produced in the electronically-excited state, the molecule may relax to its ground state through the emission of a photon due to spontaneous emission

$$M* \rightarrow M + h\nu.$$
(2.2.2)

where the photon energy, $E = h\nu = hc/\lambda$, represents the energy level spacing of the transition. Therefore, the wavelength, λ, of the emitted photon is indicative of a specific molecule.

In combustion systems, chemiluminescent species, such as CH* and OH*, contribute to the luminosity of a flame. CH* emits light through the $A^2\Delta \rightarrow X^2\Pi$ transition at 431.4 nm, and is responsible for the blue color associated with flames. OH* emits light through the $A^2\Sigma \rightarrow X^2\Pi$ transition at 306.4 nm, in the UV region of the spectrum. CH* and OH* have been shown to be indicative of the position of the flame front [Luque 2000]. Further, measurements of CH* can be related to the overall concentration of CH through empirical constants. As a result, simply taking images of the flame luminosity provides information of flame structure and lift-off height. This information can be compared with computational results where and used to improve the understanding of flame behavior.

2.2.2 Soot Pyrometry

Soot contained within a flame is heated to high temperatures (~1700 – 2000 K), and as a result emits radiation equivalent to blackbody modified by a wavelength and diameter dependent emissivity. This radiation is responsible for the "orange" luminosity observed in flames, and it can be sampled spectrally to gain information on flame temperatures and soot concentrations. Multi-wavelength optical pyrometry is a common measurement technique used to obtain the surface temperature of soot particles and soot concentration [Levendis 1992; Panagiotou 1996; Zhao 1998; Cignoli 2001; Snelling 2002]. Typically, soot emission is sampled at two or three different wavelengths using scientific charge-coupled-device (CCD) detectors and spectral filters. The use of multiple detectors makes it necessary to spatially match the images taken at the different wavelengths. The relative intensity of the detected radiation at the different channels can then be related to temperature using Planck's law. An absolute light calibration presents the opportunity to then determine the soot volume fraction, when images of soot luminosity are taken. In this work a color digital camera (Nikon D70) is used as an optical pyrometer, utilizing the color filter array (CFA) on the camera's detector.

2.2.2.1 Two-Color Implicit Approach

The intensity of radiation, I_λ, of a particle at wavelength λ is dependent on the particle temperature T and its monochromatic emissivity ε_λ, and follows Planck's law:

$$I_\lambda(\lambda,T) = \varepsilon_\lambda \frac{2\pi h c^2}{\lambda^5 \left[\exp(hc/k\lambda T) - 1\right]}$$

(2.2.3)

where c is the speed of light, h is Planck's constant, and k is the Boltzmann constant. The measured signal, S_λ, is the intensity of radiation integrated over the detection wavelengths

and normalized for the detection efficiency. The detected signal is then a function of the

efficiency of the detection system, η_λ, integrated over the all wavelengths

$$S_\lambda = 2\pi hc^2 \int \eta_\lambda \frac{\varepsilon_\lambda}{\lambda^5} \left[\exp\left(hc/k\lambda T\right) - 1\right]^{-1} d\lambda \tag{2.2.4}$$

where the detected signal is a function of temperature. Following the development of

multi-wavelength ratio pyrometry by Levendis *et al.* [Levendis 1992], the signal ratio at

two detection wavelengths λ_1 and λ_2 is

$$\frac{S_{\lambda_1}}{S_{\lambda_2}} = C_{\lambda_1 \lambda_2} \left(\frac{\varepsilon_{\lambda_1}}{\varepsilon_{\lambda_2}}\right) \left[\frac{\exp\left(hc/k\lambda_1 T\right) - 1}{\exp\left(hc/k\lambda_2 T\right) - 1}\right]. \tag{2.2.5}$$

The instrument constant $C_{\lambda_1 \lambda_2}$ is a function of the collection efficiency of the detector, η_D,

the combined lens and filter transmittance, η_L, the ratio of detection wavelengths, and the

ratio of spectral bandwidths, $\Delta\lambda$, at the two detection wavelengths 1 and 2:

$$C_{\lambda_1 \lambda_2} = \left(\frac{\eta_{L_1}}{\eta_{L_2}}\right) \left(\frac{\eta_{D_1}}{\eta_{D_2}}\right) \left(\frac{\lambda_2}{\lambda_1}\right)^5 \left(\frac{\Delta\lambda_1}{\Delta\lambda_2}\right). \tag{2.2.6}$$

The spectral bandwidth of the filters, $\Delta\lambda$, accounts for the effects of the approximation

λ = constant made when performing the spectral integration (Eq. 2.2.4 → Eq. 2.2.5), i.e.,

$\Delta\lambda_1$ and $\Delta\lambda_2$ are assumed to be small compared to their central wavelength difference,

$\lambda_1 - \lambda_2$. $C_{\lambda_1 \lambda_2}$ can be determined using a blackbody source of known temperature for

calibration. Alternatively, the parameters (or their ratios) appearing in Eq. 2.2.6 can be

measured and $C_{\lambda_1 \lambda_2}$ can then be calculated. Both methods have been utilized in this work.

Further manipulation of Eq. 2.2.5 yields the expression:

$$T = \cfrac{\dfrac{hc}{k}\left(\dfrac{1}{\lambda_2} - \dfrac{1}{\lambda_1}\right)}{\ln\left[\dfrac{1}{C_{\lambda_1\lambda_2}}\dfrac{\varepsilon_{\lambda_2}}{\varepsilon_{\lambda_1}}\dfrac{S_{\lambda_1}}{S_{\lambda_2}}\left(\dfrac{1-\exp(-hc/k\lambda_1 T)}{1-\exp(-hc/k\lambda_2 T)}\right)\right]} .$$

(2.2.7)

The emissivity, ε_λ, is assumed to have an inverse-dependence on wavelength [Snelling 2002]. Then the emissivity ratio provides an additional ratio between detection wavelengths, which is grouped into the calibration factor for experimental temperature calculations. Since Eq. 2.2.7 is implicit in T, a solution must be determined iteratively. A starting value can be obtained using the Wien approximation to assume the temperature-dependent term, in parentheses on the right side of the equation, to be unity. Further iterations are carried out using the full formulation of Eq. 2.2.7.

Thus, it is also necessary to carry out iterations of the central detection wavelengths λ_1 and λ_2. The assumption of narrowband detection filters, made to derive Eq. 2.2.5, is too restrictive for the filter characteristics of typical CFAs used in color cameras, because the Planck function varies significantly within the spectral detection window. When the Planck function is sampled by the CFA, the central wavelength of the detected spectral signal shifts significantly from the original central wavelength of the CFA. The result is a new effective wavelength that must be used to calculate the temperature [Boslough 1989; Anselmitamburini 1995]. This effective wavelength is inserted into Eqs. 2.2.6 and 2.2.7 for further iterations. A blackbody temperature calibration of the instrument constant would directly provide an effective $C_{\lambda_1\lambda_2}$ as well as an effective λ_1 and λ_2, leaving only the iteration for T. The effect of wavelength shifting will be illustrated in the next section when the detector characterization is discussed.

2.2.2.2   Calibration with a Blackbody Source

Equation 2.2.7 can be rewritten as

$$\ln\left[\frac{\varepsilon_{\lambda_2}}{\varepsilon_{\lambda_1}}\frac{S_{\lambda_1}}{S_{\lambda_2}}\right] = \frac{hc}{k}\left(\frac{1}{\lambda_2}-\frac{1}{\lambda_1}\right)\left(\frac{1}{T}\right) - \ln\left[\frac{1}{C_{\lambda_1\lambda_2}}\left(\frac{1-\exp(-hc/k\lambda_1 T)}{1-\exp(-hc/k\lambda_2 T)}\right)\right] \qquad (2.2.8)$$

In this form of the temperature equation, the log of the signal ratio is inversely dependent on the temperature. A blackbody calibration can be performed by taking images over a range of oven temperatures. Plotting the log of the resulting signal ratios as a function of $1/T$ produces a linear relationship with a slope of

$$\frac{hc}{k}\left(\frac{1}{\lambda_2}-\frac{1}{\lambda_1}\right) \qquad (2.2.9)$$

and an intercept of

$$-\ln\left[\frac{1}{C_{\lambda_1\lambda_2}}\left(\frac{1-\exp(-hc/k\lambda_1 T)}{1-\exp(-hc/k\lambda_2 T)}\right)\right]. \qquad (2.2.10)$$

These relations can then be used to determine flame temperatures using the signal ratio, and the wavelength dependence of the soot emissivity.

Further, use of the blackbody calibration provides a reference to an absolute light intensity for a given temperature and experimental geometry. This can then be used to relate the intensity of radiation, $I_{b,\lambda}(T_a)$, at the measured/apparent temperature of a non-blackbody, T_a, to a reference intensity, $I_{b,\lambda}(T)$, of a blackbody at temperature, T, through the monochromatic emissivity [Zhao 1998]

$$\varepsilon_\lambda = \frac{I_{b,\lambda}(T_a)}{I_{b,\lambda}(T)} = \frac{\exp(hc/k\lambda T)-1}{\exp(hc/k\lambda T_a)-1}. \qquad (2.2.11)$$

11

The emissivity of the soot is then estimated using an empirical relation provided by Hottel and Broughton [Hottel 1932]

$$\varepsilon_\lambda = 1 - \exp(-k_\lambda l) \qquad (2.2.12)$$

where k_λ is the absorption coefficient and l is the geometric thickness of the flame along the axis of the detection system. Finally, determination of the "$k_\lambda l$" factor can then be related to the soot volume fraction through the following relationship

$$f_V = \frac{k_\lambda l}{K_{ext} L / \lambda} \qquad (2.2.13)$$

where K_{ext} is the dimensionless extinction coefficient (discussed in Section 2.3.1.1), L is the characteristic length of the detection system, and λ is the detection wavelength. This formulation for the soot volume fraction is used to determine the experimental soot volume fraction from the pyrometer data.

2.2.2.3   Look-up Table Approach

An alternative to the approach described in Section 2.2.2.1 has recently been proposed by Professor Marshall Long and Peter Kuhn. It was noted that the assumption of narrowband filters made to derive Eq. 2.2.5 from 2.2.4 is poor in the case of the typical color camera filters. In this approach, the approximation of narrowband filters and the signal ratio is derived directly from Eq. 2.2.4 to be

$$\frac{S_{F_1}}{S_{F_2}} = \frac{\int \eta_{F_1} \frac{\varepsilon_\lambda}{\lambda^5} \left[\exp(hc/\lambda kT) - 1\right]^{-1} d\lambda}{\int \eta_{F_2} \frac{\varepsilon_\lambda}{\lambda^5} \left[\exp(hc/\lambda kT) - 1\right]^{-1} d\lambda} \qquad (2.2.14)$$

for filters F_1 and F_2, where η_{F_1} and η_{F_2} are the respective transmission efficiencies for each filter as a function of wavelength. The ratio is calculated by evaluating the integrals

in Eq. 2.2.14 numerically based on the characteristics of the detection system for a range of input temperatures. A look-up table is then generated to determine the temperature based on the measured signal ratio. A preliminary comparison between the look-up table approach and the iterative two-color approach will be examined here.

2.2.3   Tomographic Inversion

Most diagnostic techniques that measure flame luminosity are line-of-sight imaging techniques. As a result, spatial information is lost through the projection of the object onto the image plane. Fortunately, one can take advantage of the cylindrical symmetry that exists in axisymmetric laminar diffusion flames and perform a tomographic inversion to deconvolve the data to a radial profile.

For an object in the xy-plane, the intensity of the projection onto y is

$$I(y) = \int_{-\infty}^{\infty} F[(x^2 + y^2)^{1/2}]dx$$

(2.2.15)

For a cylindrically-symmetric object, the radial profile of can be recovered from the projection using the following analytical expression for the Abel transform [Cormack 1982]:

$$F(r) = -\frac{1}{\pi} \int_{r}^{\infty} \frac{I'(y)}{(y^2 - r^2)^{1/2}} dy$$

(2.2.16)

where $I'(y) = dI/dy$. The geometry of this problem is represented in Figure 2.2.1.

There are a number of algorithms available to perform the inversion in Eq. 2.2.15. Dasch [Dasch 1992] presents a comparison of three deconvolution techniques: the Abel inversion, onion-peeling, and filtered backprojection methods. He concludes that the three-point Abel inversion is the most robust approach, due to the ease of use and the

13
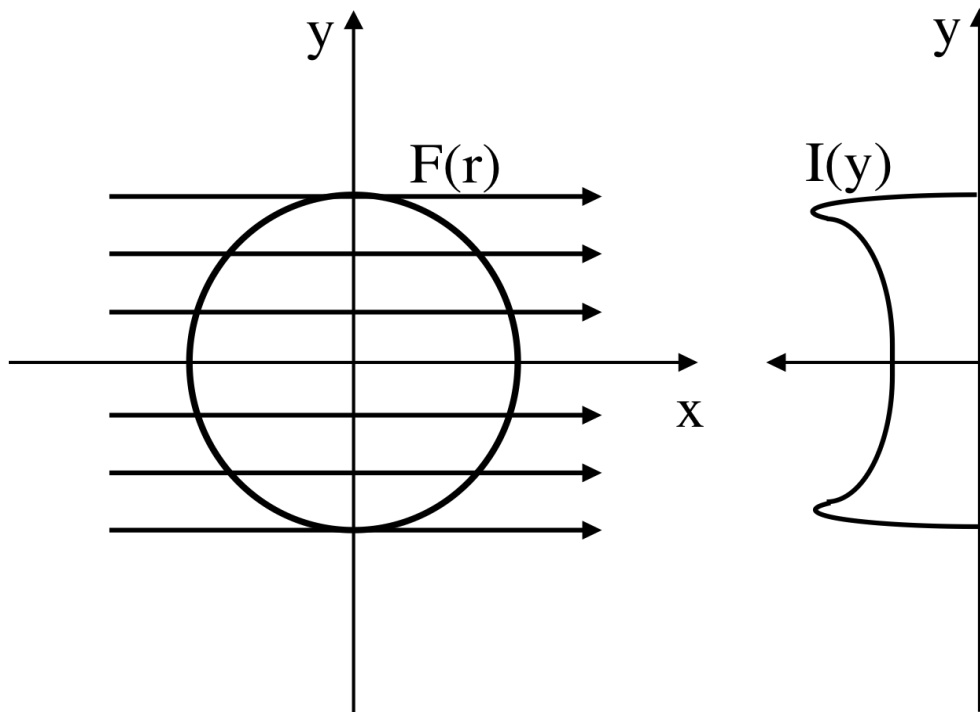
Figure 2.2.1: Schematic of projection of cylindrically symmetric object F(r), projected onto dimension y as I(y).

relative noise performance. The three-point Abel inversion is the approach used in this work, and will be outlined here.

The three-point Abel inversion breaks Eq. 2.2.15 into segments of length δ around each point r_j:

$$F(r_i) = -\frac{1}{\pi} \sum_{j=i}^{\infty} \int_{\substack{0, j=i \\ -\Delta r/2, j>i}}^{\Delta r/2} \frac{I'(r_j + \delta)}{\left[(r_j + \delta)^2 - r_i^2\right]^{1/2}} d\delta \tag{2.2.17}$$

$I(y)$ is then approximated in the region around r_j in quadratic form, resulting in a modified expression for $F(r)$

$$F(r_i) = -\frac{1}{\Delta r} \sum_{j=i}^{\infty} \left[\mathbf{I}_{ij}(1) - \mathbf{I}_{ij}(0)\right] P(r_{j-1}) - 2\mathbf{I}_{ij}(1) P(r_j) + \sum_{j=i}^{\infty} \left[\mathbf{I}_{ij}(1) + \mathbf{I}_{ij}(0)\right] P(r_{j+1}) \tag{2.2.18}$$

where $P(r)$ is the line-of-sight projection data and

$$\mathbf{I}_{ij}(n) = \frac{1}{2\pi} \int_{\substack{0, j=i \\ -1, j>i}}^{1} \frac{\delta^n}{\left[(2j + \delta)^2 - 4i^2\right]^{1/2}} d\delta . \tag{2.2.19}$$

Deconvolution procedures, such as an Abel inversion, require the solution of an ill-posed problem, where the solution for the radial profile is sensitive to small perturbations in the line-of-sight projection [Daun 2006]. Errors in the deconvolution tend to carry inwards and increase, as the radius approaches zero. The result can be a substantial amount of noise in the center of the flame, particularly when the peak signals occur at a radius greater than zero [Walsh 2000b].

As is evident in Figure 2.2.1, this, and other line-of-sight techniques, assume parallel ray collection of the projected object. Typically the experimental apparatus is arranged to approximate the assumption of parallel ray collection as well as possible. For

example, maximizing the focal length of the collection lens and distance to the object, and minimizing the lens aperture will aid this assumption. Walsh *et. al* [Walsh 2000b] investigated the effect of light-collection geometry on reconstruction errors in Abel inversions. He performed a ray-tracing simulation in an effort to understand how the collection geometry affected the reconstruction of the radial profile. It was found that there existed a 1-pixel shift in the peak location of the reconstruction of the simulated signal, and that a low-magnitude residual noise existed from the centerline to the location of the distribution peak. A general trend was found that errors in the reconstructed profiles tended to diminish as the ratio of the lens focal length to the object distance approached infinity (specifically above a ratio of 100), as the collected rays better approximate parallel rays. Use of a smaller detection aperture will help to alleviate this problem [Snelling 2002].

Regularization techniques can be used to create a well-posed problem, where an additional "smoothing" constraint is added to the system of equations. An algorithm that applies a Tikhonov regularization to tomographic inversions, by avoiding the problem of over-smoothing, is reported in [Daun 2006]. Current efforts to minimize reconstructed noise characteristics employ a manual smoothing of the data that is careful to avoid under prediction of the reconstructed signal peak. Implementation of this regularization technique in the future should provide cleaner and more accurate radial profiles, which will improve the soot temperature and concentration images.

2.3   Laser-Based Techniques

2.3.1   Laser-Induced Incandescence

A common quantity of interest in combustion systems is the soot volume fraction, f_v, which can be defined in terms of the primary particle diameter, d_p, the average number of primary particles per aggregate, n_p, and the number of aggregates, N_p:

$$f_V = \frac{\pi}{6} N_p n_p d_p^3 \qquad\qquad (2.3.1)$$

Laser-induced incandescence (LII) is a useful tool for studying particle characteristics in flames [Schulz 2006b], as well as other systems [Kock 2005] where the material heat transfer properties are well known. Briefly, LII uses a pulsed laser to heat soot particles to temperatures above the ambient flame temperature. The increased particle temperature results in an increase in radiative emission. The LII phenomenon was first observed by Eckbreth [Eckbreth 1977] as a source of broadband interference in a Raman scattering experiment. Then termed "laser-modulated incandescence", Eckbreth correlated the signal with particle heating then cooling, and found an indirect dependence of the signal's time dependence on particle size. He also found that the LII signal saturated when excited by laser fluence above a threshold, while the Raman signal did not, enabling the maximization of his signal to noise by using high laser fluences. LII was first considered for use as an experimental tool by Melton [Melton 1984]. He performed numerical calculations that determined that LII could be used to infer information of relative soot volume fraction, particle temperature and primary particle size distributions.

17

It took another decade for Melton's theoretical framework to be demonstrated as an effective technique for measuring soot volume fraction [Tait 1993; Cignoli 1994; Quay 1994; Shaddix 1994b; Vanderwal 1994]. These investigations, and others that followed (see, e.g., [Mewes 1997; Snelling 1999; Axelsson 2000; Axelsson 2001]), utilized detection of the "prompt" signal (signal around the maximum particle temperature) to determine soot volume fractions. These approaches require calibration using an independent measurement technique. More recently, it has been shown that two-color detection of the LII signal provides a continuous *in situ* self-calibration of the LII signal using optical pyrometry [Smallwood 2002; De Iuliis 2005; Snelling 2005]. This approach is considered to be auto-compensating, as it accounts for variations in particle temperature due to experimental conditions. Time-resolved detection of the decay rate of the LII signal as the particles cool back down to flame temperatures can be used to determine particle sizes [Will 1995; Mewes 1997; Will 1998; Vander Wal 1999; Hofmann 2003; Michelsen 2003a; Dankers 2004; Kock 2006; Liu 2006b; Michelsen 2006]. The decay rate is dependent on the particle's volume-to-area ratio and can be directly related to a particle diameter.

Though the object of many investigations over the years, LII is still developing as a measurement technique. Recent international workshops [2005; 2006; 2008] have sought to resolve discrepancies that exist relating to experimental issues, modeling of the process and interpretation of the signal [Schulz 2006b; Michelsen 2007].

2.3.1.1 LII Physical Model

Though some discrepancies have been identified in Melton's original formalism [Smallwood 2001], particularly in regards to the vaporization term, most LII experiments

to date employ an adaptation of Melton's model. A number of detailed presentations of

the LII model exist in the literature (see, e.g., [Michelsen 2003a; Hofmann 2007;

Michelsen 2007]). I will outline the approach presented in [Hofmann 2007] for

consistency, as it is the modeling tool that I employed in the work presented in

Section 3.4.

Models of the LII process consider the energy conservation of a spherical particle

heated by a laser pulse to temperatures above the ambient flame temperature, followed by

the subsequent cooling of the particle due to vaporization of material, heat conduction to

the surrounding gas and radiation:

$$\dot{Q}_{abs} = \dot{Q}_{int} + \dot{Q}_{vap} + \dot{Q}_{cond} + \dot{Q}_{rad} \qquad (2.3.2)$$

where $\dot{Q}_{abs}$ is the energy flux from absorption, $\dot{Q}_{int}$ is the change in internal energy, $\dot{Q}_{vap}$

is the change in energy due to vaporization (sublimation), $\dot{Q}_{cond}$ is the change in energy

due to conductive cooling of the particle, and $\dot{Q}_{rad}$ is the heat loss due to radiation. Figure

2.3.1 illustrates this process, and reduces each term to its dependence on particle

diameter. Models for higher order modes of heat transfer (such as oxidation, annealing,

photoionization, etc.) and to account for aggregation are still under development

[Michelsen 2003a].

The mass loss of the particle can be described by

$$\frac{dm_p}{dt} = J_{vap} \qquad (2.3.3)$$

19

$$\dot{Q}_{int} = \dot{Q}_{abs} - \dot{Q}_{cond} - \dot{Q}_{rad} - \dot{Q}_{vap}$$

Laser Heating

Absorption

$$\dot{Q}_{abs} \propto d^3 \frac{E(m)}{\lambda_{ex}}$$

$$\dot{Q}_{int} \propto d^3 \frac{dT}{dt}$$

$$\dot{Q}_{vap} = \frac{\Delta H_v}{M} \frac{dm_p}{dt}$$

$$\propto d^2$$

Vaporization

Radiation

$$\dot{Q}_{rad} \propto d^3 T^5$$

$$\dot{Q}_{cond} \propto d^2 \alpha_T (T - T_{gas})$$

Conduction

Signal Detection

Particle Cooling
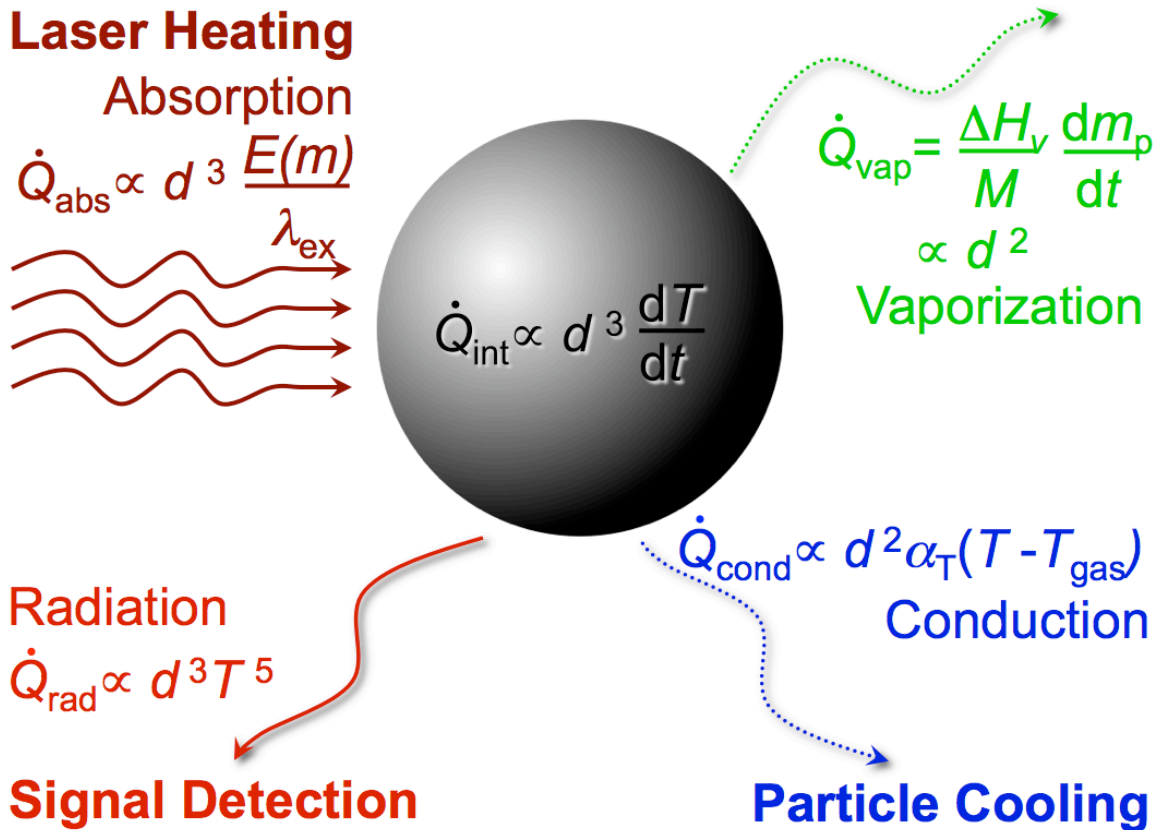
Figure 2.3.1: Representation of the laser-induced incandescence (LII) process. Models of the process consider the change in internal energy $\dot{Q}_{int}$ of a particle of diameter d due to the rate of energy absorption due to laser heating, $\dot{Q}_{abs}$. After heating, the particle then cools down to the ambient gas temperature T_{gas} at a rate determined by modeling contributions from conduction, $\dot{Q}_{cond}$, radiation, $\dot{Q}_{rad}$, and vaporization, $\dot{Q}_{vap}$.

where m_p is the particle mass, and J_{vap} is the mass flux. Equations 2.3.2 and 2.3.3 are coupled and can be solved numerically for particle temperature and diameter as a function of time, t.

First, the individual components of Eq. 2.3.2 must be defined. The rate of absorption of laser energy is dependent upon the laser intensity $I(t)$ and the absorption cross section C_{abs}

$$\dot{Q}_{abs} = C_{abs}I(t) \tag{2.3.4}$$

where $C_{abs} = \dfrac{\pi^2 d_p^3}{\lambda_{ex}} E(m)$, and $E(m)$ is the soot absorption function. The change in internal energy is

$$\dot{Q}_{int} = \frac{d(m_p c_p T_p)}{dt} \tag{2.3.5}$$

where T_p is the particle temperature and c_p is the heat capacity of soot. The heat conduction term can be described in terms of a number of different heat transfer models. Here the McCoy and Cha model [McCoy 1974] is used to describe the heat conduction model:

$$\dot{Q}_{cond,Trans} = \frac{2k_g(T_g)\pi d_p^2(T_p - T_g)}{(d_p + G\lambda_{MFP})} \tag{2.3.6}$$

where k_g is the thermal conductivity of the ambient gas at temperature T_g and λ_{MFP} is the mean free path length. The heat-transfer factor, G, is given by

$$G = \frac{8f}{\alpha_T(\gamma + 1)} \tag{2.3.7}$$

where f is the Eucken correction to the thermal conductivity for a polyatomic gas, α_T is the thermal accommodation coefficient, and $\gamma = c_P/c_V$ is the ratio of heat capacities c_P (the heat capacity of air at constant pressure) and c_V (the heat capacity of air at constant volume). This model provides a smooth transition between the free-molecular regime, where molecule-molecule collisions dominate, and the continuum regime, where conduction to the surrounding gas is diffusion controlled; it can be used for all heat conduction regimes and provides a smooth transition between the continuum and free-molecular regime. The heat loss from vaporization can be expressed in terms of the molar mass of soot, M_s, and the enthalpy of vaporization of soot, ΔH_v:

$$\dot{Q}_{\text{vap}} = \frac{\Delta H_v}{M_s}\frac{dm_p}{dt} = \frac{\Delta H_v}{M_s}J_{\text{vap}}. \tag{2.3.8}$$

The heat loss due to radiation can be described by the Stefan-Boltzmann law:

$$\dot{Q}_{\text{rad}} = \pi d_p^2 \sigma_B (T_p^4 - T_g^4) \tag{2.3.9}$$

where σ_B is the Stefan-Boltzmann constant.

Equations 2.3.4 – 2.3.6, 2.3.8 and 2.3.9 are then inserted into Eq. 2.3.3, and solved using a fourth-order Runge-Kutta algorithm for $d_p(t)$ and $T_p(t)$. The LII signal intensity is then determined from the particle temperature using Planck's law (Eq. 2.2.1), integrated for the wavelength range used for detection

$$S_{\text{LII}} = 2\pi^2 hc^2 d_p^2 \int_{\lambda_1}^{\lambda_2} \frac{\eta(\lambda)\varepsilon(\lambda)}{\lambda^5 \left[\exp(hc/\lambda k_B T_p) - 1\right]} d\lambda \tag{2.3.10}$$

where $\eta(\lambda)$ is the response of the detection system as a function of wavelength and $\varepsilon(\lambda)$ is the "emissivity" of the soot. Under the Rayleigh approximation ($\pi d_p/\lambda \ll 1$)

22

$$\varepsilon(\lambda) = \frac{4C_{abs}}{\pi d_p^2} = \frac{4\pi d_p E(m)}{\lambda}$$

(2.3.11)

where $E(m) = \frac{m^2 - 1}{m^2 + 2}$ and $m = n + ik$ is the complex index of refraction. It should be

noted that the concept of emissivity does not precisely apply to soot, as emissivity is a

bulk property. The emissivity here should be viewed as more of an efficiency of radiation

and absorption that is dependent on $E(m)$. Further, the value $E(m)$ is still not particularly

well defined, and is the subject of a number of ongoing investigations [Smyth 1996;

Krishnan 2000; Krishnan 2001; Snelling 2004; Williams 2005].

2.3.1.2   Evaluation of "Prompt" Signal

Numerical integration of Eq. 2.3.10 at the maximum temperature, called prompt

LII, yields:

$$\text{prompt LII} \propto d^x$$

(2.3.12)

for
$$x = 3 + \frac{hcR}{k_B \Delta H_v} \frac{1}{\lambda_{det}} = 3 + 0.154/\lambda_{det}$$

(2.3.13)

where λ_{det} is the averaged detection wavelength in microns. The maximum temperature

occurs when the radiative flux absorbed from the laser is balanced by the heat flux from

vaporization / sublimation. Comparison of Eqs. 2.3.1 and 2.3.12 shows that the prompt

LII signal is approximately proportional to the soot volume fraction:

$$f_V \propto \text{prompt LII}$$

(2.3.14)

The next step is to determine the calibration constant, which relates the LII signal to the

soot volume fraction.

2.3.1.3   Laser Extinction Calibration

There are a number of different methods used to calibrate the LII signal: probe sampling techniques [Koylu 1997; McEnally 1998], self-calibrating two-color LII (see next section), and on-line extinction measurements [Geitlinger 1998; Axelsson 2001]. The extinction calibration will be discussed here, as it is the calibration method employed for experiments outlined in Section 3.4.

Light incident on a cloud of particles will be both scattered and absorbed by the particles. The dimensionless extinction coefficient, K_{ext}, is defined as the sum of the absorption and scattering coefficients, or

$$K_{ext} = 6\pi E(m)\left(1 + \rho_{sa}\right)$$ (2.3.15)

where ρ_{sa} is the ratio of total scattering to absorption cross sections.

For conditions where soot properties are uniform along an optical path, L, the average soot volume fraction can be related to the ratio of the intensity of transmitted to incident light, I / I_0, through Lambert-Beer's law:

$$\bar{f}_v = -\frac{\lambda}{K_{ext}L}\ln\left(\frac{I}{I_0}\right)$$ (2.3.16)

Consequently, the soot volume fraction of a flame cross-section can be determined by measuring the fraction of light transmitted by a flame. Combining Eqs. 2.3.14 and 2.3.16 provides quantitative results for the LII measurements.

As with the absorption coefficient, K_{ext} is difficult to determine because it is a function of the particular soot properties (e.g., primary particle size, aggregate size), which vary with the fuel used and the exact location within each flame [Krishnan 2000; Krishnan 2001; Williams 2005]. The model of light scattering used in each determination

24

of K_{ext} can also vary. In the Rayleigh approximation of small particles K_{ext} is dominated by absorption. As the soot particles aggregate into larger structures, this approximation is no longer valid and the soot must be considered as fractal aggregates. Without an independent scattering measurement to quantify the contribution of scattering to the laser beam extinction an even greater uncertainty is expected. Since it is impractical to independently measure K_{ext} for all flame cross sections, an average value is used, which contributes a majority of the uncertainty for this method of calibration in LII measurements.

2.3.1.1   Time-Resolved LII

Detection of the LII signal as the particle cools can be used to determine information about particle size distributions, as the cooling rate is inversely proportional to the volume-to-surface area ratio. It is important to use moderate laser fluences for particle sizing to avoid causing issues with soot morphology and consequently altering the very properties that are under investigation.

Typically, particle size distributions are determined using point measurements by evaluating the temporal decay of the LII signal detected by a PMT (photomultiplier tube). For the work presented here, two-dimensional detection of particle sizes is desired in order to make an effective comparison with the computational results. As this implies detection at discrete gate times, rather than acquiring the full time trace of the signal decay, appropriate treatment of the data analysis will be necessary.

The ability to determine accurate particle sizes is dependent on accurate modeling of the cooling process. As mentioned above, Eqs. 2.3.4 – 2.3.6, 2.3.8 and 2.3.9 are solved numerically to determine the time dependence of the particle diameter and temperature.

The temperature is then used to determine the LII signal, based on Planck's law, and the spectral properties of the detection system. More information on the method used to model the LII signal here can be found in [Hofmann 2007].

2.3.1.2   Two-Color LII

For a typical detection wavelength, the exponent in Eq. 2.3.12 becomes ~3.2. While it is clear $3.2 \neq 3$, it is a fair approximation for a first approach. It has been shown that this discrepancy can be corrected for if the particle size distribution is known [Reimann 2008]. Alternatively, Smallwood *et. al* [Smallwood 2002; Snelling 2005] have proposed a novel approach where the soot volume fraction is determined by measuring the absolute incandescence intensity. The LII system must first by calibrated with a light source of known radiance, then the signal detected at two or more wavelengths. The signals can then be related to a temperature using two-color pyrometry and the soot volume fraction expressed as

$$f_V = \frac{V_{\mathrm{EXP}}\left[\exp(hc/k_{\mathrm{B}}\lambda_{\mathrm{det}}T_p)-1\right]}{\eta G_{\mathrm{EXP}}\dfrac{12\pi c^2 h}{\lambda_{\mathrm{det}}^6}E(m_{\lambda_{\mathrm{det}}})w} \qquad (2.3.17)$$

where w is the laser sheet thickness, G_{EXP} is the detector gain, η is a calibration constant and V_{EXP} is the experimental signal (or voltage here).

This approach has a number of advantages over alternative approaches. There is no longer a need to make the approximation that $3 \approx 3.2$. Coupling this approach with low fluence LII is know as auto-compensating LII because it accounts for variations in particle temperature across the measurement volume due to variations in the experimental conditions. As a result, it is no longer necessary to operate an experiment in the saturation

26

regime, where significant morphological changes to the soot particles are observed, in order to compensate for fluctuations in beam intensity. This approach also provides quantitative soot volume fraction without having to apply an independent calibration to the results. Further, this approach is dependent only on knowledge of $E(m)$ and not K_{ext}, improving the reliability of the calibration. The two-color LII approach could also be applied to TR-LII for the determination of particle sizes using the time dependence of the particle temperature, but that is outside the scope of this work.

2.3.2   Laser-Induced Fluorescence

Fluorescence is the spontaneous emission of radiation from an upper energy level, which has been excited by an external source of energy, to a lower energy state. In laser-induced fluorescence (LIF), a molecule is promoted to the excited state when it absorbs a photon from the laser. Since the laser is tuned to a resonant transition in the molecule, the LIF cross sections can be quite large. As a result, LIF from certain species may be measured in concentrations below one part-per-million (ppm).

To first order, the process is modeled as a two-level problem, which is a reasonable starting point for a simple diatomic molecule such as NO, OH, CH, etc. A schematic of the process is shown in Figure 2.3.1. All "wavy" lines correspond to processes that involve radiative energy transfer (i.e., emit or absorb a photon), while the straight lines correspond to nonradiative energy transfer. b_{12} and b_{21} are the rate coefficients of stimulated absorption and emission respectively; where $b_{ij}=B_{ij}I_v/c$, where B_{ij} is the Einstein rate coefficient for stimulated absorption/emission respectively, I_v is the laser irradiance per unit frequency (in W/cm^2/s), and c is the speed of light. A_{21} is the Einstein rate coefficient rate for spontaneous emission; Q_{21} represents the collisional

quenching rate constant; W is the photoionization rate constant; P is the predissociation rate constant.

Writing the rate equations for the temporal derivatives of the state population densities N for states 1 and 2 gives:

$$\frac{dN_1}{dt} = -N_1 b_{12} + N_2(b_{21} + A_{21} + Q_{21}) \qquad (2.3.17)$$

$$\frac{dN_2}{dt} = N_1 b_{12} - N_2(b_{21} + A_{21} + Q_{21} + P + W_{2i}) \qquad (2.3.18)$$

where the population densities are multiplied by the rate coefficients into and out of the states as appropriate. If P and W_{2i} are considered to be negligible, which is a reasonable assumption if moderate laser energies are used, then

$$\frac{dN_1}{dt} = -\frac{dN_2}{dt} \qquad (2.3.19)$$

and

$$N_1 + N_2 = N_1^0 \qquad (2.3.20)$$

is the total population density, which is a constant. Under steady-state conditions Eq. 2.3.19 = 0, and the fluorescence rate F can be written as

$$F = CN_1^0 \frac{B_{12}}{B_{12} + B_{21}} \cdot \frac{A_{21}}{1 + I_v^{sat}/I_v} \qquad (2.3.21)$$

where C is an experimental constant and the saturation spectral intensity, I_v^{sat}, is

$$I_v^{sat} = \frac{Q_{21} + A_{21}}{B_{12} + B_{21}} \cdot c. \qquad (2.3.22)$$

In the linear regime (where $I_v \ll I_v^{sat}$), F becomes
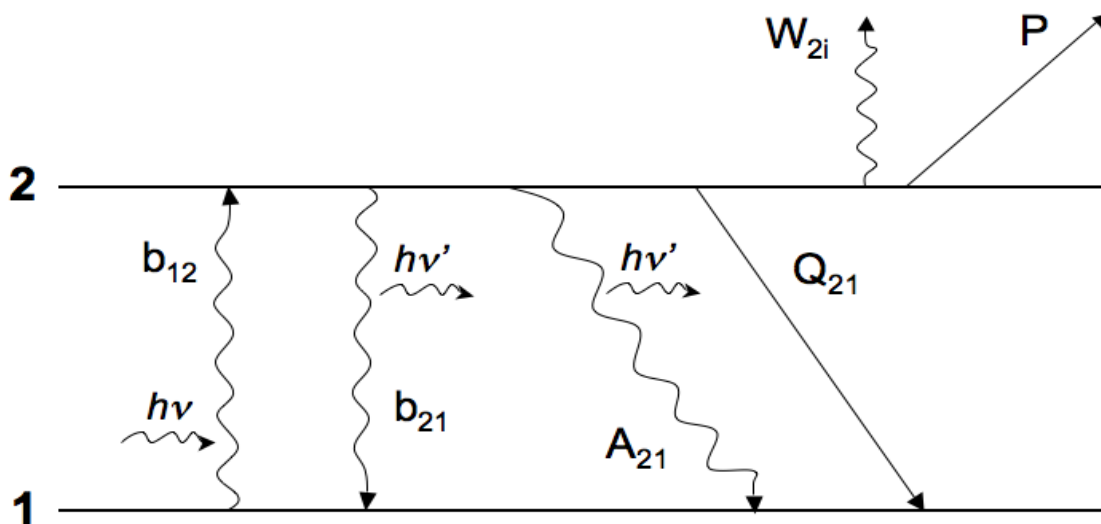
Figure 2.3.1: Two-level energy diagram used to model the laser-induced fluorescence process.

$$F = C_{\text{exp}} B_{12} I_v N_1^0 \frac{A_{21}}{A_{21} + Q_{21}}. \tag{2.3.23}$$

Here C_{exp} is an experimental constant that can be determined using calibration gases, B_{21}

and I_v are constant. N_1^0 is the number density of target molecules in the ground state being

pumped by the laser; $\dfrac{A_{21}}{A_{21} + Q_{21}}$ is the efficiency that an excited molecule will fluoresce.

A_{21} is tabulated for most targeted molecules; N_1^0 and Q_{21} must be modeled for the

particular molecule under investigation in order to obtain quantitative results. Typically,

$A_{21} \ll Q_{21}$ and *can* be neglected.

2.3.2.1   Boltzmann Correction

In order to represent a real molecule, the two-state fluorescence model must be

expanded to include the rotational and vibrational population distribution of the lower

electronic state. The fraction of molecules in a particular energy state j may be related to

the total number density using Boltzmann statistics. Where $N_j = N_{\text{tot}} f_j$ is the number

density of molecules in state j, N_{tot} is the total number density of molecules and f_j is the

fraction of these molecules in state j due to thermal population.

f_j can be expressed as

$$f_j = \frac{g_j e^{-E_j/k_b T}}{\sum_i g_i e^{-E_i/k_b T}} \tag{2.3.24}$$

where E_j is the energy of molecular state j, k_b is the Boltzmann constant, and T is the

temperature; the denominator is the partition function of the system. To first

approximation the electronic, rotational, and vibrational energies of a molecule are

30

separable, so the total fraction of molecules in a given electronic (f_n) / rotational (f_J) / vibrational (f_v) level is simply the product of the individual state fractional populations:

$$f_{n,v,J} = f_n f_v f_J .$$

(2.3.25)

For most species and temperatures encountered in combustion applications, the energy of the first electronic state is significantly larger than $k_b T$, so all molecules may be assumed to reside in the ground electronic level ($f_n = 1$).

The rotational fraction is derived from modeling a rigid rotor:

$$f_J = (2J + 1)\frac{\overline{B}}{k_b T}e^{-\frac{\overline{B}}{k_b T}J(J+1)}$$

(2.3.26)

where J is the rotational quantum number, and B is the rotational constant. ($2J+1$) is the degeneracy of the partition function and energy in state J. The vibrational fraction

$$f_v = e^{-vhc\omega_e/k_b T}\left(1 - e^{-hc\omega_e/k_b T}\right)$$

(2.3.27)

considers a harmonic oscillator with an energy $E_v = \omega_e(v + 1/2)$, where v is the vibrational quantum number and ω_e represents the spacing between energy levels (in cm^{-1}).

Accounting for the Boltzmann correction, the fluorescence signal can now be rewritten to account for our the particular energy level:

$$F = C_{exp}B_{12}I_v N_{tot}f_1 \frac{A_{21}}{A_{21} + Q_{21}} .$$

(2.3.28)

N_{tot} is now the total number density, and f_1 is the population fraction in state 1 (the initial state).

2.3.2.2　Quenching Correction

If we assume that collisional quenching is the dominant term in Q_{21}, the total

quenching rate can be calculated from the number density of the ith collision partner (N_i),

the collision cross section (σ_i), and the relative velocity of the collision partner and the

excited molecule (v_i)

$$Q_{21} = \sum_i N_i \sigma_i v_i$$

(2.3.29)

This is summed over all collision partners. Here the individual collisional cross sections

may be a function of temperature and pressure, and can vary drastically from collision

partner to collision partner. The relative velocity, v_i, is based on the thermally averaged

velocity of the reduced mass pair

$$v_i = \left\langle v_{i,m} \right\rangle = \left(\frac{8k_b T}{\pi \mu_{i,m}} \right)^{1/2}$$

(2.3.30)

where $\mu_{i,m}$ is the reduced mass of species i and excited molecule m. This can easily be

calculated given the temperature. Assuming a knowledge of the temperature and number

densities, determination the relevant quenching cross sections requires a detailed

understanding of the energy transfer parameters for the excited molecule.

2.3.2.3　LIF in a Molecule

C_{exp} and I_v are known from experimental parameters; A_{21} and B_{12} are tabulated

values that can be determined from references (see, e.g., [Eckbreth 1996]). In order to

determine N_{tot} from measurements of F, the Boltzmann correction, f_1, and the quenching

correction, Q_{21}, must be determined. Figure 2.3.2 shows a Jablonski energy level diagram

plotted as a function of the nuclear coordinate for the LIF process in a more realistic

molecule. In this case, the laser excites the (0, 0) transition (where the notation is (υ', υ'') for (upper, lower)) A$\rightarrow$ X band. Laser-induced fluorescence is best viewed as an absorption followed after some finite amount of time by spontaneous emission from the excited manifold (termed manifold, because the fluorescence observed may not be from the directly pumped state). In practice, the observed fluorescence wavelength is different from that of the incident excitation, and occurs primarily at longer wavelengths, termed Stokes shifted. Though present, the fluorescence that occurs at the excitation wavelength, termed resonant fluorescence, is not frequently used because it is difficult to distinguish it from the Rayleigh scattered light.
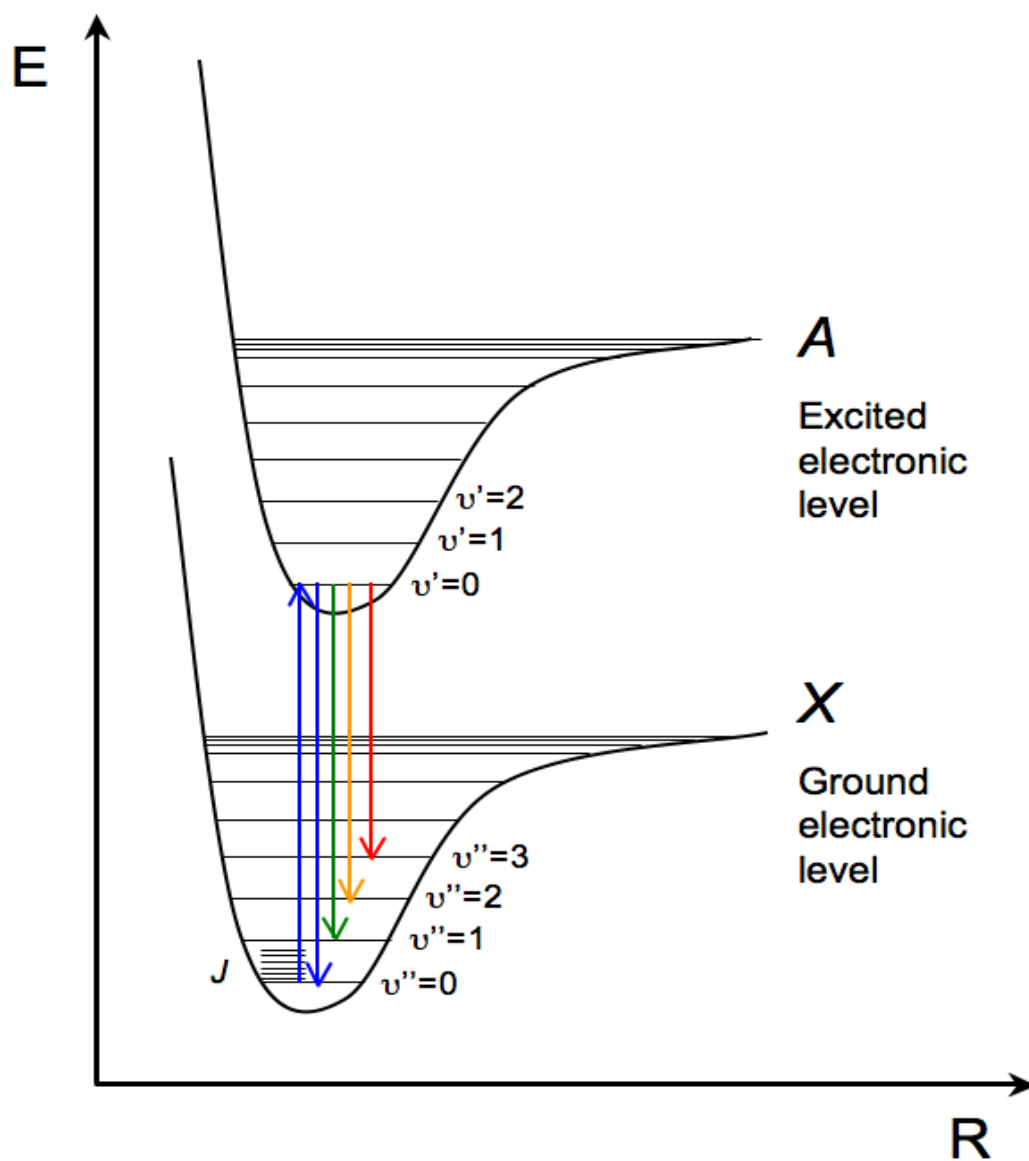
Figure 2.3.2: Jablonski (energy level) diagram plotted as a function of nuclear coordinate for an LIF process pumping the (0,0) transition in the A➔X band of a molecule.

CHAPTER 3

3 Measurements in Steady Flames

3.1 Introduction

Steady, laminar diffusion flames provide an interesting study for the comparison of experiments and computations. The steady nature of the flames affords the ability to take time-averaged measurements of a number of flame characteristics including temperature, major and minor species, and sooting characteristics. Further, these systems enable straightforward resolution of the spatial and temporal scales involved. The large quantity of information that can be gained provides a substantial database for comparison with computational results.

As confidence in the ability of the computational model to predict the details within a given flame configuration improves, the level of complexity of the problem can be increased. This can be done by generating perturbations in the flow field, or by increasing the level of chemical complexity in the system through the addition of more complex fuels and by moving toward sooting conditions.

Measurements in sooting flames can be complex due to interferences from soot and soot precursors, and due to uncertainties in the optical properties of soot. In an effort to provide more confidence in the experimental techniques employed, data is first taken in the Santoro burner, as the soot characteristics in that flame have been well characterized.

3.1.1   Santoro Burner

Initial measurements are carried out on a Santoro burner [Santoro 1983], run under nominal operating conditions [Santoro 1983; Koylu 1997; Schulz 2006b] (condition 1 (NS) in [Santoro 1983]). Briefly, the burner is composed of two concentric brass tubes of 11.1 mm and 101.6 mm inner diameter, with the fuel flowing through the central tube and air flowing through the coflow. A variety of inserts (glass beads, ceramic honeycomb) are used as flow straighteners. The fuel tube extends 4 mm beyond the exit plane of the coflow. A 405 mm long brass cylinder is used as a chimney to isolate the flame from air currents in the laboratory. Slots and windows are cut in the chimney to provide optical access, with the windows sealed as well as possible to avoid entraining air into the chimney. The condition tested here (1 (NS)) consists of pure ethylene in the fuel tube at a flow rate of 3.85 cm^3/s (3.98 cm/s exit velocity) with an air flow rate of 713.3 cm^3/s (8.90 cm/s exit velocity) in the coflow.

This burner has been the subject of numerous studies that measured soot temperature from pyrometry and thermocouple measurements, soot volume fraction and particle size characteristics using LII [Schulz 2006b], laser extinction and scattering [Santoro 1983], and probe sampling techniques (with TEM) [Dobbins 1987; Puri 1993; Koylu 1997; Vander Wal 1999]. This burner is used as one of the target flames for the LII workshops in order to provide a point of comparison between investigators.

3.2   Burner Configuration

The base flame used in previous experimental and numerical investigations has been an atmospheric pressure, axisymmetric, coflowing, nonpremixed laminar flame. The burner used in this study, shown in Figure 3.2.1, shares all of the characteristics of the burners used in previous studies. Flames are generated with a burner in which the fuel flows from an uncooled 4.0 mm inner diameter vertical tube (wall thickness 0.38 mm, parabolic flow) into a concentric, 74 mm diameter air coflow (plug flow). Older versions of the burner use a 50 mm diameter coflow, but the same flame structure is expected. The details of the burner are kept consistent with previous studies in order to provide continuity between earlier experiments and numerical calculations, and further studies. The fuel and oxidizer flows are set with an average cold-flow velocity of 35 cm/sec. The flame is lifted above the burner surface (~6 mm for methane, ~3 mm for ethylene), preventing heat transfer from the flame to the burner. As a result, adiabatic boundary conditions can be used at the burner surface for the numerical calculations. Various fuels (e.g., ethylene, C_2H_4, and methane, CH_4) are investigated with differing percentages of nitrogen (N_2) dilution (by volume). Dilution of the fuel with inert nitrogen provides the ability to vary the soot loading within the flame. Further, a speaker is placed in the fuel plenum to allow for modulation of the fuel flow rate to produce forced, time-varying flames (see Chapter 4).
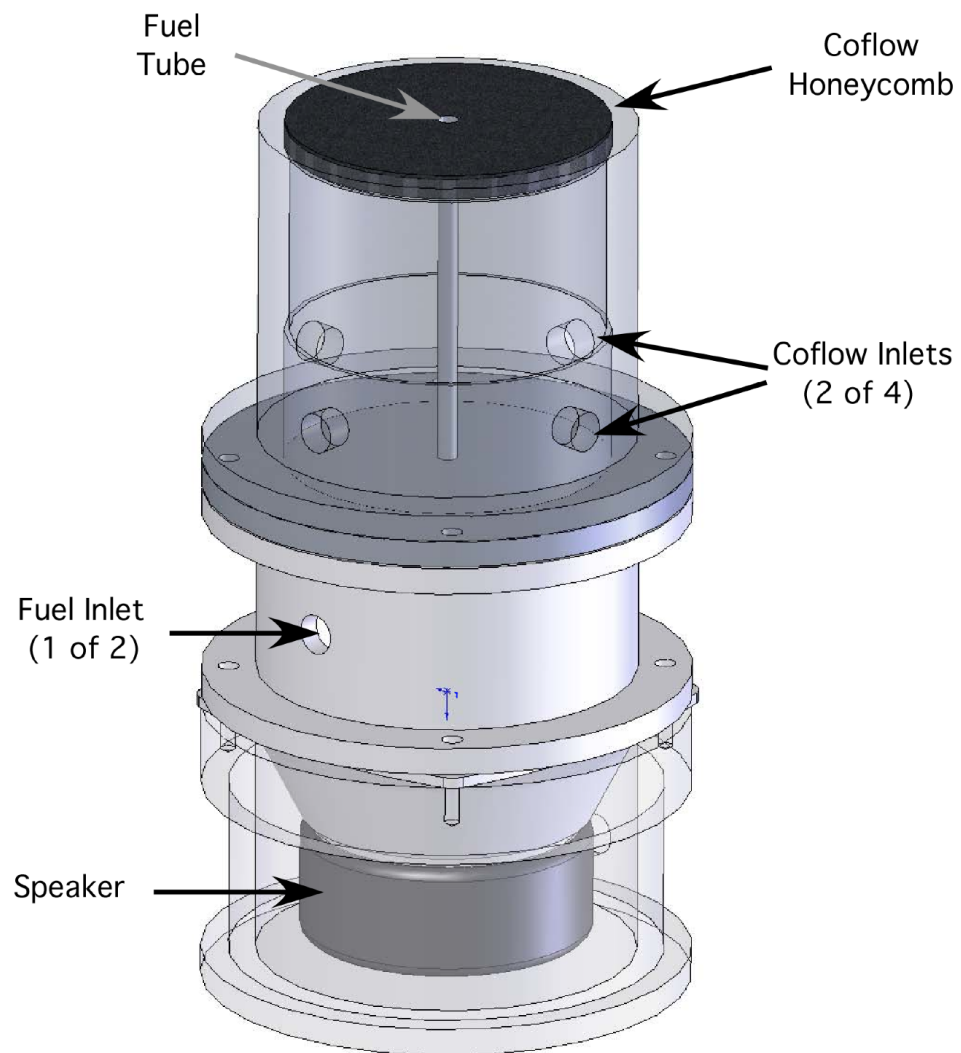
Figure 3.1.1: Experimental coflow diffusion flame burner.

3.3 Computational Model

All computational work in this document was carried out in Professor Mitchell Smooke's laboratory at Yale University. The computational work for the study of sooting flames was carried out by Professor Mitchell Smooke, in collaboration with Dr. Meredith Colket and Dr. Robert Hall at United Technologies Research Center (UTRC); the computational work for the forced flames in Chapter 4 was carried out by Dr. Seth Dworkin; the computational work for the nonsooting NO study in Section 5.2 was carried out by Dr. Beth Anne Bennett; the computational work for the study on PAH formation was carried out by Luca Tossato. The computational approach will be outlined in this section, along with the soot model. Any variations to the details given here will be outlined in the appropriate sections.

3.3.1 Numerical Model

The model considers an unconfined, axisymmetric, laminar diffusion flame in which a cylindrical fuel stream is surrounded by a coflowing oxidizer jet. The full set of elliptic two-dimensional governing equations – mass, momentum, species and energy are solved in a vorticity-velocity formulation [Ern 1993], using a flame sheet as a starting estimate [Keyes 1987], and the differential operators are discretized on an adaptively refined mesh. The resulting nonlinear equations are solved by a combination of time integration and Newton's method with several theoretical estimates [Smooke 1983] that help determine when a new Jacobian should be reformed. The Newton equations are solved by a preconditioned Bi-CGSTAB iteration with a Gauss-Seidel preconditioner.

Pseudo time-stepping is used to ease convergence difficulties associated with the starting estimate. The size of the time steps is chosen by monitoring the local truncation error of the time discretization process (see also, [Smooke 1989]). The binary diffusion coefficients, the viscosity, the thermal conductivity of the mixture, the chemical production rates as well as the thermodynamic quantities were evaluated using vectorized and highly optimized transport and chemistry libraries [Giovangigli 1987].

3.3.2 Soot Model

The inception model is based on the sequence of growing naphthalenyl to pyrenyl through sequential acetylene addition, H-atom elimination, H-atom abstraction, and acetylene addition followed by ring closure. Overall, the reaction can be written $C_{10}H_7 + 3C_2H_2 \Leftrightarrow C_{16}H_9 + 2H + H_2$. This sequence is assumed to continue to form yet larger polycyclic aromatic hydrocarbon (PAH) structures with the overall balance of $C_{10}H_7 + 3nC_2H_2 \Leftrightarrow C_{10+6n}H_{7+2n} + 2nH + nH_2$. Quasi steady-state concentrations of intermediate PAHs are assumed, leading to steady-state expressions for the formation rates of these high molecular weight condensed PAHs. The computed soot results are relatively independent of the number, n, assigned to the inception species and equal to 21 in this work.

The surface growth model used in the simulations is based on the premixed flame data of Harris-Weiner [Harris 1983] where we assumed an activation energy of $E_s = 31.8$ kcal/mole [Hura 1988] and where we multiplied the nominal Arrhenius factor by two (see also [McEnally 1998; Smooke 1999a; Smooke 2004]). Surface growth is first order in acetylene concentration in this model. Oxidation of soot by O_2 and OH is treated as described in [McEnally 1998; Smooke 1999a]. In the assumed free-molecule,

large Knudsen number regime, surface growth and oxidation rates are proportional to particle surface area.

The growth of soot particles is modeled as an aerosol dynamics problem, using the well-known sectional particle size representation for spheres [Gelbard 1980]. The application of this approach to soot modeling is described in [Hall 1997; McEnally 1998; Smooke 1999a; Smooke 2004; Smooke 2005]. The contributions from the inception processes are incorporated as a source term in the dynamical equation for the first sectional bin, whose lower mass boundary is set equal to the mass of the assumed inception species. Calculated results were not significantly sensitive to the number of sections assumed, with 20 sections used in all the calculations reported here.

Radiative losses can have a significant influence on NO levels in flames where soot is present compared to nonsooting systems [Naik 2003b; Naik 2003a; Zhu 2005]. For the small flames computed in this study with low soot volume fractions, the power radiated from soot and gas bands (CO_2, H_2O, and CO) can be computed in the optically thin limit using the expressions in [Hall 1994]. While temperature changes associated with radiation are not large, the great sensitivity of soot growth (and NO) to temperatures makes the incorporation of radiation effects important. It should be noted that in higher soot loading flames, the optically thin model tends to overestimate the radiation losses and, in principle, some re-absorption of thermal emissions can occur, particularly on or near the centerline, which receives emissions from surrounding regions of the flame. This optical   thickness effect reduces the net rate of thermal radiation energy loss and locally raises the temperature. Future work should include the use of a more sophisticated soot radiation model that doesn't rely on an optically thin approximation (see [Liu 2002],

e.g.). Overall, however, the soot formation model has given quite satisfactory agreement with measured peak soot volume fractions as well as soot spatial distributions and temperatures in the flames studied (see, e.g., [McEnally 1998; Smooke 1999a; Smooke 2004; Smooke 2005]).

The chemical mechanism was derived from one of the more comprehensive and well-validated sets available for ethylene [Sun 1996]. The resultant mechanism contains 476 reactions and 66 chemical species. Twenty soot sections are included in the formulation. The result is a model that requires a total of 90 dependent variables to be solved at each grid point. The system is closed with the ideal gas law and appropriate boundary conditions are applied on each side of the computational domain. Local properties are evaluated via transport and chemistry libraries. The sectional thermophoretic velocities in the free molecule regime are given in [Hall 1997] as are the sectional diffusion velocities written with a mass-weighted mean diffusion coefficient for each size class.

3.4   Soot Pyrometry

The objective of this work was to examine the possibility and application of using a relatively low-cost color digital camera as an optical pyrometer. The camera's detector uses a color filter array (CFA), coated directly onto the monochrome detector, to sample red, green, and blue (RGB) signals. Ordinarily, the camera's processor recreates scenes by combining the RGB signals to determine the image color at each pixel. A demosaicing algorithm, which combines the color values at a pixel and its neighbor pixels, is used to interpolate color values from a GRGB Bayer Pattern and provide the full color at each pixel [Bayer 1976; Chang 2004]. The maximum pixel mismatch from this interpolation is expected to be less than one pixel. Alternatively, the RGB color data can be used separately as three two-dimensional images that do not need to be spatially matched. The intensity of radiation of soot particles at flame temperatures can be imaged at the three wavelengths of the CFA and the temperature can then be calculated using two-color ratio pyrometry. Since consumer digital cameras are not intended for use as scientific detectors, it is necessary to investigate some aspects of the data acquisition that for a scientific detector are usually manufacturer-tested and specified. The camera can then be used to image the soot emissions in flames.

3.4.1   Digital Camera

Normally used as a consumer product, the Nikon D70 single lens reflex (SLR) digital camera has been used here as a multi-wavelength optical pyrometer. The D70 was chosen because it offered the necessary manual user control of settings at a reasonable price. The CCD detector is 23.7 mm by 15.6 mm and has 6.1 million (effective) pixels (2012 x 3038). Data were taken using the Nikon Capture Control software to operate the

camera remotely and to transfer the images to a computer. All image enhancement options, such as sharpness, contrast, color, and saturation, were set to either "normal" or "none," as applicable, in order to ensure shot-to-shot consistency. A white balance of "direct sunlight," with a color temperature of 5200 K, was selected. Once chosen, the same settings were used for all data acquisition.

Files were saved in the camera's "NEF" format, which is Nikon's 12-bit lossless compressed "RAW" format. Although used by many camera manufacturers as a designation for unprocessed images, "RAW" is not a standardized format (unlike TIF, JPG, etc.). Consequently, some careful examination of the resulting image is necessary to ensure consistent reconstruction of the underlying intensity data. To facilitate a more transparent analysis, the open-source image-processing software OMA [Kalt 2009] was modified to be able to import and appropriately display this Nikon-specific data format. Suitable ANSI C-code was adapted from a publicly available software library on the World-Wide Web [Coffin 2005].

3.4.2   Detector Analysis

The performance of the D70 was investigated under controlled conditions. It was verified that the detector signal in all three channels decreased linearly with attenuation and increased linearly with exposure, up to the point where the channels saturate. Figure 3.4.1 demonstrates this linearity of signal as a function of exposure using a region with significant soot incandescence in an ethylene flame as the light source. A colored glass filter was also used as discussed below. Figure 3.4.1 displays the average signal in the center of the sooting region of a 40% C_2H_4 flame as a function of increasing exposure time. Images were taken through a colored glass filter. The data is seen to increase
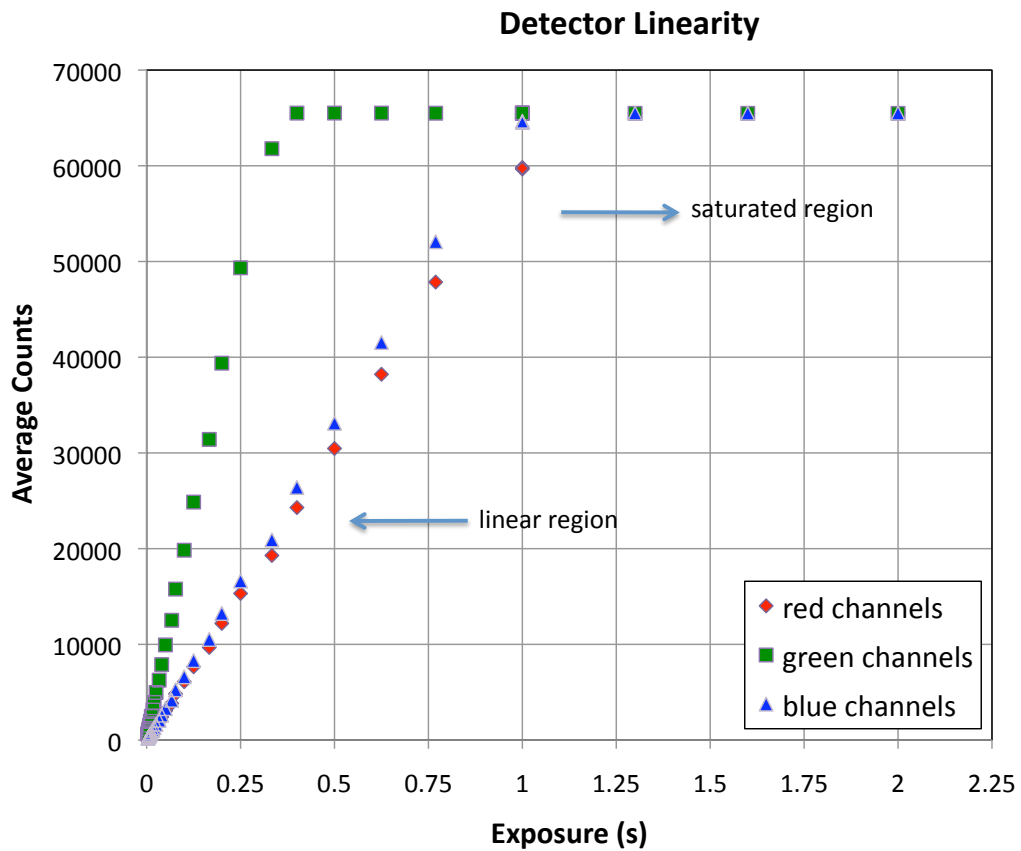
Figure 3.4.1: Measured signals from the three color channels as a function of camera exposure time. Data correspond to a central position of the sooting portion of a 40% ethylene flame. The data demonstrates linear behavior ($R^2 > 0.999$) as the exposure time is increased. The data saturates at the maximum pixel value of 65534.

linearly with increasing exposure time until it saturates at a maximum pixel value of 65534, which is characteristic for 16-bit camera's. A line fit to the data in the linear region results in an R^2 value that is greater than 0.999 for all three color channels. This increase in signal to the point of saturation is what would be expected from a scientific CCD-detector. Within the linear region, the signal ratio between the different color channels exhibits a standard deviation of 1% across all data triplets. In the following, the camera was operated in this linear regime, ensuring proportionality of the channels for a given spectral signal.

It is important to note that the RAW files must be carefully decoded. Early attempts to decipher the RAW files resulted an arbitrarily assigned scale factors to the color channels as a function of detected signal. Though a single color channel did not increase linearly, signal ratios were still consistent and independent of exposure time. So long as the calibration files and the data files are read in consistently, any scale factors should be accounted for. Further, by reading in all three color channels in the same image it is ensured that each color image is treated in the same way. Although this issue has since been resolved, it is important to pay careful attention to the problems that may arise when using a consumer product with proprietary file formats.

3.4.3 CFA Calibration

The next step was the characterization of the detector's spectral response. The detection wavelengths and spectral bandwidth of the CFA were measured in order to calibrate the digital camera. The CFA characterization setup is shown in Figure 3.4.2. The spectrum of an illumination source was imaged using an imaging spectrograph (Jobin Yvon CP200), using a 200 grooves/mm grating and a 0.1-mm entrance slit. The

resultant images of the spectrum are shown in Figure 3.4.3. Images were obtained by the digital camera, and the data were separated into three images corresponding to the red, green and blue channels of the CFA. Spectral scaling was determined by imaging laser lines at 532 nm and at 632.8 nm, and by assuming linear dispersion. The dispersed spectrum was imaged across the camera's detector providing a sample over the visible region of the spectrum, sampled in a single image. Normalization for the spectrum of the illumination source and optical throughput of the spectrograph was obtained by imaging the spectrum with a CCD camera (Photometrics CH350), whose typical spectral response has been tabulated.

Figure 3.4.4a plots the resulting detected light intensity from the spectrograph, as a function of wavelength, for each color channel. A BG colored-glass filter (unmarked, assumed to be BG 7) was placed in front of the camera, in order to achieve a better match in signal magnitudes across the three channels and hence make better use of the dynamic range of the detector. The effect from this filter is accounted for in the measured filter profiles, as data were obtained through the BG filter. Figure 3.4.4b plots the light intensity detected by the CCD camera, the tabulated quantum efficiency of the CH350, and the wavelength dependence of the resulting light source optical throughput normalization.
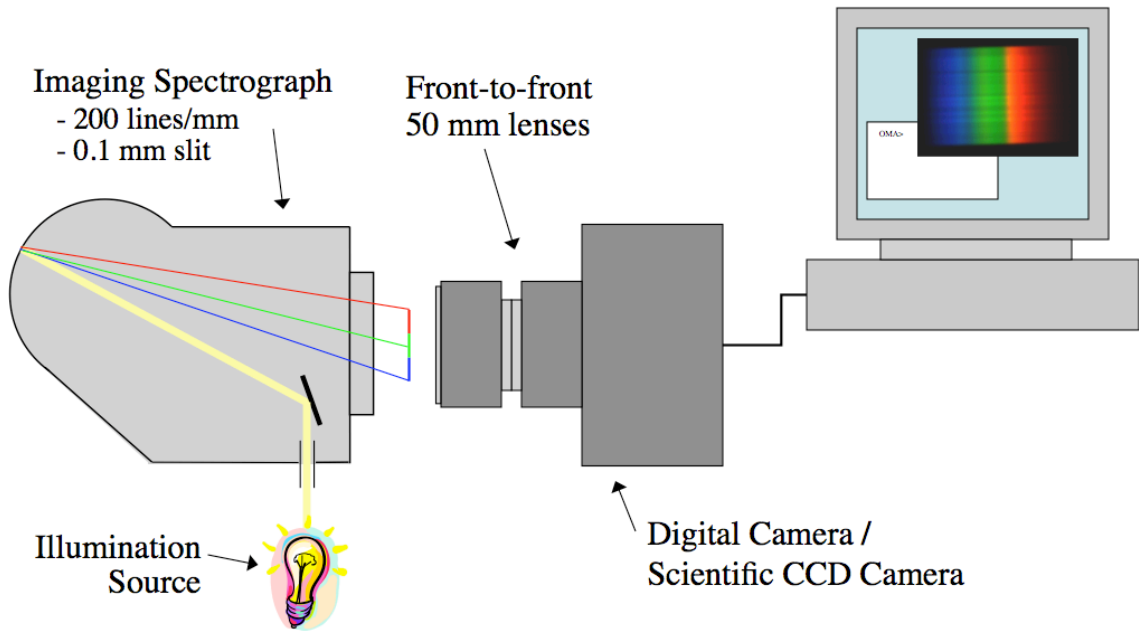
Figure 3.4.2: Setup to characterize the Nikon D70 color filter array (CFA).
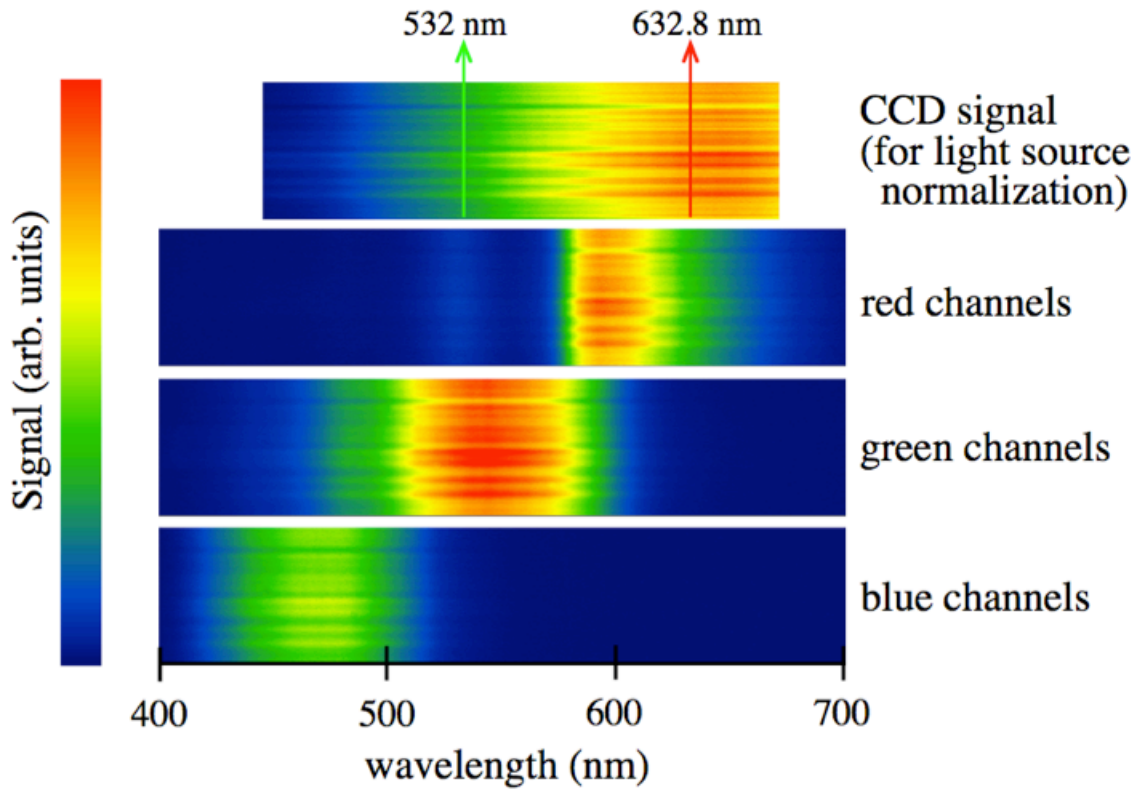
Figure 3.4.3: Resultant images from the calibration of the Nikon D70 color filter array (CFA). The imaged spectrum from the light source was imaged, and separated into the red, green and blue channels. A scientific CCD camera was used to normalize for the spectral response of the illumination and laser lines at 532 nm and 632.8 nm were used to calibrate the spectral dimension.

(a)

Detected Light: Color Filter Array

(b)

Light Source Normalization
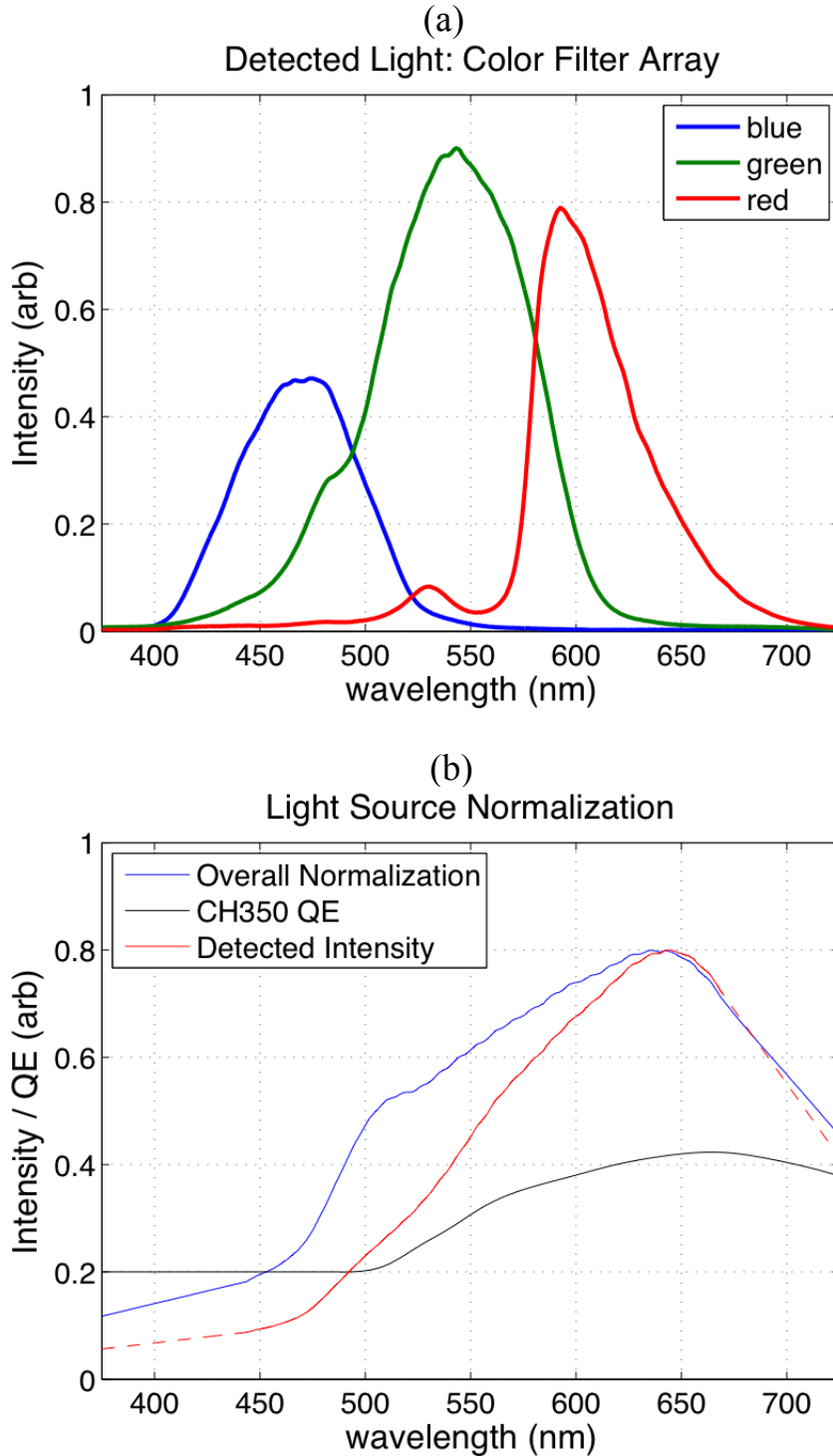
Figure 3.4.4: (a) The resulting detected light intensity from the spectrograph, as a function of wavelength, for each color channel. (b) The light intensity detected by the CCD camera, the tabulated quantum efficiency of the CH350, and the wavelength dependence of the resulting light source optical throughput normalization. The dashed red line indicates where the detected intensity from the CH350 has been extrapolated to cover the range of desired wavelengths.

The curves from Figures 3.4.4a and 3.4.4b are combined to determine the normalized, calibrated filter functions of the digital camera CFA. The overall normalization is applied to the red, green and blue curves and plotted in Figure 3.4.5a for all three color channels. Also plotted is the filter function of the BG colored glass filter, which is already included in the profiles shown. The two-color method requires determination of the filters' central wavelengths, approximated here to be of 579.8, 514.1, 459.3 nm, and bandwidths of 44, 76, and 56 nm, respectively.

The emitted incandescence signal of soot particles at typical flame temperatures (1800 - 2000 K) decreases very rapidly in the visible region from red to blue. The variation in throughput across the channels now should balance the variation in input from the Planck emission spectrum, shown here for a nominal temperature of 2000 K. The effect of the BG filter is to "mirror" the Planck curve, in an effort to provide a consistent signal level across all color channels to best use the dynamic range of the detector. Figure 3.4.5b shows the resulting spectral signal, detected by the each color channel. There are two features worth noting in this plot: the maximum signals across all three channels are reasonably equalized, and the central wavelengths have been red-shifted. The new effective wavelengths of the detected spectrum are now 614.7, 545.7, and 480.0 nm, for the red, green, and blue channels, respectively. The shifts are due to the significant variation of the unfiltered Planck spectrum within the range of wavelengths covered by each channel. It is for this reason that the algorithm used to calculate the temperature iterates the detector's central wavelengths along with the calculated temperature.
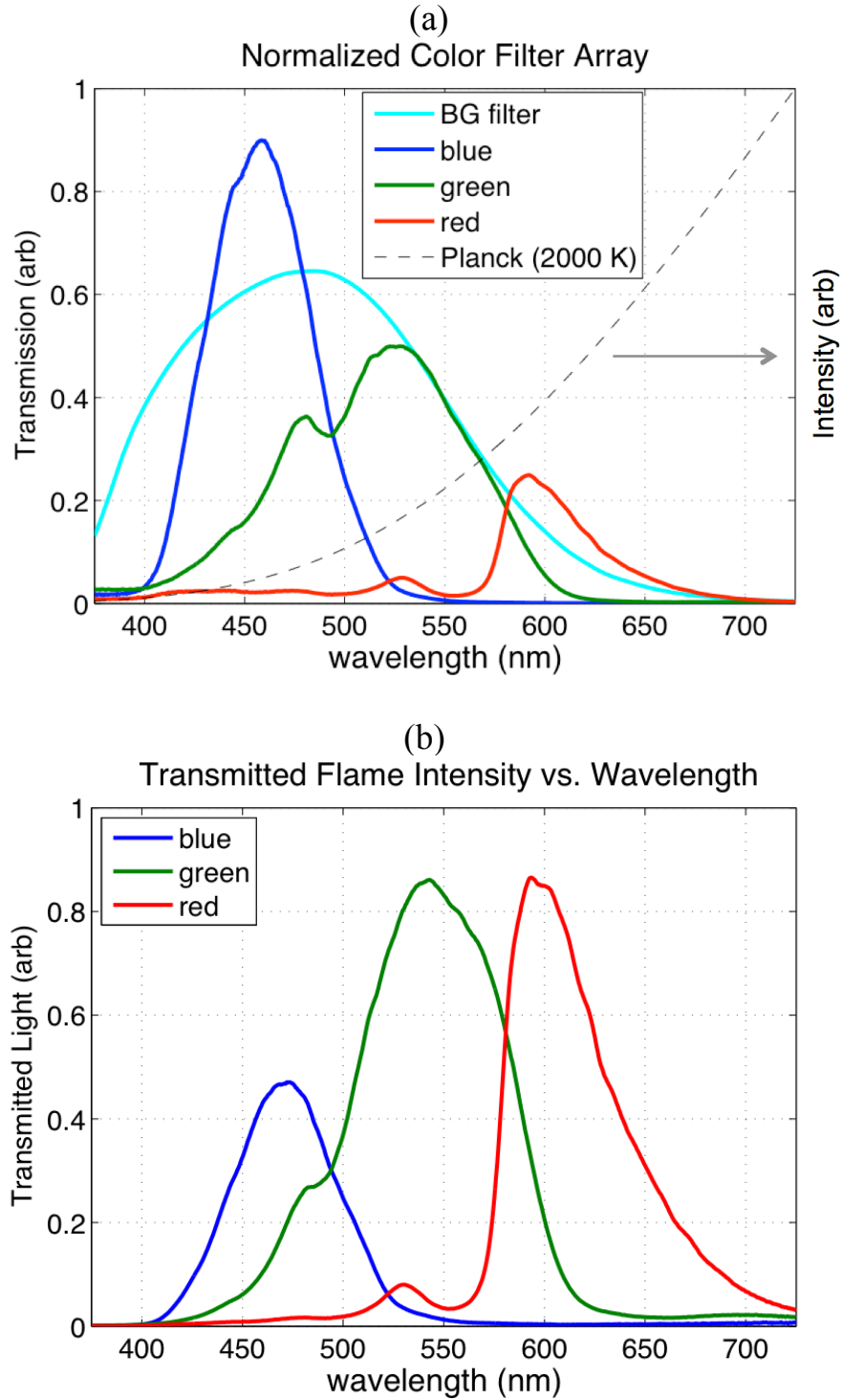
Figure 3.4.5: (a) The calibrated filter functions of the color filter array (CFA) are plotted for the red, green and blue channels. Also plotted is the BG filter and the Planck spectrum at 2000 K. (b) The Planck spectrum is combined with the CFA profiles to determine the spectral dependence of the detected signal for each channel.

3.4.4 Blackbody Calibration

To improve the method's performance, an independent blackbody calibration was performed. Images were taken of an oven at varying temperatures by Sebastian Kaiser at the Combustion Research Facility at the Sandia National Laboratories. In order to check the consistency of the two independent calibration techniques, temperature values for the data from the oven were determined using the CFA calibration. The calculated temperatures were found to be ~100 K higher, on average, than the temperature that was set on the oven. A sensitivity analysis of the CFA calibration, which depends on contributions from a number of different measurements, shows the determination of the measured filter profiles to be critical to the final temperatures calculated, e.g., a shift of the red-channel's central wavelength of 5 nm corresponds to change in calculated temperature of 50 K. Therefore, a blackbody calibration can be considered more robust than a calibration of the camera's CFA. Figure 3.4.6a plots the three color ratios as a function of oven temperature. A plot of the log of the signal ratio between two color channels vs. inverse temperature (see Figure 3.4.6b) is found to be linear, as expected, for all three two-color combinations. Lines fit to this data have R^2 values better than 0.998, providing further validation of the use of the digital camera as a scientific instrument.
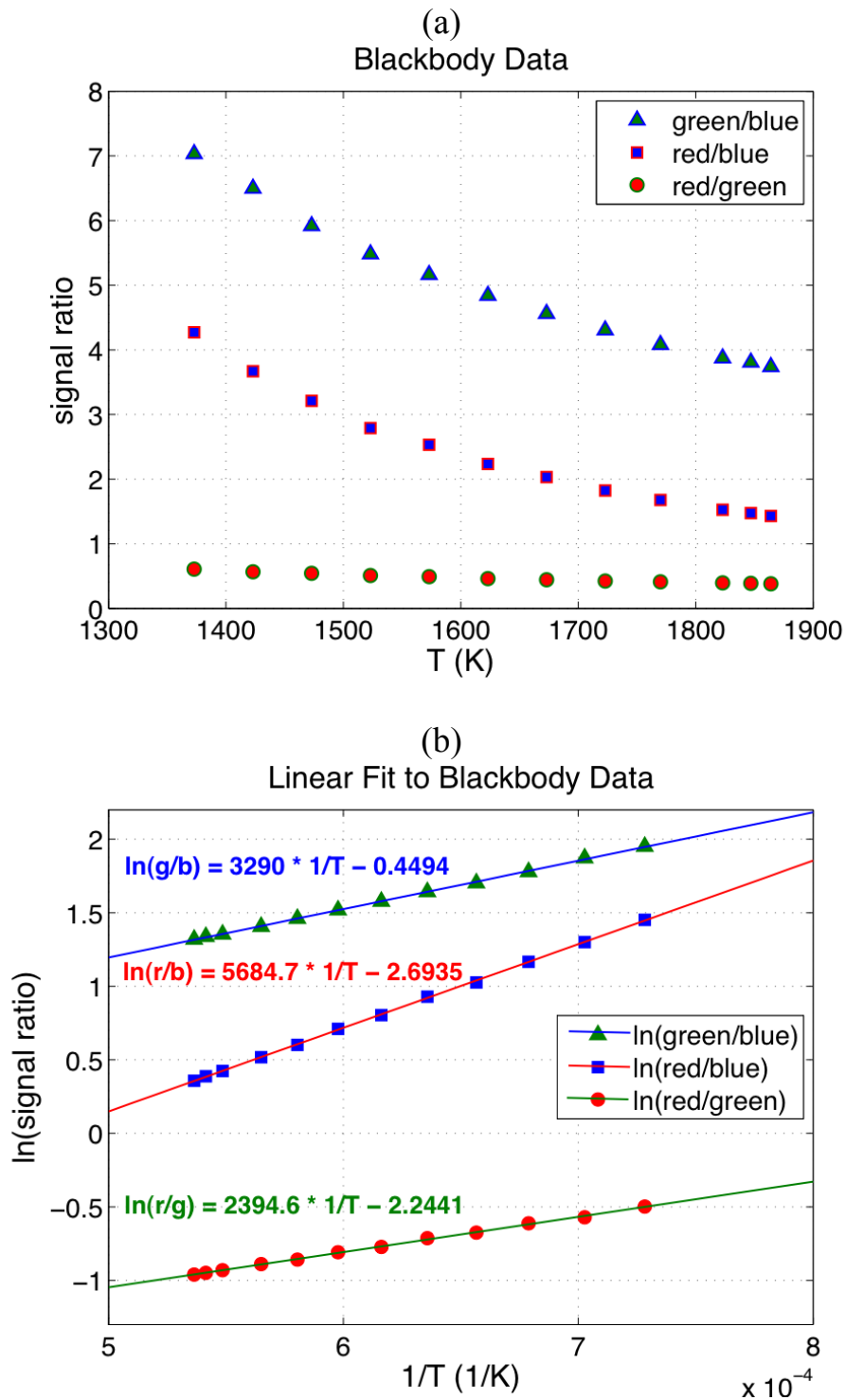
Figure 3.4.6: (a) Results from the blackbody calibration for the Nikon D70 for all three color ratios. (b) The blackbody data is plotted as the log of the signal ratios vs. the inverse of temperature. The fit lines are also shown.

3.4.5   Experimental Images

Following the detector characterization, data were taken in sooting, axisymmetric, laminar ethylene diffusion flames, with varying degrees of fuel-dilution by nitrogen. Details on the burner configuration were given in Section 3.2. Images were taken of the soot radiation at C_2H_4 concentrations of 32%, 40%, 60%, and 80% (by volume), in a balance of N_2. The flames were imaged through the BG filter at f/16 with an 85 mm focal length lens, offset from the camera body with an extension ring. The lens configuration was chosen to approximate parallel ray collection, which is a necessary assumption of an Abel inversion [Dasch 1992; Walsh 2000b]. Figure 3.4.7 shows a sample image from the 60% flame, and the process to produce three radial profiles for each color channel. First, the image from the digital camera is separated into its red, green and blue components. This provides a projected image for each color channel. Because the flames are axisymmetric, an Abel inversion is then used to reconstruct the two-dimensional radial profile of soot emission. Experimental temperatures can then be computed using the two-color method by taking the signal ratio for each color combination. The resulting temperature calculations will be compared with the computational results.
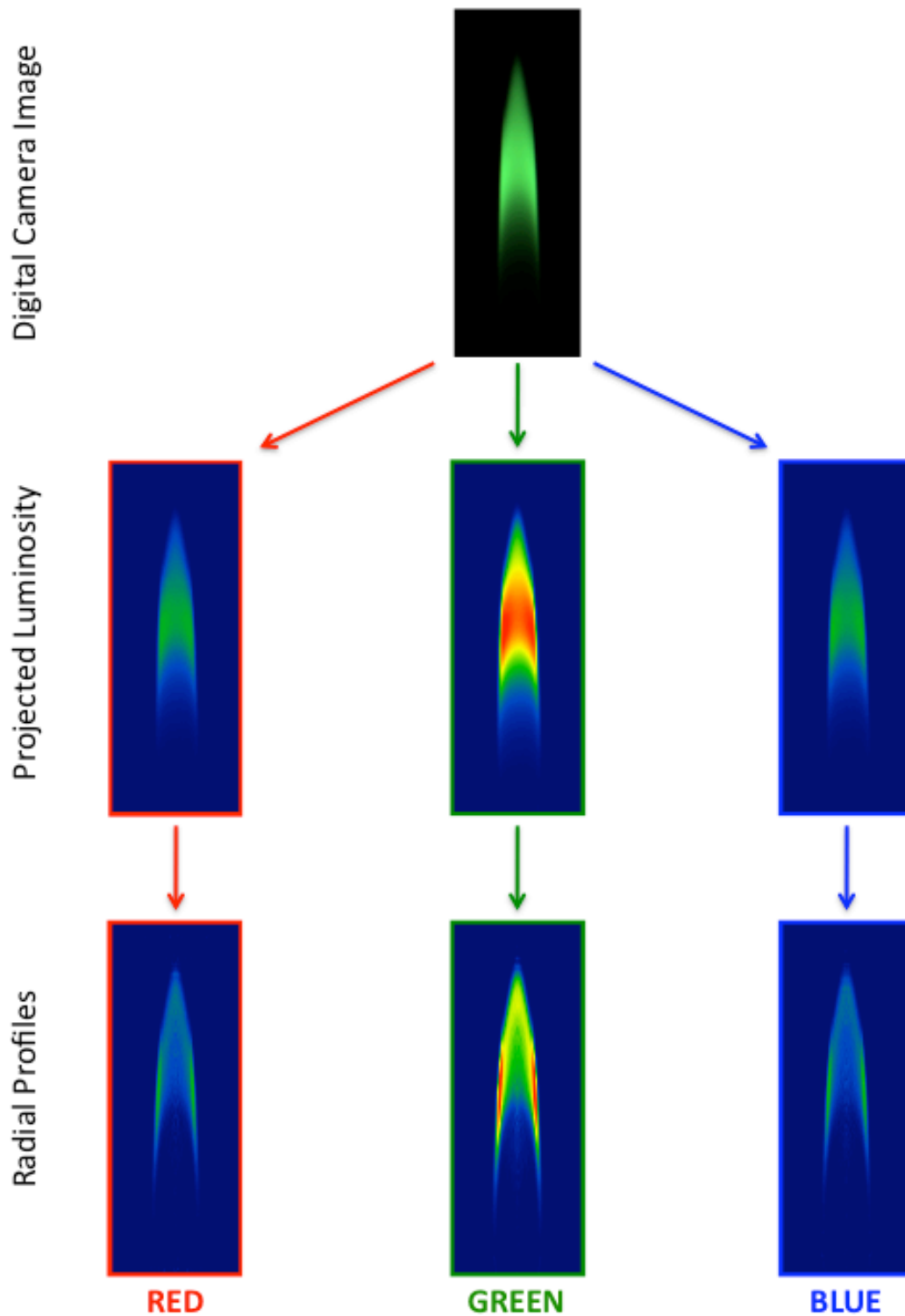
Figure 3.4.7: An image of a 60% C_2H_4 flame using the Nikon D70 digital camera is separated into its red, green and blue components. This projected luminosity is then Abel inverted to produce a radial profile for each color channel.

3.4.6   Comparison of Results

Experimental temperatures are plotted in Figure 3.4.8a. Computational

temperatures are plotted in Figure 3.4.8b for regions where the local soot volume fraction

is at least 10% of the flame's maximum soot volume fraction. All results indicate a

decrease in flame temperature as the fuel mole fraction increases, as the increased levels

of soot results in a radiative loss of flame temperature. The lower-concentration flames

tend to have higher peak temperatures, with their highest temperatures located more

towards the top of the soot cone. The higher-concentration flames tend to have lower

peak temperatures, with their highest temperatures located along the edges of the flame.

Also, lower temperatures are observed on the interior of the flame, compared with the

wings and tip, both computationally and experimentally. The computations predict lower

temperatures overall that what is observed experimentally.

Use of the blackbody calibration provides a reference to an absolute light intensity

for a given temperature and experimental geometry. This can then be used to relate the

calculated temperature to the apparent temperature. This formulation for the soot volume

fraction was used to determine the experimental soot volume fraction from the pyrometer

data (shown in Figure 3.4.9). Comparing the temperature fields to the images of soot

volume fraction shows a correlation between the higher temperatures and soot location.

The lower-concentration flames tend to have higher peak temperatures, with their highest

temperatures located more towards the top of the soot cone. The higher-concentration

flames tend to have lower peak temperatures, with their highest temperatures located

along the edges of the flame. Results from soot volume fraction measurements will be

57
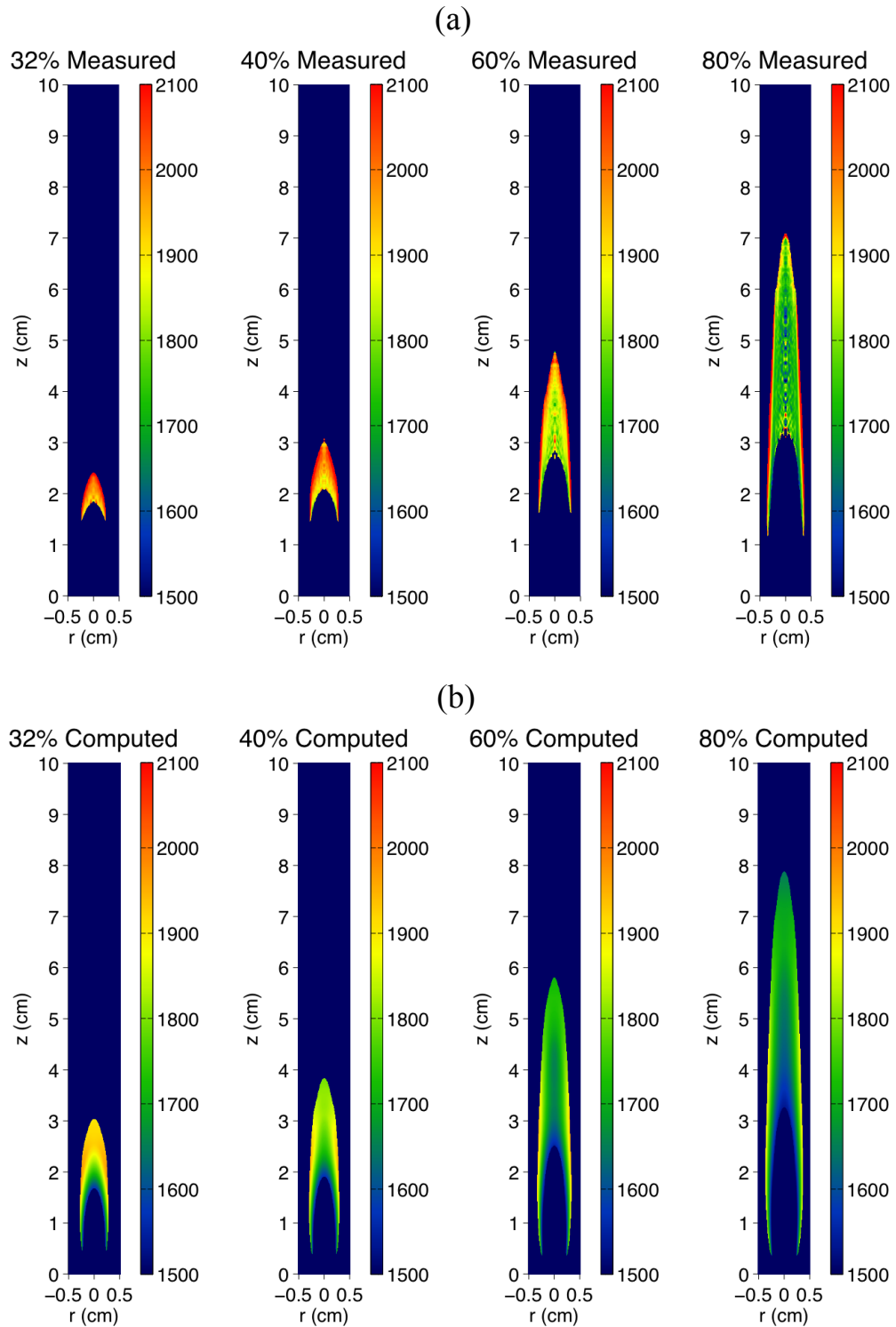
Figure 3.4.8: (a) Experimentally determined temperatures using pyrometer data and (b) computational temperatures in the sooting region for a series of ethylene flames (32%, 40%, 60% and 80% C_2H_4, diluted by N_2). All flames are shown on the same spatial and color scales.
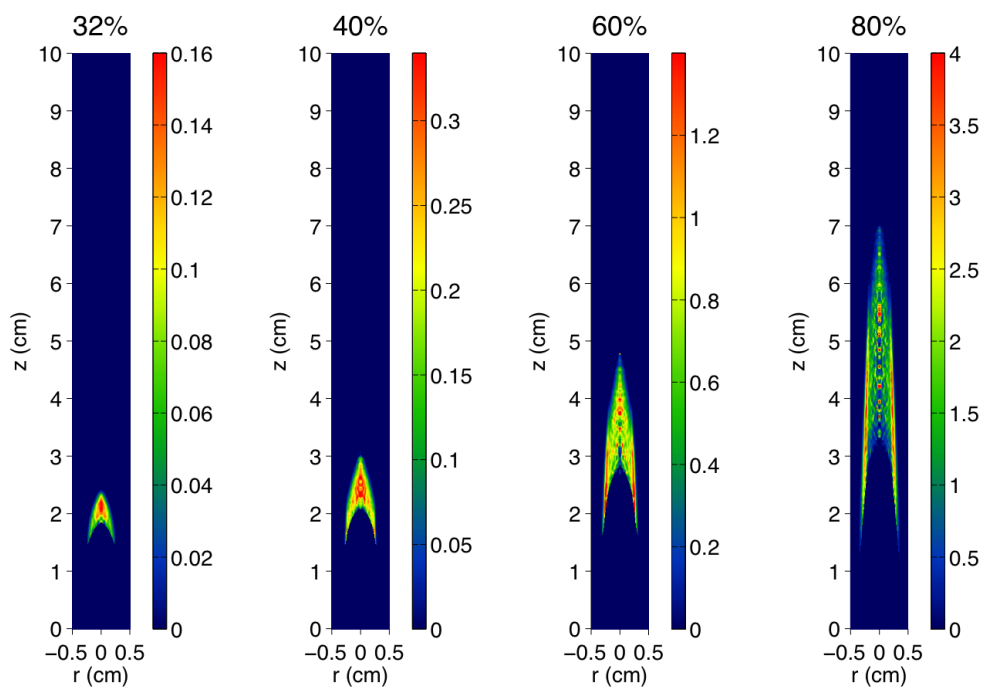
Figure 3.4.9: Experimentally determined soot volume fraction (in ppm) for a series of ethylene flames (32%, 40%, 60% and 80% C_2H_4, diluted by N_2) using pyrometer data. All flames are shown on the same spatial scale, with varying color scales. Data is shown here using $K_{ext} = 8.6$.

discussed in more detail in Section 3.5. Results from Section 3.5 will be compared with the results shown here in Chapter 5.

3.4.7 Conclusions

The Nikon D70 consumer digital camera was examined as a practical, low-cost alternative to scientific CCD cameras, for use as an optical pyrometer. It was verified that the D70 could be operated with settings that provided a linear response to a constant signal, and signal values were consistent from shot to shot. Tests of the validity of using a consumer digital camera as a pyrometer were promising, as reasonable temperature measurements were obtained from axisymmetric laminar ethylene flames. Comparisons were made with a numerical model that calculates the soot and temperature field. The experimental temperatures were $\sim 100 - 150$ K above those from the calculations, and showed a slightly different distribution of the high temperatures along the centerline.

Future work in the development of consumer digital cameras as optical pyrometers is ongoing, and primarily involves further optimizing the detector characterization and improving the approach to signal evaluation. Since it was shown that the temperature calculation is quite sensitive to the filter profiles of the CFA, continuing characterization of the CFA is desirable. Further, implementation of the look-up table approach outlined in Section 2.2.2.3 has shown encouraging results that are consistent with the results presented here.

3.5 Laser-Induced Incandescence

3.5.1 Soot Volume Fraction Measurements using Saturated LII

Initial measurements of soot volume fraction in the 32%, 40%, 60% and 80% C_2H_4 flames (in a balance of N_2) were made using prompt detection of the saturated LII signal, and calibrated using an on-line extinction calibration. Results from this study were compared to computational results in [Smooke 2005]. In that paper, the computational work was carried out by Professor Mitchell Smooke, in collaboration with Dr. Meredith Colket and Dr. Robert Hall at UTRC.

The experimental setup for this work is shown in Figure 3.5.1. The second harmonic of a pulsed Nd:YAG laser (Continuum NY-82, ~10 ns pulses at 10 Hz) at 532 nm is used to excite the LII. Soot absorbs laser energy over a broad band of wavelengths. Excitation using UV light is typically avoided because it can cause interferences from fluorescent species, as well as causing photofragmentation from the soot particles [Stipe 2004]. Excitation using the Nd:YAG fundamental wavelength at 1064 nm is preferred since it typically results in fewer interferences than the second harmonic. Excitation at 532 nm has been shown to cause interferences from two-photon excitation of PAH fluorescence [Moreau 2004], excitation and emission from C_2 Swan bands [Bengtsson 1995], and elastically-scattered light from the soot. Still, excitation was initially carried out at 532 nm because it corresponds to the best detector sensitivity and largest particle cross sections of any of the Nd:YAG harmonics. The detector sensitivity is important because the calibration using laser extinction would not be possible at the preferred excitation wavelength of 1064 nm given available resources.
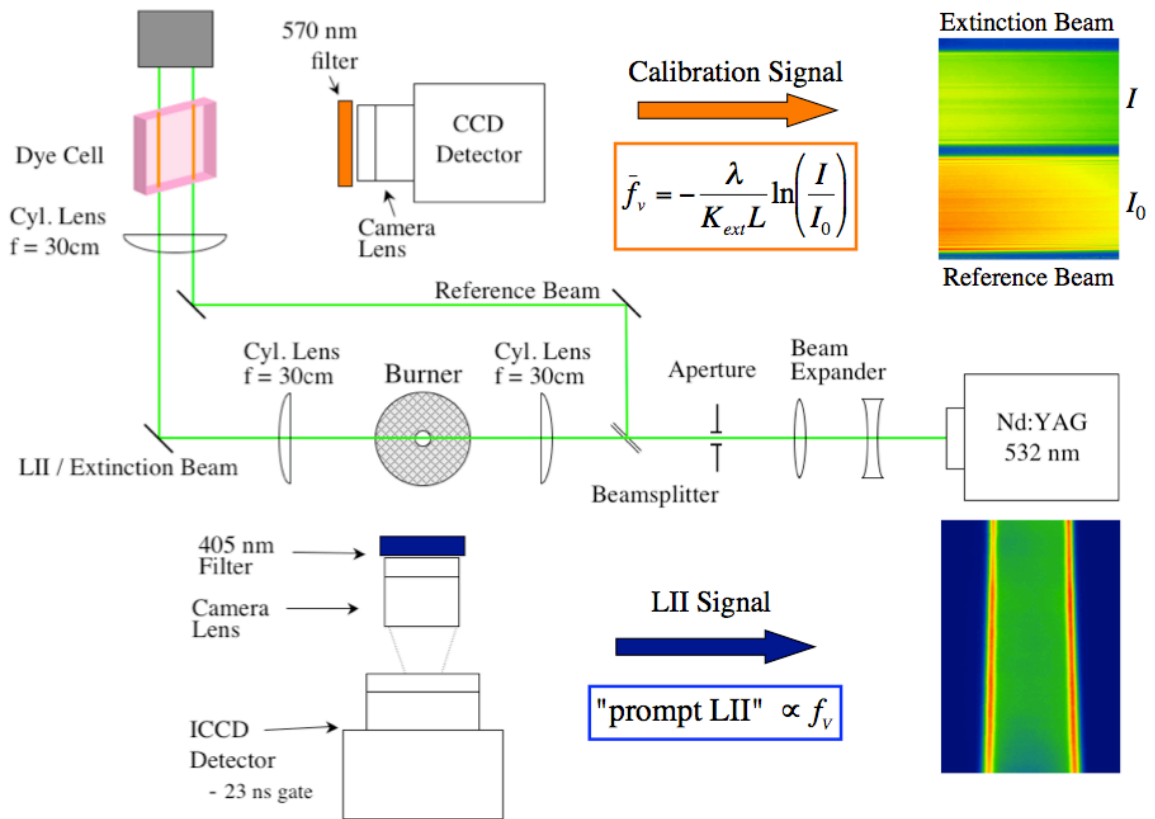
Figure 3.5.1: Two-dimensional LII setup using an extinction calibration.

Detection of the LII signal occurs around 405 nm. This is accomplished using a colored glass filter (BG 34) coupled with a blue additive filter. The purpose of the additive filter is to reject any near-IR light transmitted by the colored glass filter. It was discovered years after running this experiment that the additive filter did transmit somewhat in the range of 800 – 1100 nm, a defect that was discovered while investigating some anomalous behavior of a blackbody calibration for the LII system. Nonetheless, the results here should account for that, as the signal detection and calibration were self-consistent. The resulting primary detection window was centered on 405 nm with a full width at half maximum (FWHM) of 70 nm. This detection band was chosen because it avoids emission from C_2 Swan bands and most of the bands associated with PAH emission. This should minimize the interferences caused by excitation at 532 nm.

The output of the laser is first sent through a vertical beam expander. The beam expander consists of a Galilean telescope using a -2.5 cm lens to expand the beam followed by a 10 cm lens to re-collimate the beam, resulting in a beam expansion by a factor of 4. A 1.2 cm vertical aperture then clips the beam in order to select the most uniform portion of the beam. Since the edges of the aperture cause interference fringes from diffraction, only the central 1 cm portion of the beam is used for data acquisition. This diffraction effect can be remedied by relay imaging the aperture to the measurement volume [Smallwood 2002; Michelsen 2003b], and this approach is utilized in the most current version of the experiment. The beam is focused into a sheet across the centerline of the burner using a 300 mm cylindrical lens. A relatively long focal length lens is used in order to provide a gradual focus that doesn't vary significantly in beam waist across

the measurement volume. The LII signal was captured using a fast-gate (10-ns response time) intensified CCD (ICCD) camera (Princeton Instruments ICCD-576TE/RB, fiber optically coupled to the intensifier). A Princeton Instruments FG-100 pulse generator is used to control the intensifier gating. A 50 mm Nikon camera lens, coupled with a Sigma achromatic +1 macro lens, is used to capture the signal that is transmitted by the filter pair described above, and image the measurement volume on the front of the intensifier.

The laser fluence is chosen so that the detected signal is in the saturation regime. Figure 3.5.2 shows the dependence of the LII signal as a function of laser fluence. A fluence of ~0.05 J/cm^2 is required to heat the particles and cause a detectable incandescence signal. Above that threshold, the detected LII signal rises almost linearly up to a fluence of ~0.15 J/cm^2, where the signal no longer increases linearly with laser power. At fluences above ~0.2 J/cm^2, the signal saturates. This level signal region occurs when the soot is heated to its maximum temperature and mass redistribution and vaporization balance the increased laser power. In the case presented here, the signal begins to increase at fluences above 0.6 J/cm^2. This is due to wing effects of particles on the wings of the laser sheet beginning to heat and incandesce. A laser fluence of approximately 0.3 J/cm^2 was used for this set of LII measurements since, in this range, the detected signal was independent of small variations in the laser sheet profile and beam extinction across the flame did not result in a significant loss of signal.
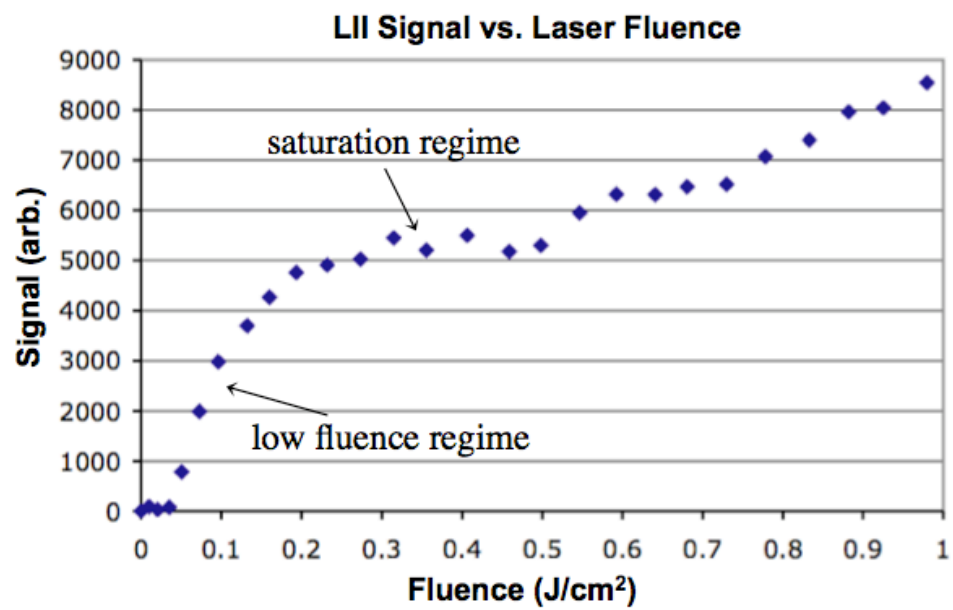
Figure 3.5.2: LII signal dependence on laser fluence.

In the last few years, investigators have moved towards carrying out experiments in the low fluence regime to avoid problems associated with morphological changes to the soot due to laser heating, an approach that is required if measurements of particle sizes are the goal. This requires detection at multiple colors and a determination of soot temperatures during laser heating to account for loss of laser power across the flame.

Previous experiments [McEnally 1998; Smooke 2004] used an intensifier gate time of 1 μs, due to slow intensifier response times. Such long gate times, however, tend to over-count the larger particles with respect to the smaller ones. Typically, large particles have signal lifetimes of ~500 – 1000 ns; smaller particles have lifetimes of ~200 – 500 ns. This effect can cause problems with both the soot volume fraction distribution as well as with the calibration procedure. The on-line extinction calibration was performed only on the higher concentration flames (80% and 60% C_2H_4), and the results were extrapolated to the lower concentration flames (40% and 32% C_2H_4), since uncertainties in the calibration of the lower concentration flames began to dominate when the total extinction dropped below a few percent. The lower concentration flames tend to have smaller particles, which are therefore undercounted.

As an illustration of the need for short gate times, Figure 3.5.3 displays the ratio of the peak soot volume fraction for the 80% and 32% C_2H_4 flames as a function of intensifier gate time. The gate time is varied from 5 – 1000 ns. The ratio decreases steadily as the gate time is reduced from 1000 ns, and levels off for gate times below 50 ns. It can be seen that an error in the calibration of the 32% flame of more than a factor of two would result if the longer gate times were used for the LII detection. The
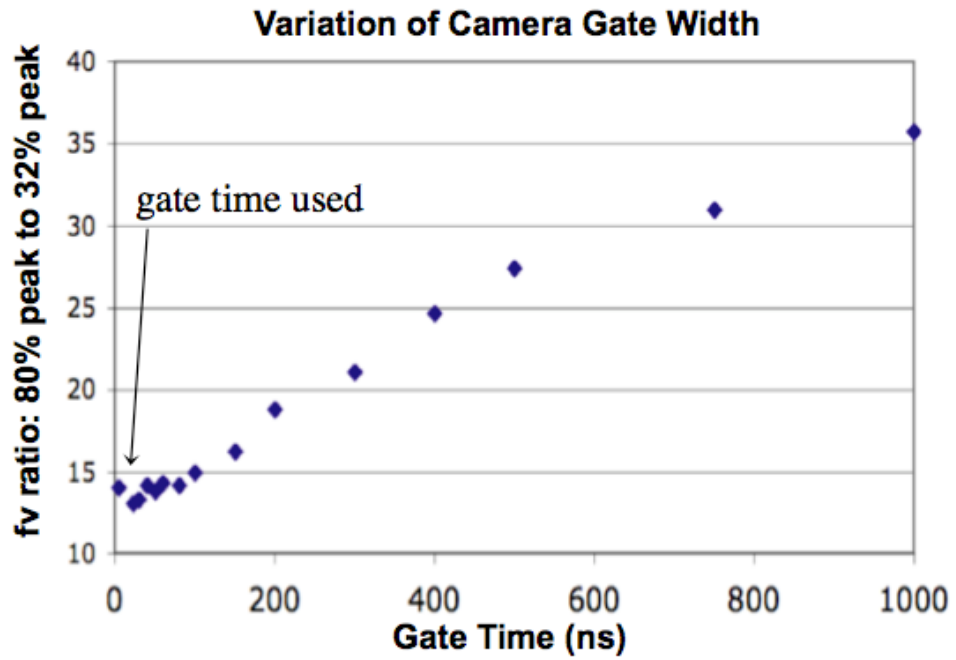
Figure 3.5.3: The ratio of peak soot volume fraction between the 80% and 32% C_2H_4 flames is plotted as a function of intensifier gate time. It was found that gates that are longer than ~50 ns bias the LII measurement to large particles.

detection gate must be less than 50 ns to avoid measurement bias towards larger particles. The old detection gate of 1 μs would cause a discrepancy of more than a factor of 2.5 in the calibrated results for the 32% flame. For this study, a detection gate of 23 ns was used.

Once the experimental parameters were set, experimental data quantifying the soot volume fraction of the set of ethylene flames were obtained using two-dimensional LII measurements calibrated with an on-line extinction method (shown in Figure 3.5.1). The raw LII images detected with the ICCD camera were averaged and corrected for luminosity and optical throughput. These images were further corrected for a left-right nonuniformity characteristic of the fast-gate intensifier and the 10-mm data slices were then combined to generate composite soot volume fraction images covering the entire flame.

The extinction calibration follows the approach in [Axelsson 2001], and was carried out at a laser fluence of less than 0.01 J/cm^2, low enough to avoid unwanted LII effects and altering the properties of the soot. This fluence was achieved by attenuating the beam used to excite the LII, as it was important to ensure the beam used for the extinction measurement was spatially coincident with the LII beam. The laser beam was separated by a beam splitter into an extinction beam, which follows the same path through the flame as the LII beam, and a reference beam, which does not traverse the flame. After it is partially extinguished by the flame, the extinction beam is re-collimated, and the extinction and reference beams are then aligned so that they travel parallel to one another, but at different heights. The two beams are focused into sheets by a 10 cm cylindrical lens, and are incident on a dye cell containing a mixture of Rhodamine 640

and ethanol. The focus of the beam was placed behind the dye cell, to ensure that the resulting dye fluorescence occurred in the linear regime. The fluorescence of the dye cell is imaged by a CCD camera (Photometrics Star-1) through a long-pass filter at 570 nm, which filters out light scattered from the incident laser, but passes a majority of the fluorescence. The relative intensities of the extinction and reference beams are used to determine how much of the laser is extinguished by the flame. The relative intensities are normalized for shot-to-shot variability and optical throughput of each beam path by taking data both with and without the flame. The average soot volume fraction across the flame diameter is then determined using the Lambert-Beer law in the Rayleigh approximation [Zhao 1998], and the result is used to calibrate the LII images.

As discussed in Section 2.3.1.3, a large source of error in a majority of techniques used to determine sooting characteristics relates to the optical properties of the soot. The values of the soot absorption function, $E(m)$, and the dimensionless extinction coefficient, K_{ext}, have been the subject of numerous investigations, and they are known to vary by as much as 20%. For the experiments, the dimensionless soot extinction coefficient is taken to be 8.6 [Krishnan 2000; Krishnan 2001]. In the experimental and computational results presented in [Smooke 2005] an average value of 10 was used because it is the same value used in the radiation submodel calculation. It makes sense to use a higher value in the computations as the radiation will be weighted to the IR, where $K_{ext} \approx 10$, and constant. However, the value of K_{ext} decreases when moving towards shorter wavelengths in the visible region of the spectrum. Therefore, it makes more sense to use a value for K_{ext} of 8.6, which is more accurate at the experimental wavelength of 532 nm [Krishnan 2000].

3.5.1.1   Results in Santoro Burner

Data were initially taken in the well-characterized Santoro burner to verify the reliability of the measurements. Figure 3.5.4 plots the soot volume fraction in the Santoro burner for (a) a two-dimensional window centered at a height of 5 cm and (b) a radial profile for the 5 cm height (indicated by a grey dashed line in (a)). The centerline value at 5 cm is shown to be 2.5 ppm (with a peak of 7.5 ppm on the wings). This can be compared with other results in the literature. A value of 3.7 ppm was reported in [Schulz 2006b], which was measured using LII. Köylu *et. al* [Koylu 1997] report a value of 3.8 ppm, measured using the thermophoretic sampling particle diagnostic (TSPD). McEnally *et. al* [McEnally 1997] report a value of 5.5 ppm, measured using thermocouple particle densitometry (TPD). Santoro *et. al* [Santoro 1983] report a value of 4.3 ppm (and ~12 ppm on the wings), measured using laser scattering and extinction.

While many of these results suggest the value obtained here is under predicting the level of soot in the flame, it should be noted that there are discrepancies across these measurement techniques. Sampling techniques can probe a larger volume than what is detected using two-dimensional imaging. Earlier studies that probed the flame optically have been shown to under predict K_{ext} by ignoring the scattering component of the term and simply using $K_{abs} = 6\pi E(m)$. Using the data from [Krishnan 2000], where $E(m) = 0.29$ near 532 nm, results in $K_{abs} = 5.5$. This value would change the results measured here to be 3.9 ppm on the centerline and 11.2 ppm on the wings. That change corresponds to a variation of ~50%, demonstrating the need to quantify better the optical properties of soot. Another possible explanation relates to the issue of signal trapping. The large quantity of soot on the wings of the flame will also extinguish the LII signal.
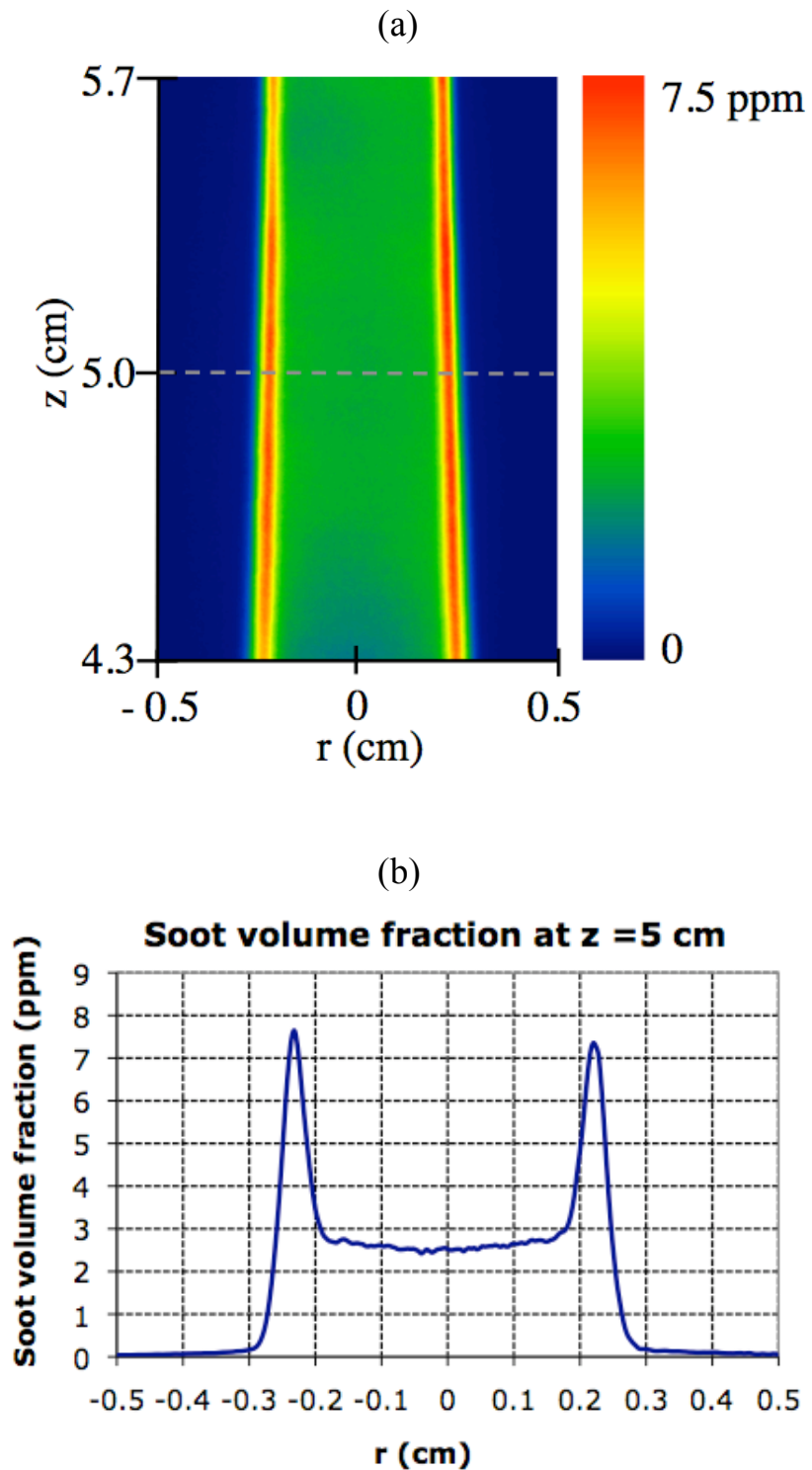
Figure 3.5.4: Soot volume fraction in the Santoro burner for (a) a two-dimensional window centered at a height of 5 cm, (b) a radial profile for the 5 cm height (indicated by a grey dashed line in (a)).

Calibration of this flame showed that there was ~24.5% extinction across the flame. That effect has not been corrected for here. Further, information at recent conferences suggests the soot volume fraction in this flame has been over predicted in the literature. That information has not yet been published.

3.5.1.2   Numerical Computations

The computational work for the study of sooting flames was carried out by Professor Mitchell Smooke, in collaboration with Dr. Meredith Colket and Dr. Robert Hall at United Technologies Research Center (UTRC). The computational approach for the set of sooting ethylene diffusion flames is described in Section 3.3.

3.5.1.3   Comparison of Results

Figure 3.5.4 plots the soot volume fraction contours as the fuel fraction in the central tube changes from 32% to 80% for both the experimental results (a) and computational results (b). Note that both the computational and experimental soot volume fraction plots have their own color scale. Both the computational and the experimental results indicate that, as the fuel mole fraction increases, the location of the peak soot transitions from the tip of the flame along the centerline to the wings of the flame. This movement of the location of the peak soot is qualitatively consistent with the early work of Santoro and coworkers (see, e.g., [Santoro 1983]), although in their work the fuel jet was undiluted and the transition in the soot field was observed by increasing the fuel jet velocity. Computations predict soot over a larger area than is measured for all dilutions.
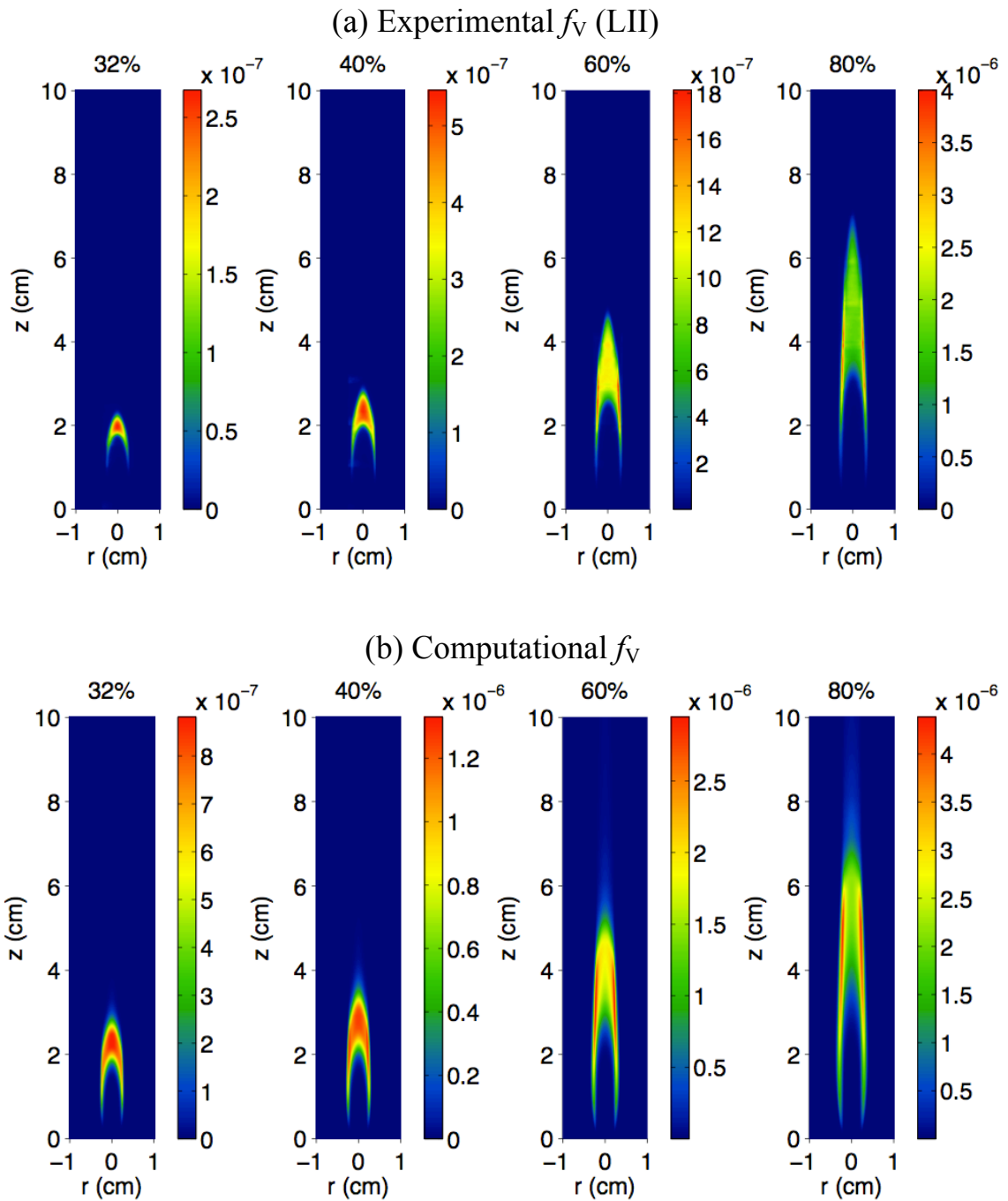
Figure 3.5.4: (a) Experimental soot volume fractions measured using LII, with $K_{ext} = 8.6$. (b) Computational soot volume fractions for the 32%, 40%, 60% and 80% flames.

To illustrate the comparison between the experiments and computations better, the peak soot volume fractions are plotted for both the overall and centerline values in Figure 3.5.5. Peak values of soot volume fraction are over predicted for all cases, but show better relative agreement for the 60% and 80% flames. Both the computational and the experimental results indicate that as the fuel mole fraction increases, the level of peak and integrated soot increases and the location of the peak soot transitions from the tip of the flame along the centerline to the wings of the flame. Also, the percentage ratio of the peak soot along the centerline to the overall peak soot decreases from 100% in the 32% flame to approximately 50% in the 80% flame.

To understand the centerline to wing transition more fully, the relative contributions of the three submodel processes contributing to soot formation – inception, surface growth and oxidation – were examined. The maximum inception and surface growth rates were found to occur along the centerline near the tip of the flame and the maximum inception rate increases from the 32% to the 40% flame. Above the soot tip, oxidation increases and soot is removed from the flames. The highest oxidation rates are along the centerline of the flames, directly downstream of the high soot concentrations. The high inception rates and corresponding high surface growth rates near the peak of the flames are the direct cause of the peak soot concentrations along the centerline for these flames.
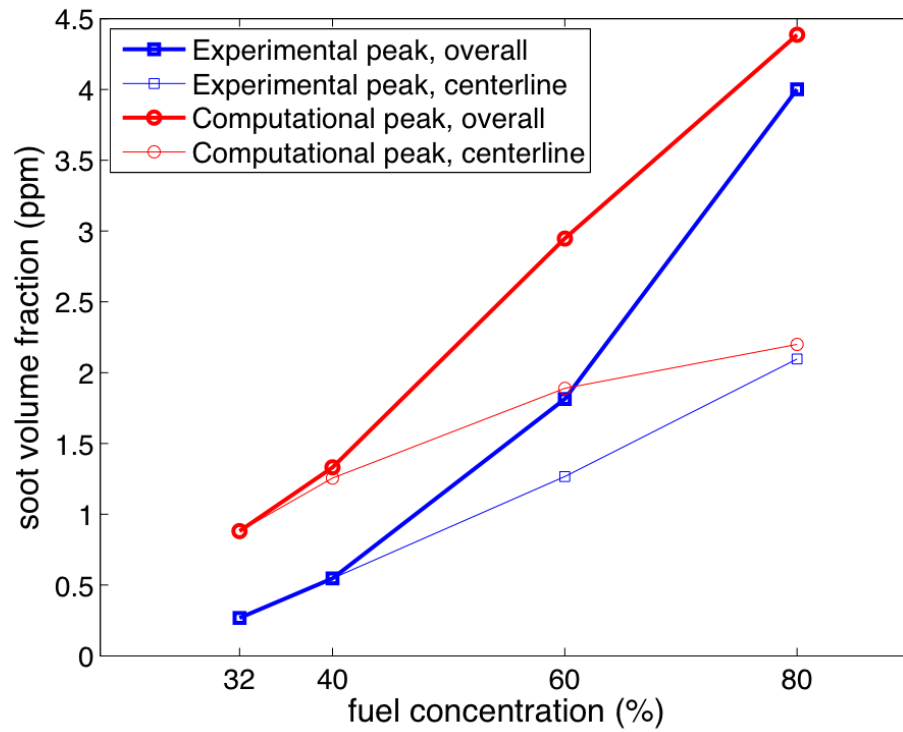
Figure 3.5.5: Experimental (blue) and numerical (red) peak soot volume fractions (thick line) and peak centerline soot volume fractions (thin line) as a function of the fuel mole fraction.

Meanwhile, the location of the peak soot volume fraction is noticeably shifted in the higher fuel flames. In the 60% and 80% C_2H_4 flames, the peak inception rate still occurs along the centerline near the tip of the flame. However, these values are about a factor of two lower than the corresponding peak surface growth rates that occur fairly low in the flame along the wings. Also, the surface growth rates along the sides of these flames are larger relative to those along the centerline. As a result, the peak soot volume fractions in these flames occur along the wings. In addition, as the ratio of the peak inception rate along the centerline to the peak surface growth rate along the wings decreases, the corresponding ratio of soot volume fraction also decreases. Soot oxidation increases further downstream and is largest in the upper portions of the wings where the highest soot levels occur.

For the 32% and 40% C_2H_4 flames, the transit time through the soot cone is about 10 to 15 milliseconds while in the 60% and 80% C_2H_4 flames this value increases from 25 to 40 milliseconds. There is more than a factor of four increase in the available time for inception and growth as dilution decreases. For the 80% flame, a significant reduction in the soot formation rates is apparent due to the decrease in flame temperatures along the flame centerline, caused by increased radiative losses in the less diluted flames. More details on this residence time analysis can be found in [Smooke 2005].

3.5.1.4 Conclusions

Laminar, sooting, coflow diffusion flames have been studied experimentally and computationally as a function of ethylene fuel dilution. Soot profiles obtained from laser-induced soot incandescence undergo a shift away from the flame centerline toward the wings of the flame as the ethylene fraction and sooting levels increase. Numerical

76

simulations agree well with these results. Model predictions have been improved by approximate treatments of particle ageing and aggregate formation, as well as by a precise treatment of radiative re-absorption effects. The large impact of radiative power loss on temperature has a significant effect on soot formation.

Investigation of the relative rates of inception, surface growth, and oxidation, along with a particle residence time analysis, are shown to explain the shift of soot away from the centerline as the fuel fraction increases. While inception tends to peak on the centerline, the maximum in surface growth migrates from the centerline to the wings of the flame as the fuel fraction increases. Concurrently, the relative importance of surface growth and inception reverses. This change in the relative importance of these two subprocesses is due to the significant increase in residence time available for soot growth in the flame wings. To investigate this effect the 80% C_2H_4 flame was studied at half velocity (17.5 cm/s average exit velocity in the fuel tube and coflow), both experimentally and computationally (See [Smooke 2005] for more detail.). By altering the inlet velocities of the higher fuel fraction flame, we are able to modify the available residence time along the wings so as to generate soot profiles similar to those of the 60% C_2H_4 flame, a lower fuel fraction flame. The level of soot on the centerline increases with respect to that on the wings as the peak centerline to wing temperature also increases.

3.5.2   Two-Dimensional Particle Size Distributions

For the purpose of this study, two-dimensional measurements of particle sizes are the most practical for comparison with the computational results. For two-dimensional particle sizing, images are taken at two or more different time delays. Care must be taken when choosing the delays because this technique suffers from a decrease in the temporal

77

resolution and signal-to-noise characteristics that are available in point measurements. While a greater spacing between detection gates improves the sensitivity to varying particle sizes, later gates suffer from low signal-to-noise ratios. Will *et al.* performed an analysis of optimal gate timing that suggested camera gates at 100 ns and 1.2 μs in [Will 1995], while a second gate of 600-800 ns was suggested in [Will 1998]. Recent workshops on LII [2005; 2006] have found that further investigation into two-dimensional particle sizing techniques would be beneficial [Schulz 2006b].

The goal of this study is to improve on previous two-dimensional TR-LII measurement techniques for the determination of soot particle size distributions. Images are taken on a fast-gate intensified CCD (ICCD) camera at discrete gate times. An analysis is performed to determine if particular sets of gate pairs or multiple gates produce the best results. Comparison of results with these studies should help guide improvements to the imaging technique. The approach is then applied to the Santoro burner and our coflow burner [McEnally 1998; Smooke 1999b; Smooke 2004; Smooke 2005] for preliminary comparison with computational results.

3.5.2.1   Experimental Approach

The experimental setup (see Figure 3.5.6) for two-dimensional LII has been modified from the approach used in [Smooke 2005]. Laser excitation is achieved using a pulsed, Nd:YAG laser (~10 ns FWHM, at 10 Hz) operating at the 1064 nm fundamental wavelength. This wavelength was chosen because the commonly used second harmonic at 532 nm has been found to cause interferences from two-photon excitation of PAH fluorescence [Moreau 2004], excitation and emission from C_2 Swan bands [Bengtsson 1995], and elastically scattered light from the soot. A fast-gate ICCD camera is used to

detect the temporally-resolved LII signal. The detection wavelength, centered on 455 nm (32 nm filter width), minimizes any remaining interferences while maximizing the detected signal.

A laser sheet is used to excite LII for two-dimensional excitation and detection. A significant amount of care was taken in designing the beam shaping apertures and lenses. When the LII process is modeled, it is assumed that all particles in the measurement volume are heated to the same temperature. This is particularly important when measuring the cooling rate of the heated particles, and it requires the use of a laser with a uniform, or top-hat, profile. Simply using a lens to focus the beam into a sheet would result in an intensity profile similar to the laser's far-field intensity profile, which is approximately Gaussian. This would cause a lower level of heating along the wings of the beam. Point measurements use an aperture to clip the beam to a desired size and then relay image that aperture to the measurement volume [Michelsen 2003b]. Imaging the aperture to the measurement volume is important to avoid diffraction effects that cause interference patterns in the laser beam. This approach should form a top-hat profile, but at a single plane only, requiring modification for use in two-dimensional experiments.

If a single lens is used to image the aperture, the beam will diverge as it passes through the image plane. This causes a variation in laser energy across a measurement volume. The use of a "4F system", a pair of lenses two focal lengths apart and each a focal length away from the object and image plane, respectively, creates an image of the aperture at the measurement plane, while also collimating the beam to avoid divergence. As shown in Figure 3.5.6, this technique is utilized to image a 2 cm vertical aperture with
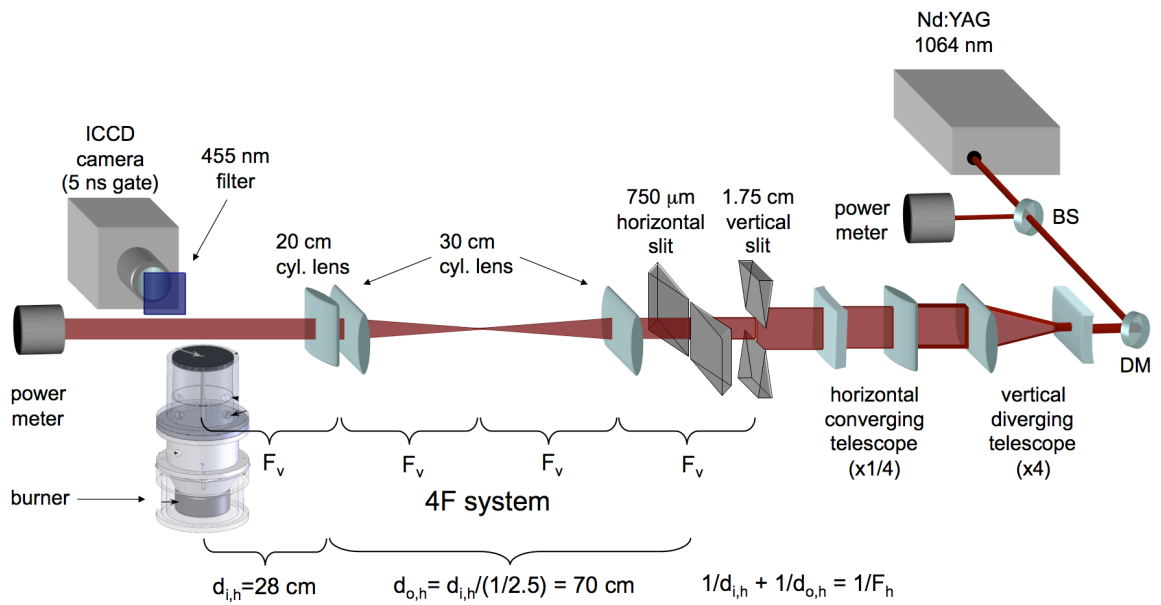
Figure 3.5.6: Experimental setup for two-dimensional time-resolved LII.

1:1 magnification onto a plane that is centered on the burner, using a pair of $F_v = 30$ cm focal length cylindrical lenses.

A 4F system cannot be used to shape the beam in the horizontal direction since the desired narrow slit size at the measurement volume (~300 μm) would damage the second lens in the system. Instead a single lens must be used to image the horizontal aperture. In this case, the magnification and lens focal length must be chosen to maximize the depth of field of the image. This is accomplished by maximizing the lens focal length and minimizing the change in magnification for the imaged slit. Due to space restrictions, an $F_h = 20$ cm focal length cylindrical lens is used to image a 750 μm horizontal aperture with a demagnification of 1:2.5. Similarly, long focal length lenses were used to image the vertical slit to obtain a large depth of field in that plane.

The beam shaping optics create a sheet across the measurement volume that is ~ 2 cm tall and 300 μm wide. Before the apertures, a diverging telescope expands the beam by a factor of 4 in the vertical direction, and a converging telescope condenses the beam by a factor of 4 in the horizontal direction. In each direction the apertures select the middle third of the beam. Each laser pulse contains an energy of 9 mJ, resulting in a maximum fluence of 0.15 J/cm^2 at the measurement volume, which produces an LII signal that is ~1/3 of the saturation level. This fluence is considered to be low enough to avoid changes to the particle morphology [Vander Wal 1998; Snelling 2004].

Since the experiment is operated in the low fluence regime, different regions in the flame are going to experience slightly different laser fluences as the beam is extinguished as it travels through the flame. In an effort to compensate for this effect, the horizontal converging telescope is slightly detuned to produce a beam that gradually

converges as it traverses the optical path. This way, as the beam is attenuated the laser fluence remains roughly constant as the beam waist is decreased. This alignment was verified by taking LII images of using two different color filters (at 455 nm and 700 nm) and ensuring the signal ratio was constant on opposite sides of the flame. A constant signal ratio indicates that the soot has been heated to a consistent temperature, which is a consequence of the assumption that a constant fluence is used to heat the particles within the measurement volume.

The LII signal is detected by a fast-gate ICCD camera at discrete gate times relative to the temporal peak of the LII signal. The laser pulse heats the soot to a maximum temperature, which corresponds to a maximum detected signal. This signal peaks roughly 10 ns after the laser's maximum intensity. Pulse delay generators are used to scan the camera gate (~5 ns FWHM) through time to determine the maximum signal, which is then defined as time = 0 ns. Images are taken at delays of 0, 50, 100, 200, 300, 400, 500, 600, 700, 800, 900 and 1000 ns. Multiple laser pulses (1, 2, 4, 8, 8, 8, 16, 16, 16, 32, 32 and 32, respectively) are averaged on the CCD chip, and 10 −50 images are taken at each delay (depending on signal strength). Increasing the number of pulses per exposure compensates for the decreasing signal at later delay times, and improves the signal-to-noise ratio. The laser energy is measured by a pyroelectric energy meter (Scientech PHD25), synchronized with the camera exposures, and recorded on an oscilloscope. Each image is corrected for detector and soot incandescence backgrounds, normalized by the recorded laser energy, and corrected for nonuniform detector gain and optical throughput. The final images have a pixel volume of 0.4 x 0.4 x 0.3 mm^3 and a

signal-to-noise ratio of ~47 in the center of the 100 ns image. This reduces to ~37 in the 500 ns image and ~22 in the 900 ns image.

3.5.2.2   Time-Dependent LII Simulations

Experimental particle sizes are determined by modeling the LII signal decay rate to evaluate the experimentally measured decay rate. Evaluation techniques require a number of assumptions about soot properties, particle size distributions and model parameters. Before beginning to approach this problem, it is first necessary to make an assumption about the type of distribution under consideration. Some investigations assume a monodisperse distribution, however studies have shown that there is a spread to the particles. Most investigations that assume a polydisperse distribution assume a lognormal form

$$f(d_p) = \frac{1}{d_p \sqrt{2\pi} \ln \sigma_g} \cdot \exp\left[-\frac{1}{2\ln^2 \sigma_g} \ln^2\left(\frac{d_p}{d_{med}} \right) \right] \tag{3.5.1}$$

where the probability $f(d_p)$ of a particle with a diameter d_p is dependent on the geometric mean diameter d_{med}, and the geometric width of the distribution σ_g. Sample distributions are plotted in Figure 3.5.7 for two distributions: d_{med} = 30 nm and σ_g = 1.25, and d_{med} = 50 nm and σ_g = 1.35. A lognormal distribution is a reasonable starting assumption, as processes that exhibit exponential growth, like soot growth, are well described by this distribution. While these types of distributions have been observed experimentally, bimodal distributions have as well, though to a lesser extent. The ability to actively determine the appropriate distribution is currently beyond the capability of this approach. A number of different approaches to signal evaluation are outlined in [Schulz 2006b]; Daun *et al.* [Daun 2007] present an informative analysis and review on evaluation

83
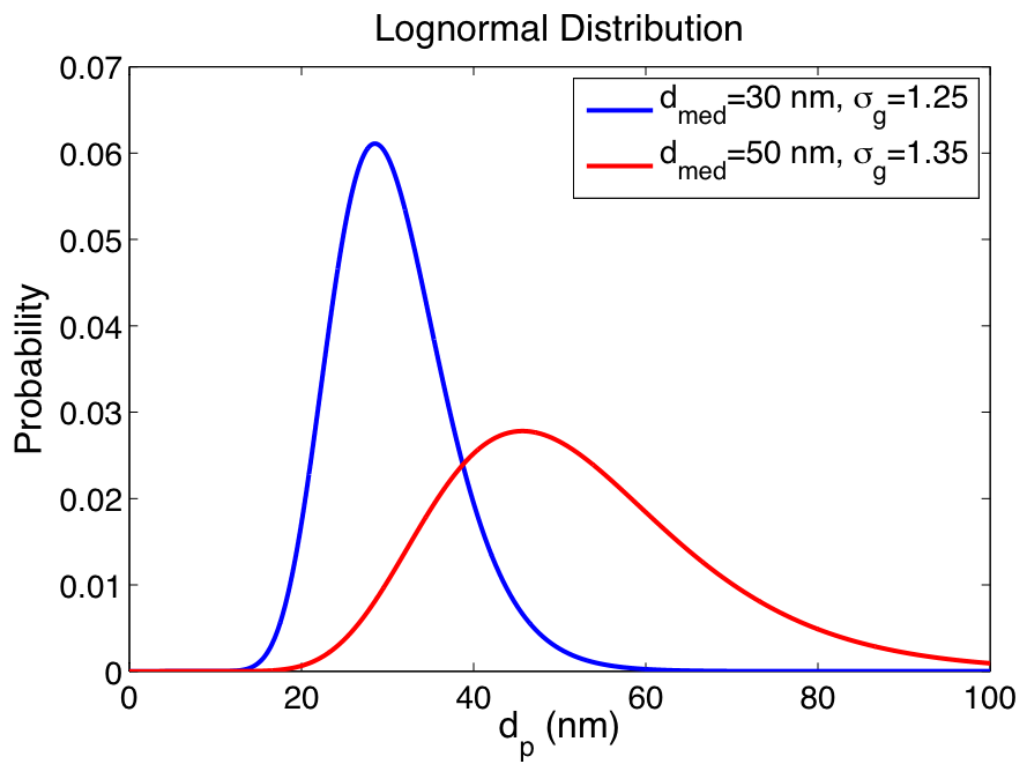
Figure 3.5.7: Lognormal distribution plotted for two distributions: d_{med} = 30 nm and σ_g = 1.25, and d_{med} = 50 nm and σ_g = 1.35.

techniques to determine the most robust approach to the problem. Because the time-dependent LII signal is composed of the superposition of different exponentially decaying functions, and not a simple exponential decay, determination of the particle-size distribution using an inverse approach is an ill-posed problem. Approaches to the problem that use a standard inversion scheme suffer from the ambiguity of a fairly wide range of satisfactory solutions. Solutions to the reverse problem have adopted a variety of approaches. Kuhlmann *et. al* [Kuhlmann 2004] developed an approach based on the method of cumulants. By relating the distribution to the measured signal through a Laplacian integral, the exponential decay of the signal could then be expressed in terms of a power series

$$S_{LII}(t) \propto \exp\left(-K_1 t + \frac{K_2}{2} t^2\right) \tag{3.5.2}$$

where $d_{med} = K_1/2\sigma_g$ and $2\sigma_g = K_2/K_1^2 + 1$.

Solution of the implicit, forward problem, by minimizing the difference between modeled and experimentally observed data, is recognized as the best way to determine experimental particle sizes. Still, solution of the forward problem is dominated by a long, range of potential solutions with similar minima. This makes sense, as lognormal distributions have persistent tails that are weighted towards larger particles. It is not difficult to conclude that a distribution with a small geometric mean diameter coupled with a large geometric width can produce a similar signal to a distribution with a large geometric mean diameter and a small geometric width. It is important to attempt to reduce this uncertainty, especially in experiments where experimental noise can easily shift the resulting solution along this range of ambiguous results.

Coupling LII with a second measurement, such as soot volume fraction or elastic scattering, can help to reduce this uncertainty. Liu *et. al* [Liu 2006a] utilize the observation that the initial temperature decay is dependent on the d_{32} moment, also known as the Sauter mean diameter. They fit that initial temperature decay, then use the signal from the later time decay, with the relationship $d_{32} = d_{pg} \exp[5/2\ln(\sigma_g)^2]$ to determine lognormal distribution. Dankers and Leipertz [Dankers 2004] used fits to two time intervals – an early time trace coupled with a later time trace – to minimize the uncertainty. They observed that the initial signal decay is primarily dependent on the particle size, while the later decay is more heavily dependent on the width of the distribution. Daun cited the suggestion by Stagg [Stagg 2006] that using an orthogonal minimization criteria could be used to reduce the ambiguity, and he proposed that perhaps a fit to the characteristic time of the decay could accomplish this.

Solution of the forward problem is time intensive, as guesses to the particle size distribution are used to calculate a signal repeatedly until the result is sufficiently comparable to the experimentally measured signal. Extrapolate this to a two-dimensional image, and this time increases rapidly. To speed image analysis, a "library" of time-resolved LII signals were simulated for a range of particle sizes using LIISim [Hofmann 2007]. LIISim simulates the time-dependent LII signal based on a number of input parameters, including mean particle size, particle size distribution, excitation wavelength and energy, detection wavelengths, optical and heat transfer properties of the soot, conduction model, etc. For this study parameters are selected to match the experimental conditions along with the following input parameters: single particles, polydisperse distribution, Fuchs heat conduction model, soot absorption function, *E(m)*, of 0.4

[Snelling 2004], 1860 kg/m^3 particle density, initial gas phase and particle temperature of 1600 K [Schulz 2006b], gas pressure of 1 bar, gas molar mass of 0.028 kg/mol, thermal accommodation coefficient of 0.3, and mass accommodation coefficient of 1.

Figure 3.5.8 plots the results of the LIIsim signal simulations. Signals are simulated for mean particle diameters from 5 to 100 nm, at 5 nm intervals, and for geometric widths from 1.01 to 1.6. The time-dependent signal for each particle size has been shifted in time so the signal maximum occurs at t = 0 ns. The signal from the smallest particles decays the fastest, while that from the largest particles decays more slowly. The experimental detection gates (shown as dashed lines in Figure 3.5.8) are applied to the simulated signals to determine a discrete, time-dependent signal for each simulated particle size. The resulting signals are shown as a function of particle size and gate time in Figure 3.5.9a. Signal ratios are calculated, for each particle size, using initial gates of 50 ns (not shown) and 100 ns (shown in Figure 3.5.9b), paired with the later gates.

A database of signal ratios is created for every 0.1 nm between 5 nm and 100 nm, and every 0.05 in geometric width, by interpolating between the simulated ratios. Experimental particle sizes are determined by minimizing the square of the deviation of the experimental signal ratios from the library of simulated ratios. This minimization is executed at each point in the LII image that contains a signal larger than a set threshold, and for each gate pair listed in Figure 3.5.8b.

87
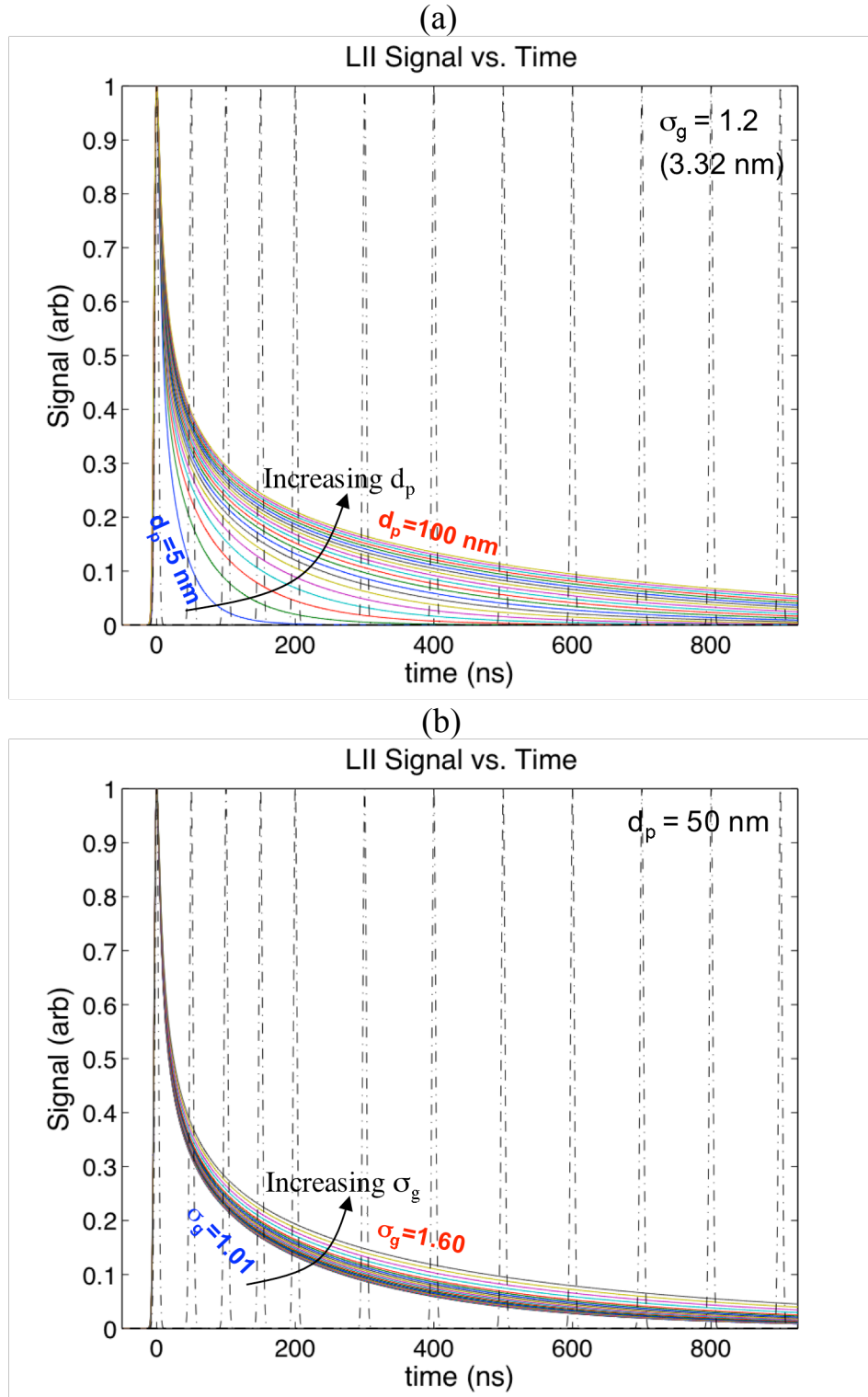
Figure 3.5.8: Simulated LII signals as a function of time for selected primary particle sizes: (a) plots d_p = 5 to 100 nm, with σ_g=1.2; (b) plots σ_g = 1.01 to 1.6 for d_p = 50 nm. The dashed lines represent the discrete camera gate times.
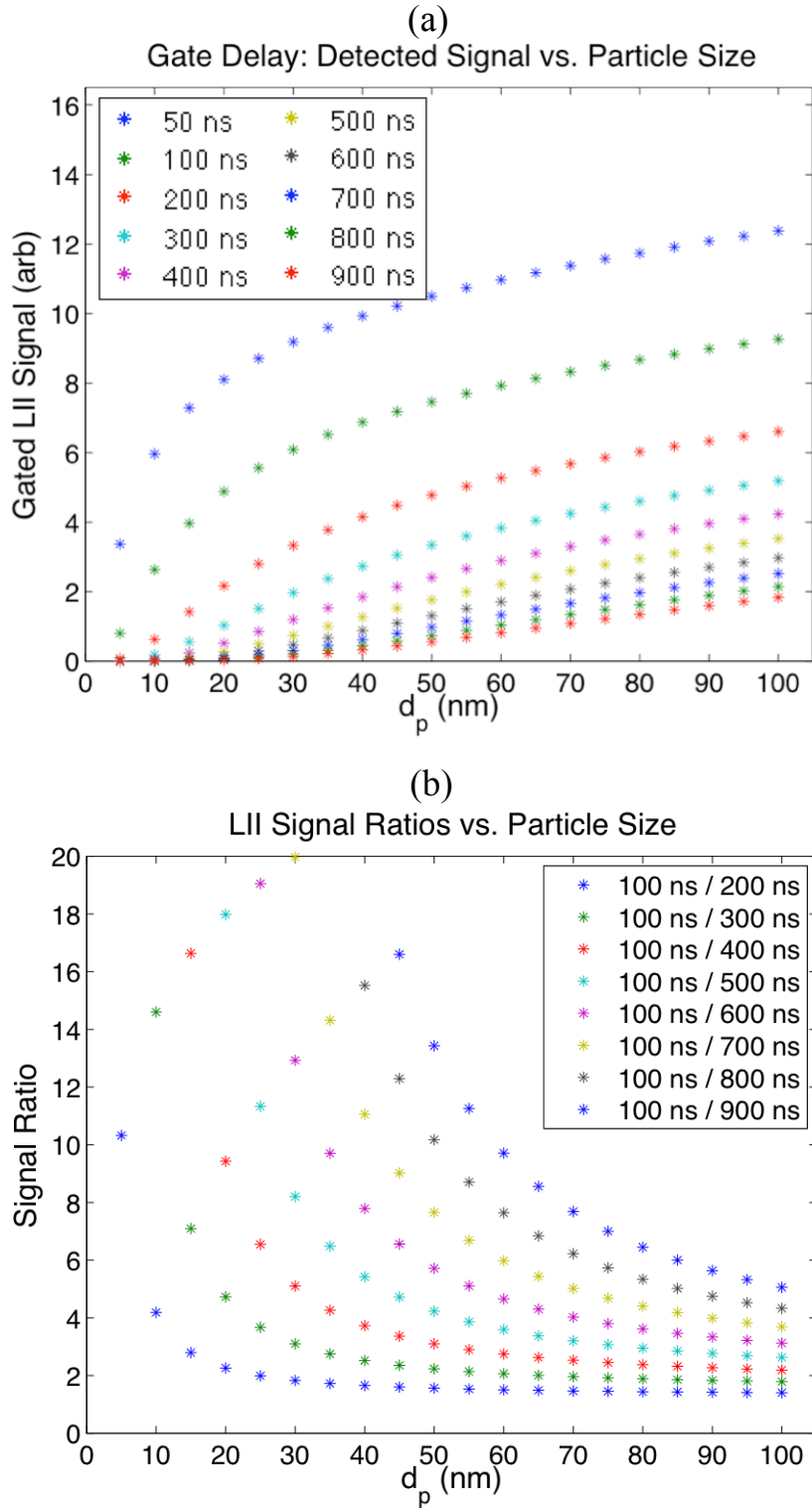
Figure 3.5.9: (a) Discrete LII signal for different gates and (b) signal ratios for gate pairs, as a function of particle size ($\sigma_g = 1.2$).

3.5.2.3   Minimization Criteria

Following the approach of Daun *et al.* [Daun 2007] a selection of minimization criteria utilizing signal ratios at discrete gate times has been applied to three test cases: $d_p = 34.2$ nm, $\sigma_g = 1.22$, $d_p = 34.2$ nm, $\sigma_g = 1.37$, and $d_p = 56.8$ nm, $\sigma_g = 1.37$. The results of this minimization for the three test cases are plotted in Figures 3.5.10, 3.5.11 and 3.5.12, respectively, for four different minimization criteria. In these plots, blue indicates a good fit to the data, while red indicates a poor fit. Minimization 1 minimizes the function

$$F_{\min,1}\left(d_p;\sigma_g\right) = \left[\left.\frac{S_{100 \text{ ns}}}{S_{400 \text{ ns}}}\right|_{\text{measured}} - \left.\frac{S_{100 \text{ ns}}}{S_{400 \text{ ns}}}\right|_{\text{simulated}} \right]^2. \tag{3.5.3}$$

Minimization 2 minimizes the function

$$F_{\min,2}\left(d_p;\sigma_g\right) = \left[\left.\frac{S_{100 \text{ ns}}}{S_{400 \text{ ns}}}\right|_{\text{measured}} - \left.\frac{S_{100 \text{ ns}}}{S_{400 \text{ ns}}}\right|_{\text{simulated}} \right]^2 + \left[\left.\frac{S_{500 \text{ ns}}}{S_{800 \text{ ns}}}\right|_{\text{measured}} - \left.\frac{S_{500 \text{ ns}}}{S_{800 \text{ ns}}}\right|_{\text{simulated}} \right]^2. \tag{3.5.4}$$

Minimization 3 minimizes the function

$$F_{\min,2}\left(d_p;\sigma_g\right) = \left[\left.\frac{\tau_{100 \text{ ns} \to 400 \text{ ns}}}{\tau_{500 \text{ ns} \to 800 \text{ ns}}}\right|_{\text{measured}} - \left.\frac{\tau_{100 \text{ ns} \to 400 \text{ ns}}}{\tau_{500 \text{ ns} \to 800 \text{ ns}}}\right|_{\text{simulated}} \right]^2. \tag{3.5.5}$$

The time constant, τ, in this case has been approximated by assuming a simple exponential dependence

$$S_2 = S_1 \exp(-\tau/\Delta\tau_{1\to2}) \tag{3.5.6}$$

where $\Delta\tau_{1\to2}$ is the time interval from time 1 to 2, and S_1 and S_2 are the signals at the respective times.
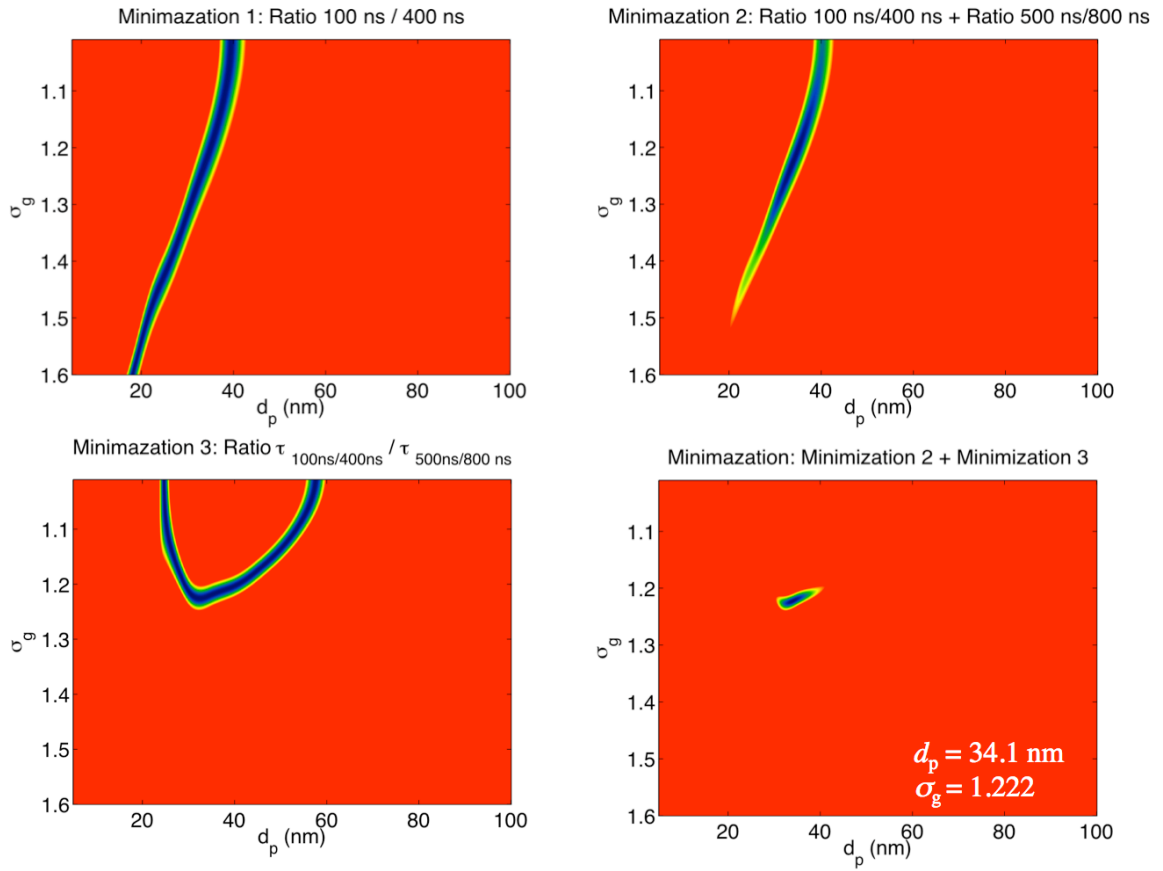
Figure 3.5.10: Minimization criteria for test case 1: $d_p = 34.2$ nm, $\sigma_g = 1.22$. The result of combining Minimization 2 with 3 is shown in the lower-right panel.
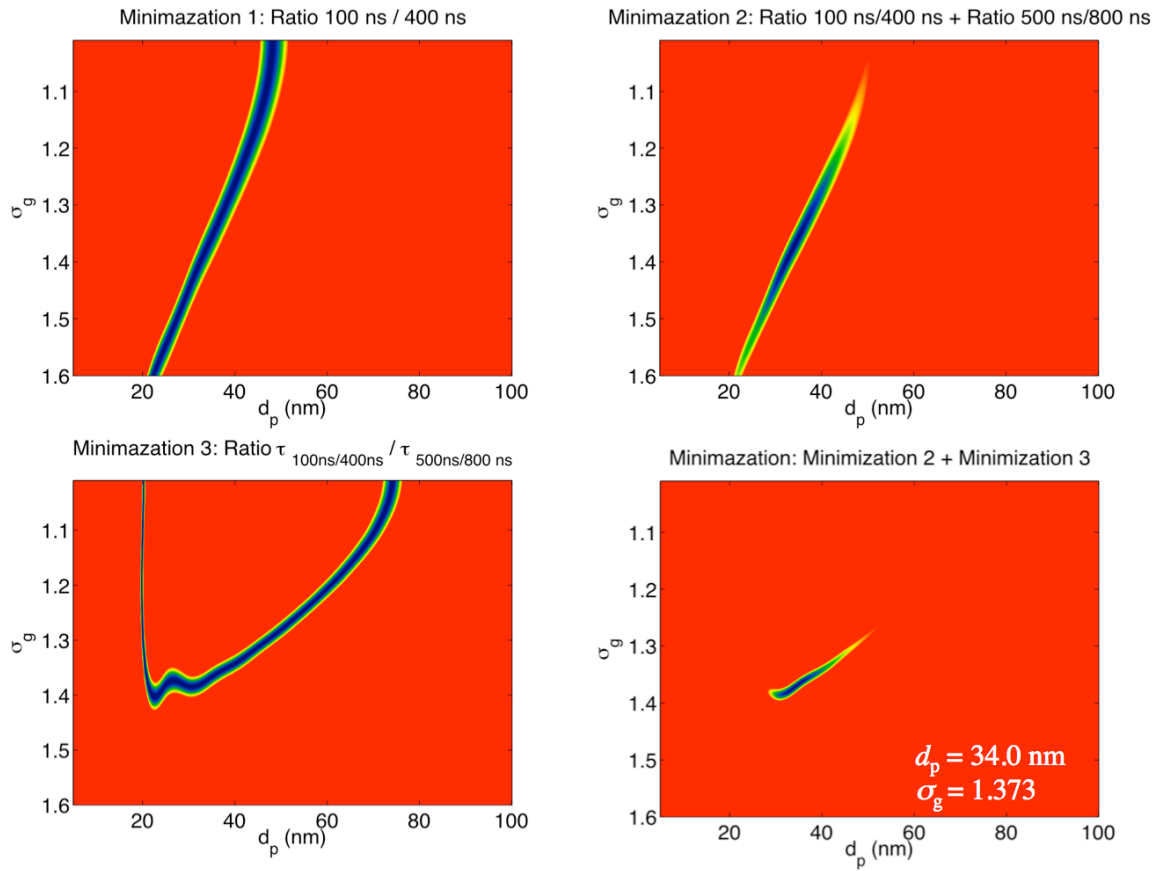
Figure 3.5.11: Minimization criteria for test case 2: d_p = 34.2 nm, σ_g = 1.37. The result of combining Minimization 2 with 3 is shown in the lower-right panel.
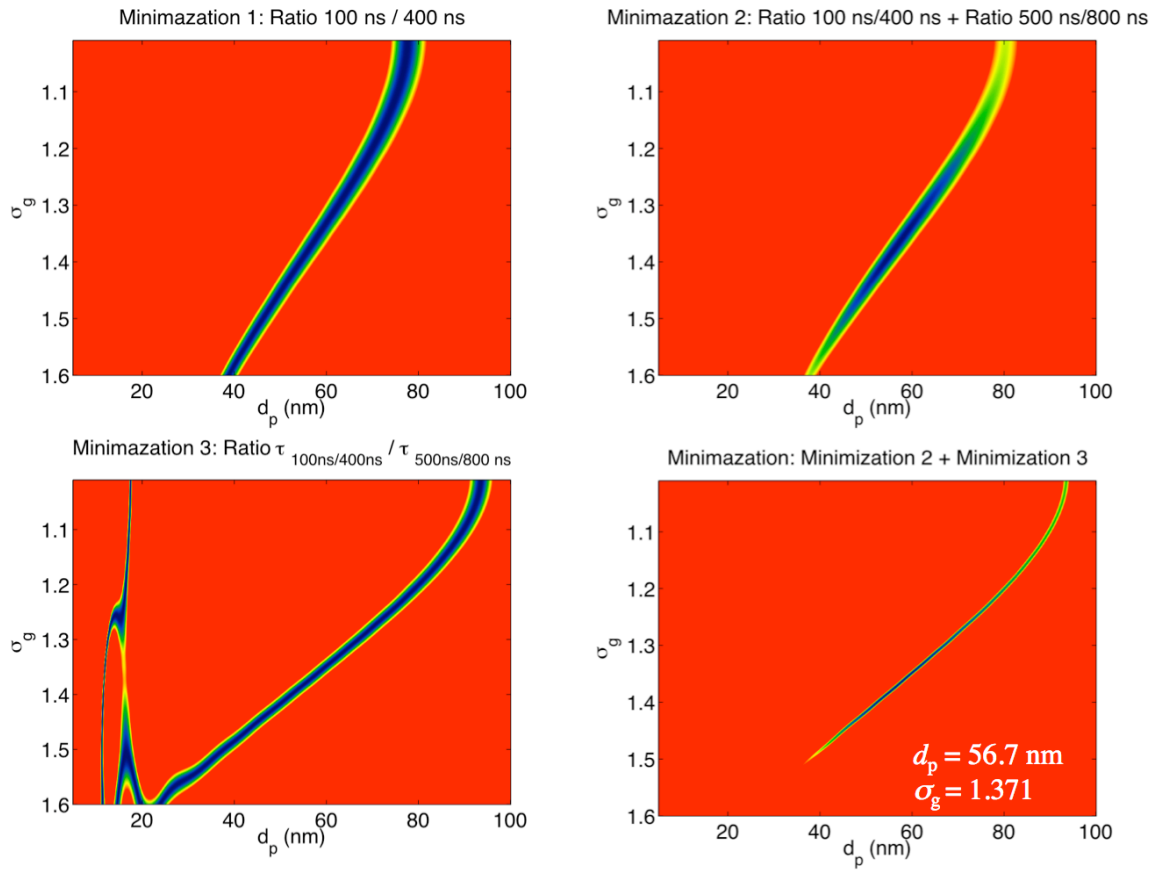
Figure 3.5.12: Minimization criteria for test case 3: d_p = 56.8 nm, σ_g = 1.37. The result of combining Minimization 2 with 3 is shown in the lower-right panel.

In all three cases, Minimization 1 is dominated by the characteristic long range of acceptable solutions. By adding a second time interval to Minimization 2, the length of this range of possible solutions has been substantially reduced for all cases. Still, a further improvement is desired. Minimization 3 was chosen in an effort to complement the curvature in Minimization 2. Clearly, Minimization 3 has a rather interesting, and unpredictable, behavior. For test cases 1 and 2, where the particle sizes are somewhat smaller, combining Minimization 2 with 3 has remarkably successful results, substantially reducing the region of acceptable results. For test case 3 the results are not nearly as dramatic. The region of acceptable solutions has been improved, though not as much as with the smaller particle test cases. This is due to the fact that the long range of potential solutions in Minimization 3 now runs almost parallel to that in Minimization 2. Further size-dependent gate optimization will have to be performed, and early indications are that a later secondary interval is required for the larger particles.

3.5.2.4   Results in the Santoro Burner

Initial time-resolved LII images were taken of the Santoro burner at twelve gate delays after the signal maximum: 0, 50, 100, 200, 300, 400, 500, 600, 700, 800, 900 and 1000 ns. Images were taken of a 1.75 cm slice of the flame, centered at an axial height of 5 cm. The resulting data are shown in Figure 3.5.13. All images have been normalized with respect the maximum of the 100 ns image (set to unity). Each image is displayed on its own color scale. The maximum signal is reduced by 66% (65% on the centerline) in the first 50 ns; by 79% (80%, centerline) after 100 ns; by 94% (97%, centerline) after 500 ns; by 97% (99%, centerline) after 900 ns. This indicates the existence of smaller particles on the flame's centerline, due to the faster decay, and implies the need to use

94

earlier gates, as most of the signal is lost in the first 50 ns. Accordingly, the earlier gates of 50 and 100 ns are used as the initial gates for this study, and are paired with the remaining gates. The resulting signal ratios, determined by dividing the initial gate's LII signal by the later gate's signal, are shown in Figure 3.5.14 for an initial gate of 100 ns.

Initial observations show that larger ratios exist for gates that are further apart, which is to be expected, and also that the variation across the image increases for larger gate spacing. An increased variation across this image will help to distinguish between particle sizes. For example, the gate pair of 100ns/200ns has a variation in signal ratio across the flame of 14%. This gate pair will be more susceptible to experimental noise, as small variations in signal ratio correspond to large variations in particle size. Meanwhile, the gate pair of 100ns/500ns shows a variation in signal ratio of 51%. This variation in signal ratio is seen to increase linearly as the gate spacing increases up to a ~200 ns gate separation. After that the benefit of increasing the gate spacing provides diminishing returns. Efforts to increase the variation in the signal ratio will eventually be outweighed by the decline in signal at later gates. Optimal timing is dependent on the particular range of particles sizes that are being measured.

The experimental signal ratios are combined with the results of the time-dependent LII signal simulation to determine particle sizes in two-dimensions. Results that utilized an initial gate time of 50 ns exhibited somewhat smaller particles than those using a 100 ns initial gate time due to the overestimation of the decay rate from the small, but non-negligible, contribution from particle vaporization. As a result is it necessary to use an initial gate of 100 ns in order to ensure that the dominant mode of heat transfer

95
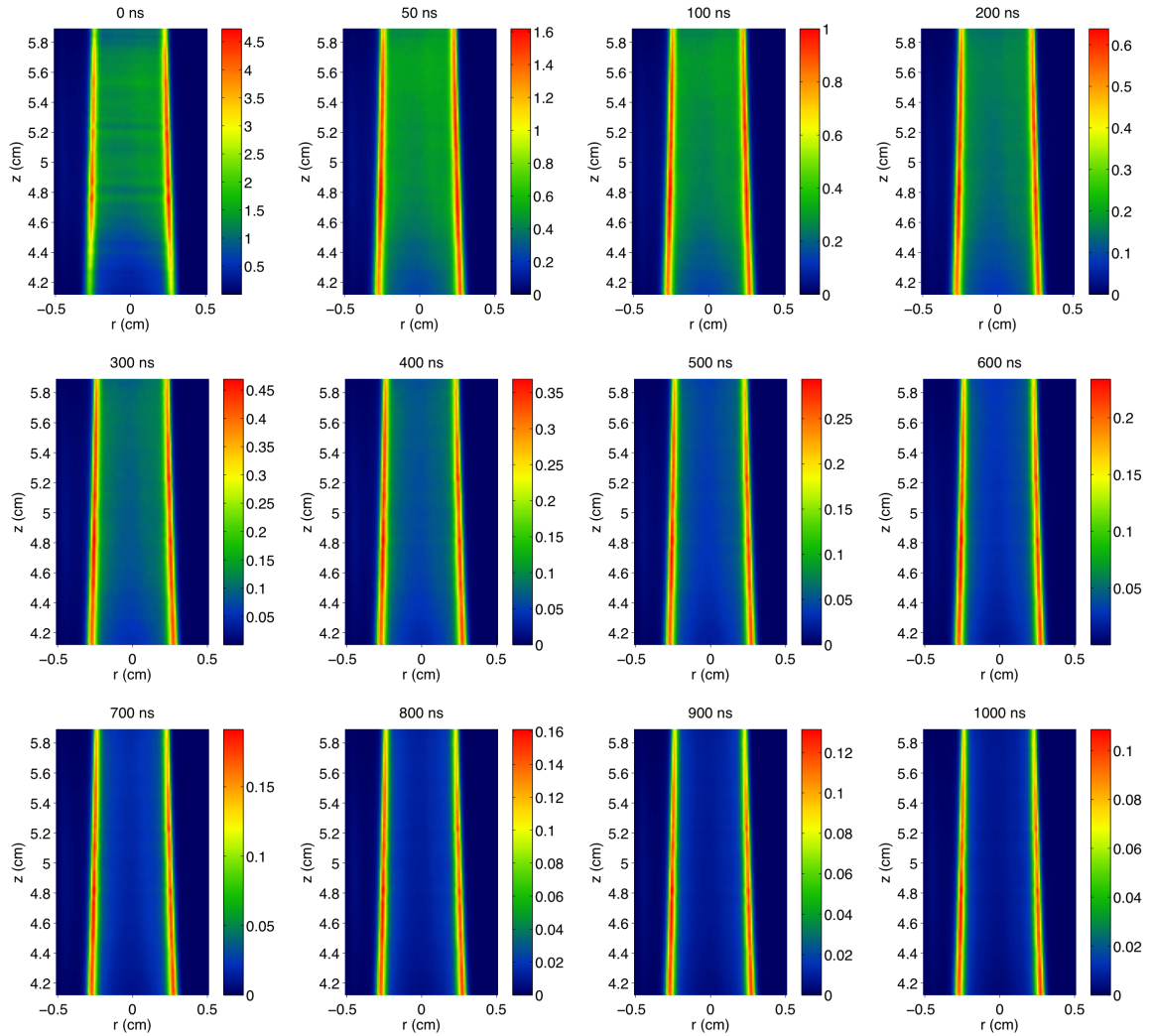
Figure 3.5.13: Time-resolved LII images for different gate delays. Each panel is normalized with respect to the t=100 ns panel, with the maximum of that panel set to unity.
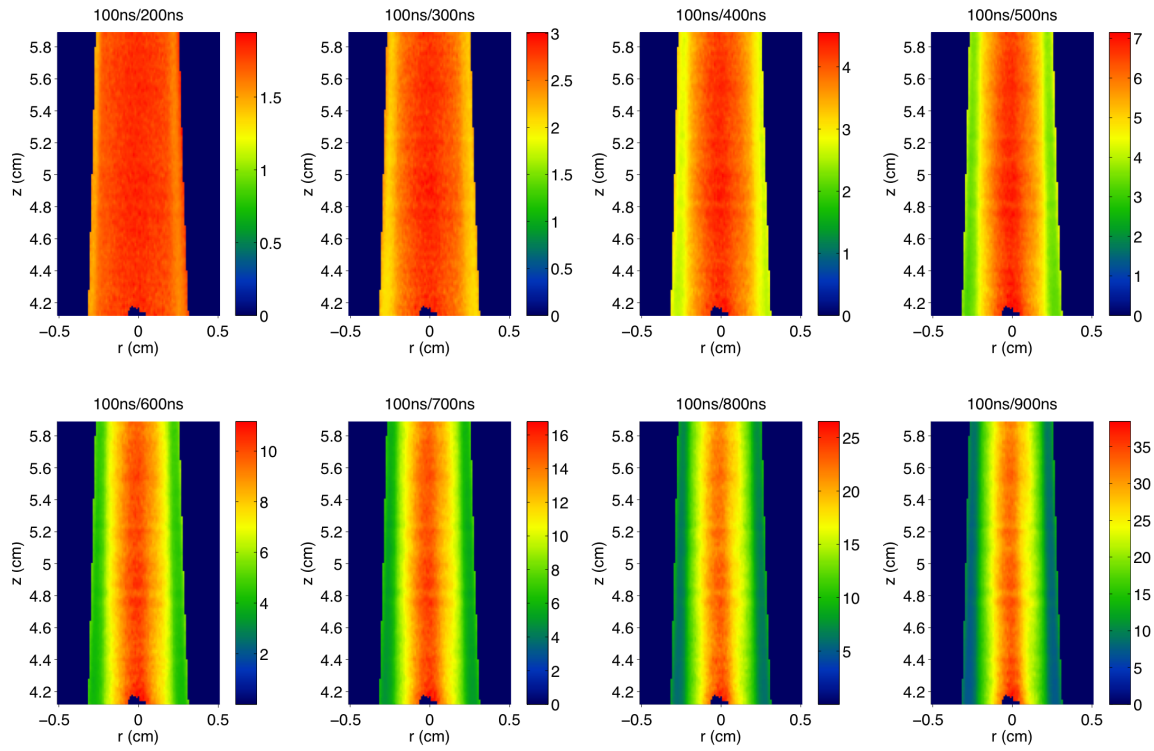
Figure 3.5.14: LII signal ratios for initial gate of 100 ns for the gate pair shown.

is due to conduction. Efforts to minimize this effect by using a low laser fluence were not sufficient. Results for gate pairs that are spaced by 150 ns, or less, are dominated by experimental noise. This was expected due to the small variation in the signal ratio across the image.

Figure 3.5.15 plots the resulting particle size distribution using the minimization criteria discussed in Section 3.5.2.3. Here, a combination of Minimization 2 and Minimization 3 is used with a 100 ns and 400 ns gate pair and 500 ns and 800 ns gate pair. While not shown, results are consistent across all three minimization approaches, though calculation of the larger particles that exist on the wings are highly sensitive to the selection of gate pairs when using earlier gates, or when the gate spacing is insufficient. In this case, use of Minimization 3, where a characteristic time constant is estimated, is particularly valuable. Though use of Minimization 3 output considerably more noise in the image of calculated particle sizes, it predicts the variation in particle sizes more robustly. Failure to use Minimization 3 in the calculation, or the use of experimental gates that are too early in the signal decay process, will not capture the larger particles on the wings and will produce a relatively flat distribution of particle sizes. The results in Figure 3.5.15 show smaller particles on the centerline, with larger particles on the wings of the flame. The geometric width of the distribution exhibits a similar behavior. Examining the calculated diameter and width gives: d_p = 35.1 nm, σ_g = 1.17 (3.2 nm) on the centerline, and d_p = 53.1 nm σ_g = 1.59 on the wings. The centerline results compare well with values found in the literature: 29.3 nm, 1.18 geometric width, in [Schulz 2006a]; 35 ± 3 nm in [Dobbins 1987]; 31 nm in [Koylu 1997]; 33.3 ± 3.2 nm in [Vander Wal 1998]; 32 nm in [Puri 1993].
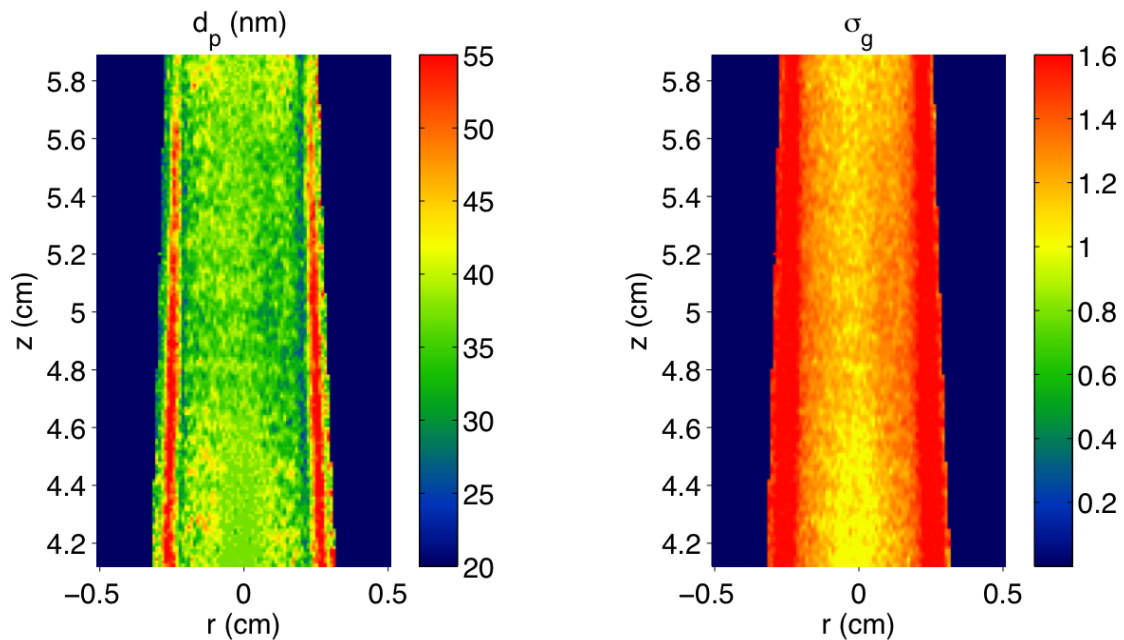
Figure 3.5.15: Experimental particle sizes in the Santoro burner calculating both d_p and σ_g. The combination of Minimization 2 and Minimization 3 was used here, with gate pairs of 100 ns/400 ns and 500 ns/800 ns.

The value found on the wings is rather large and unlikely to occur, particularly when the geometric width is considered, and is most likely biased due to aggregation effects. A possible explanation for the large size and width is the fact that the particles on the wings are heavily aggregated. This will lead to a slower LII signal decay from shielding by closely packed particles that can not be considered as individual spheres under point contact, an assumption of the measurement technique. There is little data in the literature taken on the wings of the flame. Santoro *et. al* [Santoro 1983] measured the diameter using scattering, and found the diameter to be even larger (though difficult to quantify since it is plotted on a log plot it is ~80 – 100 nm). However, scattering techniques make large assumptions about fractal structure, and it is that structure that is responsible for the size bias. An independent scattering measurement would be required to verify the degree of aggregation in the region, and to make the appropriate corrections to the measured particle sizes.

3.5.2.5   TR-LII Method Conclusions

A two-dimensional approach to particle size measurements using time-resolved LII was presented. Images were taken at discrete times after the arrival of the laser pulse, and the resulting signal ratios from different gate pairs were used to determine experimental particle sizes using a library of results for LII signal simulations by solving the forward problem. Gate and minimization criteria were optimized, though further investigation is needed. The resulting particle size and geometric width compares well with results from the literature.

Gate pairs that were separated by larger times showed a larger variation in signal ratio for variations in particle size. Therefore, a larger gate spacing was seen to be more

robust. Gate pairs that were closely spaced were dominated by experimental noise. This occurred because the signal ratio exhibited small variations over the range of particle sizes present. Gate pairs with an early initial gate of 50 ns resulted in particle sizes that were smaller than those predicted using later gate pairs. Measured particle sizes that used an initial gate of 100 ns gave consistent results for all gate pairs investigated. The resulting particle sizes showed good agreement with results from other investigations using other measurement techniques.

Current work includes taking data at later time delays to improve the signal-to-noise and provide greater sensitivity to variations in distribution geometric width (σ_g). Data is currently being taken with improvements to the beam shaping optics that attempt to minimize particle temperature variations across the flame.

3.5.2.6   Computational Particle Sizes

Following the favorable comparisons with previous results in the Santoro burner, the approach is applied to our coflow burner for comparison with computational results. The burner configuration and soot formation model are described in detail in Section 3.2 and Section 3.2.2, respectively. The particle dynamics component is briefly highlighted again here, due to its importance to this topic. The growth of soot particles is modeled as an aerosol dynamics problem, using a sectional particle size representation for spheres [Gelbard 1980]. The contributions from the inception processes are incorporated as a source term in the dynamical equation for the first sectional bin, whose lower mass boundary is set equal to the mass of the assumed inception species. Calculated results were not significantly sensitive to the number of sections assumed, with 20 sections used in the reported calculations.

Each of the 20 sections represents a range of particle sizes, where the total mass of each section is computed. The total mass in each section is used to determine a soot volume fraction of each individual size section $f_{v,i}$, which is used as a weighting function in the particle size distribution's probability density function (*pdf*). If the particle sizes are assumed to follow a lognormal size distribution the geometric mean diameter d_{med} can be computed using

$$d_{med} = \left(\prod_{i=1}^{20} d_{section,i}^{f_{v,i}} \right)^{1/\sum_{i=1}^{20} f_{v,i}} = \exp\left(\frac{\sum_{i=1}^{20} f_{v,i} \ln d_{section,i}}{\sum_{i=1}^{20} f_{v,i}} \right) \tag{3.5.7}$$

where the size class is identified by the average particle size in the section $d_{section,i}$. Figure 3.5.16a plots the average particle size and limits for each of the 20 size bins. The size and location of each bin is not equally spaced. A logarithmic distribution is used to determine the bin spacing. All particle sizes are accounted for, as the top of one bin is coincident with the bottom of the next bin. A histogram indicating the soot volume fraction in each individual bin is plotted in Figure 3.5.16b for a point on the centerline of the 80% C_2H_4 flame, at an axial height of 4 cm.

The calculation in Eq. 3.5.7 is performed on the set of ethylene diffusion flames to determine the computed geometric mean diameter. The geometric mean diameter of the 32%, 40%, 60% and 80% flames are plotted in Figure 3.5.17 on a scale from 0 to 50 nm. It can be seen that the mean particle size increases as the fuel mole fraction is increased. Also, larger particles are observed on the wings of the flame compared with the centerline values for all cases.

(a)

(b)
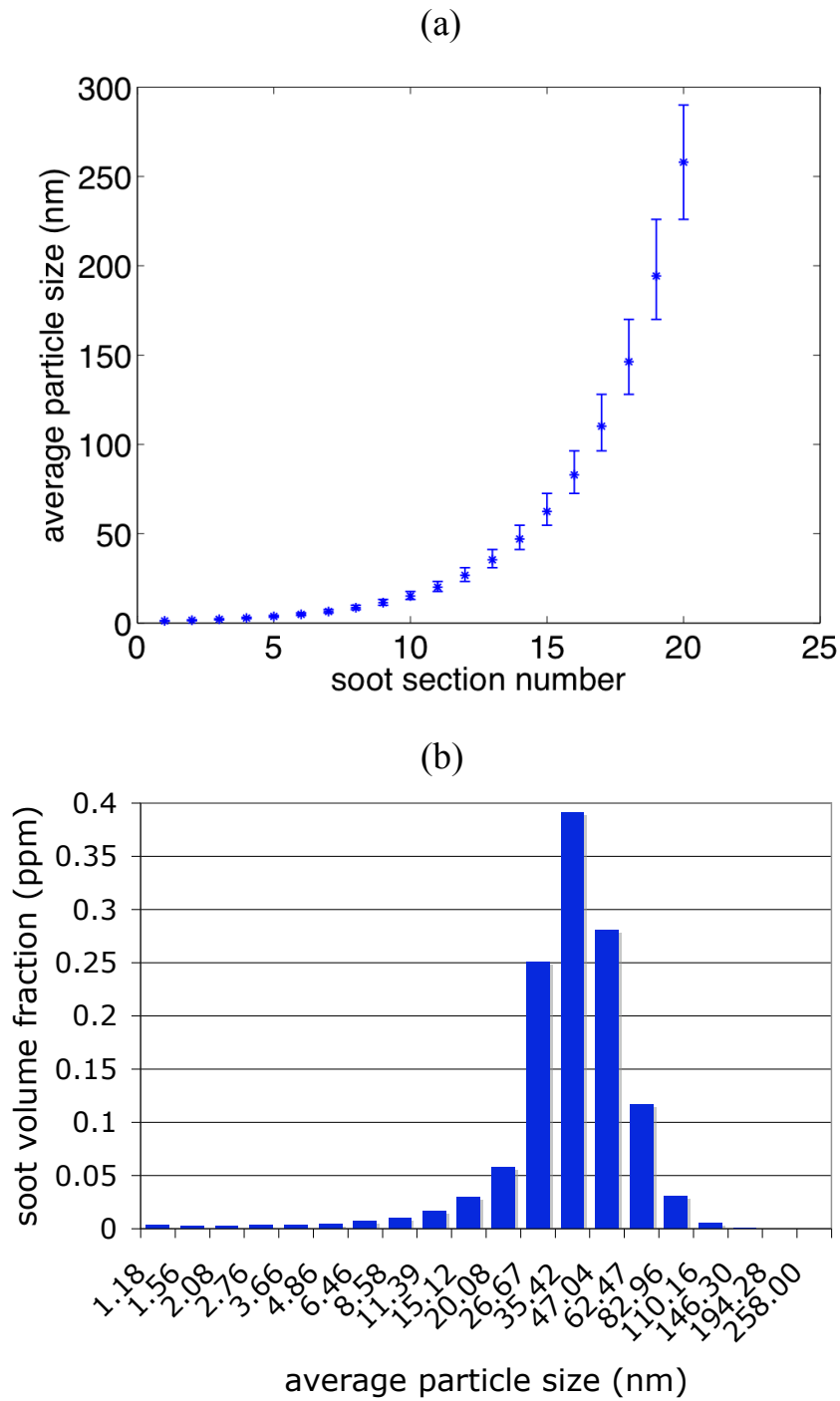
Figure 3.5.16: (a) The average particle size in the 20 bins of size classes is plotted. Error bars indicate the boundaries of each bin. (b) A histogram indicating the soot volume fraction in each individual bin for a point on the centerline of the 80% C_2H_4 flame, at an axial height of 4 cm.
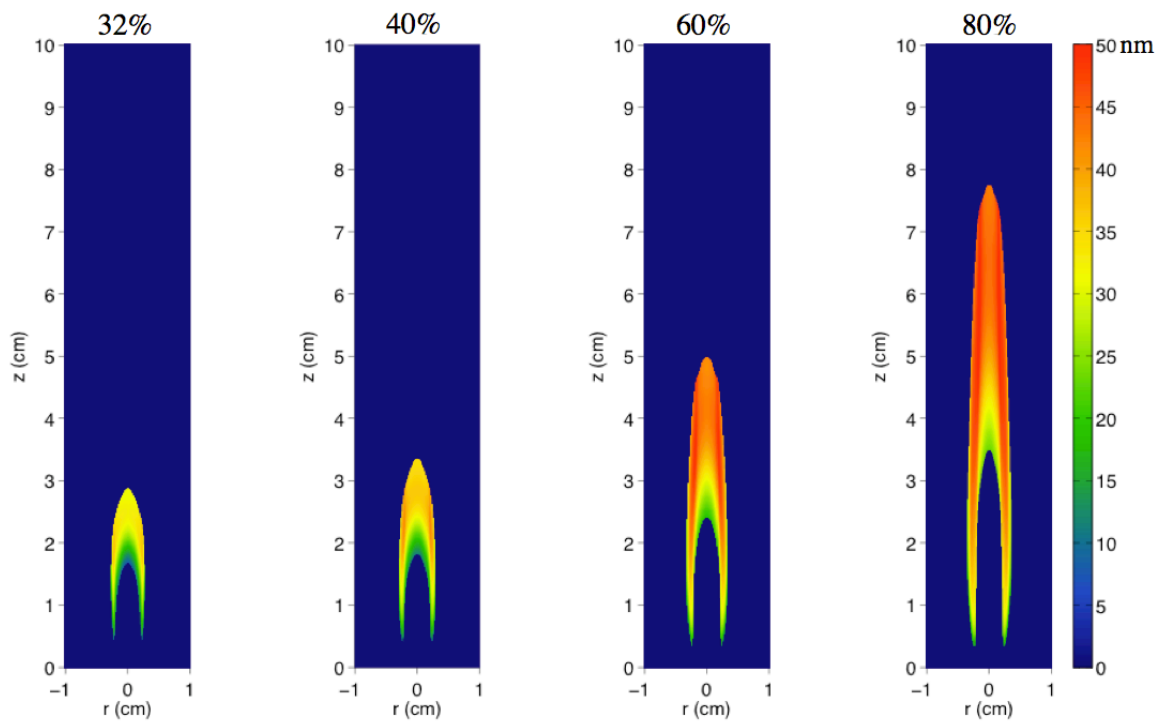
Figure 3.5.17: The geometric mean diameter of the 32%, 40%, 60% and 80% C_2H_4 flames are plotted on a scale from 0 to 50 nm.

3.5.2.7   Target Flame Results and Discussion

Preliminary data were taken in the 40% and 80% C_2H_4 flames. Figure 3.5.18a

shows five temporally-resolved LII images for the 40% flame (at 0, 100, 300, 400 and

500 ns); Figure 3.5.18b shows eight temporally-resolved LII images for the 80% flame

(at 0, 100, 300, 400, 600, 700, 800 and 900 ns). The maximum signal is reduced by a

factor of 3.8 for the 40% flame, and by a factor of 3.4 for the 80% flame in the first

100 ns. The most interesting feature of the images in Figure 3.5.18 is the migration of the

peak signal from the centerline to the wings of the 40% flame (the relative signal

becomes more heavily weighted on the wings for the 80% flame). This is clearly

indicative of the existence of larger particles on the wings of the flame. Further, the

signal from the 40% flame has reduced by almost a factor of 100 after 500 ns, while the

80% flame has a relatively persistent signal past 900 ns (particularly on the wings). This

observation suggests that the 80% flame has larger particles than the 40% flame.

Figure 3.5.19 shows the resulting particle sizes from the experiment, compared

with the computational results. Experimental particle sizes are calculated using

Minimization 2 and 3 with gate pairs of 100ns/300ns and 300ns/500ns for the 40% flame

and gate pairs of 100ns/400ns and 400ns/700ns for the 80% flame. The comparison is

encouraging, as the trends in the computation are captured well both qualitatively and

quantitatively. Compared with the experiments, the computations predict both larger

particles overall and less variation in size on the centerline, relative to the wings. It

should be noted that the computational results do not properly account for bias due to the

presence of aggregate structures in the larger size bins. Instead, surface growth is
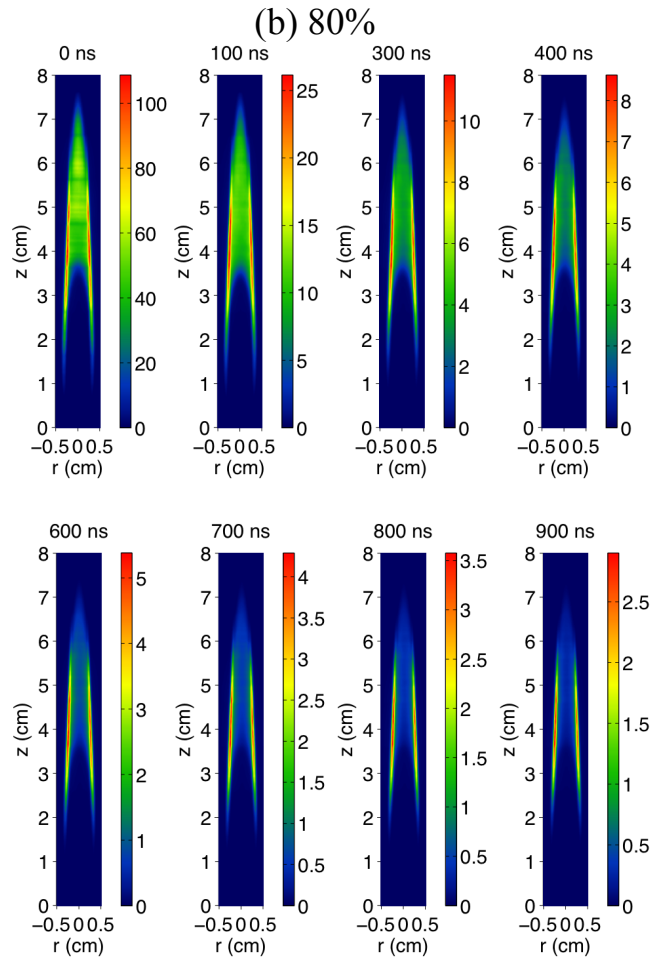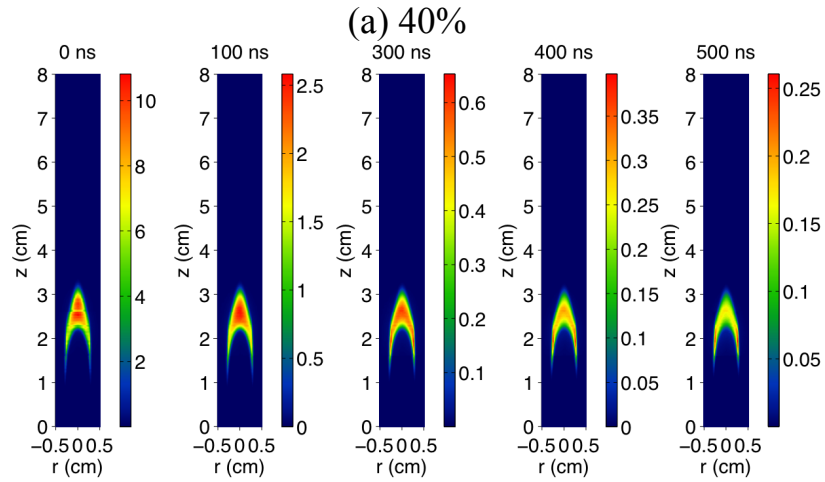
Figure 3.5.18: (a) Plots of five temporally-resolved LII images for the 40% C_2H_4 flame (at 0, 100, 300, 400 and 500 ns). (b) Plots of eight temporally-resolved LII images for the 80% C_2H_4 flame (at 0, 100, 300, 400, 600, 700, 800 and 900 ns).
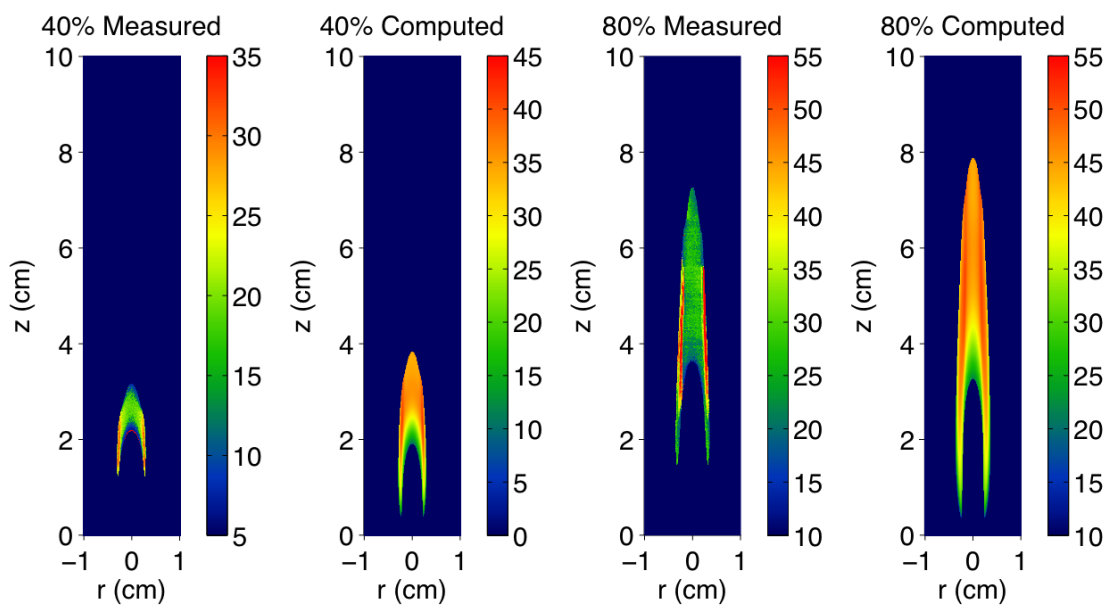
Figure 3.5.19: Comparison of experimental and computational particle sizes for the 40% and 80% C_2H_4 flames.

artificially cut off at 25 nm, and the existing bins are permitted to coalesce into seemingly larger particles. As with the Santoro burner, the experimental results on the flame wings are most likely biased towards larger particles due to aggregation effects. In order to properly quantify the particle morphology in these regions, a complementary measurement such as laser scattering is necessary.

3.6 Laser-Induced Fluorescence

3.6.1 LIF of NO in a Sooting Flame

The goal of this study was to determine the interdependency between soot and NO formation in coflow diffusion flames [Connelly 2009c]. While both NO and soot formation are often studied independently, there is a need to understand their coupled relationship as a function of system parameters such as fuel type, temperature and pressure. The temperature decrease due to radiative losses in systems in which significant soot is produced can affect flame length and other temperature-dependent processes such as the formation of NO. A computational study into the interaction of soot and NO formation was carried out by Guo *et al.* [Guo 2007], where a detailed gas-phase reaction scheme and simplified soot model were applied to a coflow ethylene/air diffusion flame. They found that the formation of NO has little effect on that of soot, while the formation of soot significantly suppressed the formation of NO. This suppression was due to both the radiation-induced thermal and chemical effects. The formation of soot both lowers the flame temperature and consumes acetylene, lowering the formation rate of the radical CH (affecting a rate-limiting reaction important in the formation of Fenimore NO).

The study presented here is a joint computational and experimental work that looks at this problem for flames with different levels of soot loading. The results of a computational model that includes a sectional representation for soot formation with a radiation model are compared against laser-induced fluorescence measurements of NO. Because of signal interferences that occur due to the presence of soot in these flames, it is difficult to perform the necessary corrections to the fluorescence data to make quantitative comparisons with the computational results. Instead, a reverse quenching

correction is applied to the computational results to determine an expected fluorescence signal for comparison with experimental results. The approach of comparing signals, rather than fundamental quantities like mole fractions, is developed in Chapter 5.

3.6.1.1   Linear Fluorescence in NO

The two-level model for linear fluorescence is outlined in Section 2.3.2, where the fluorescence rate is found to have the following dependence

$$F = C_{exp} B_{12} I_v N_{tot} f_1 \frac{A_{21}}{A_{21} + Q_{21}}.$$

(3.6.1)

For many simple molcules, the spectrum of the molecule of interest is known. Here, we're concerned with the spectrum of NO. The laser is tuned to a specific wavelength to excite a transition. The excitation spectrum of NO was simulated using LIFBASE, which is a spectral simulator for diatomic molecules. Results for typical flame conditions, using an approximate laser linewidth of 0.75 cm^{-1} are shown in Figure 3.6.1a. The (0,0) band is chosen for excitation here. Once excited, the electron can relax to a number of states by emitting a photon. In reality, certain transitions are more likely than others. This probability is determined by the Franck-Condon factor, which arises by the assumption that electronic transitions occur much more quickly than nuclear motions, so that transitions occur straight up and down along the nuclear coordinate, R. This factor can be calculated by determining the overlap integral of the wave functions of the relevant states, integrating over R. The emission spectrum of NO is shown for excitation in the (0,0) band in Figure 3.6.1b. The spectral resolution in this plot accounts for a detection resolution typical of an imaging spectrograph (~1 nm).
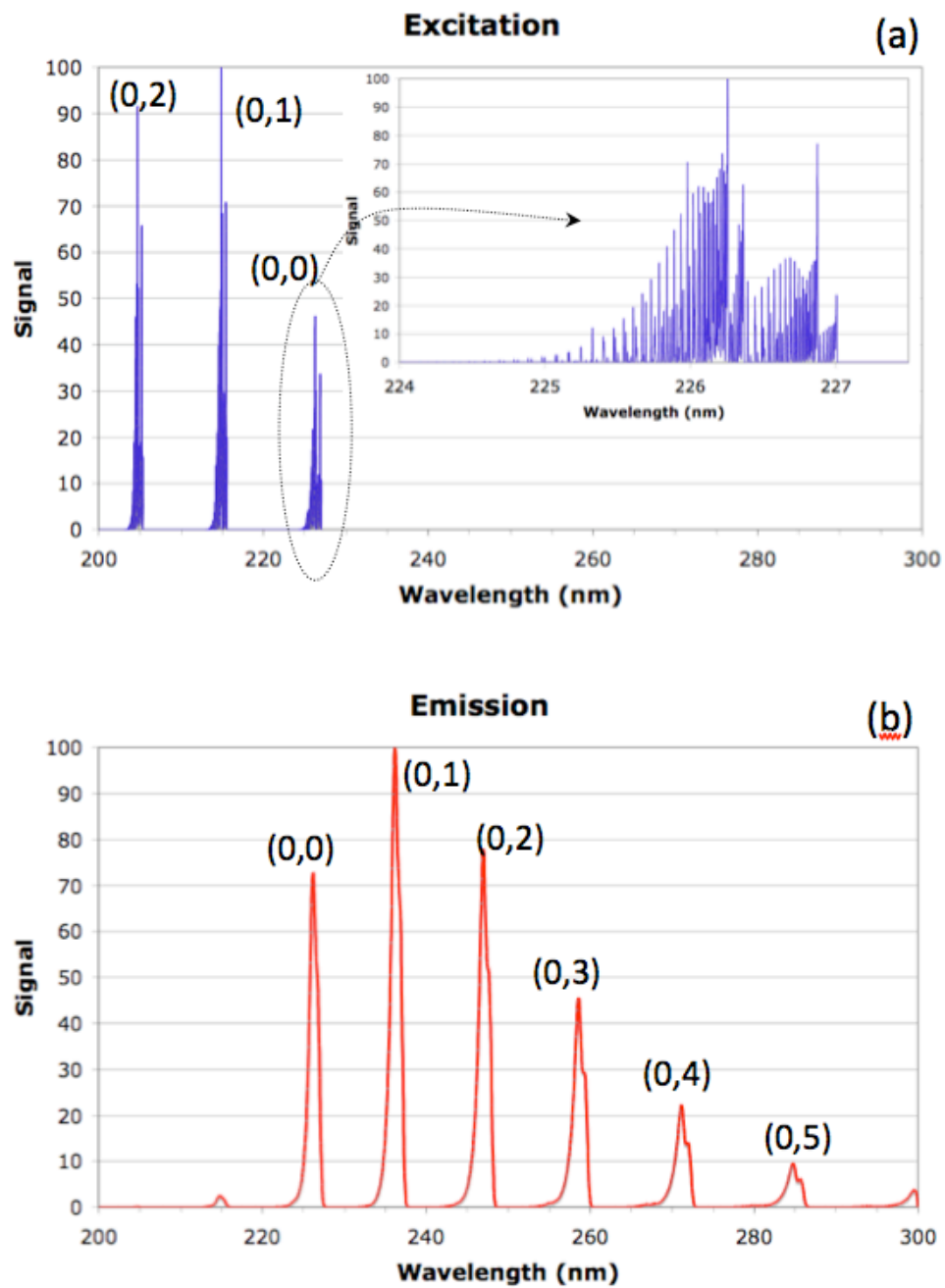
Figure 3.6.1: Spectrum of NO. (a) The excitation spectrum of NO, where the (0,0) excitation band has been expanded in the upper-right corner. (b) Emission spectrum of NO, where the spectral resolution of detection systems has been taken into account.

The $Q_1(18)$ transition (44275.684 cm^{-1}) was selected for this work. This transition is reasonably well separated from neighboring transitions and has significant population from room temperature to the flame temperatures investigated. Aside from soot interferences, which posses a broadband spectrum, no significant spectral interferences from molecules such as O_2 were encountered in the laminar flames investigated [Carter 1994]. This transition corresponds to an initial electronic state of $n = 1$, $\upsilon = 0$ and $J = 18$. Using the formulation for the fraction of molecules in the initial state, f_1, being pumped from Boltzmann statistics in Section 2.3.2.1, the temperature dependence of f_1 can be determined. Figure 3.6.2a plots the total number of molecules in each rotational state J. It can be seen that there is significant population in this state as the temperature varies from room temperature (300 K) to a typical flame temperature (2000 K). Also plotted in Figure 3.6.2b are the relative population fractions for the vibrational correction, the rotational correction, and the total for the $J = 18$ state, where the fraction at room temperature is set equal to one here.

For NO, the quenching term, Q_{21} in Eq. 3.6.1, is particularly important, and varies significantly with temperature as well as with quenching partners. Fortunately, a good deal of information is available on NO quenching, both in the form of experimental measurements and models [Drake 1993; Paul 1993; Settersten 2006]. Figure 3.6.3 plots the quenching cross-sections for a selection of species from the recent study by Settersten *et. al.* [Settersten 2006]. It is only necessary to consider species that have both a significant quenching cross section and are present in significant concentrations in the flame. N_2, for example, is present in rather large quantities, but has a negligible cross section. Alternatively, NO_2, which is not plotted, has a large cross section due to a near
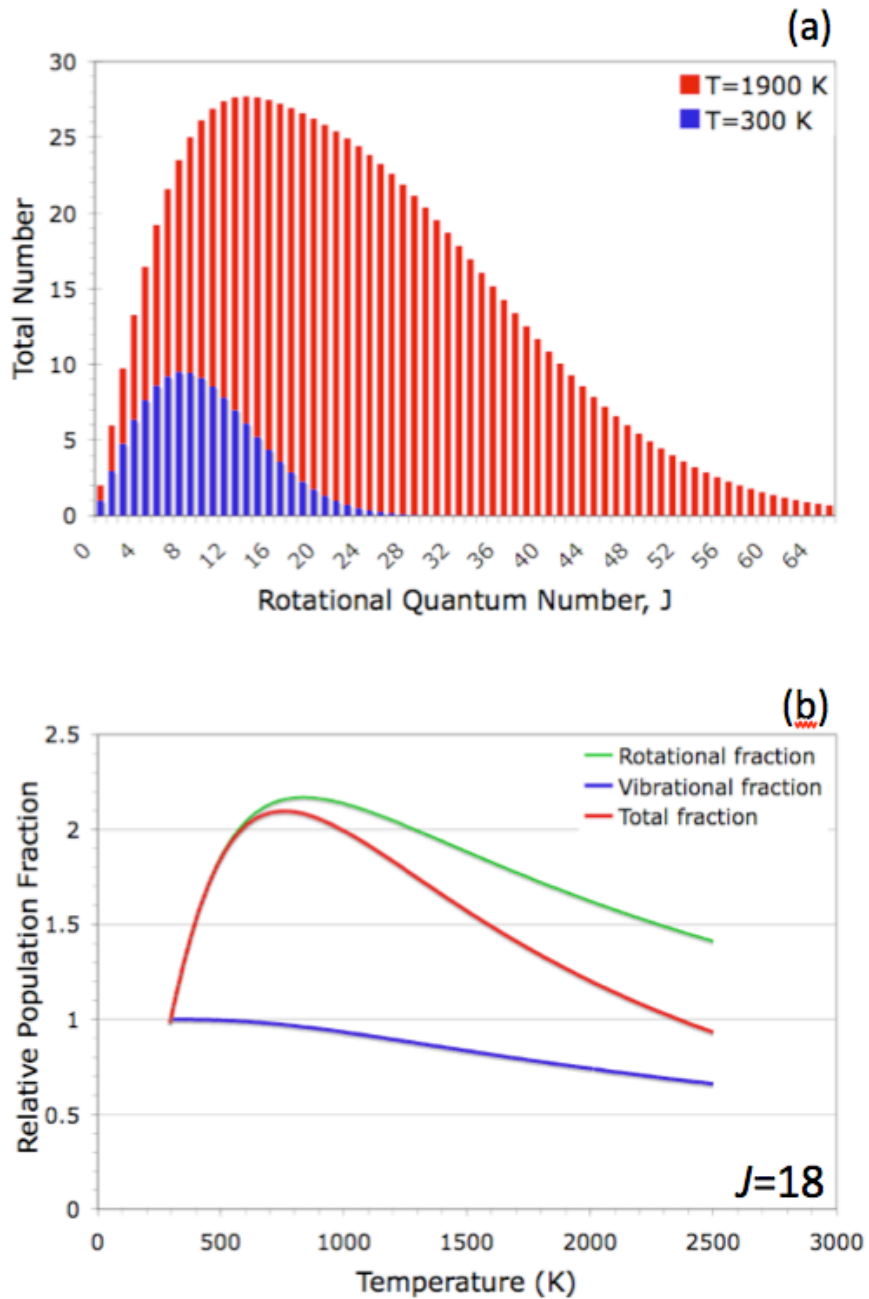
Figure 3.6.2: (a) Plots the total number of molecules in each rotational state J at room temperature (300 K) and a typical flame temperature (1900 K). (b) The relative population fractions for the vibrational correction, the rotational correction, and the total for the $J = 18$ state, where the fraction at room temperature is set equal to unity.
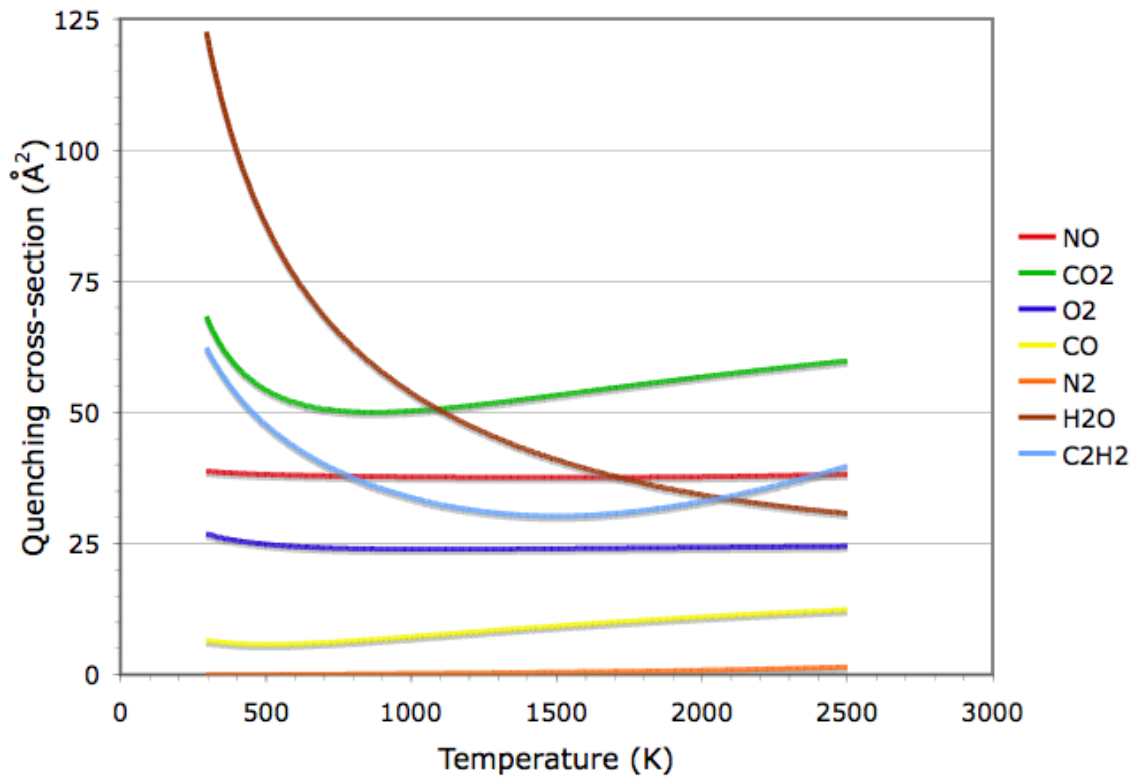
Figure 3.6.3: Temperature dependent quenching cross sections for NO, plotted for species that are important in the combustion process. The model of Settersten *et al.* is used here.

resonance with NO, but is only present in the ppm range.

Since the rotational and vibrational level population fractions change significantly with temperature and the quenching correction is heavily dependent on temperature and quenching partner concentration, it is important to know the ambient temperature and composition of the measurement volume. Since it is difficult to measure the ambient gas temperature or concentration of major species in a sooting flame, a different approach is needed. Instead, an alternative approach of applying a reverse quenching correction [Smooke 1996; Sick 1998] to the calculated flame to determine an expected fluorescence signal for comparison with the experimental results [Bell 2003] is applied. The model of Settersten et al. is used to account for the temperature-dependent quenching by CO_2, H_2O, O_2, N_2, and CO. See Chapter 5 for a more detailed analysis of this approach.

3.6.1.1   NO LIF Experiment

The experimental layout used to measure NO fluorescence is shown in Figure 3.6.4. The third harmonic of a Nd:YAG laser pumps a dye laser containing coumarin 450 dye. The 452 nm dye laser output is doubled using a BBO crystal, producing an ultraviolet (UV) beam near 225.8 nm, which is used to excite transitions in the $A^2\Sigma^+$-$X^2\Pi$ (0,0) band of NO.

3.6.1.1.1   Excitation Scan

As shown in Section 3.6.1.1, it is important to know exactly which transition is being pumped. Consequently, an excitation scan of the A$\rightarrow$X (0, 0) band must be carried out. After the beam splitter in Figure 3.6.4, the laser is steered over a lean premixed propane flame and excites NO fluorescence. Fluorescence passes through an interference filter centered at 260 nm and detected with a UV sensitive PMT (Hamamatsu R166UH)
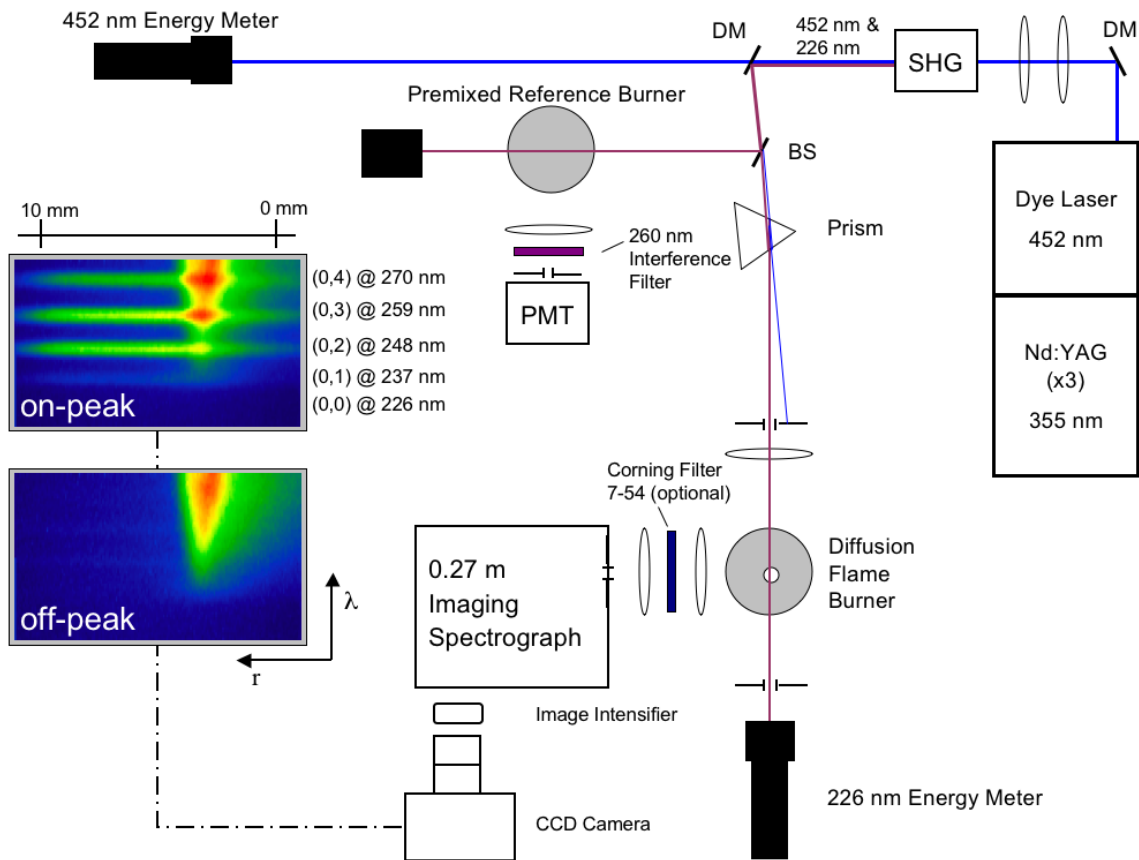
Figure 3.6.4: Experimental setup for NO LIF experiment.

connected to a digital oscilloscope. This detection band corresponds to the (0,3) vibrational transition in NO. The dye laser is scanned in 0.004 nm increments, corresponding to 0.78 cm^{-1} steps for the doubled UV beam, over the range of 1 nm (225.5-226.5 nm) in the (0,0) excitation band. The laser energy of both wavelengths is also monitored, and the 225.8 nm energy is used to normalize the fluorescence signal over the scan.

Figure 3.6.5a shows the data taken for one excitation scan. The normalized fluorescence signal is shown as a function of excitation wavelength. The data is composed of the averaged fluorescence signal for 16 laser pulses, normalized by the measured laser energy. The spectrum is matched with the various spectral features of NO [Engleman Jr. 1970] and the results of several scans are plotted against an NO spectrum output from LIFBASE in Figure 3.5b. The excellent agreement between each scan and the simulated NO spectrum allows for easy identification of the $Q_1(18)$ peak. Additionally, a suitable off-peak location is identified in order to provide a correction for background signals from interfering effects such as soot.
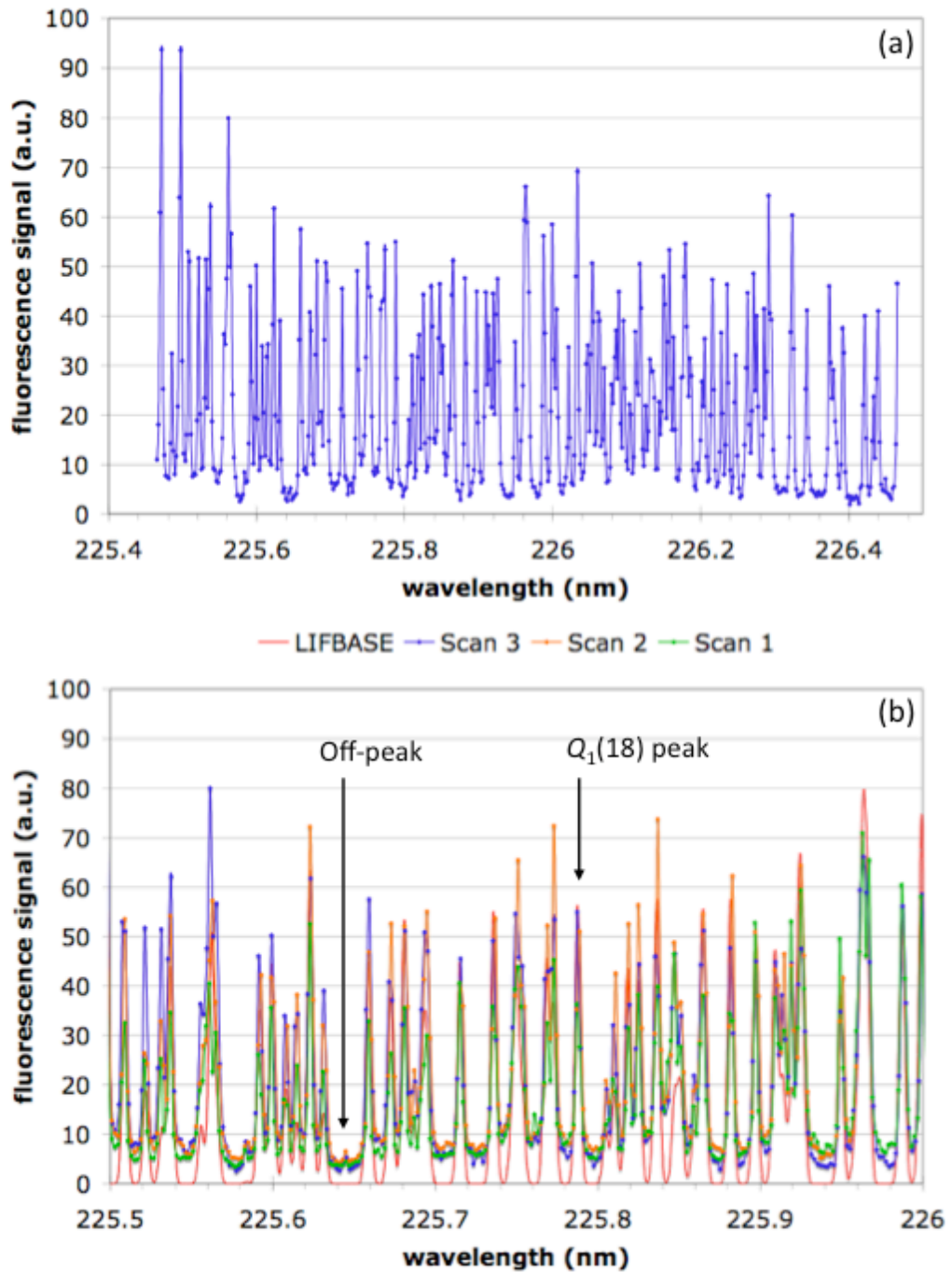
Figure 3.6.5: (a) Excitation scan of NO fluorescence in a premixed burner. (b) Several excitation scans matched spectrally to the output of LIFBASE, a spectral simulator.

3.6.1.1.2   LIF Measurement

There are two burners in the optical path (Figure 3.6.4). A dichroic mirror steers the UV beam down the measurement path, and removes the majority of the laser energy at 452 nm. A beamsplitter steers ~30% of the energy in the UV beam 4 cm above a premixed reference burner. NO fluorescence from the center of a lean propane flame is imaged with a quartz lens onto a 1 mm slit, through an interference filter at 260 nm (12.5 nm bandwidth) centered on the (0,3) vibrational band. The signal is detected with a PMT (Hamamatsu R166UH) connected to a digital oscilloscope. This signal is used to provide a fluorescence normalization that accounts for variations in laser energy and ensures that the laser wavelength does not shift off of the peak of the NO transition being pumped.

The UV beam remaining after the beamsplitter (~60 µJ per pulse) is directed across the target diffusion flame burner. Because the remaining energy from the 452 nm beam (~100 µJ) causes interference in sooting regions of the flame, the two wavelengths are separated using a quartz prism. The remaining UV beam still produces unavoidable soot interferences. A 25 cm focal length quartz lens focuses the UV beam across the diffusion flame. To ensure that the fluorescence is in the linear regime, the measurements are made 10 cm before the focus of the UV beam, resulting in a beam diameter of 0.5 mm in the measurement region. While this beam diameter sacrifices some spatial resolution in the axial direction, features of the NO LIF in the axial direction are observed (both experimentally and computationally) to be larger than the beam diameter. Finer structures in the NO LIF occur in the radial direction, where the spatial resolution is superior. Using Nyquist sampling criteria the spatial resolution is 0.13 mm in the raw images and 0.2 mm

in the final, corrected images. The laser energies at 225.8 nm and at 452 nm are monitored using two pyroelectric energy meters (LaserProbe RjP-734) connected to a second oscilloscope.

NO fluorescence in the diffusion flame is imaged onto a 500-µm entrance slit of a spectrograph (SPEX 270M) using a UV camera lens (UV-Nikkor 105 mm, f/4.5) and a 10 cm focal length quartz lens. When taking data in the sooting regions within the flame, a colored glass filter (Corning 7-54) is placed between the two collection lenses to suppress the Rayleigh scattering by the soot, which would otherwise saturate the detector. Spectral resolution is sacrificed by using a relatively wide entrance slit to compensate better for wandering of the beam through the measurement volume. The fluorescence is dispersed with a 300 groove/mm grating (250 nm blaze angle) and imaged with an intensified CCD detector (a gated Gen II intensifier optically coupled to a Princeton Instruments TE/CCD-512 CCD). The CCD image contains information in one spatial and one spectral dimension. Spatially, a line extending from the centerline to 10 mm in the radial direction is imaged, and spectrally the region from 220-300 nm is recorded. The spectral region includes Rayleigh scattering (overlapped with the (0,0) fluorescence) as well as the (0,1), (0,2), (0,3) and (0,4) vibrational fluorescence bands. The fluorescence signal is integrated on the detector for 12.8 seconds (128 laser pulses), chosen to correspond to event sampling on the oscilloscopes. The experiment is controlled through a computer, which records synchronized data from the CCD camera and the digital oscilloscopes. Data are acquired both with the laser tuned to the $Q_1(18)$ peak (see, e.g., the spectrum labeled "on peak" in Figure 3.6.5), and with the laser tuned off-resonance

120

(near 225.65 nm), to provide a correction for soot interferences (see the spectrum labeled "off-peak").

The final fluorescence image is obtained by summing the fluorescence intensity over a 7.5 nm spectral region centered on the (0,2) transition [Drake 1993]. No significant difference is noted when the detection band is centered on the (0,1) or on the (0,3) transition. A two-dimensional image of the NO fluorescence distribution is created by tiling together a series of spatial/spectral images recorded at 0.5-mm intervals from 2-100 mm above the burner. Each image is corrected for detector and soot incandescence backgrounds, normalized by the reference fluorescence signal recorded by the PMT, and corrected for nonuniform detector gain and optical throughput. This latter "response" correction is obtained by imaging the fluorescence from a calibration gas (45.2 ppm NO in N_2 mixed with 3% O_2, by volume), which results in a uniform NO concentration field in the imaged region that also provides a room temperature signal calibration. The final corrected fluorescence image has a signal-to-noise ratio of ~50 in the downstream region, where the NO signal was highest, and a pixel volume of 0.1 x 0.5 x 0.5 mm^3.

The addition of O_2 to the calibration gas was chosen to both reduce the LIF signal so that it could be detected within the dynamic range of the experimental setup, and more importantly to control the quenching rate of the gas. The quenching cross section of NO by N_2 is both negligibly small (~0.01 Å^2) and not well known, as the value can vary by an order of magnitude in the literature (see, e.g., [Paul 1993; Settersten 2006]). Because more than 99% of the calibration gas is composed on N_2, even a small cross section becomes important, leading to a substantial uncertainty in the calibration. O_2, on the other hand, has large and well-characterized cross section (26.8 Å^2 at room temperature).

Simply adding 3% O_2, by volume, to the calibration gas of 45.2 ppm NO in N_2, changes the room-temperature quenching rate by two orders of magnitude (from $1.89 * 10^6$ to $1.28 * 10^8$ s^{-1}). This provides greater confidence in the experimental calibration.

3.6.1.2   NO Formation Submodel

The computational work for this study was carried out by Professor Mitchell Smooke, in collaboration with Dr. Meredith Colket and Dr. Robert Hall at UTRC. The soot formation model is described in detail in Section 3.3 [Smooke 2004]. The computations employ the ethylene mechanism in [Sun 1996] coupled with the nitrogen chemistry submechanism in GRI 2.11 [Bowman 1995]. The GRI 2.11 submechanism was decided upon, as opposed to the newer one in GRI 3.0 [Smith], as the latter significantly over-predicts (by a factor of 2.5) NO downstream in our coflow flames [Bennett 2008b]. The result is a reaction network containing 84 chemical species with 578 reactions. The velocity profile of the ethylene fuel tube was parabolic with an average velocity of 35 cm/sec. The air coflow was a plug flow profile with a velocity of 35 cm/sec. The gases emerged from the burner at 298 K. All computations were performed on a 1.4 GHz AMD Dual Opteron processor.

NO can be formed in hydrocarbon flames by several different mechanisms (see e.g., [Miller 1989; Drake 1991; Bozzelli 1995]). The Zeldovich or thermal NO mechanism [Zeldovich 1946] as extended by Bowman and Seery [Bowman 1972] is initiated by the reaction of N_2 with O. This well known 3-step reaction sequence is the dominant NO forming route at temperatures above 1850 K. A second path consists of reactions involving N_2O, which form NO. NO formed via this mechanism increases at higher pressures. A third mechanism responsible for NO formation is (prompt)

122

"Fenimore NO." The main steps influencing this reaction sequence are $N_2+CH=HCN+N$, $N_2+CH_2=HCN+NH$ and other reactions involving N_2 and hydrocarbon radicals. Lastly, NO can be formed via the $H+N_2=NNH$, followed by $O+NNH=NO+NH$ sequence. GRI 2.11 includes these latter reactions but not with the higher rates suggested by Bozzelli and Dean [Bozzelli 1995]. The NO formation rates of each of these reaction sequences can be enhanced through super-equilibrium levels of O-atoms and other radical species in the flame front.

3.6.1.3   Analysis of Computational Results

In this work two flames with different fuel dilutions are examined: a 40% ethylene/60% nitrogen flame and an 80% ethylene/20% nitrogen flame (by mole fraction). To assess the Zeldovich/non-Zeldovich NO distribution, additional computations were carried out with only the extended Zeldovich submechanism appended to the hydrocarbon mechanism. Note that in prior work in which we examined the origins of NO in atmospheric pressure coflow methane-air diffusion flames [Smooke 1996], we found that the N_2O and NNH submechanisms contributed minimally to overall NO levels. As a result, the impact of these two submechanisms specifically on the overall NO levels is not examined, but all NO above the Zeldovich mole fraction levels is assigned as non-Zeldovich NO (in practice, this is almost totally Fenimore NO).

Figure 3.6.6 plots the NO mole fractions for the 40% ethylene/60% nitrogen flame computed with the extended Zeldovich submechanism. When soot is included in the model (Figure 3.6.6a), we obtain a maximum soot volume fraction of 1.3 ppm with a peak NO of 22 ppm. The peak temperature is 2006 K. When the computation was performed without the inclusion of soot (Figure 3.6.6b), the peak temperature increased

to 2055 K and the NO increased to 40 ppm. From the isopleths in the figure, we note that the region of NO above 20 ppm is larger in extent in the nonsooting flame compared to that of the sooting flame.

The NO mole fractions for the 40% flame computed with the complete NO mechanism are also illustrated in Figure 3.6.6. When soot is included in the computation (Figure 3.6.6c), the peak NO increases to 140 ppm. Most of the 118 ppm increase compared to the Zeldovich computation is due to Fenimore NO. If soot is removed from the computation (Figure 3.6.6d), the NO increases to 160 ppm and again the 120 ppm increase over the Zeldovich computation is due mostly to Fenimore NO. The spatial distribution of the NO is generally quite similar for these two computations. For reference purposes, we point out that the sooting 40% flame had an overall power loss of 16.1 W of the total 102 W generated due to radiation.
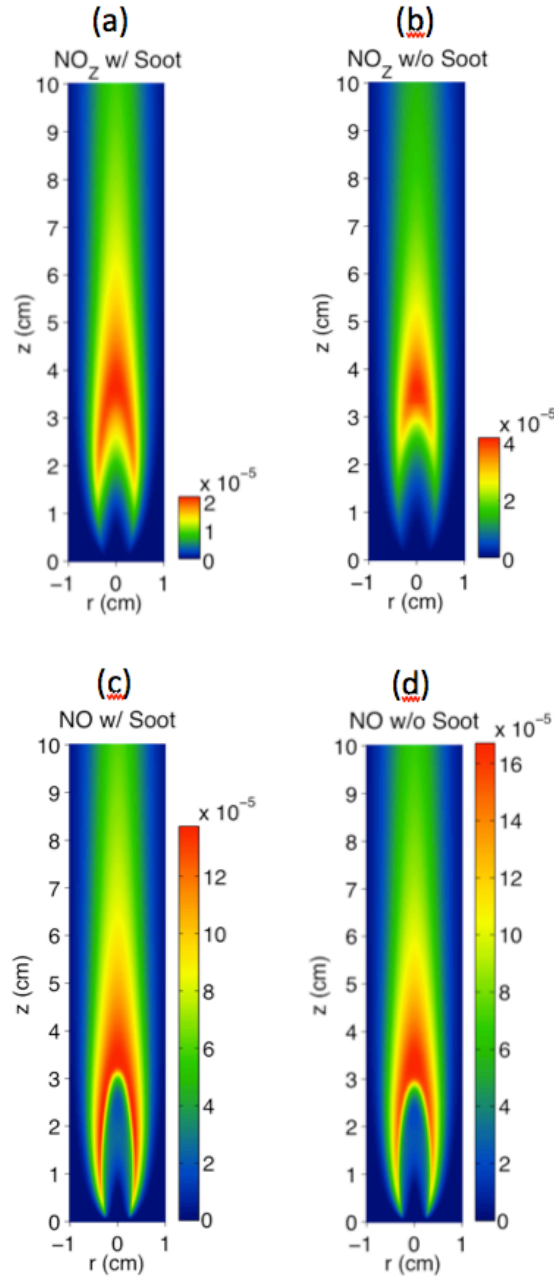
Figure 3.6.6: Computational NO mole fractions for the 40% ethylene/60% nitrogen flame generated with: (a) the extended Zeldovich submechanism, including soot; (b) the extended Zeldovich submechanism, neglecting soot; (c) the complete NO_x submechanism, including soot; (d) the complete NO_x submechanism, neglecting soot.

Next computations for the 80% ethylene/20% nitrogen flame were performed. In Figure 3.6.7a and 3.6.7b NO mole fractions are plotted for computations with only the Zeldovich submechanism. When soot is included (Figure 3.6.7a), we obtain a maximum soot volume fraction of 4.4 ppm and a total of 40 ppm of NO. The peak temperature of 2083 K occurred in the wings of the flame while the peak centerline temperature was 1736 K. When the computation is performed without soot (Figure 3.6.7b), the NO increases to 110 ppm and the peak temperature of 2107 K occurs on the centerline. Once again the spatial extent of the high NO levels is significantly larger for the computation in which soot is not included though the higher region of NO in the sooting flame extends further down the wings of the flame.

The 80% flame was then rerun with the complete NO mechanism. In the sooting case (Figure 3.6.7c), the peak NO increased to 170 ppm. Most of the 130 ppm increase was due to Fenimore NO. If soot was removed from this computation (Figure 3.6.7d), the NO increased to 240 ppm and again the 130 ppm increase over the Zeldovich submechanism computation was due mostly to Fenimore NO. What is striking in these two results is the change in the spatial distribution of the NO with or without soot. For the sooting flame, the highest NO extends in a narrow region in the wings of the flame. For the case when soot was neglected, the NO extends much further downstream with somewhat smaller extent in the wings. The 80% sooting flame had an overall power loss of 53.3 W of the total 203 W generated due to radiation.
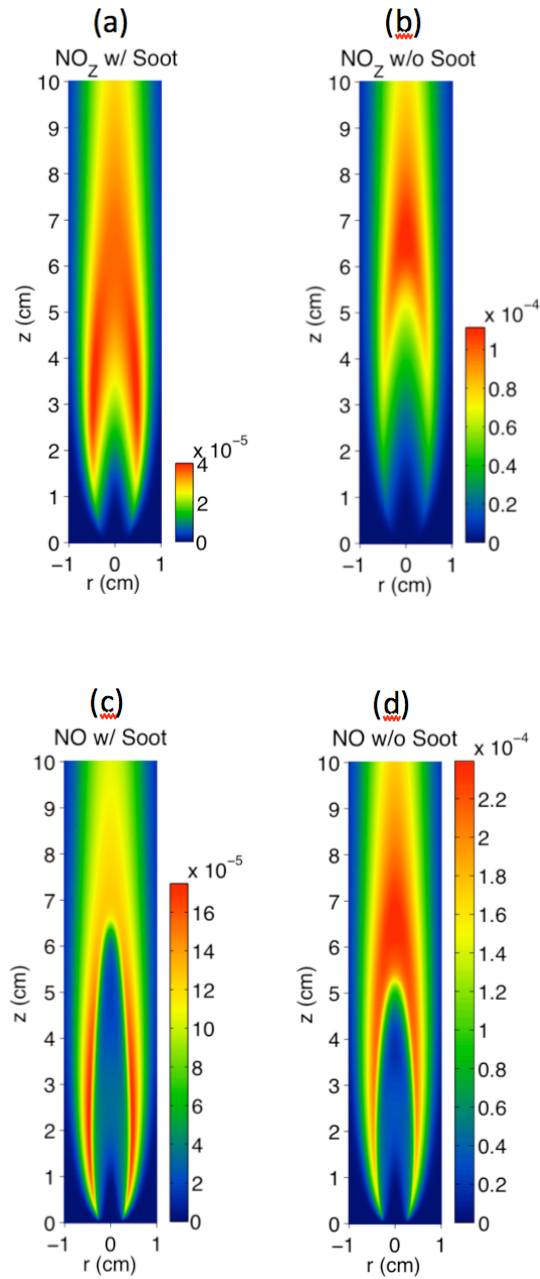
Figure 3.6.7: Computational NO mole fractions for the 80% ethylene/20% nitrogen flame generated with: (a) the extended Zeldovich submechanism, including soot; (b) the extended Zeldovich submechanism, neglecting soot; (c) the complete NO_x submechanism, including soot; (d) the complete NO_x submechanism, neglecting soot.

A clear contrast exists in the NO and temperature levels between the two flame solutions for the 80% ethylene flames, with and without soot (and related radiation). In the complete solution the NO levels and temperature are noticeably depressed along the centerline relative to the off-centerline conditions in the "wings" of the flame. Such results not only contrast with the 40% flame solutions, but also for the 80% flame solutions without any soot or its radiation. In the latter case, elimination of soot removes an important loss of energy from the flame and centerline temperatures nearly recover and peak NO levels occur on the centerline.

3.6.1.4   Comparison of NO Fluorescence Results

As mentioned in Section 3.6.1.1 and discussed in further depth in Chapter 5, due to soot formation within the flame, we cannot easily characterize the flame temperature and major species. Hence, the quenching and Boltzmann corrections cannot be applied to the measured fluorescence signal. Instead, we have applied a reverse quenching and Boltzmann correction to the computed flame profiles to determine an expected fluorescence signal. This simulated signal is calibrated by an expected fluorescence signal, from a gas of the same composition as in the experiment, to provide a quantitative comparison. In Figure 3.6.8 the reverse quenching and Boltzmann correction is applied to both the 40% flame (a) and the 80% flame (b) using the computational results. Rewriting Eq. 2.3.28, the fluorescence signal can be written in terms of the mole fraction of NO, X_{NO}:

$$F = C \frac{P X_{NO}}{k_b T} f_1 \frac{A_{21}}{A_{21} + Q_{21}}.$$

(3.5.1)

(a) 40% C₂H₄
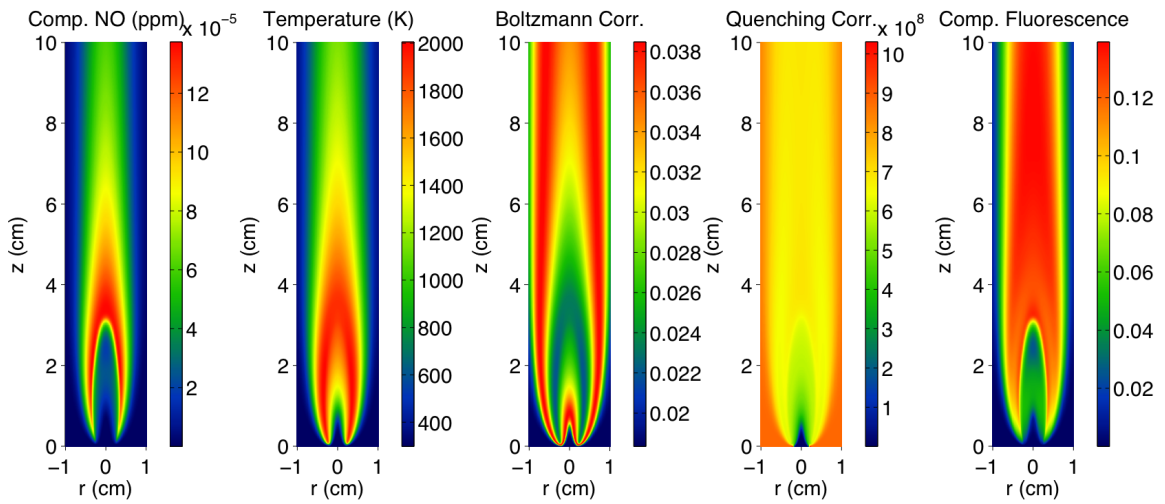
(b) 80% C₂H₄
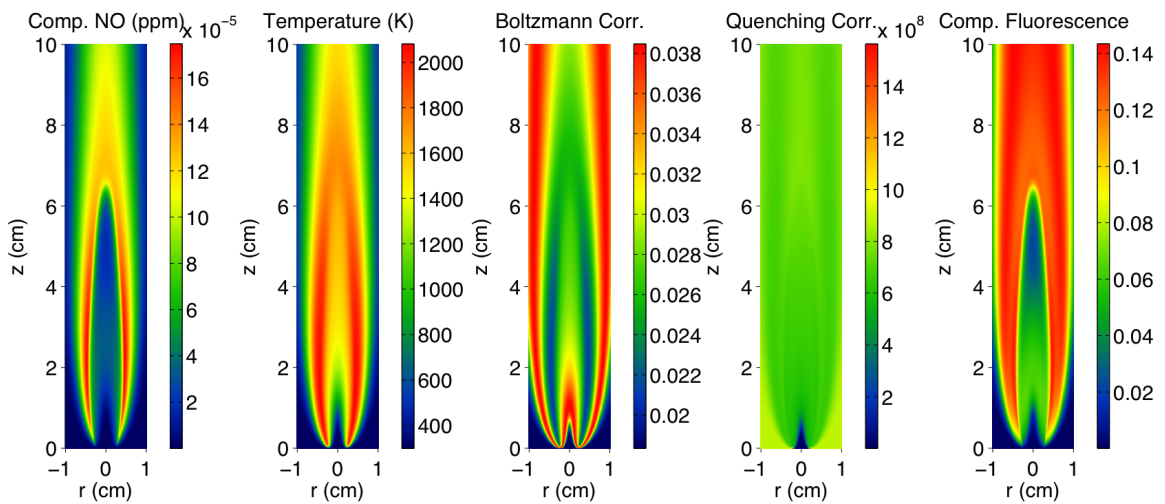
Figure 3.6.8: Computed fluorescence for the (a) 40% ethylene/60% nitrogen flame; (b) 40% ethylene/60% nitrogen flame. The fluorescence signal is computed using the computed NO mole fraction, temperature and major species. The temperature is used to determine the Boltzmann correction; the temperature and major species are used to determine the quenching correction using the model of Settersten *et. al*. The final computed fluorescence signal is then calibrated with respect to a calibration gas.

The computed temperature is used to determine f_1 for the excitation scheme used in the experiment, and the temperature and major species are used to determine the quenching correction. The final fluorescence image is then normalized with respect to the expected fluorescence signal generated by the experimental calibration gas (45.2 ppm NO in N_2 mixed with 3% O_2, by volume). This provides a quantitative comparison with the experimental results.

Figure 3.6.9 plots the computed and measured NO fluorescence signals as a function of the spatial variables for the 40% (a) and 80% flames (b). Also plotted is the soot volume fraction measured using laser-induced incandescence (LII). For details on the LII experiment for both the 40% and 80% flames, as well as comparison to numerically computed soot volume fractions, see Section 3.4 and [Smooke 2005]. First focusing on the results for the 40% flame in Figure 3.6.9a, the results show good qualitative agreement overall; for example, the fairly constant signal level in the regions above the flames, as well as the lower signal inside the flame/sooting areas, are captured. It should be noted that the computed fluorescence signal under-predicts the measured fluorescence signal by approximately 30%.

Figure 3.6.9b plots the computed and measured NO fluorescence signals and the measured soot volume fraction as a function of the spatial variables for the 80% flame. As with the 40% flame, there is qualitative agreement between the computed and measured fluorescence signals, with the computed signal approximately 30% lower overall than the measured signal.
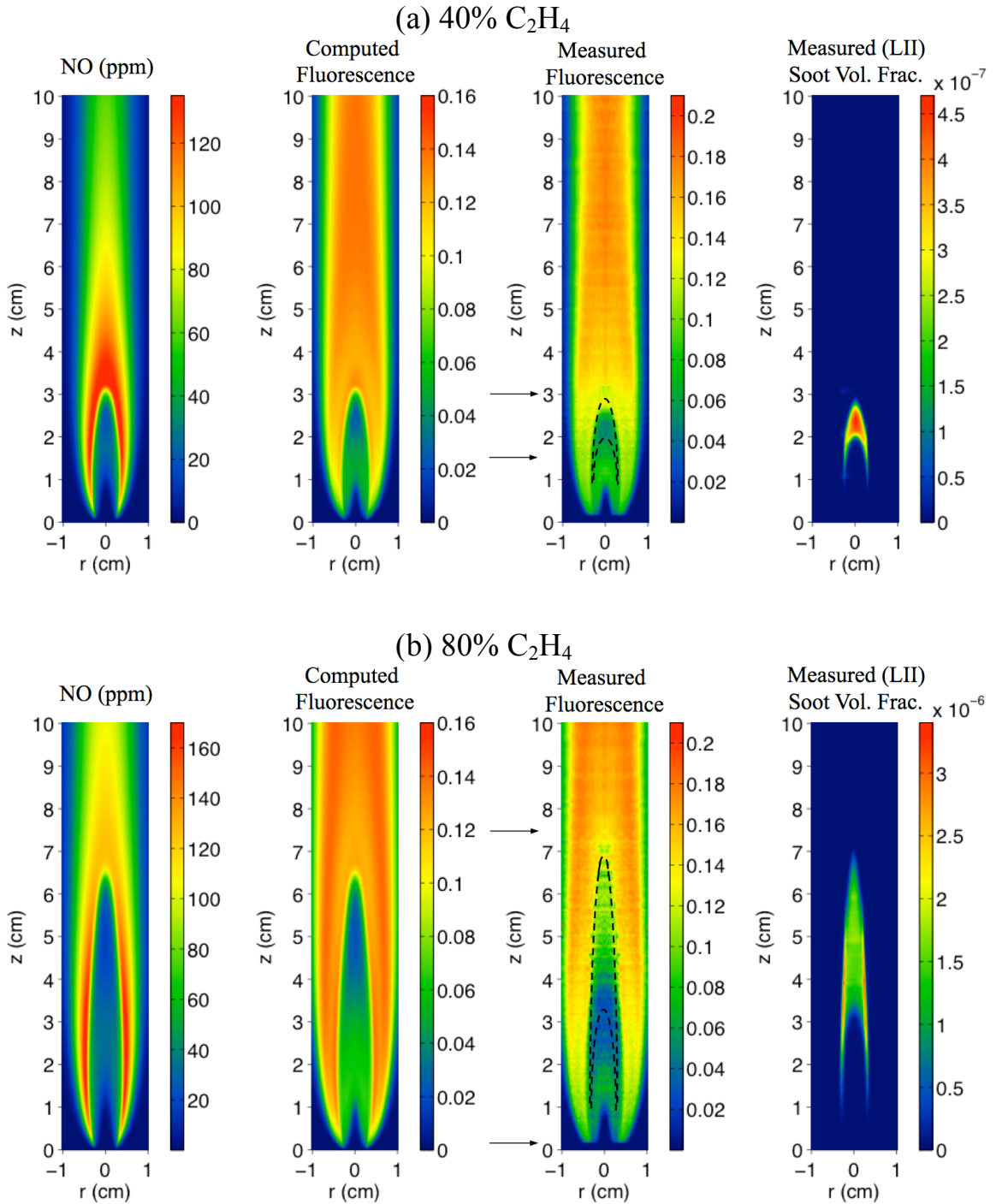
Figure 3.6.9: Comparison of the computed and measured fluorescence signal from NO for the (a) 40% ethylene/60% nitrogen flame and (b) 80% ethylene/20% nitrogen flame. The fluorescence signal has been normalized with respect to a calibration gas for both the computed and measured plots. Experimentally, a colored glass filter was added to the input optics in the region between the arrows to minimize soot interferences. The soot volume fraction, measured using LII, and the computed NO mole fractions are also shown.

131

Perhaps the most unusual feature of the computed NO mole fraction in Figure 3.6.9b is the depression of NO concentration in the upper centerline region. (A similar depression did not exist for the 40% flame depicted in Figure 3.6.9a) The NO concentration in this upper centerline region is ~120 ppm vs. the 170 ppm in the side wings of the flame. Given that the Zeldovich mechanism gives a large broad contour in this region, it can be deduced that the Fenimore mechanism is suppressed in this region. To examine whether this is soot-related, the difference between the computed NO mole fraction using the full NO chemistry and only the extended Zeldovich submechanism is calculated and plotted in Figure 3.6.10. This is done for the 40% flame (Figure 3.6.10a) and the 80% flame (Figure 3.6.10b), both without soot included in the computation (left) and with soot included (right). These figures provide a qualitative assessment on the change in Fenimore NO with and without soot. The depression in the upper centerline region for the 80% flame with soot is quite significant. The plot for the 40% flame does exhibit this strong effect.

As Fenimore NO is weakly dependent on temperature, the results in Figure 3.6.10b (right) are clearly due to the presence of soot in the flame. To help appreciate the effect that soot has on NO formation, it is worthwhile to recognize that in premixed flames with soot levels of $f_v = 4E-6$ and $\phi = 2$, about ¼ of the total fuel carbon is converted to soot. It is proposed that some of the difference in the upper centerline regions between the right and left panels in Figure 3.6.10 may be due simply to fewer hydrocarbon fuel fragments available to form CH or CH_2 as the soot oxidizes directly to CO and H after attack by OH. In addition, soot oxidation along the centerline slightly delays the completion of combustion (relative to that by gas phase species). The slower
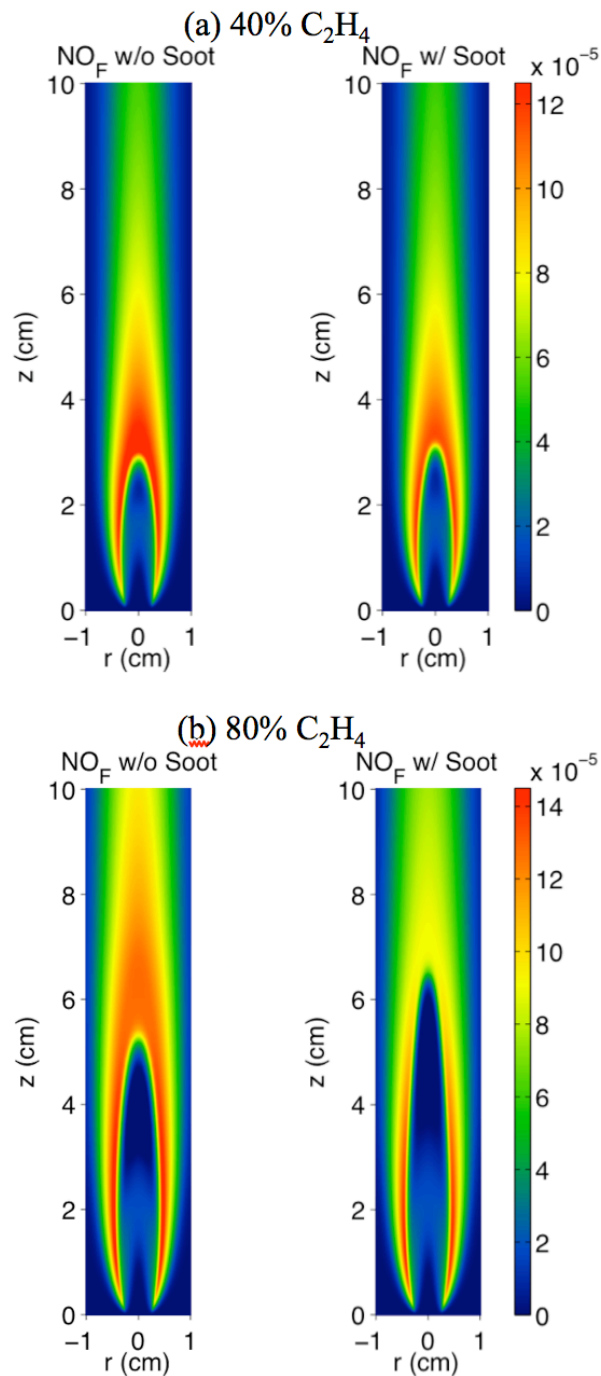
Figure 3.6.10: Computational NO mole fractions for the 80% ethylene/20% nitrogen flame (a) and the 40% ethylene/20% nitrogen flame (b), plotted as differences between the complete NO_x submechanism and the extended Zeldovich submechansim to approximate Fenimore NO. The left panels represent this calculation without considering soot; the right panels represent the calculation for the sooting case.

oxidation rate reduces local super-equilibrium radical levels that promote NO formation and reduce the driving force for diffusion of molecular oxygen to the centerline of the flame, reducing NO production rates and lengthening the flame in the process. The relative importance of each of these phenomena will take additional computation and analysis.

3.6.1.5   Conclusions

We have combined LIF measurements and computations using a detailed chemistry, coflow diffusion flame model with a sectional aerosol model to examine the effects of soot formation on NO levels in ethylene-air diffusion flames. Comparison between experimental and computed fluorescence signals shows good quantitative agreement, with the computations approximately 30% lower overall. Computational results indicate that while the dominant route to NO in these flames is due to non-Zeldovich NO (primarily prompt), Zeldovich NO is more pronounced in the 80% ethylene flame compared to the 40% ethylene flame. Moreover, when the soot field is removed from the model and the solution recomputed with a new radiation field, Zeldovich NO accounts for nearly 46% of total NO in the 80% flame and 25% of total NO for the 40% flame, which are significantly larger than 24% and 16%, respectively, for the sooting flames. Furthermore, the results indicate that not only does soot and accompanying radiation loss reduce the levels of NO throughout the flame (virtually all from Zeldovich NO), but for heavier sooting flames, the shape of the NO profile shifts, with NO levels in the wings noticeably higher than centerline levels. These results imply a coupled relationship between soot levels and NO that requires a careful application of diagnostics and computations to help elucidate our understanding of these flames.

These results are comparable to the results of Guo *et al.* [Guo 2007], where it was found that the presence of soot reduced the peak NO concentration by 28%, with most of the suppression of NO (25%) being due to thermal losses. The case presented in [Guo 2007] seems to be equivalent to the 40% flame presented in this work. Guo *et al.* also observed that losses in Fenimore NO were attributed to a reduction in the levels of CH due to the soot formation. We saw a similar effect, though it was more pronounced in the more heavily sooting 80% flame presented here.

It is well established that, as we have found, many practical systems exhibit a reverse trend in NO and sooting levels. Typically, it is assumed that this is at least partially a result of local conditions, with more soot formed in a local fuel-rich environment and more NO formed in the near stoichiometric regions. The present results from both the 40% and the 80% flames imply a complication of this interdependency, with mitigation of NO production rates directly due to the formation of soot and local radiation losses. For the 80% flames the affects are so significant that they alter the NO profile shape in the flame, shifting the peak NO from the centerline to the wings of the flame.

In fact, the approximation for "Fenimore NO" by taking the difference between the full NO mole fraction and only the computed Zeldovich NO may be an insufficient approach to this problem as the two NO formation pathways are not additive. To study this problem with sufficient rigor, the Fenimore NO contribution must be calculated directly by disabling the coupling reaction that links it to the Zeldovich mechanism. This is part of a current study and cannot be added to this document at this time.

3.6.2   Formaldehyde Fluorescence: Implications on Heat Release

3.6.2.1   Introduction

This study is part of a coordinated program, the objective of which is an improved

understanding of the complex interaction between flame chemistry and fluid motion

[Dworkin 2009b]. Here, specific attention is paid to formaldehyde (HCHO)

concentrations with the goal of understanding the correlation between formaldehyde

production and heat release rates within the flame.

A non-sooting, lifted, methane/air, coflowing, non-premixed flame has been

studied experimentally and computationally. The flame structure was computed by

solving the fully elliptic governing equations, utilizing a 35 species chemical kinetic

mechanism, detailed transport coefficients and an optically thin radiation submodel. The

computational work for this study was carried out by Seth Dworkin, in Professor Mitchell

Smooke's group. The burner geometry used is described in Section 3.2. The fuel flow

was composed of 65% CH_4 and 35% N_2. Gas temperature, major species mole fractions,

and non-fuel hydrocarbon concentrations were experimentally mapped in two dimensions

with both probe techniques (coupled to infrared absorption spectroscopy and on-line

mass spectrometry) and *in situ* optical diagnostics (Rayleigh and Raman scattering).

Measurements of temperature and major species were made by Andrew Schaffer

[Schaffer 2001] in Professor Marshall Long's group. Extractive measurements were

carried out in Professor J. Houston Miller's group at the George Washington University:

probe measurements coupled with on-line mass spectroscopy were carried out by Maria

Puccio; tunable diode laser absorption spectroscopy measurements were carried out by

Brendan McAndrew. Measurements were of formaldehyde fluorescence were carried out

to complement extractive measurements of formaldehyde concentrations. Only the aspects of the fluorescence measurement and major conclusions of the study will be highlighted here.

Comparisons were first made between the computational results and the Rayleigh and Raman scattering results (for T, CO_2, H_2O, CO, N_2, O_2, etc.) (see [Dworkin 2009b] for details). In each case, these contours showed good agreement with both the Raman measurements and the computed profiles. Of particular interest in these plots is the triple flame structure at the base of the lifted diffusion flame, most evident in profiles of CO. As the results from the probe measurements of formaldehyde were inconclusive due to insufficient spatial resolution, measurements of fluorescence were undertaken.

3.6.2.2   Laser-Induced Fluorescence of Formaldehyde

The experimental layout used to measure fluorescence from formaldehyde (HCHO) is shown in Figure 3.6.11. The third harmonic of a Nd:YAG laser (Continuum NY 82, ~ 10 ns pulse width at 10 Hz and 355 nm) is used to excite a weak rotational transition in the $\tilde{A}^1A_2 - \tilde{X}^1A_1$ 4_0^1 vibronic manifold of formaldehyde [Harrington 1993b; Kyritsis 2004]. A 30 cm focal length quartz lens is used to focus the UV beam across the diffusion flame. To ensure that the fluorescence is in the linear regime, with no partial saturation, the measurements are made 5 cm before the focus of the UV beam, resulting in a beam diameter of roughly 0.5 mm in the measurement region. The laser energy is monitored using a pyroelectric energy meter (Scientech PHD25) connected to a digital oscilloscope.
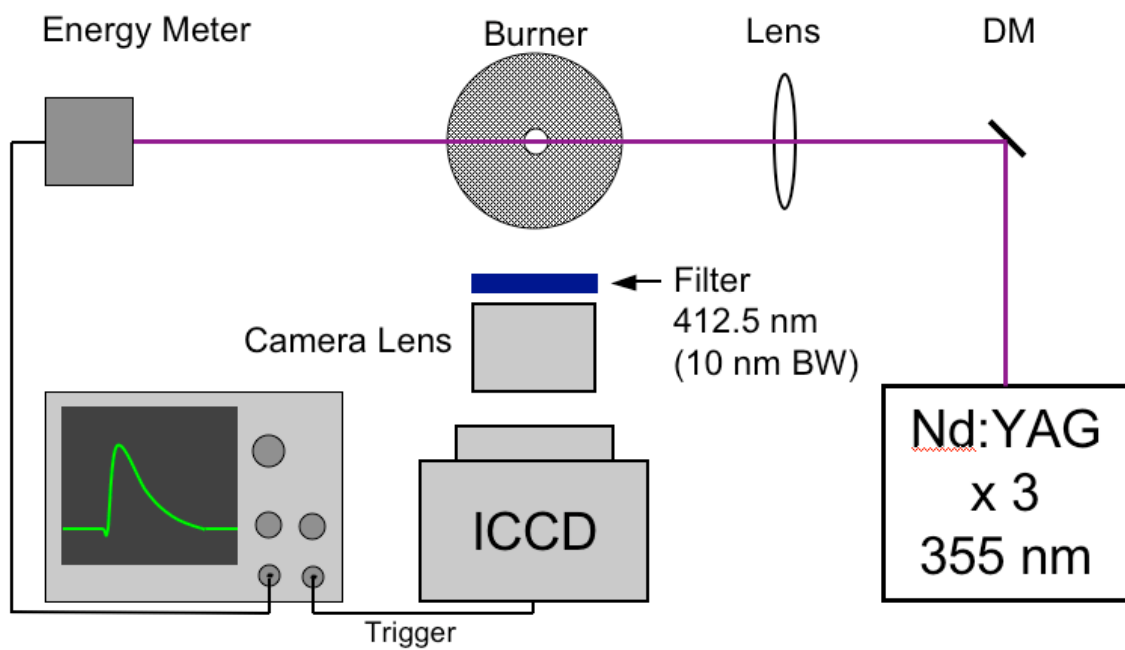
Figure 3.6.11: Experimental setup for formaldehyde fluorescence measurement.

The linear fluorescence is imaged onto an intensified CCD camera (Princeton Instruments ICCD-576TG/RB) by a camera lens (Nikon 50 mm, f/1.8). The intensifier is gated so that it is fully on upon arrival of the laser pulse. A gate time of 70 ns was chosen to guarantee collection of the full formaldehyde fluorescence signal (maximum lifetime of 18 ± 8 ns [Shin 2001]) and to minimize interferences from signals with longer lifetimes. An interference filter centered at 412.5 nm (10 nm bandwidth) is placed in front of the camera lens to image the $2_1^0\, 4_2^1$ vibrational fluorescence band and to filter out interferences and flame luminosity [Harrington 1993b]. Some interference from the broadband PAH fluorescence is still transmitted by the filter. Efforts to subtract out the background PAH fluorescence using an off-resonance signal above the formaldehyde bandhead (after 550 nm) were unsuccessful, as this background signal possesses a temperature-dependent bias with respect to the on-resonance signal. The fluorescence signal is integrated on the detector for 64 laser pulses, chosen to correspond to event sampling on the oscilloscope. The experiment is controlled through a computer, which records synchronized data from both the CCD camera and the digital oscilloscope. A two-dimensional image of the formaldehyde fluorescence distribution is created by tiling together a series of images recorded at 0.1-mm intervals from 2–35 mm above the burner. Each image is normalized by the recorded laser energy, and corrected for detector background and for nonuniform detector gain and optical throughput.

For linear fluorescence, the scattered intensity has the form $S_f \propto N_g\, f_1/Q_{21}$, where N_g is the total number density in the ground electronic state, f_1 is the Boltzmann population fraction, and Q_{21} represents the total collisional quenching rate. In this example, Eq. 2.3.28 has been simplified using the information that $Q_{21} \gg A_{21}$. The

Boltzmann correction for formaldehyde is well accounted for using the analysis of

Clouthier and Ramsay [Clouthier 1983; Kyritsis 2004]. A model that accounts for the

species dependent quenching rate is not available, however. Instead, the quenching rate is

determined by assuming a temperature dependence of the quenching cross section [Paul

1998]. The result provides an upper and lower bound on the temperature dependence of

the overall correction [Paul 1998; Kyritsis 2004], where the quenching rate is found to

vary between $Q_{21} \sim T^{-0.5}$ and $Q_{21} \sim T^{-1}$. Figure 3.6.12 plots the temperature corrections

for the formaldehyde fluorescence. The temperature (shown here as $1/T$, since that is the

quantity used to convert mole fraction to number density) is used to determine the

Boltzmann correction, which increases slightly from 300 K to 500 K before decreasing as

temperature increases. The quenching correction (plotted as $1/Q_{21}$) is plotted for the two

bounds of the calculation; the Boltzmann and quenching corrections are then combined to

determine the temperature dependence of the overall correction.

To make a direct comparison with computational results the Boltzmann and

quenching corrections must be accounted for. Instead of using the experimental data from

Rayleigh and Raman experiments to determine an experimental mole fraction, a reverse

quenching correction to the calculated flame is used to determine an expected

fluorescence signal for comparison with the experimental results. Figure 3.6.13 plots the

computational formaldehyde mole fraction and temperature, and the expected

fluorescence signal that defines the bounds for comparison. This approach has the

advantage of comparing quantities with less uncertainty than the traditional approach of

determining an experimental mole fraction, where the noise level increases as multiple

measurements are combined.
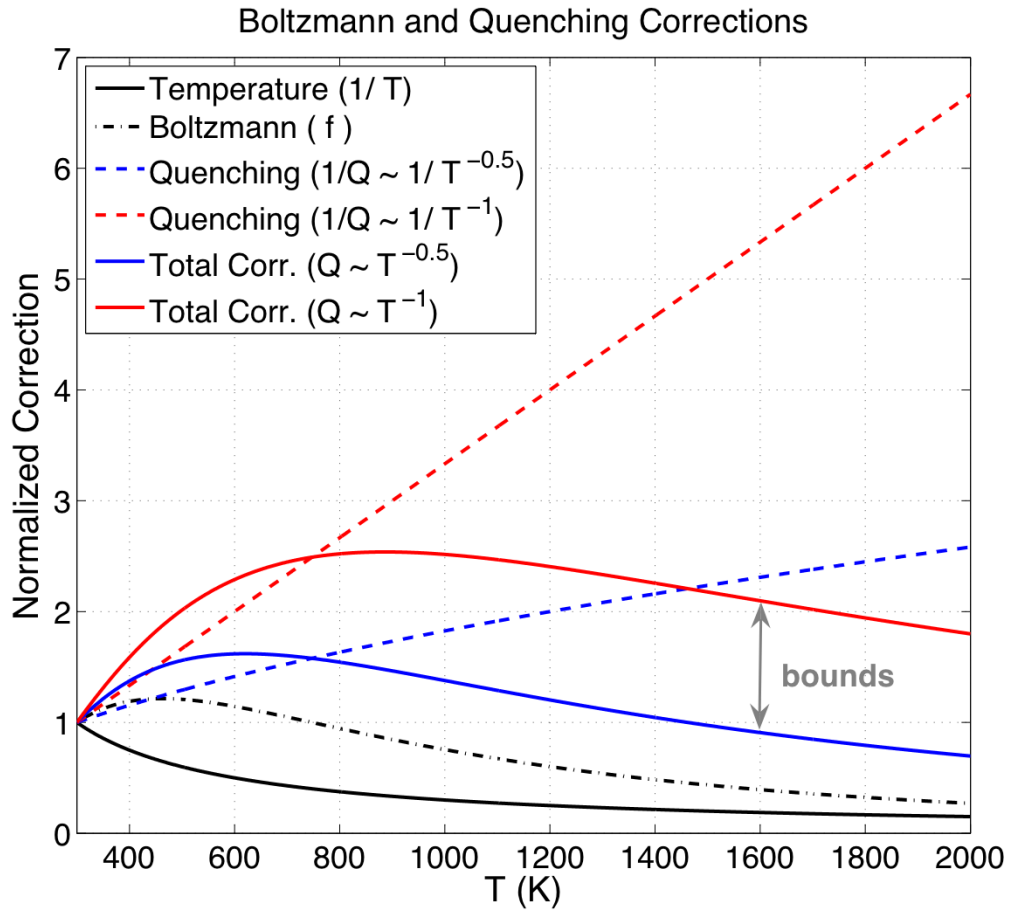
Figure 3.6.12: The temperature dependence of the Boltzmann correction and the bounds of the quenching correction for formaldehyde fluorescence. The corrections are combined to determine the bounds of the total correction.
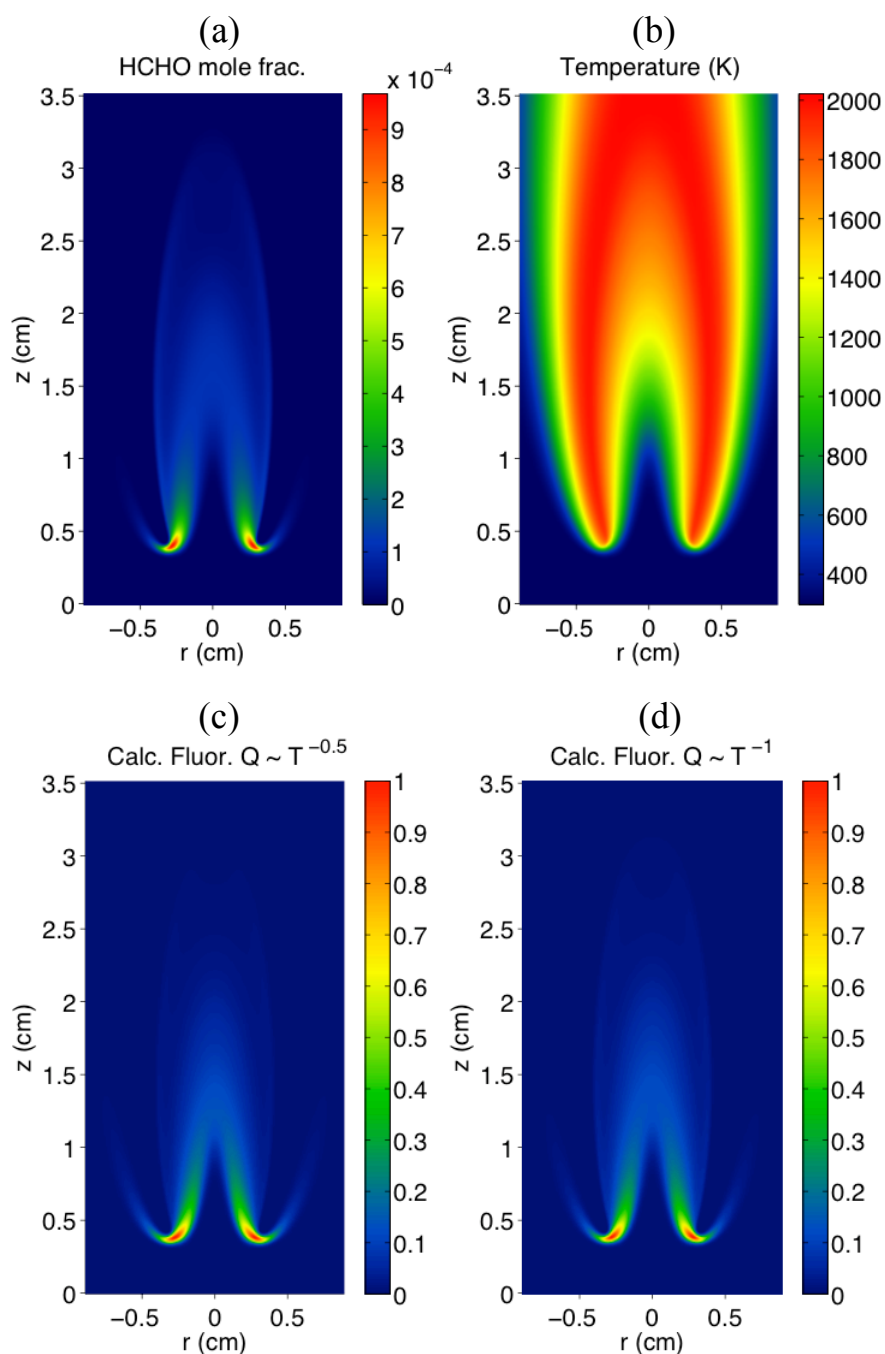
Figure 3.6.13: Computational formaldehyde mole fraction (a) and temperature (b) are used to compute the expected fluorescence signal for two bounds of the Boltzmann and quenching corrections: for $Q_{21} \sim T^{-0.5}$ (c) and $Q_{21} \sim T^{-1}$ (d). The maximum of each fluorescence image has been normalized to unity.

3.6.2.3   Comparison of Formaldehyde Results

Figure 3.6.14 compares computed contour plots of formaldehyde with those determined experimentally. The computed mole fraction is compared with the measured mole fraction from the gas sampled with the quartz microprobe. Also, an expected fluorescence signal is determined from the computational results, for the upper and lower bounds of the quenching correction, and compared with the measured formaldehyde fluorescence signal. Both computed and measured fluorescence signals have been normalized to unity since there is not a calibration of the fluorescence data currently available.

The formaldehyde profiles reveal several interesting features. First, formaldehyde, like CO, shows an unusual profile at the flame base with wispy "wings" appearing on the lean (outer) side of the flame. Second, the concentration of formaldehyde has very steep gradients in both the radial and axial directions at the flame base, much larger than those observed for most stable molecules in flames. Further, the volume of gas sampled with the quartz microprobe is generally thought to be 5-7 times the orifice diameter, which was $\approx$200 μm in these measurements. Thus, the TDLAS measurements of formaldehyde do not fully capture the fine structure predicted for the flame base, but they do show that the highest formaldehyde concentrations occur at the flame base and the general shape of the contour plots throughout the flame is in good agreement with the calculations. Further, the calculations and fluorescence measurements of formaldehyde showed excellent agreement capturing not only the steep gradients of HCHO concentration at the flame base but also all of the structural nuances of the 2D profile. The region of greatest fluorescence intensity at the base of the flame is more

143
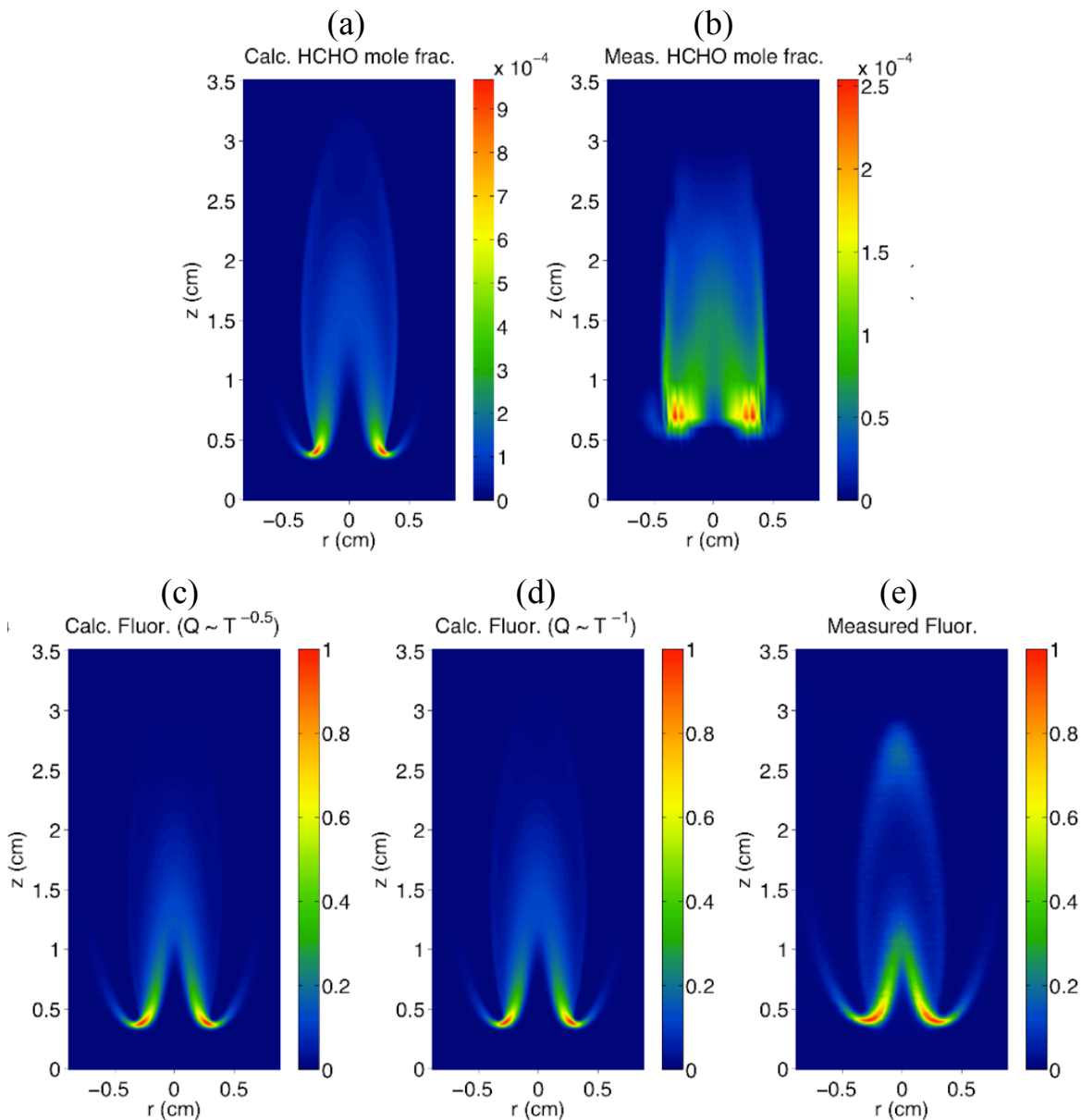
Figure 3.6.14: Comparison of computed contour plots of formaldehyde and experimental measurements. Starting from the top left: (a) the computed mole fraction, (b) the measured mole fraction, (c) the computed fluorescence signal for $Q_{21} \sim T^{-0.5}$, (d) the computed fluorescence signal for $Q_{21} \sim T^{-1}$, and (e) the measured fluorescence signal. Interference from PAH fluorescence can be seen in the upper region of the flame in (e). Both computed and measured fluorescence signals have been normalized to unity.

widely distributed in the measured fluorescence. This discrepancy is most likely due to the steep temperature gradient across that zone, which affects the Boltzmann and quenching corrections used to calculate a signal. It should be noted that there is some interference in the measured fluorescence from PAH fluorescence in the upper region of the flame on the centerline, at an axial height centered around 2.5 cm.

3.6.2.4   Analysis of Results

A lifted, methane-air coflow diffusion flame was studied using a detailed transport/finite rate chemistry computational model and compared to experimental results obtained with a variety of diagnostic methods. The gas temperature, major species mole fractions, and non-fuel hydrocarbon concentrations were experimentally mapped in two dimensions with both probe techniques (coupled to infrared absorption spectroscopy and on-line mass spectrometry) and *in situ* optical diagnostics (Rayleigh and Raman scattering and laser-induced fluorescence). Measured and computed formaldehyde concentrations and fluorescence signals were compared, and the results indicated the existence of an intense region of formaldehyde production near the lifted flame base. Computationally, it was found that high formaldehyde production rates correlated well with regions of high heat release. Further, the reactions that primarily contributed to formaldehyde production were investigated. It was found that regions where the dominant formaldehyde formation reaction, $CH_3 + O = HCHO + H$, peaked also correlated with the areas of maximum heat release rate.

CHAPTER 4

4 Measurements in Time-Varying Flames

Diffusion flames are the flame type of most practical combustion devices. The ability to predict the coupled effects of complex transport phenomena with detailed chemical kinetics in such systems is critical in the modeling of turbulent reacting flows and in understanding the processes by which extinction, soot formation and radiative transfer take place. In forced time-varying flames, a periodic fluctuation in time is imposed on the fuel flow rate of a steady laminar flame. The study of these flames helps in understanding the interactions between fluid transport and heat and mass transfer in practical combustion systems. Fundamental studies of these interactions including detailed combustion chemistry are critical to an understanding of pollutant formation processes and to the modeling of turbulent diffusion flames through the concept of laminar flamelets. A number of investigators have studied forced, time-varying laminar diffusion flames (see [Smyth 1985; Harrington 1993a; Smyth 1993b; Smyth 1993a; Shaddix 1994b; Shaddix 1994a; Smyth 1994; Skaggs 1996; Mohammed 1998; Dworkin 2006; Dworkin 2009a], e.g.). The goal in these studies primarily involved developing an understanding of flame structure and pollutant formation as the forcing level was varied. We have undertaken a study to predict the detailed behavior in forced flames through a computational and experimental study of nonsooting [Mohammed 1998; Dworkin 2006] and sooting flames [Dworkin 2009a].

146

4.1   Particle Image Velocimetry

Fuel flow in the experimental burners is forced using a speaker in the fuel plenum (see Figure 3.1.1). The speaker was driven at 20 Hz, providing straightforward synchronization with the laser pulses used for calibration and characterization of the system. The modulation of the fuel flow for the time-varying flame was calibrated using particle image velocimetry (PIV) for each of the burners. The fuel flow was seeded with sugar particles (TSI six jet atomizer model 9306, concentration 10 gm/L of sugar in a 50/50 mixture of water and ethanol). Two frequency-doubled Nd:YAG lasers (532 nm, 10 Hz rep rate), separated by an interval of 300 μs, were focused into a sheet (300 μm) across the burner centerline, and overlapped spatially. PIV images were recorded using a fast interline transfer CCD camera (Cooke Sensicam). A cross-correlation algorithm (0.084 cm x 0.042 cm FFT window, 0.042 cm step size) was used to determine the centerline exit velocity as a function of the speaker's forcing level. Figure 4.1.1 plots the phase-locked centerline velocity at three arbitrary forcing voltages. This calibration provides a relationship between applied voltage and forcing level

$$\% \text{ Modulation } = 0.175 * \text{ Voltage (mV)} - 1.806 \qquad (4.1.1)$$

Forcing levels corresponding to modulations of the fuel flow in the range of 20% to 50% were investigated experimentally and computationally.
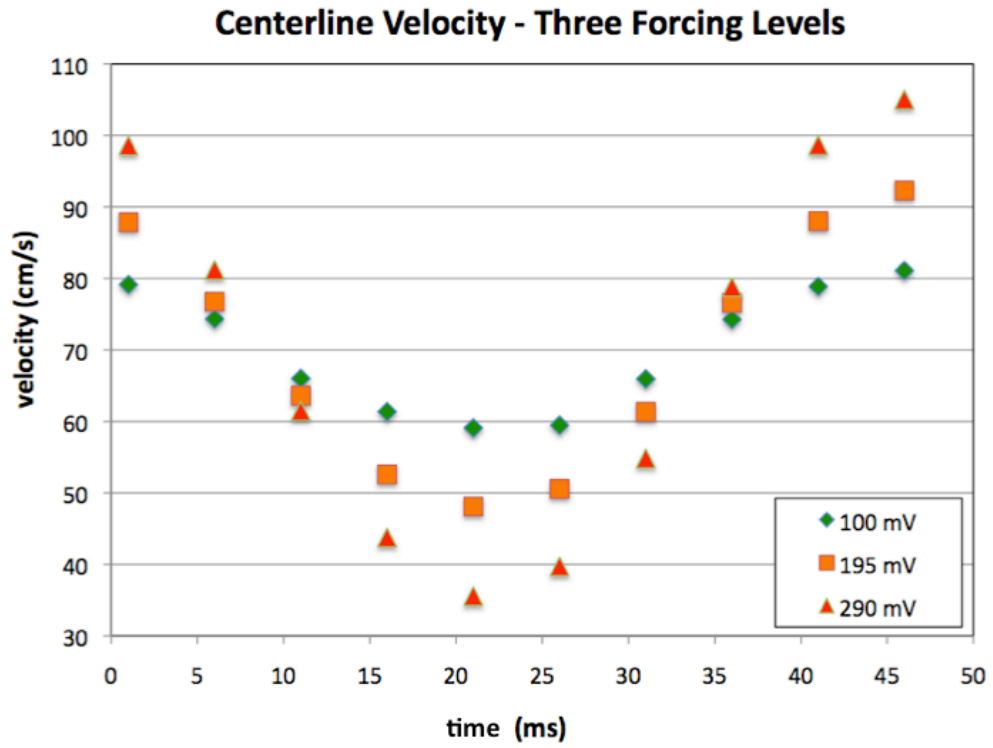
Figure 4.1.1: Measured centerline velocity as a function of time for three different forcing voltages for the time-varying flames. Measurements were made using PIV.

4.2   Nonsooting, Forced Flames

An experimental and computational investigation of the structure of a forced, time-varying, axisymmetric, coflow, laminar, 65% CH_4 / 35% N_2, diffusion flame was initially undertaken. Computationally, a modified vorticity-velocity formulation was employed to solve the transient equations for the conservation of mass, momentum, energy and chemical species. Experimentally, Rayleigh and Raman scattering are used to obtain two-dimensional fields of temperature, and of mole fractions of N_2, CO_2, CH_4, H_2, O_2, CO, and H_2O. See [Dworkin 2006] for details on this study as only some highlights and conclusions will be presented here.

4.2.1   Startup Transient

Due to the transient nature of the problem, it is necessary to first investigate the number of cycles required to reach fully periodic flame behavior. This is particularly true computationally, as the steady flame is used as the initial condition.

Experimentally, chemically-excited CH (CH*) generates flame chemiluminescence through the $A^2\Delta \rightarrow X^2\Pi$ transition at 431.4 nm, and has been shown to be indicative of the flame front position [Luque 2000]. This technique was used as a relatively simple experimental means to study the number of cycles required for the steady flame to become fully periodic after the initial forcing was applied. Measurements were taken for 10 cycles immediately following initial forcing. Line-of-sight images were integrated over 100 forcing cycles using an exposure of 1 ms. A 450 nm short-pass filter was used to image CH*, while a 650 nm long-pass filter was used to correct for soot interferences. The axisymmetric images were Abel inverted to obtain the radial profile of relative CH* concentration [Dasch 1992; Walsh 2000b].   Figure 4.2.1 plots the

computational contours of the difference between the computed CO field in the midpoint of a cycle and the computed CO field at the same point in the previous cycle (top). The experimental contours (bottom) illustrate the same quantities but for CH*. In both cases, the largest initial transients disappear within several cycles. While the experimental transients are almost totally gone by cycle four, the computational results indicate that some transient effects (while small) are still observable after 10 cycles. The difference in the speed with which these effects die off is partially related to the spatial extent and the magnitude of the two species being compared and to the numerical refinement used in the computations.

4.2.2 Discussion of Results

As an example, Figure 4.2.2 plots the computed and measured isotherms for the 30% modulated flame at 10 ms intervals of the 50 ms cycle. Due to the transient effects observed in Figure 4.2.1, we initially shifted the computational isotherm a few milliseconds compared to the experimental results to line up the features more easily. Frames (b) and (c) have been truncated due to the fact that some soot was formed in the region beyond ~3.5 cm downstream during this part of the oscillation, causing interference with the Raman and Rayleigh measurements. The overall structure of the temperature and major species profiles predicted by the computations were in good qualitative agreement with the experimental measurements. However, careful comparison of experimental features shows slightly more defined / arched contours. The species examined in this study did not possess high enough spatial gradients to come to any firm conclusions on this discrepancy. In the next study of forced, sooting flames, the discrepancies will become more obvious.
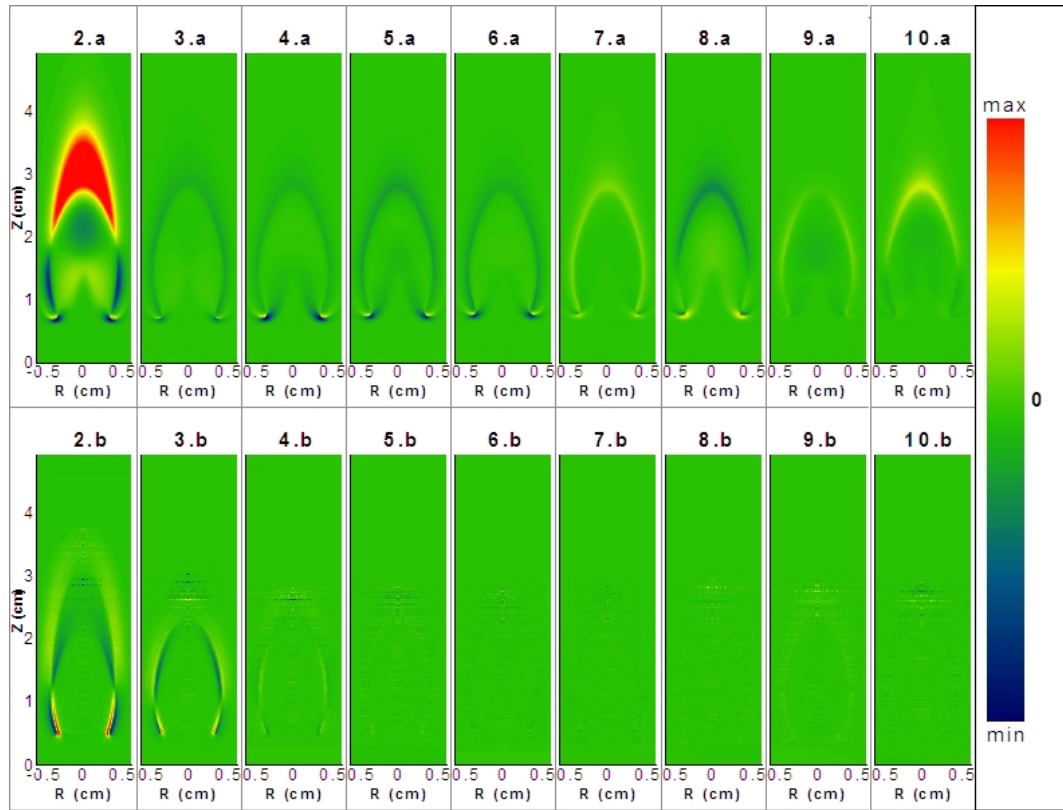
Figure 4.2.1: Computational (top) and experimental (bottom) comparison of the start-up transients in the forced flow burner. Each computational panel illustrates the difference between two consecutive cycles of the CO mole fraction. The experimental panels illustrate the difference between two consecutive cycles of CH*.
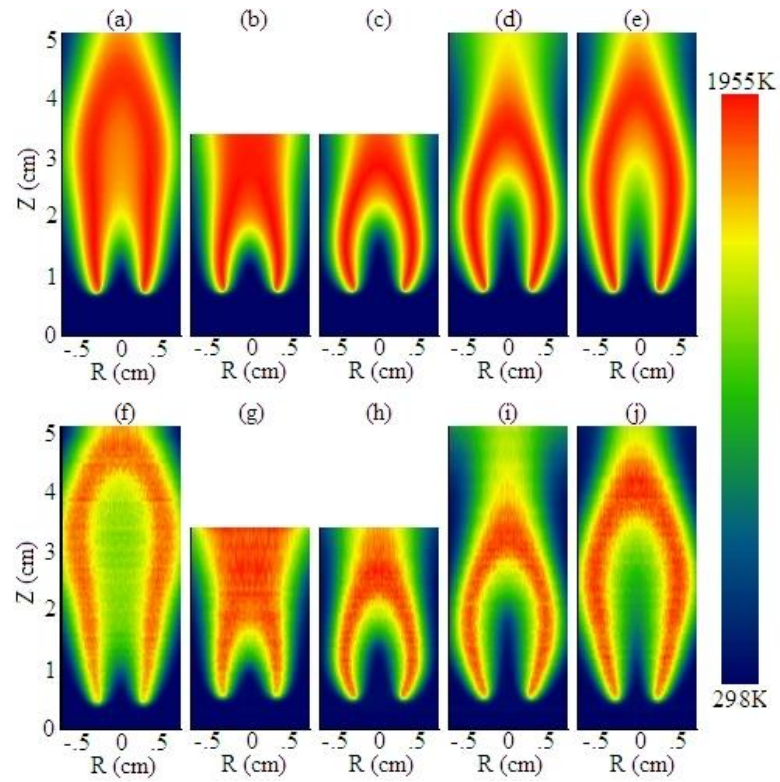
Figure 4.2.2: Computational (a-e) and experimental (f-j) isotherms shown at 10 ms intervals for the 30% modulation flame. Panels b, c, g and h between 3.5 cm and 5.0 cm are not shown as these regions exhibit the highest level of particulate interference in Rayleigh imaging.

4.3   Sooting Time-Varying Flames

Quantitative soot volume fraction measurements in time-varying diffusion flames have shown that peak soot volume fractions can increase by factors of four to five over peak values in the equivalent steady flame (i.e., a flame with the same average fuel and oxidizer flow rates, but with no pulsation) [Harrington 1993a; Smyth 1994]. In an effort to predict soot volume fractions and NO_x as a function of time, the soot model was incorporated into the time-dependent flame calculations. Given the size of the system of partial differential equations that must be solved (upwards of 100 chemical species and 20 soot sectional classes) and the number of cycles that must be computed to eliminate start-up transients (see [Dworkin 2006] and Section 4.2), it was deemed necessary to employ parallel computation in the research program.

4.3.1   Soot Measurements in a Series of Forced Flames

Because the study of sooting time-varying flames are computationally intensive it is important to determine which flow conditions are best suited for study. For this reason, an effort to map out the parameter space of sooting tendencies for various fuel dilutions and forcing levels was carried out experimentally. A fast, interline transfer camera (Cooke Sensicam) was used to acquire 1-ms exposure, phase-locked, images at 10 phases of sooting flames forced at 20 Hz. Soot luminosity images over a range of dilution levels are taken separately through two interference filters at 488 nm (blue) and at 633 nm (red). The luminosity images were Abel inverted to produce radial profiles of detected soot luminosity. Figures 4.3.1 – 4.3.5 plot the radial profiles detected using the 633-nm filter for a series of fuel dilutions (28%, 30%, 32%, 35% and 40% C_2H_4 in N_2, respectively) and for a range of fuel flow modulations (20%, 30%, 40% and 50%).

153

Figure 4.3.1: Radial profiles of soot luminosity for a series of 28% C_2H_4 time-varying flames, for a range of forcing levels (20%, 30%, 40% and 50%). All images are shown on the same color scale, which is normalized to the maximum of the series of 40% C_2H_4 flames in Figure 4.3.5.

Figure 4.3.2: Radial profiles of soot luminosity for a series of 30% C_2H_4 time-varying flames, for a range of forcing levels (20%, 30%, 40% and 50%). All images are shown on the same color scale, which is normalized to the maximum of the series of 40% C_2H_4 flames in Figure 4.3.5.

Figure 4.3.3: Radial profiles of soot luminosity for a series of 32% C_2H_4 time-varying flames, for a range of forcing levels (20%, 30%, 40% and 50%). All images are shown on the same color scale, which is normalized to the maximum of the series of 40% C_2H_4 flames in Figure 4.3.5.

Figure 4.3.4: Radial profiles of soot luminosity for a series of 35% C_2H_4 time-varying flames, for a range of forcing levels (20%, 30%, 40% and 50%). All images are shown on the same color scale, which is normalized to the maximum of the series of 40% C_2H_4 flames in Figure 4.3.5.

Figure 4.3.5: Radial profiles of soot luminosity for a series of 40% C_2H_4 time-varying flames, for a range of forcing levels (20%, 30%, 40% and 50%). All images are shown on the same color scale, which is normalized to unity. The flames in Figures 4.3.1 – 4.3.4 are normalized with respect to this color scale.

The results are combined with the luminosity images taken with the 488 nm filter and used to determine soot temperatures and soot volume fractions using optical pyrometry as a function of fuel dilution and forcing amplitude. In order to obtain quantitative results, the imaging system must first be characterized. Figure 4.3.6a plots the quantum efficiency (QE) of the Sensicam. The percent transmission of the interference filters was measured and scaled with the Sensicam's QE to produce the effective filter functions in Figure 4.3.6b. The system was also characterized by taking images of a blackbody oven (Isotech Pegasus 1200 R) over a range of temperatures from 900 C to 1200 C. Figure 4.3.7a plots the resulting signal ratios obtained by dividing the integrated red signal by the integrated blue signal, as a function of oven temperature. Figure 4.3.7b plots the natural log of the signal ratio as a function of inverse temperature. The line fit to the data is used to calibrate the two-color pyrometry measurement that is outlined in Section 2.2.2 and employed in Section 3.4.

The pyrometry calculation was applied to the series of flames, and the results are plotted in Figures 4.3.8 – 4.3.12 for the fuel dilutions (28%, 30%, 32%, 35% and 40% C_2H_4 in N_2, respectively) and the range of fuel flow modulations (20%, 30%, 40% and 50%). Temperatures are plotted on a false color scale from 1600 to 2100 K. Overall, the quantitative temperature values are within expected limits, though the temperature calculated at the spatial extremes of the soot region are higher than what is physically reasonable. This is most likely due to a slight mismatch between the red and blue images. Changing the interference filter in the imaging system slightly alters the image steering and magnification. This has been accounted for as carefully as possible by cropping the

159
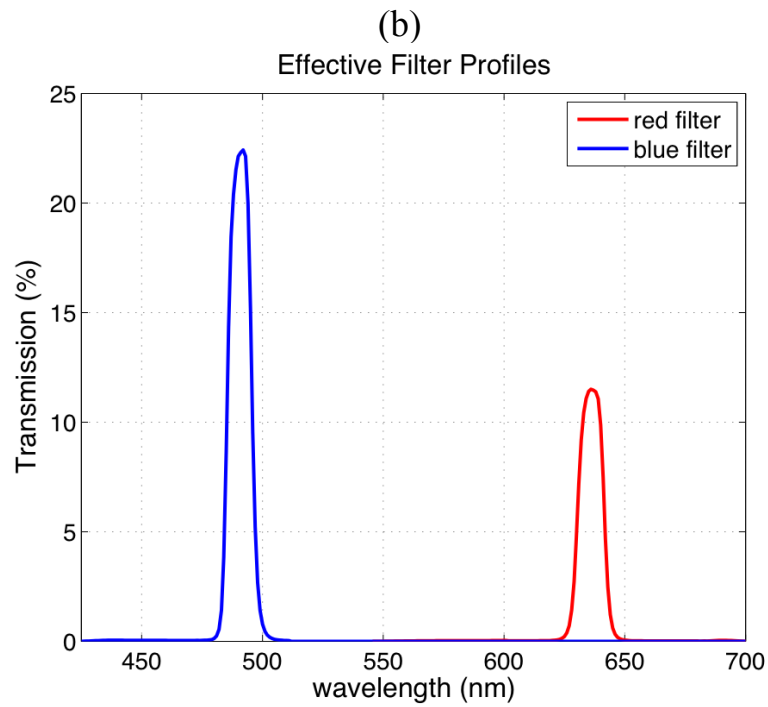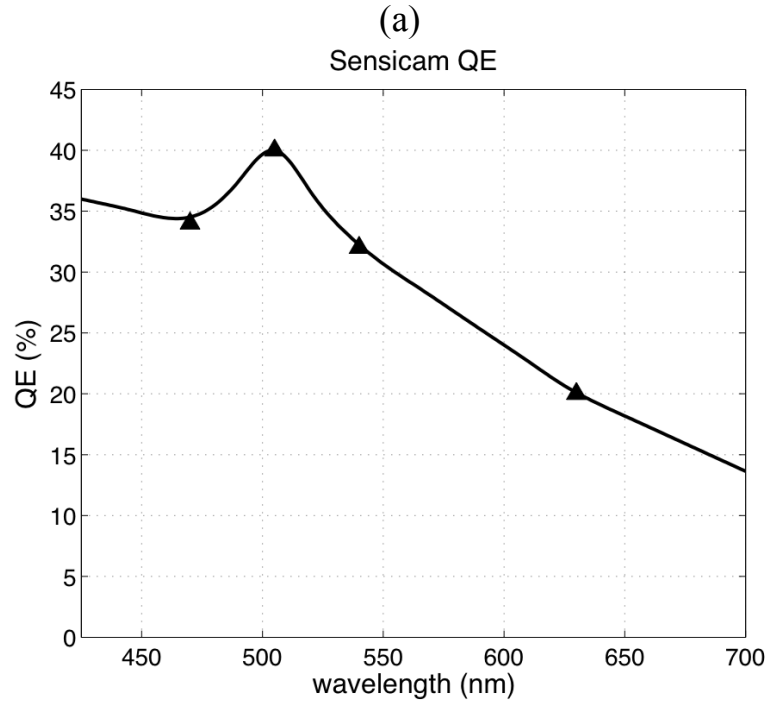
Figure 4.3.6: (a) Quantum efficiency (QE) of the Sensicam. (b) Effective filter profiles of the 633 nm filter (red filter) and 488 nm filter (blue filter) used to characterize the series of sooting, forced flames. The filter profiles have been corrected for the Sensicam's QE.
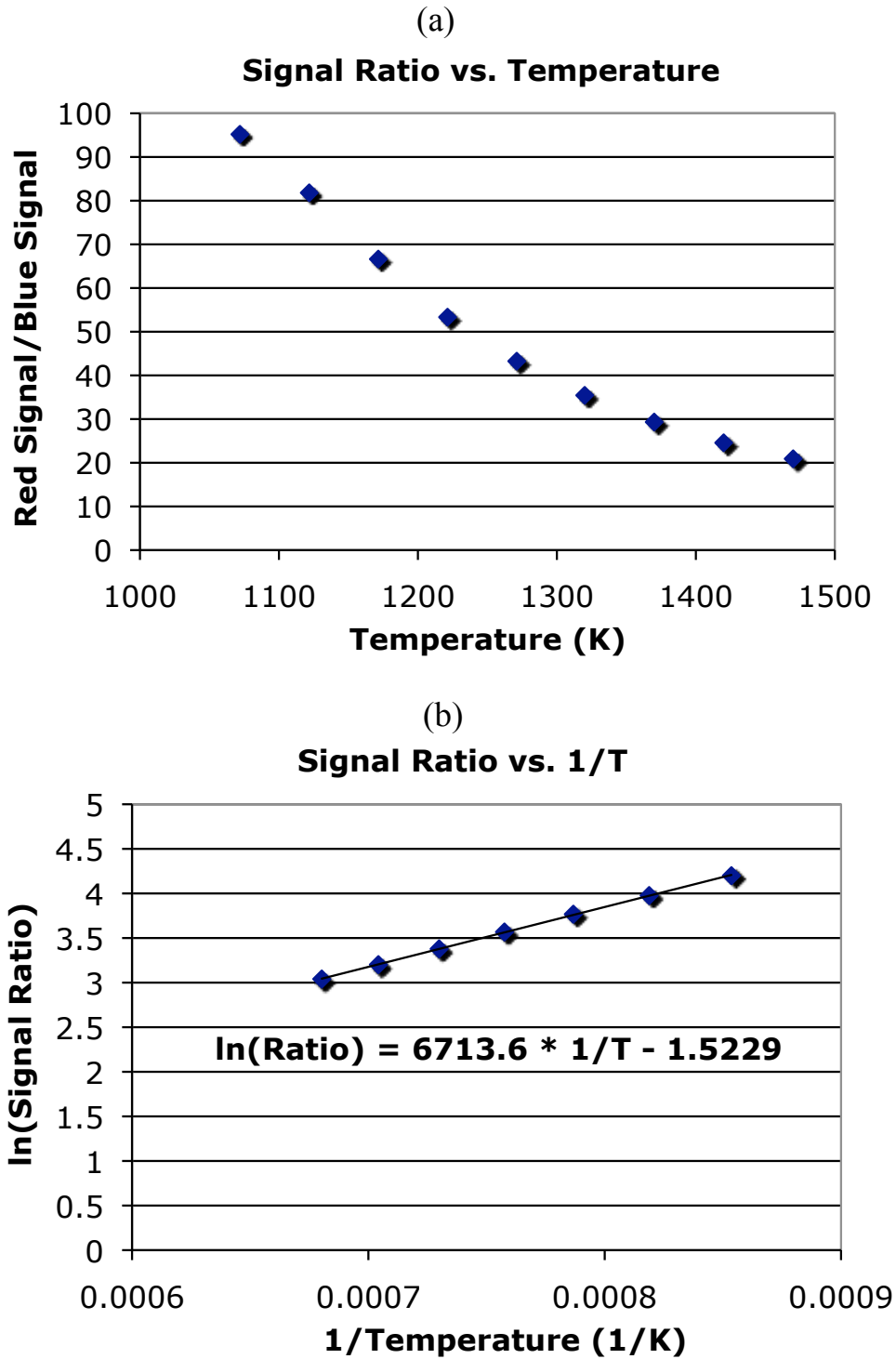
Figure 4.3.7: (a) Signal ratio plotted as a function of oven temperature for the blackbody calibration of the Sensicam with a red and blue interference filter. (b) The log of the signal ratio is plotted as a function of inverse temperature. The line fit to the data is used to calibrate the two-color pyrometry measurement.
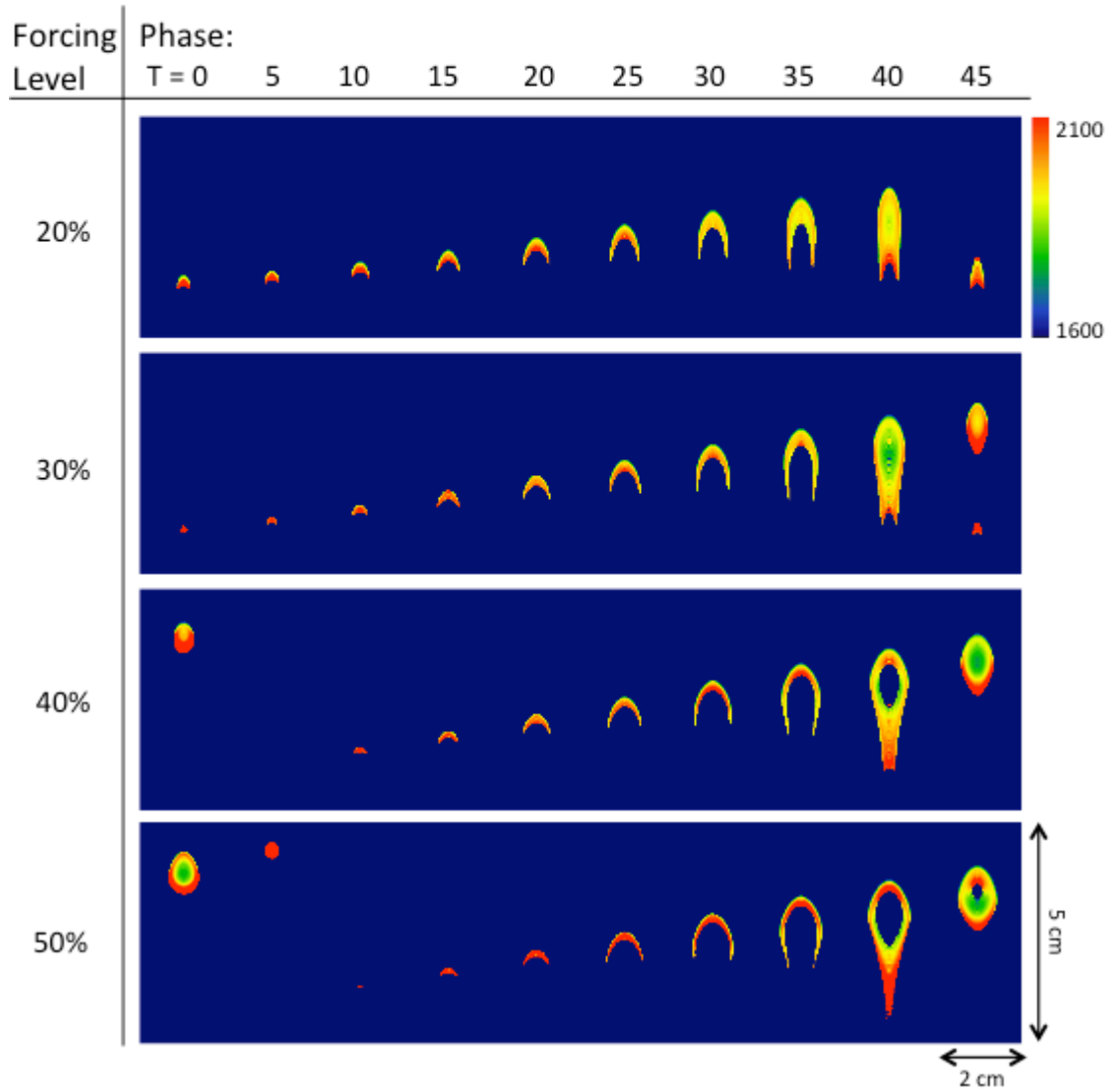
Figure 4.3.8: Soot temperatures (in K) for a series of 28% C_2H_4 time-varying flames, for a range of forcing levels (20%, 30%, 40% and 50%). All images are shown on a color scale from 1600 to 2100 K.
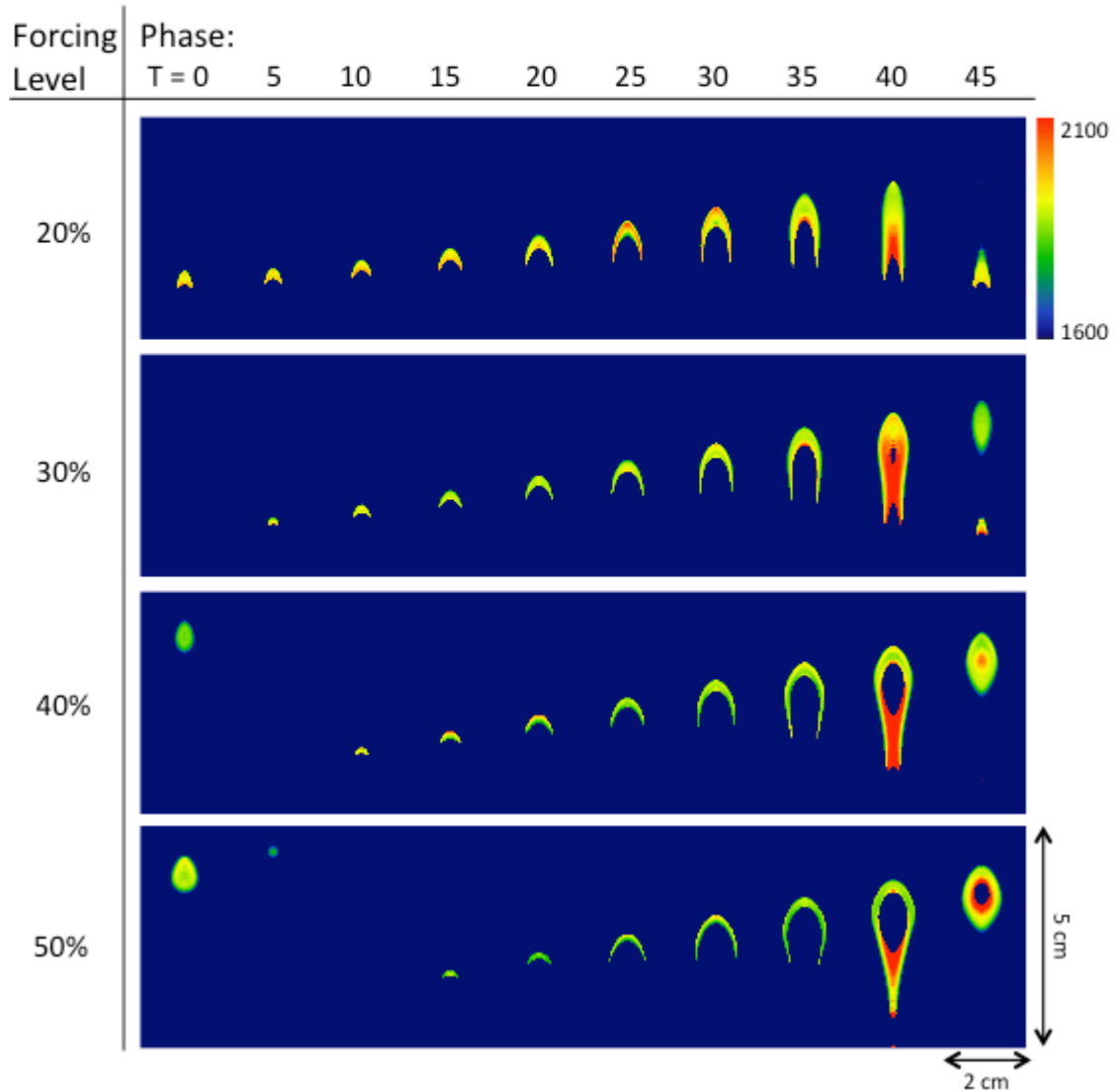
Figure 4.3.9: Soot temperatures (in K) for a series of 30% C_2H_4 time-varying flames, for a range of forcing levels (20%, 30%, 40% and 50%). All images are shown on a color scale from 1600 to 2100 K.
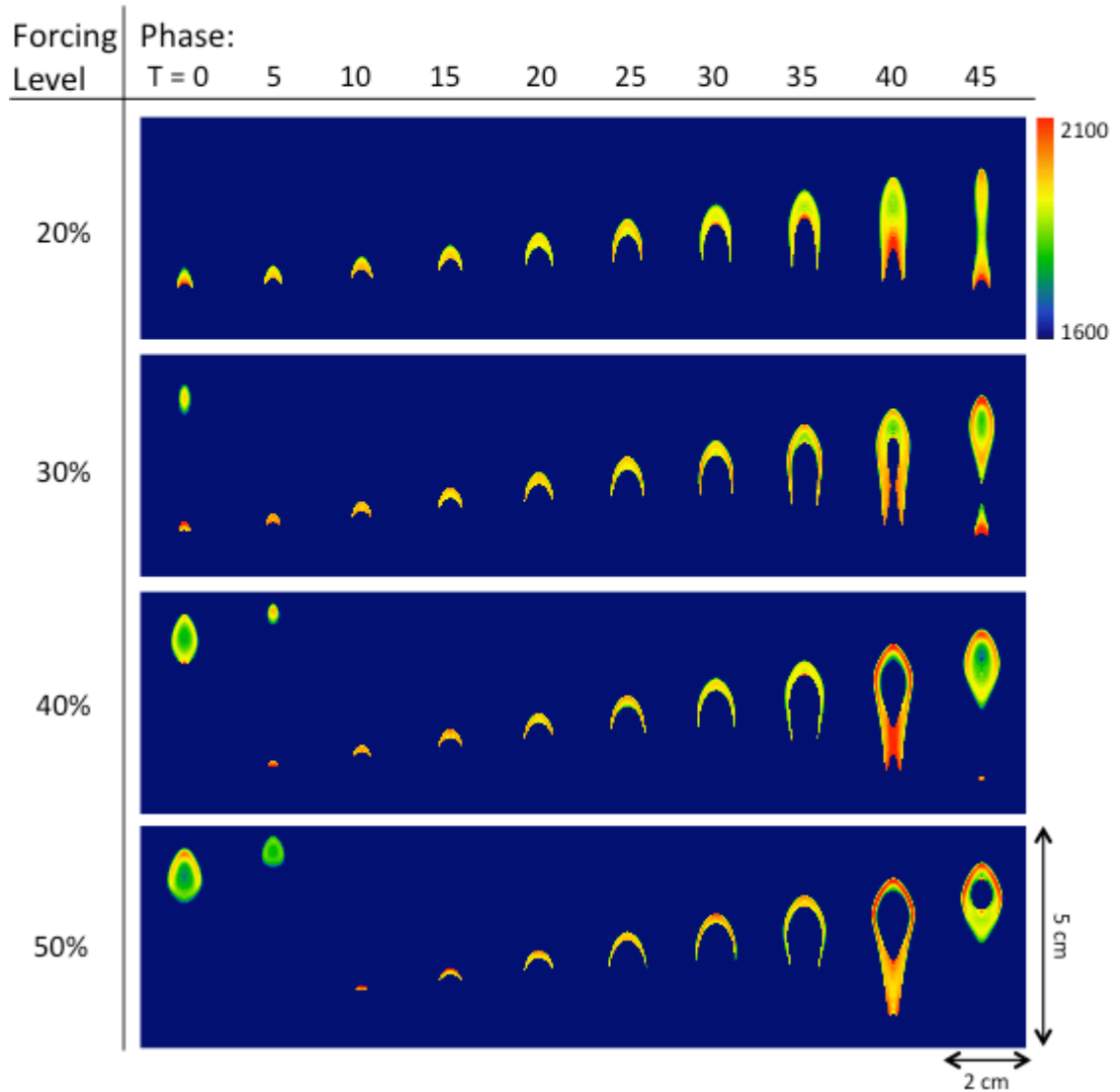
Figure 4.3.10: Soot temperatures (in K) for a series of 32% C_2H_4 time-varying flames, for a range of forcing levels (20%, 30%, 40% and 50%). All images are shown on a color scale from 1600 to 2100 K.
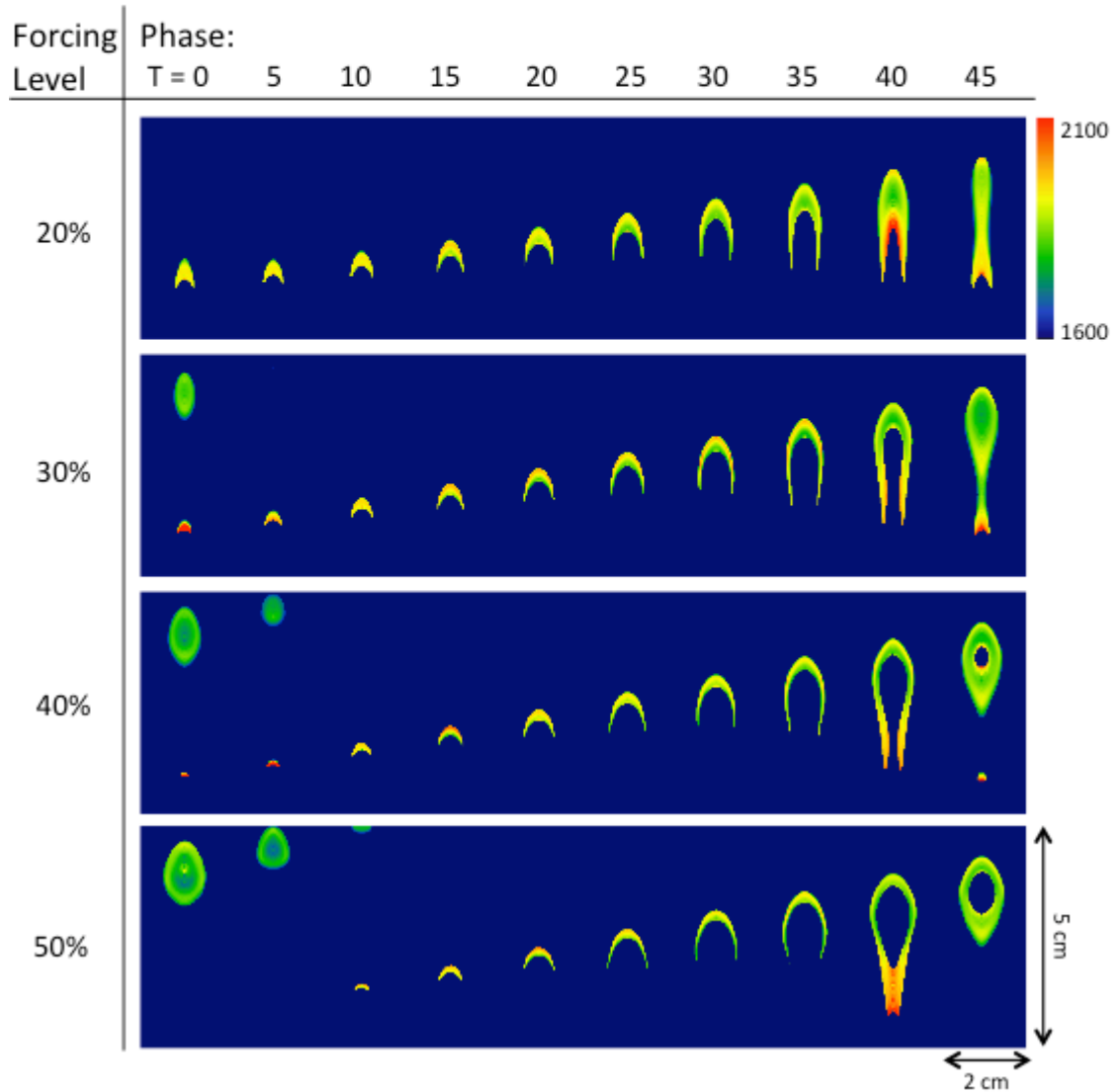
Figure 4.3.11: Soot temperatures (in K) for a series of 35% C_2H_4 time-varying flames, for a range of forcing levels (20%, 30%, 40% and 50%). All images are shown on a color scale from 1600 to 2100 K.
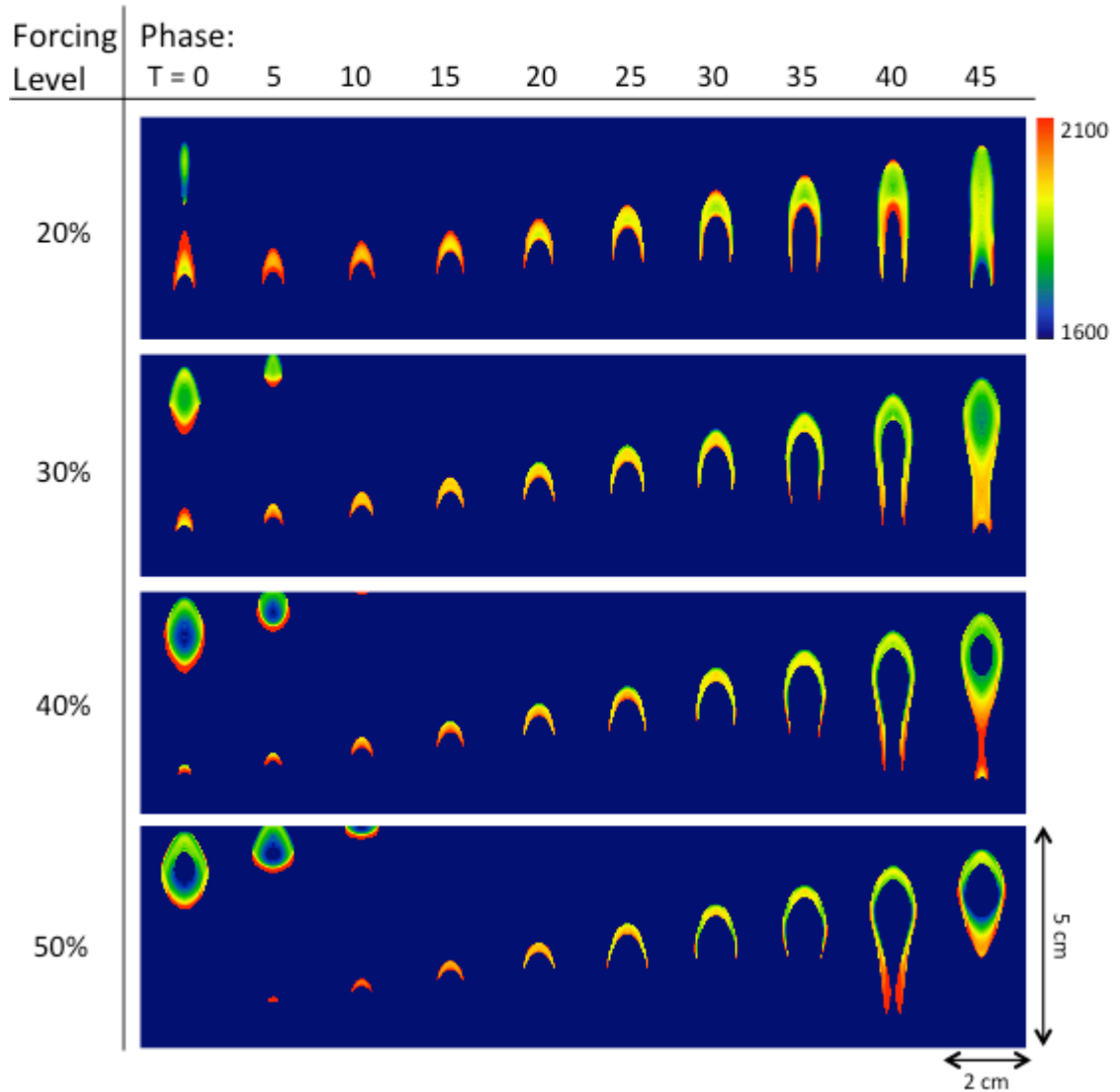
Figure 4.3.12: Soot temperatures (in K) for a series of 40% C_2H_4 time-varying flames, for a range of forcing levels (20%, 30%, 40% and 50%). All images are shown on a color scale from 1600 to 2100 K.

image area, resizing the images and by performing a cross-correlation on the alignment of the two images, and making the appropriate adjustment. Pyrometry calculations are clearly extremely sensitive to slight variations in the alignment of the two color images, particularly when the soot region exhibits such steep gradients. There can also be further mismatch associated with the temporal alignment of the images due to jitter in the triggering of the experiment, though investigation into the stability of the triggering suggested that any temporal jitter is negligible.

Still, the images taken using the 633-nm filter can be combined with the resultant temperature calculation to determine the soot volume fractions. The resulting soot volume fractions are plotted in Figures 4.3.13 – 4.3.17 for the range fuel dilutions (28%, 30%, 32%, 35% and 40% C_2H_4 in N_2, respectively) and modulations. Analysis of the results indicate a slight increase in peak soot levels as well as sooting over a much wider spatial area when compared with the equivalent steady flame. This leads to a substantial increase in the integrated soot volume fraction. Regions of higher fluid velocity drive the soot-containing areas outward, producing a narrow region of soot separating the unburned fuel from the air coflow and the burned gases over the flame. As the forcing level is increased, this sooting region becomes thinner and the peak soot volume fraction value increases. Further above the burner, the soot area pinches off from the flame region that is closer to the burner, and fuel remaining inside this sooting region is burned inward, causing a decrease in diameter. The quantitative results from this exploration were used to determine the ideal cases for further study both computationally and experimentally.
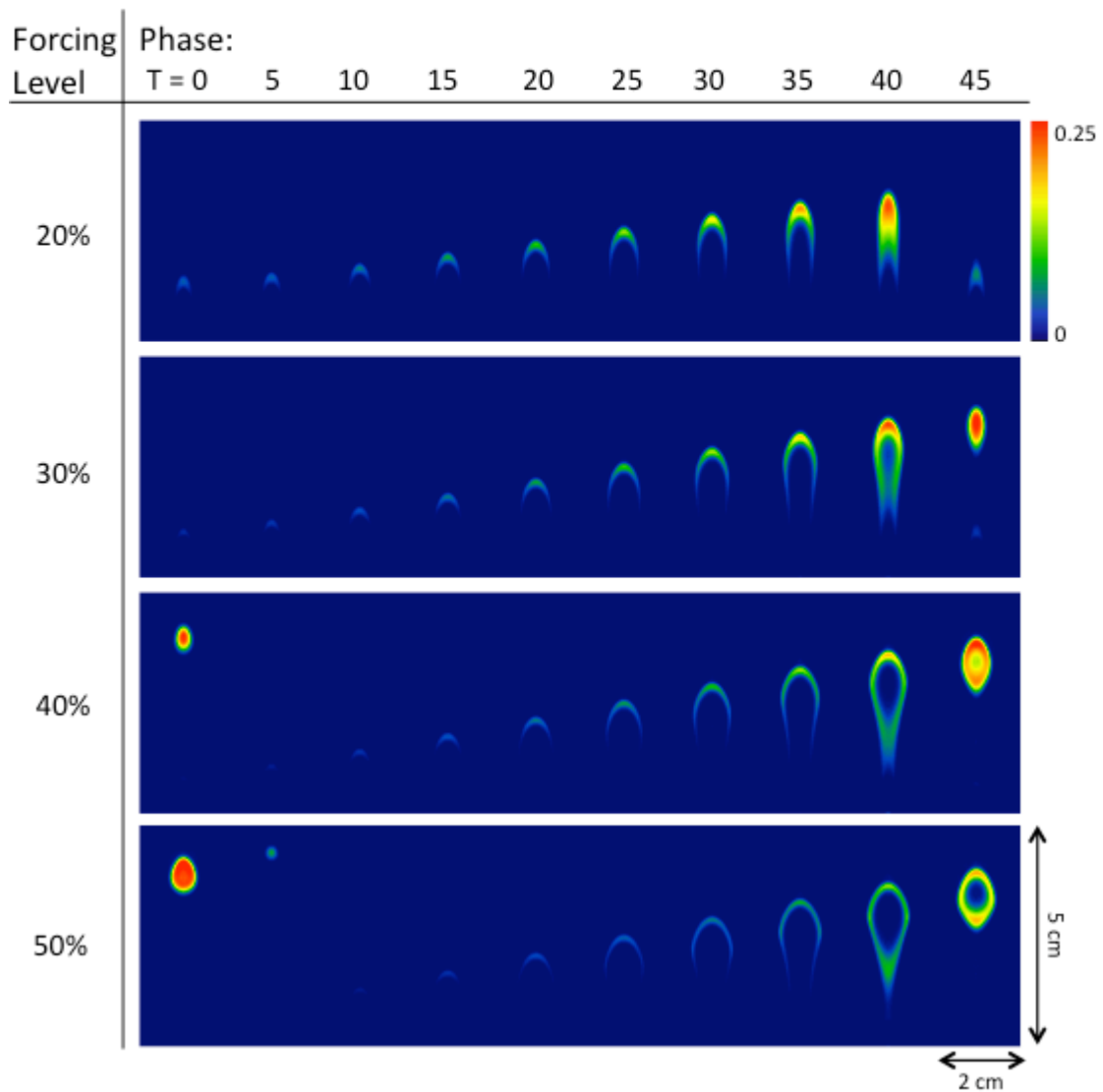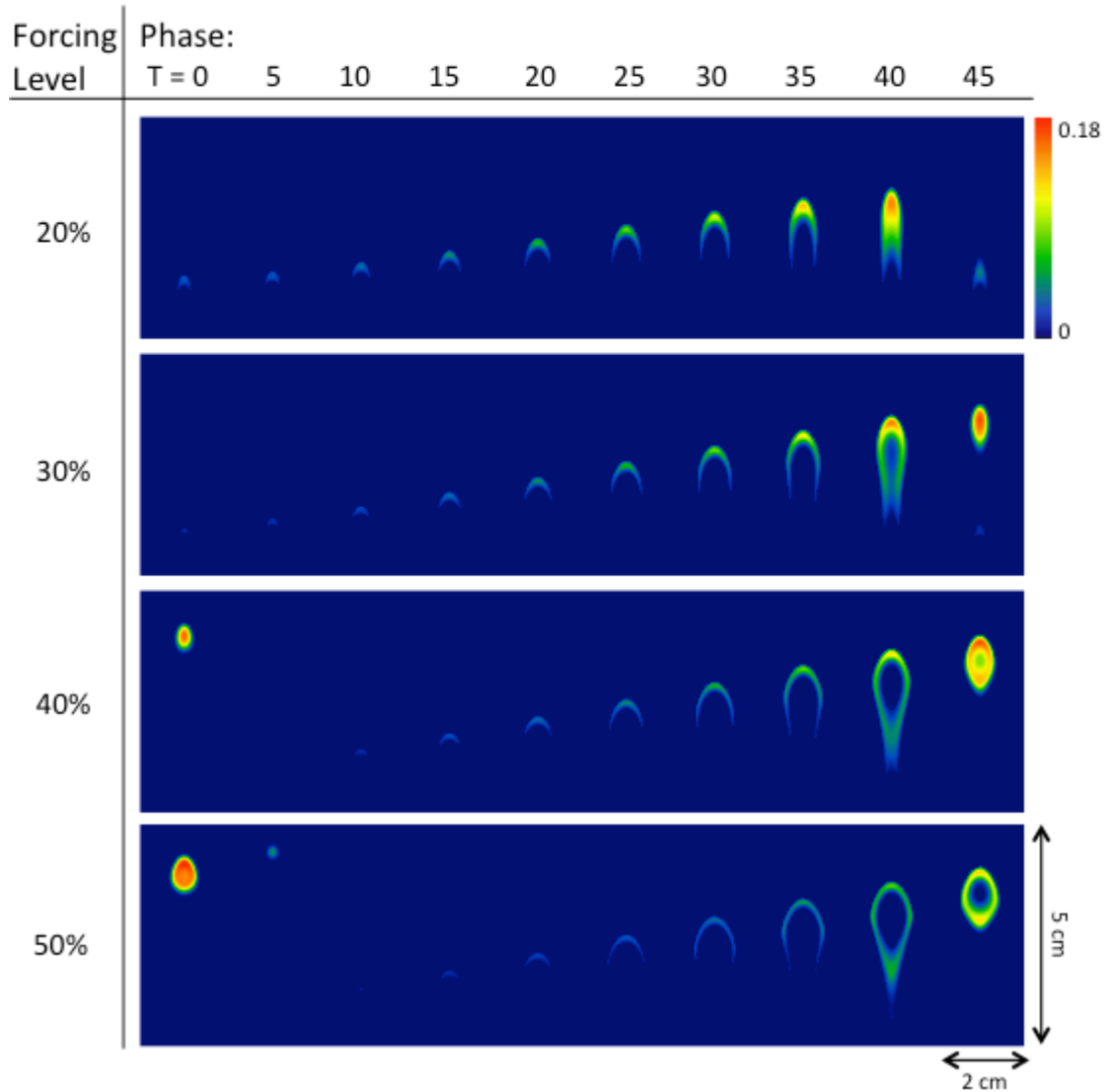
Figure 4.3.13: Soot volume fractions for a series of 28% C_2H_4 time-varying flames, for a range of forcing levels (20%, 30%, 40% and 50%). All images are shown on the same color scale (in ppm) as indicated.
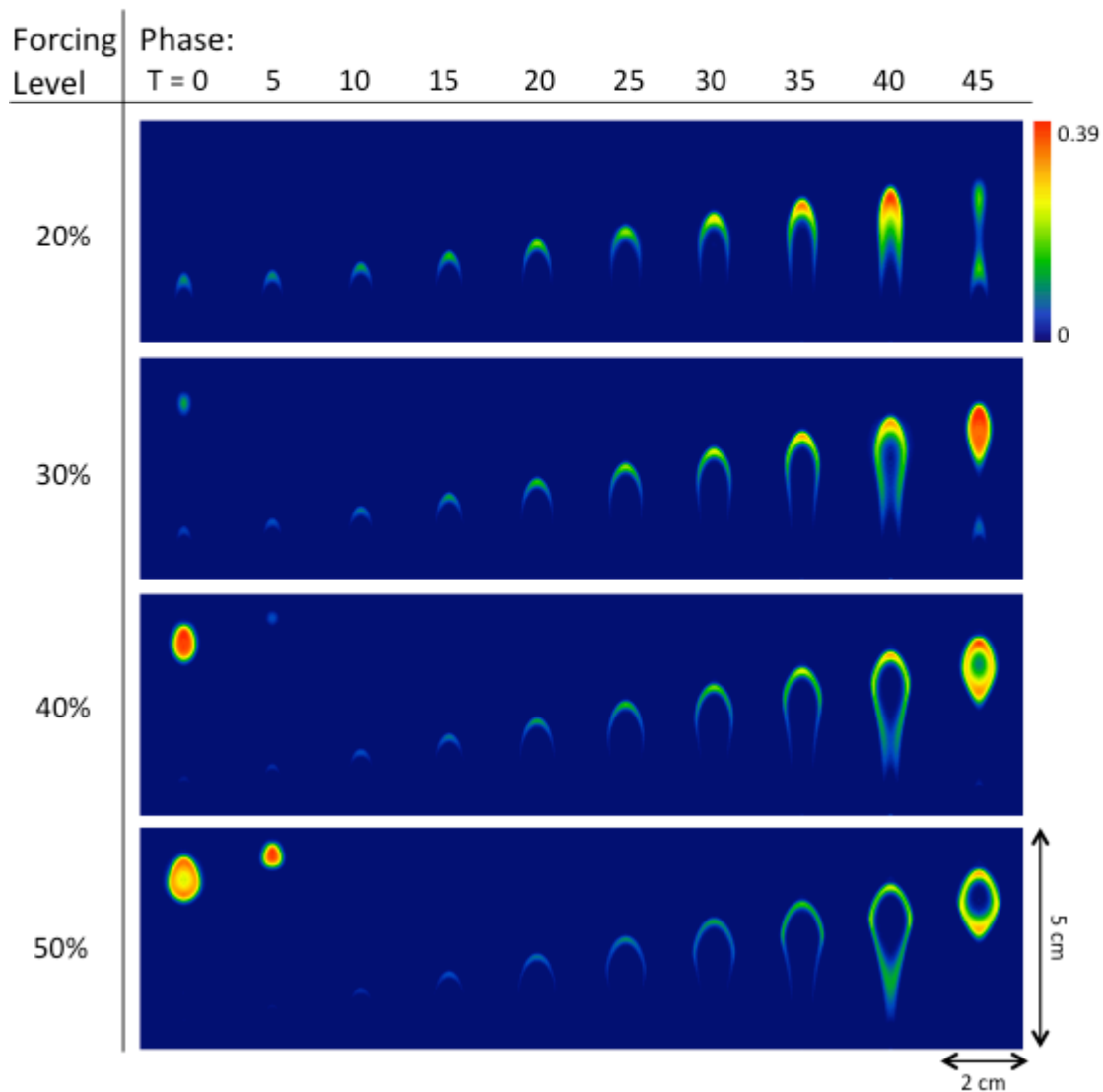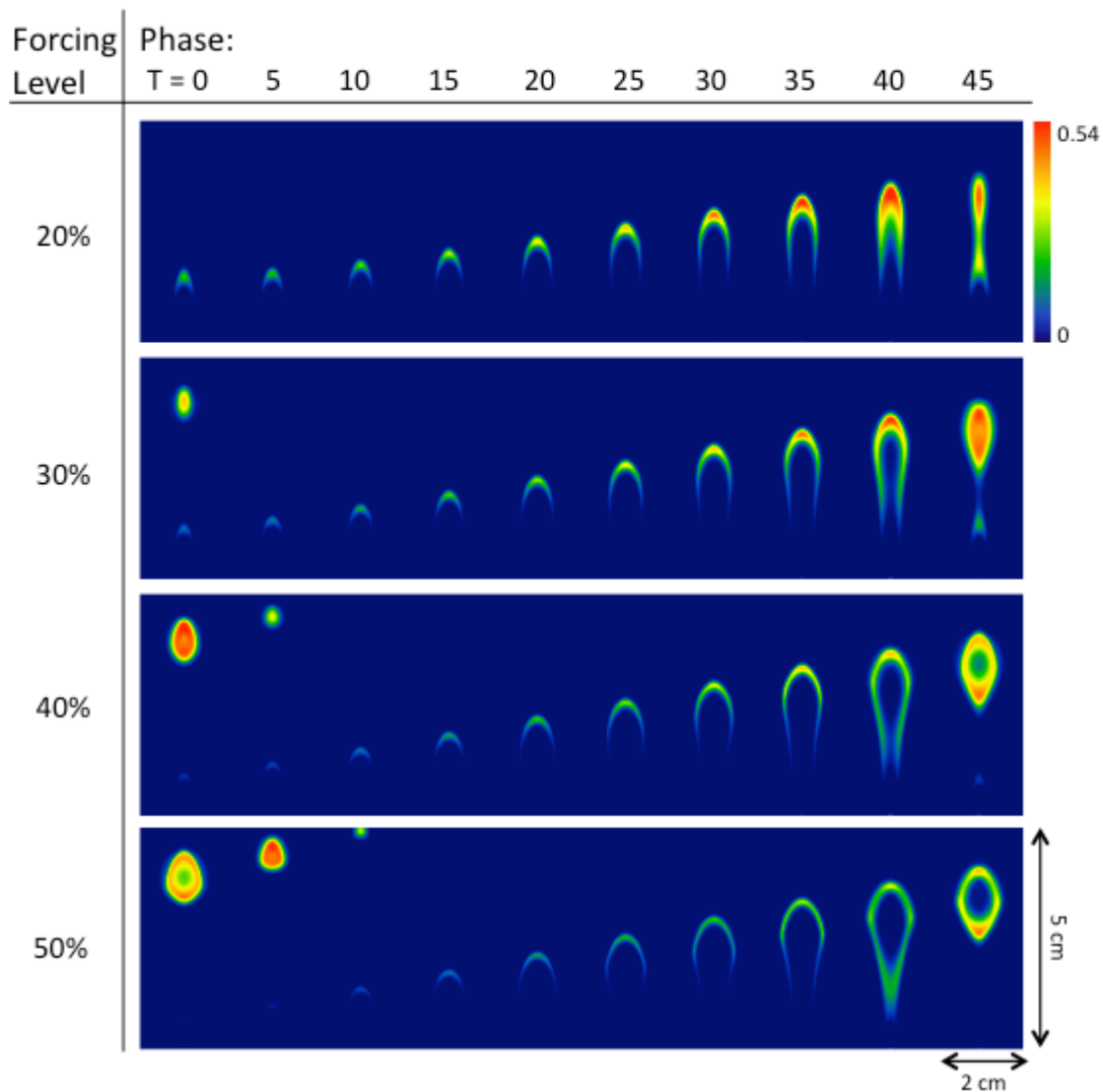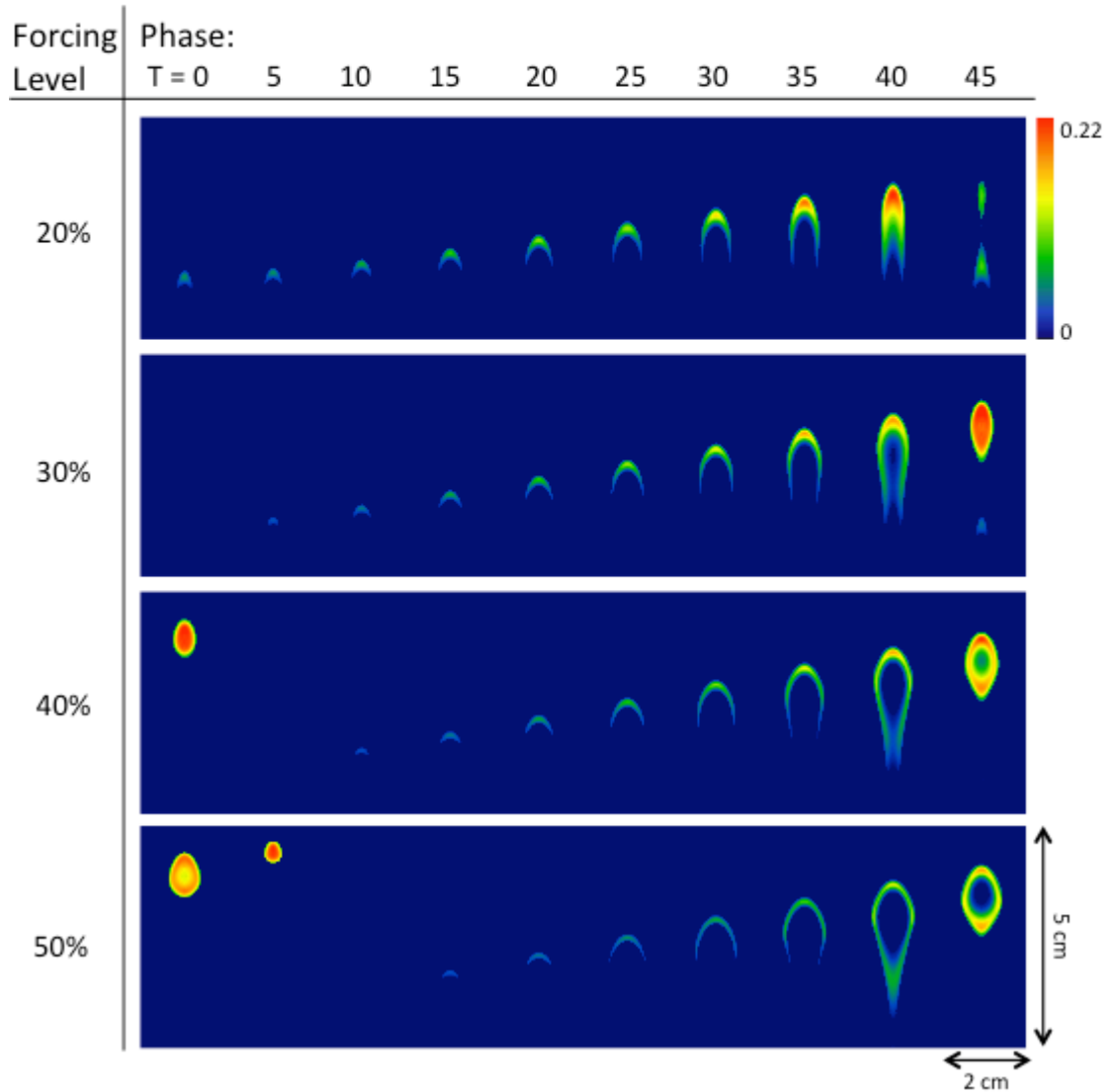
Figure 4.3.14: Soot volume fractions for a series of 30% C_2H_4 time-varying flames, for a range of forcing levels (20%, 30%, 40% and 50%). All images are shown on the same color scale (in ppm) as indicated.
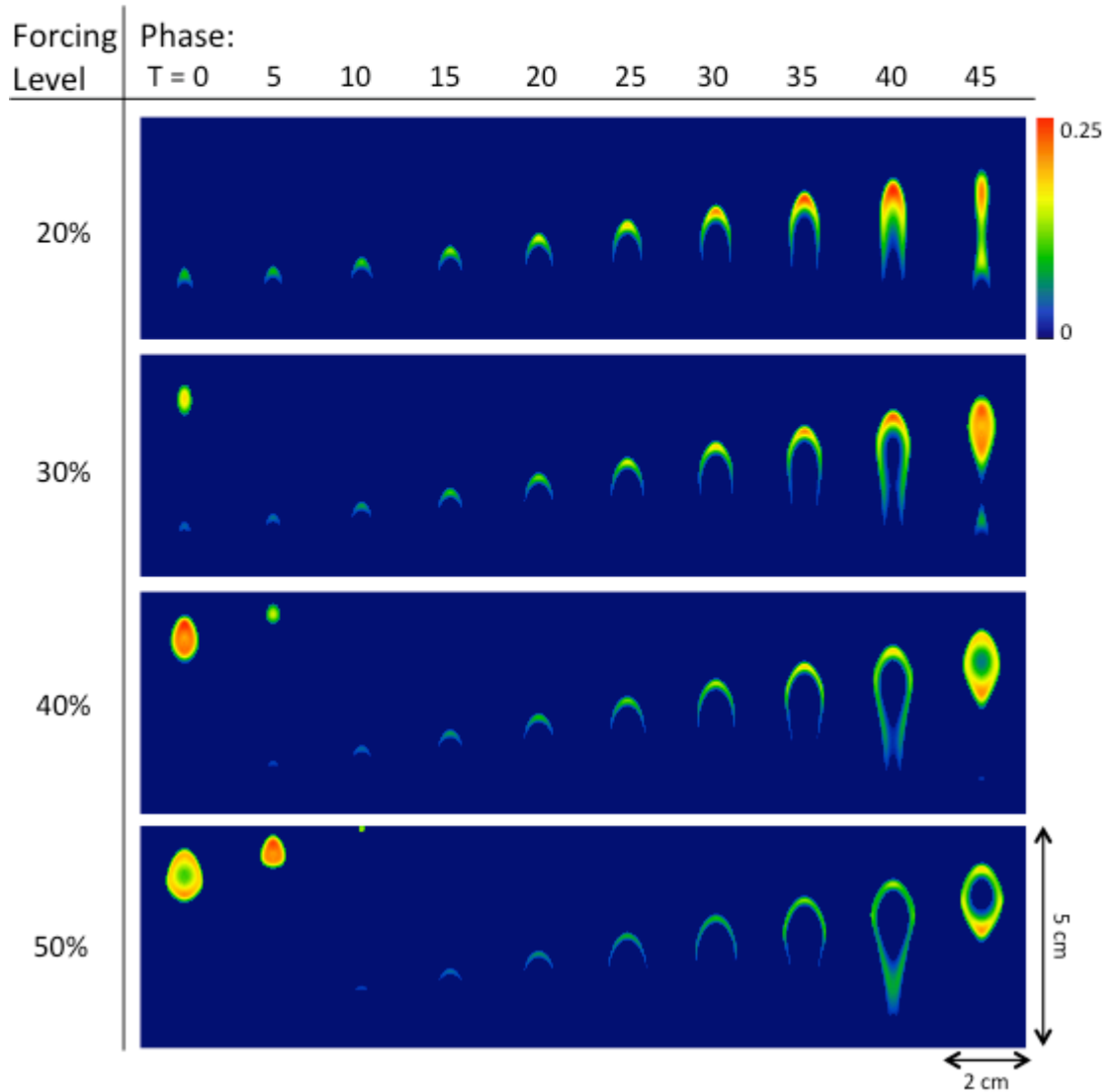
Figure 4.3.15: Soot volume fractions for a series of 32% C_2H_4 time-varying flames, for a range of forcing levels (20%, 30%, 40% and 50%). All images are shown on the same color scale (in ppm) as indicated.
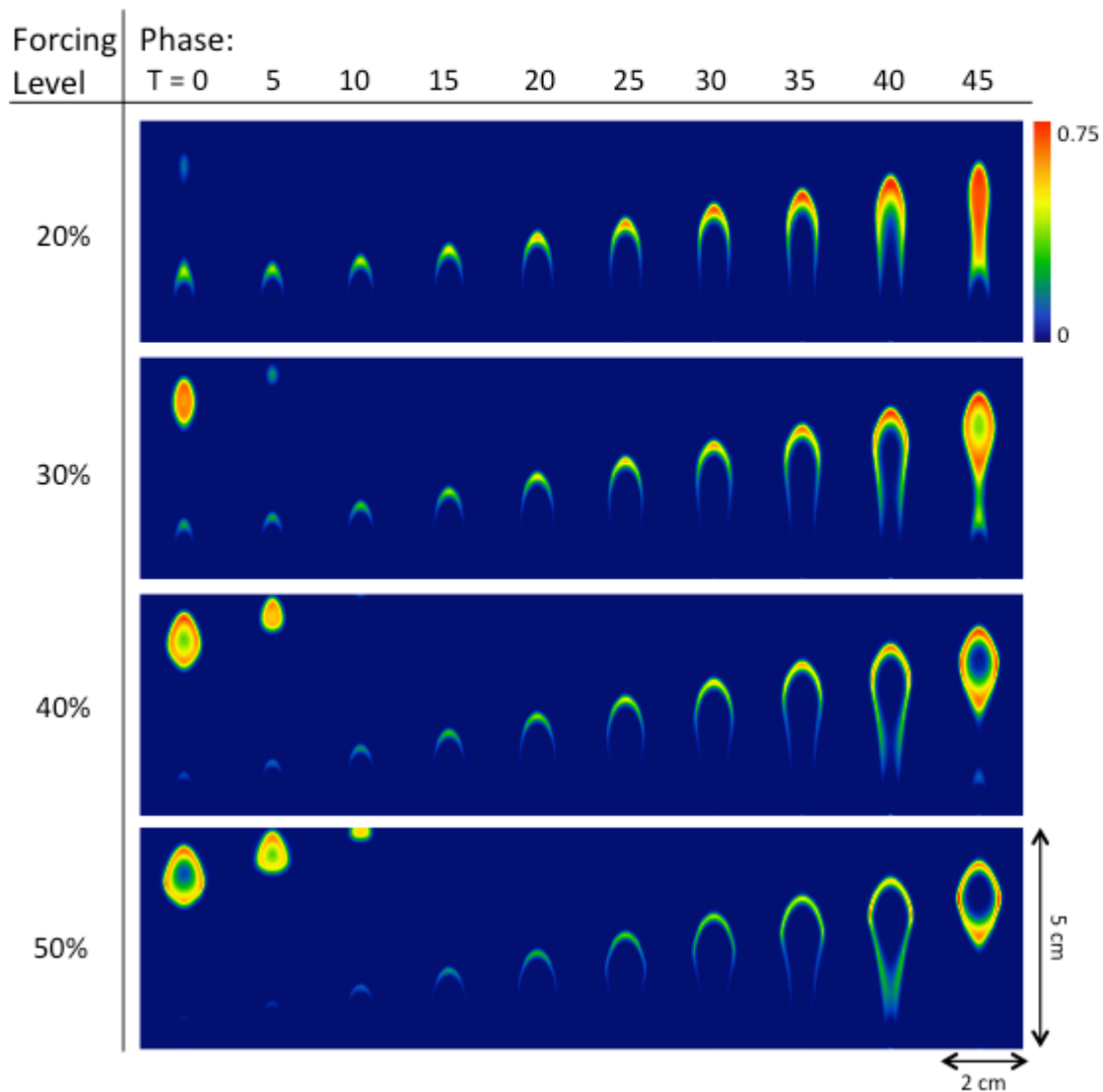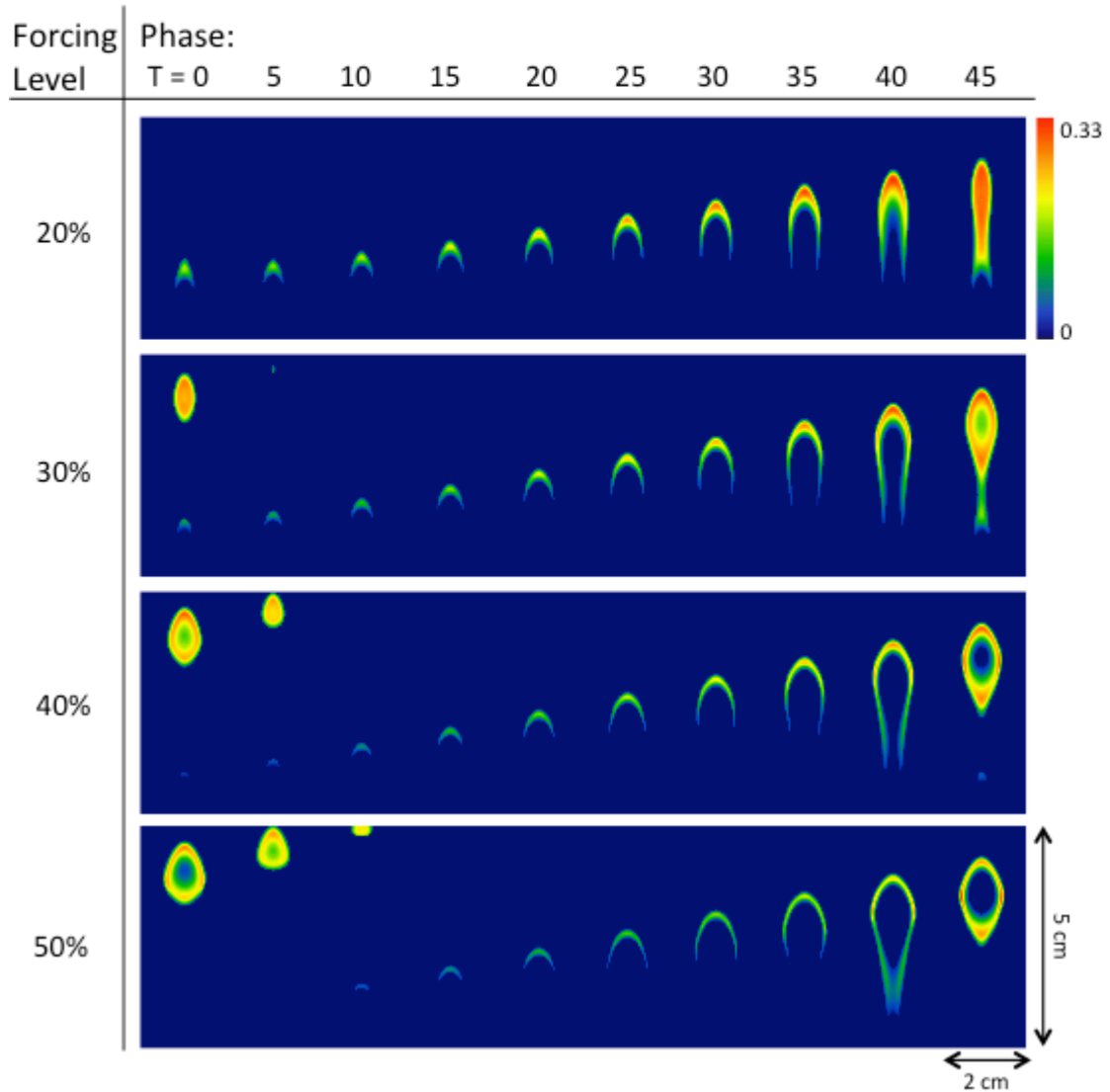
Figure 4.3.16: Soot volume fractions for a series of 35% C_2H_4 time-varying flames, for a range of forcing levels (20%, 30%, 40% and 50%). All images are shown on the same color scale (in ppm) as indicated.
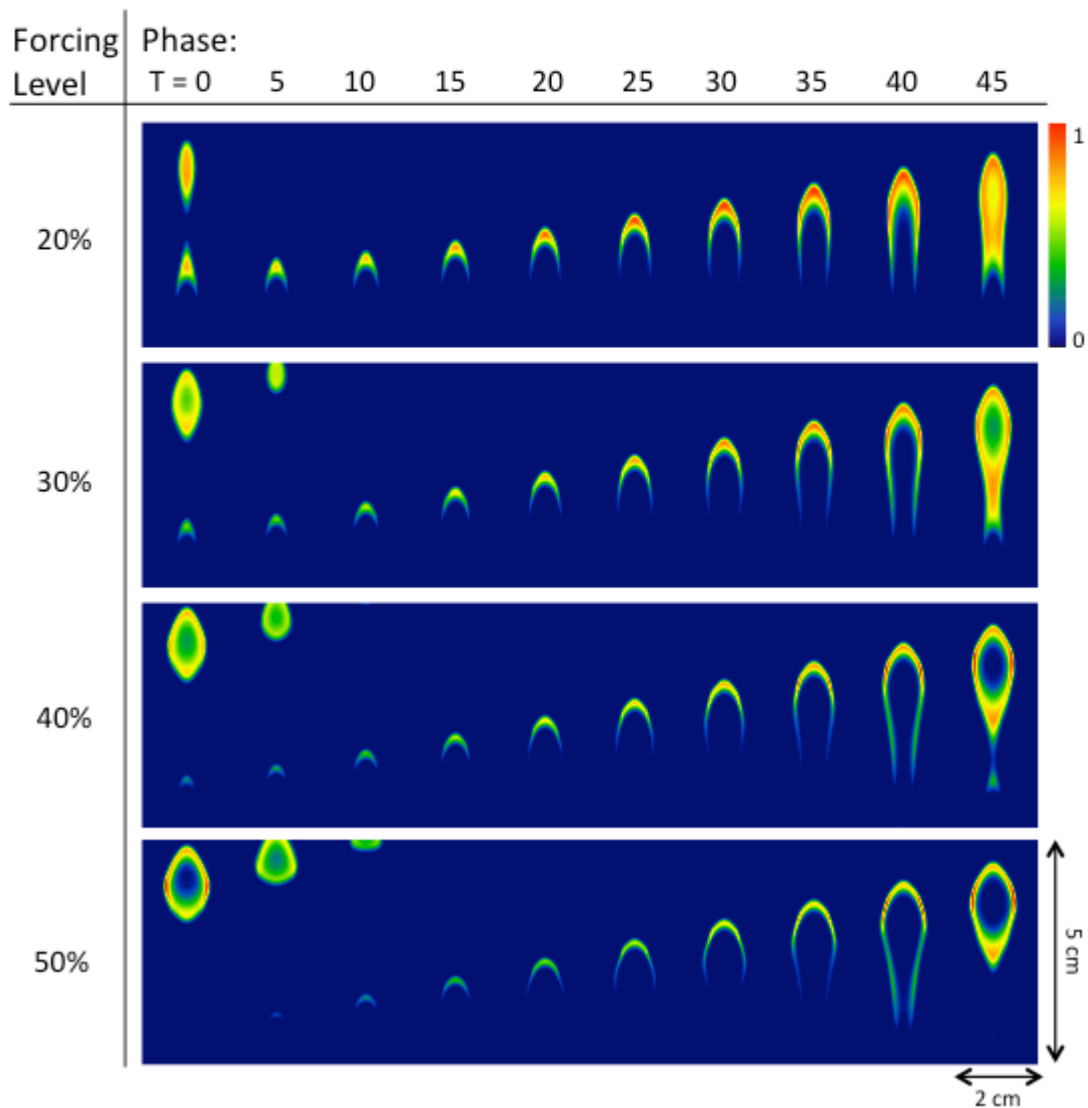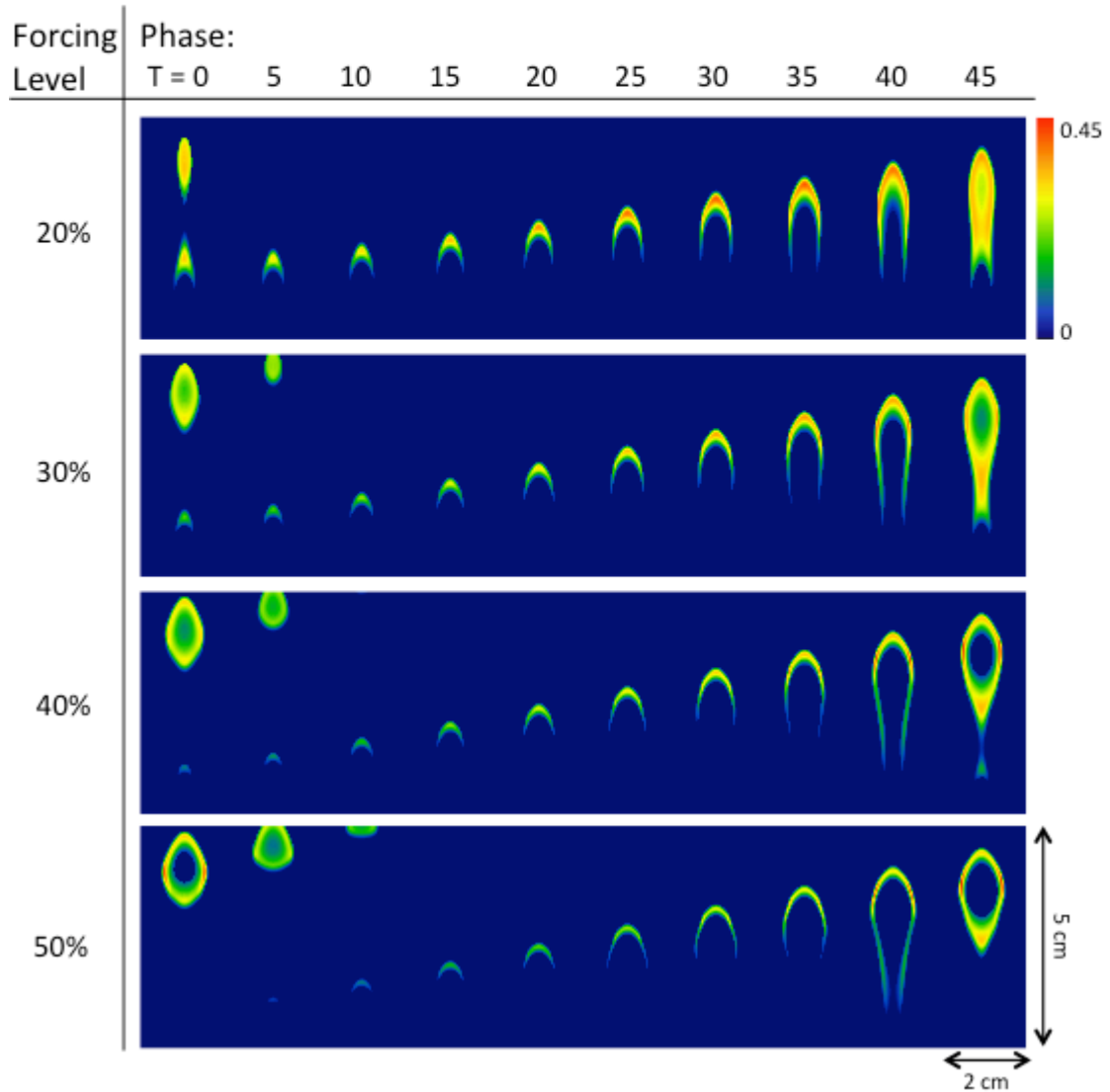
Figure 4.3.13: Soot volume fractions for a series of 40% C_2H_4 time-varying flames, for a range of forcing levels (20%, 30%, 40% and 50%). All images are shown on the same color scale (in ppm) as indicated.

4.3.2 Computational and Experimental Study of Sooting Forced Flames

The goal of the study in the previous section was to identify cases where there is a pronounced increase in sooting in the forced flame, without exceeding levels that would challenge the optically-thin approximation made in the computations. It was determined that the 32% C_2H_4 flame would be the target of the study under two forcing levels: 30% and 50% modulation.

4.3.2.1 Computational Approach

The computational work presented in this Section was carried out by Dr. Seth Dworkin in Professor Mitchell Smooke's group. Details on the approach, as well as a thorough analysis of the computational results, can be found in [Dworkin 2009a]. Briefly, a distributed-memory parallel computation of a time-dependent sooting ethylene/air coflow diffusion flame, in which a periodic fluctuation (20 Hz) is imposed on the fuel velocity for four different amplitudes of modulation, is presented. The chemical mechanism involves 66 species, and a soot sectional model is employed with 20 soot sections. The governing equations are discretised using finite differences and solved implicitly using a damped modified Newton's method. The solution proceeds in parallel using strip domain decomposition over 40 central processing units (CPUs) until full periodicity is attained. The calculation is carried out for forcing amplitudes of 30%, 50%, 70% and 90%.

4.3.2.2 Experimental Approach

The soot volume fraction was measured using the LII setup described in Section 3.5.2, with the laser fluence operating in the saturation regime (~0.6 J/cm^2). The results

shown here are calibrated with respect to the results in [Smooke 2005], where a dimensionless extinction coefficient of 10 is used.

4.3.2.3   Comparison of Results

Figure 4.3.14 plots the computational results for forcing amplitudes of 30% (A) and 50% (B) at 5 ms intervals throughout a 50 ms cycle. White curves representing the 1900 K isotherms are superimposed over the soot volume fraction contours in the next four figures. Figure 4.3.15 plots the experimental results for forcing amplitudes of 30% (A) and 50% (B) at 5 ms intervals. It should be noted that the panels of the experimental figures are offset by 2.5 ms from the panels of the computational figures.

The spatial features of the experimental soot contours in Figure 4.3.15 (for 30% and 50% forcing) are most similar to the computational for the 70% and 90% forcing cases (not shown here), respectively. In both cases, the high-velocity component of the fuel flow causes the sooting region to pinch off at approximately $t_{cycle} = 45$ ms. Experimentally, the pinched-off soot field forms a hollow shell of unburned fuel that burns inward until the region is no longer hollow at $t_{cycle} = 5$ ms. The computational soot contours in Figure 4.3.14 (for 30% and 50% forcing) show the most similarities with 10% and 20% forcing of the flame, respectively. In both the experimental and computational results, the peak soot volume fraction transitions between the centerline and wings at different phases of the forcing cycle. Discrepancies in the forcing amplitude are under investigation. Still, the transition of the peak soot from the centerline to the wings as a function of phase and the development of pinched oval-shaped soot regions transitioning to hollow shells of unburned fuel are seen in both the experiments and computations.
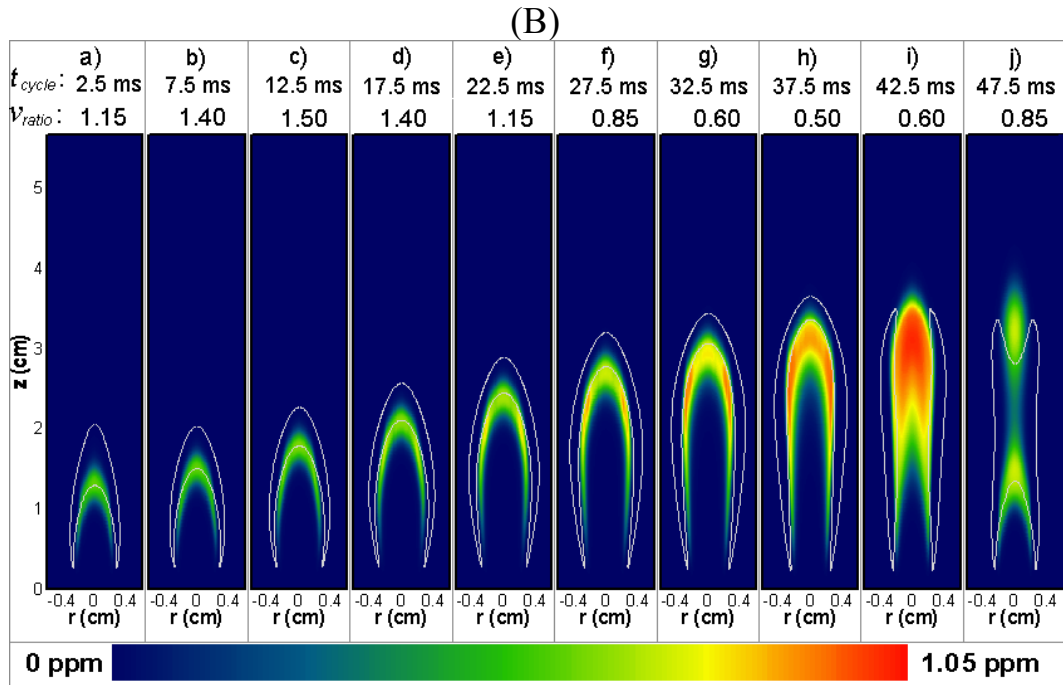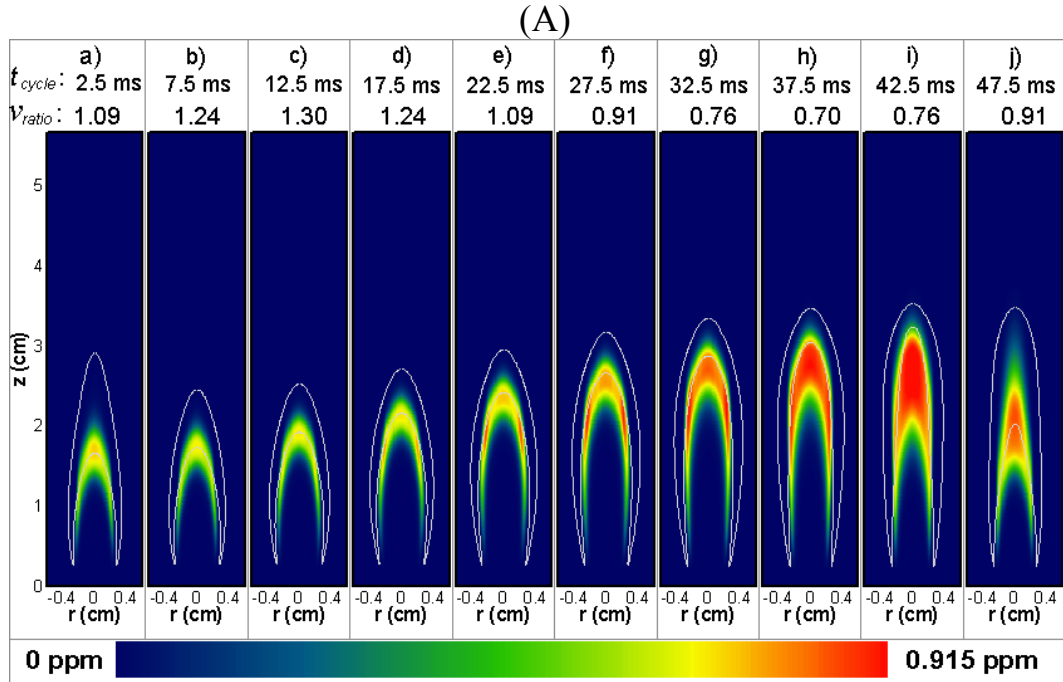
Figure 4.3.14: Computed isopleths of the soot volume fraction f_v in the coflow ethylene/air diffusion flame with (A) 30% forcing and (B) 50% forcing. For reference, the location of the 1900 K isotherm is plotted in white. Panel (a) corresponds to 0.5025 seconds after initial forcing.

(A)

175
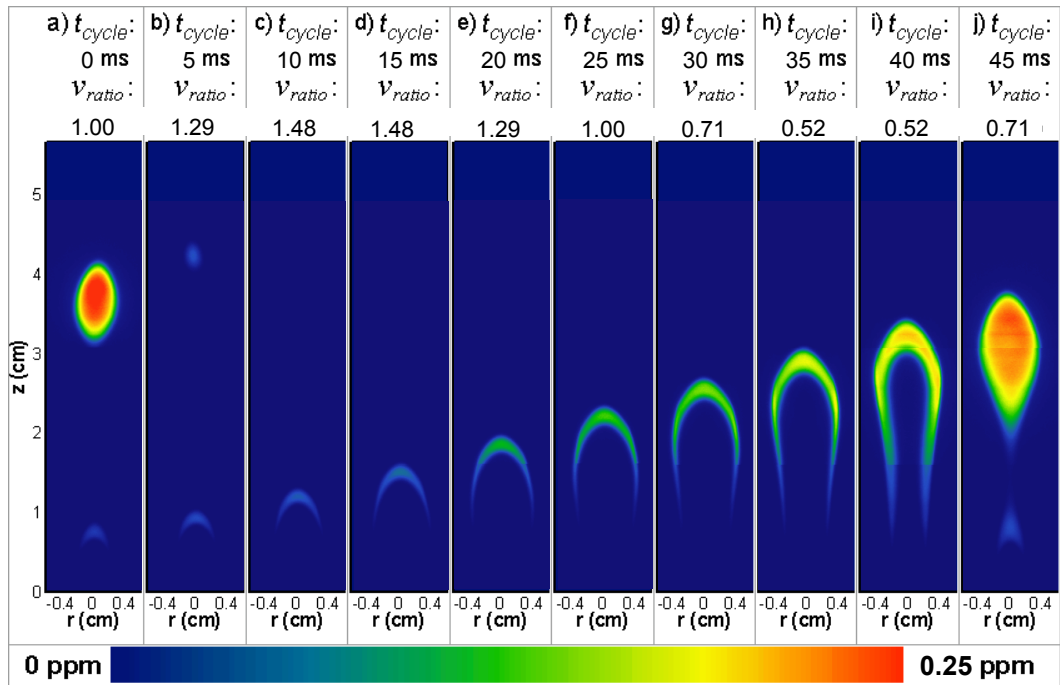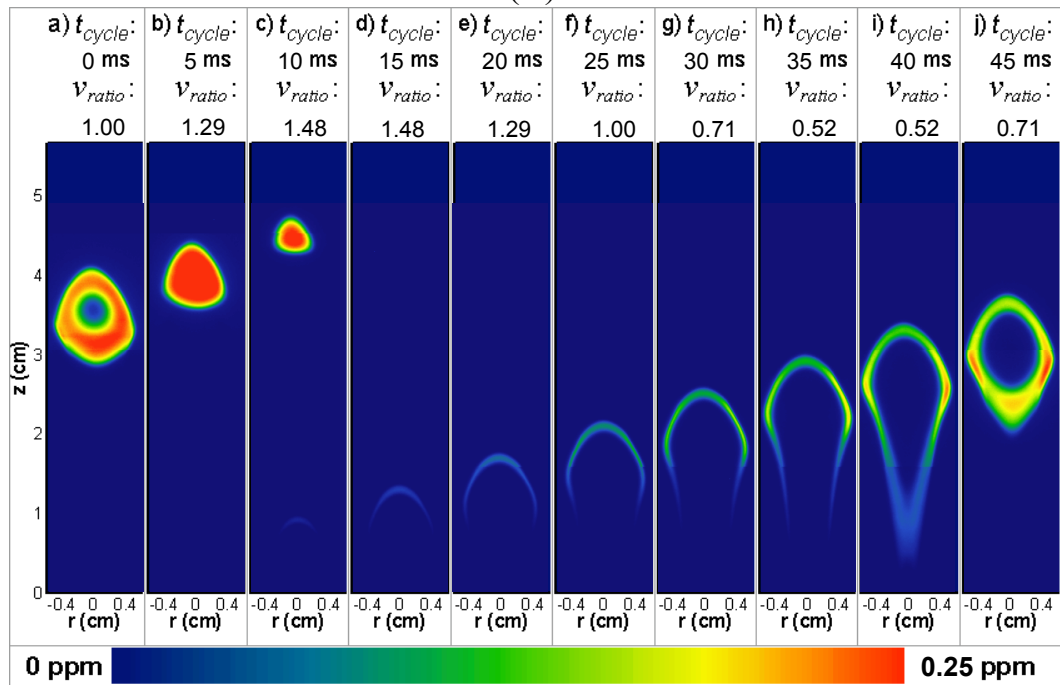
Figure 4.3.15: Experimental isopleths of the soot volume fraction f_v in the coflow ethylene/air diffusion flame with (A) 30% forcing and (B) 50% forcing. Panel (a) corresponds to the onset of the initial forcing for the cycle.

4.3.2.4   Conclusions

A primary objective of future work relating to the time-dependent sooting ethylene/air diffusion flames presented here should be to validate the model by improving comparisons to experimental data. A preliminary comparison of experimental and computational soot volume fractions, shown in the previous section, reveals a discrepancy in the relative forcing amplitudes was seen, where the computational results required roughly twice the forcing level to obtain soot features that are comparable with the experimental results.

The cause of this discrepancy is reasonably well understood, though the solution is not trivial to apply. The source of the problem stems from damping of the temporal and spatial gradients within the numerical solution. The numerical method employs a second-order approximation to the governing equations, using an implicit solver. This low-order approximation does not fully resolve spatial gradients that exhibit high spatial frequencies, and this problem is amplified when the solution of an unsteady problem is sought. Proper solution of this problem requires the application of a compact scheme to the numerical approach, which is a long-term goal of this ongoing study. It is possible to compensate for the damping of the final solution by over-resolving the computational grid. Initial attempts to apply this approach have been unsuccessful.

Regardless of these discrepancies, some interesting features of the computational soot volume fraction profiles were verified experimentally including the pinching off of the secondary soot region in the 50%, 70%, and 90% forcing cases, and the presence of the hollow shell-like structure in the 90% forcing case. Also, the transition of the region

177

of peak soot from the centerline to the wings as a function of phase of the forcing cycle

was seen in both the experimental and computational results.

CHAPTER 5

5 Comparing Experiments and Computations

5.1 Introduction

As the comparison between experimental and computational results plays a major role in this work, it is essential to investigate different approaches to making efficient comparisons. One important role for experiments in combustion research is to guide and verify computational models. The advances in lasers, detectors, and computers that occurred in the 1970's and 80's led to the development of many new techniques for gathering data in the harsh environment of combustion. For a period of time, new diagnostic techniques were themselves of interest, and the relevance of the measured quantities to the theoretical and computational models under development at the same time was of secondary importance. In fact, quantities that were easy to measure were not usually the same quantities output by the models. However, as laser diagnostic techniques matured in the 1990's, the focus shifted to measuring fundamental quantities (e.g., mole fractions) that were of more significance to the modelers. Achieving this important goal has been much harder, often involving simultaneous measurement of many quantities (each with their own noise, uncertainties, and interferences) to get the fundamental quantity of interest to compare with simulations. Errors are often very difficult to estimate in these cases. In the meantime, computational models have become more sophisticated, more quantitative, and more complete. The availability of more complete

information allows the possibility of using simulation results to derive predictions of measured signals rather than measuring many quantities to derive a single fundamental quantity. In some cases, comparison of computed and measured signals may be more informative and reliable than the comparison of computed and measured mole fractions, temperatures, mixture fractions, scalar dissipations, etc.

A few previous studies have compared measured and computed signals in an effort to validate computational fluid dynamics (CFD) models. Numerical simulation of experimental signals, known as computational flow imaging [Ruyten 1994], is particularly useful under experimental conditions that do not allow for the direct measurement of a particular parameter. Boyce *et al.* [Boyce 1996] compared experimental interferometric data with theoretical maps computed from CFD results of a hypersonic flowfield. Danehy *et al.* [Danehy 1999] used CFD models to create theoretical planar laser-induced fluorescence (PLIF) images by determining the quenching dependence for the existing flow conditions. The study found that the theoretical images were useful for choosing the best excitation scheme for yielding signal intensities within the dynamic range of their detection system. This work was later expanded upon to look at PLIF images of mixing flowfields [Gaston 2002]. Images of computational and experimental fluorescence images of mixing flows in fuel injectors were compared and favorable agreement between the fluorescence images allows for the extraction of flow parameters from the theory that were not measured. Amantini *et al.* [Amantini 2006; Amantini 2007a; Amantini 2007b] studied extinction and edge flame phenomena of counterflow diffusion flames both computationally and experimentally using OH and CO PLIF images, as well as velocities from particle image velocimetry (PIV) measurements.

Simulated PIV velocity fields included predicted thermophoresis effects and the vaporization of oil droplets (used for seeding) to remove velocity vectors in regions with temperatures exceeding the boiling point of oil. Bell *et al.* [Bell 2003] use numerical simulations to determine synthetic LIF images of NO by accounting for temperature and quenching effects for comparison with experimental results to look at NO formation pathways in both doped and undoped flames. Schieβl *et. al* [Schiessl 2009] exploit state variable correlations to improve the accuracy of measurements to determine low-dimensional manifolds of the system. This allows for an approximate description of the state using only a few variables. Oftentimes, the comparison of measured and computed signals is seen as a last resort when direct measurements of fundamental quantities are impossible due to the complexity of the flow environment, the availability of diagnostics techniques, or simply limited resources.

The ongoing computational and experimental work that has been done at Yale has led to a reconsideration of the interface between experiments and computations. Specifically, in designing experiments and choosing diagnostics, experimentalists should consider the accurate measurement of signals that can be calculated with little uncertainty as well as the more conventional approach of making direct comparison with computed results. It may be that deriving predictions of signals from numerical results is better than measuring the fundamental quantities that are normally output by simulations. Quantitative comparisons can easily be obtained by using appropriate calibration on both sides of the comparison. This approach clearly necessitates that modelers and experimentalists work together. Further, a detailed understanding of signal generation, as well as the effects of quenching, signal interferences, detector characteristics, and spatial

resolution on signals is required. Below, three examples of comparing measured and computed signals are presented: NO laser-induced fluorescence (LIF) in a non-sooting diffusion flame, luminosity images of sooting diffusion flames (see [Connelly 2009b]), and measurements of PAH fluorescence in increasingly sooting flames in an effort to improve computations for real fuels [Connelly 2009a].

5.2   NO Measurements in a Non-Sooting Laminar Flame

A non-sooting lifted methane/air coflowing non-premixed flame has been studied extensively both experimentally and computationally [Smooke 1996; Bennett 1998; McEnally 1998; McEnally 2000; Walsh 2000c]. To test the ability of different kinetics schemes to predict NO formation in the flame, computations using two mechanisms (GRI 2.11 [Bowman 1995] and GRI 3.0 [Smith]) are compared to experimental measurements of NO using LIF. The computations were performed by using the numerical techniques and model described in [Bennett 1998], with the local rectangular refinement solution-adaptive gridding carried out to one additional level of refinement beyond that in [Bennett 1998]. The experimental procedures are outlined below. This comparison of computations and experiments is performed using two approaches: comparing computed and measured mole fractions, and comparing a computed fluorescence signal to the measured LIF signal.

The first approach of comparing computed and measured NO mole fractions requires measurement of the NO LIF signal as well as measurement of the supporting data (temperature and major species concentrations) needed to apply Boltzmann and quenching corrections [Paul 1993; Settersten 2006]. Two-dimensional images of NO fluorescence are created by tiling together a series of spectrally-resolved radial images of

the (0,2) vibrational band [Smooke 1996]. Images of temperature and major species (N_2,

O_2, CO_2, H_2O, and CO) mole fractions, shown in Figure 5.2.1, were measured using

Rayleigh scattering and vibrational Stokes-shifted Raman scattering [Marran 1996;

McEnally 2000]. The quenching correction is calculated using the model of Settersten *et*

al. [Settersten 2006]. The noise level of each component used to calculatate the

quenching and Boltzmann corrections (temperature, and N_2, O_2, CO_2 and H_2O mole

fractions) is determined by calculating the *rms* fluctuation in a 4 x 3.5 mm^2 area 5.5 cm

above the burner (where the signals are reasonably constant) and dividing by the average

signal in that region. The CO noise level is determined for a 4.2 x 3.3 mm^2 area at a

position 2.5 cm above the burner (around the CO maximum). The result is corrected for

existing spatial gradients by subtracting the *rms* divided by the average in the

computational results at the same location. (See Figure 5.2.1 for the location of these

areas, indicated by the black rectangles.) Because the Rayleigh scattering data has a good

signal-to-noise ratio, the two-dimensional temperature profile has a noise level of only

1% of the local temperature of 1550 K. However, the relatively small scattering cross

sections associated with Raman scattering cause an increase in noise and experimental

uncertainty. The resulting noise levels in the N_2, O_2, CO_2, H_2O, and CO mole fractions

are 2%, 7%, 3%, 7% and 37% of the local average mole fractions of 0.78, 0.05, 0.08,

0.10 and 0.05, respectively.
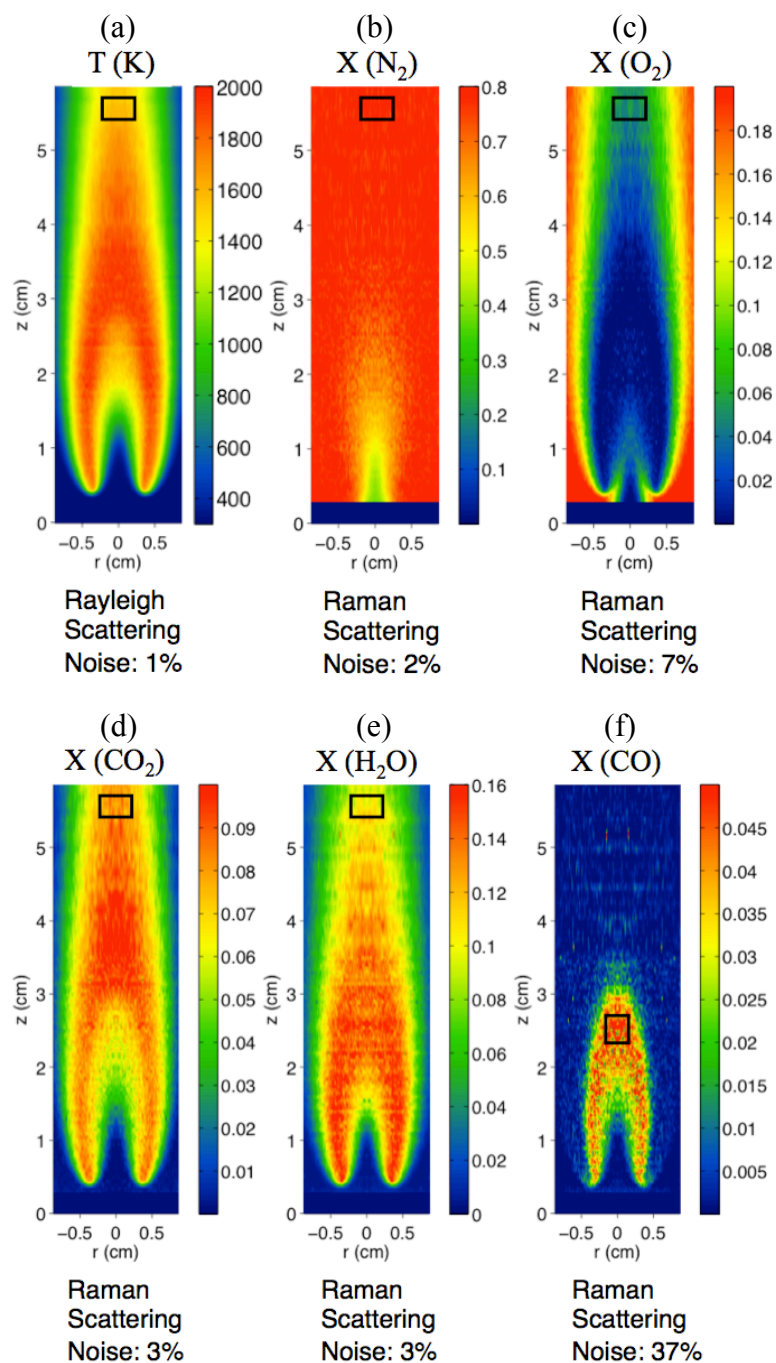
Figure 5.2.1: Temperature (a) and species mole fractions (b-f) in the nonsooting methane/nitrogen diffusion flame as measured with Rayleigh and Raman scattering. These measurements are used in conjunction with a quenching model by Settersten *et al.* to transform the NO laser-induced fluorescence signal into the NO mole fraction. The noise level of each image (in the rectangular region) is noted below each panel.

Figure 5.2.2 plots the measured NO LIF, quenching correction, Boltzmann correction, and resulting NO mole fraction. When the Boltzmann and quenching corrections are applied, the noise level nearly doubles from 3% (measured NO LIF) to 5% (measured NO mole fraction) of the 70 ppm average. The noise level here has been calculated the same way as for the species and temperature above. The resulting NO mole fraction is particularly noisy in the region where CO quenching is important due to the high level of noise associated with that measurement. A comparison can now be made to the computed NO mole fraction using GRI 2.11 and GRI 3.0 (Figure 5.2.3). It can be seen that GRI 2.11 consistently under-predicts the NO mole fraction measured, while GRI 3.0 shows good agreement on the fuel side of the flame front at distances below ~ 2.5 cm, and significantly over-predicts the NO mole fraction elsewhere. (A detailed explanation of this behavior appears in [Bennett 2008a].) For both mechanisms, the increase in NO, immediately above the flame, due to prompt NO formation occurs at an axial location that is further downstream than that observed experimentally. Additionally, the relative increase at that location is exaggerated using GRI 3.0, while the relative variations of the GRI 2.11 calculation scale well with the measurement.
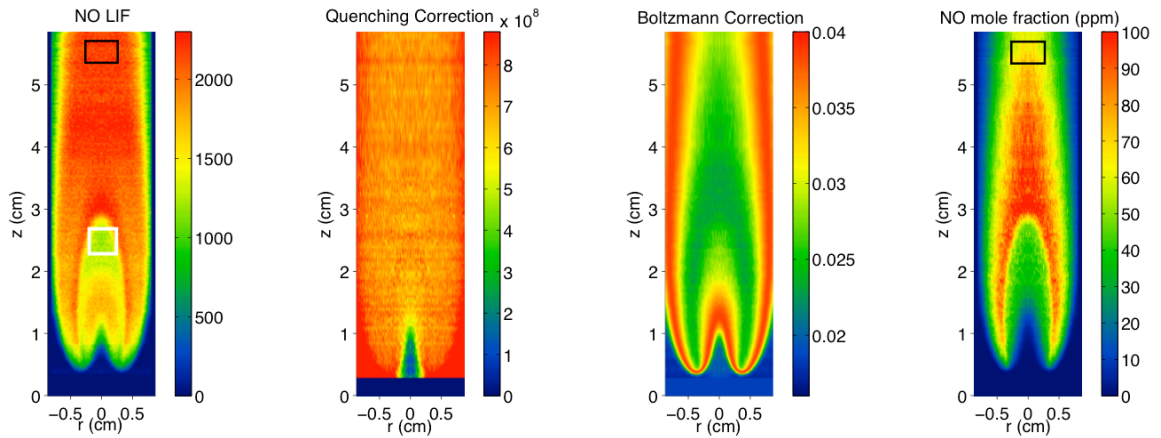
Figure 5.2.2: Experimental data of NO LIF. The quenching and Boltzmann corrections have been applied to the LIF data to obtain the measured NO mole fraction (far right). The boxes in the left-most plot indicate the areas used to determine noise levels. The upper box is used for all quantities except CO, which does not exist downstream in the flame. The lower box shows the area used to determine the noise from CO.

(a)

(b)
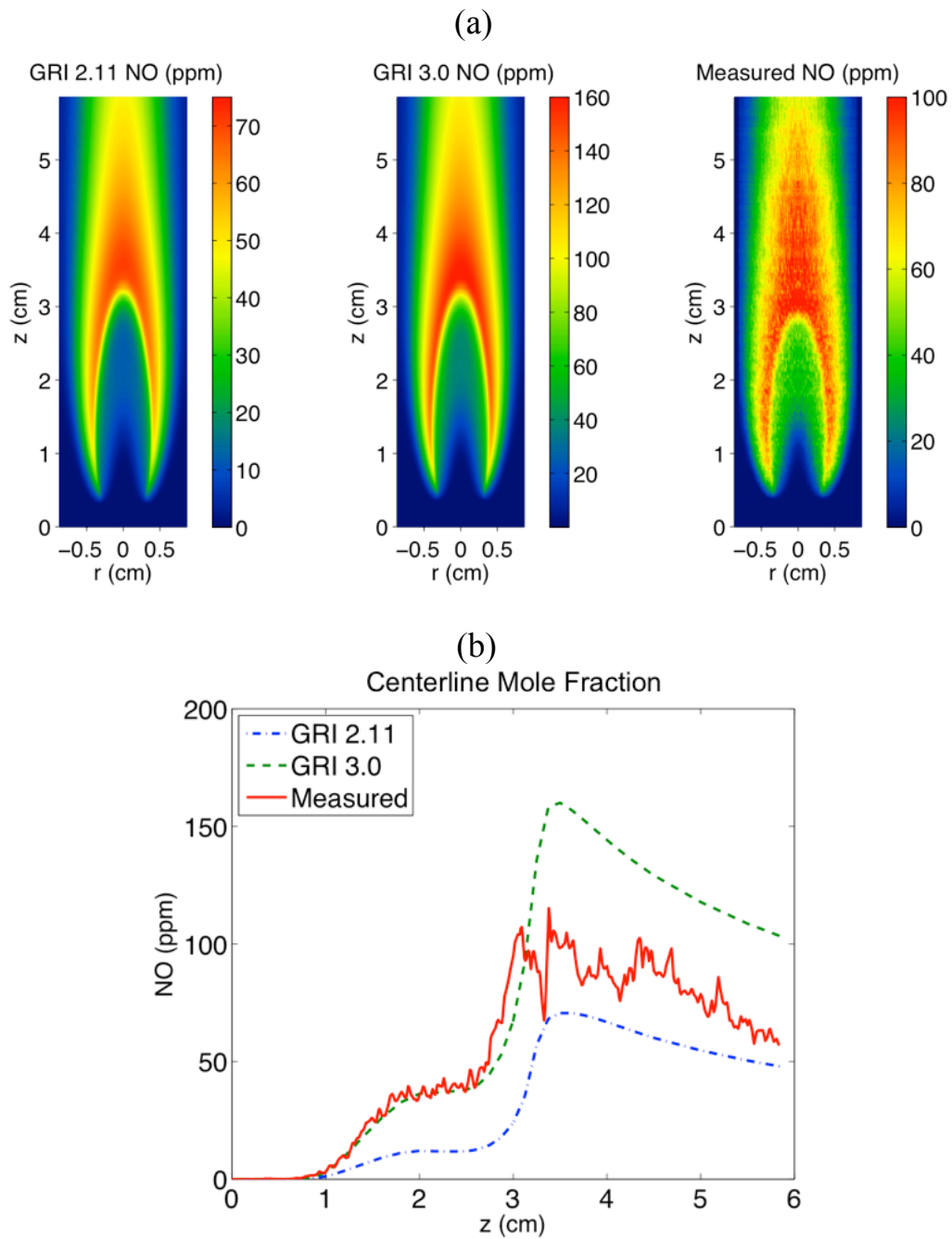
Figure 5.2.3: (a) Comparison of computed and measured NO mole fraction. The computed NO mole fraction has been obtained with two different chemical mechanisms: GRI 2.11 and GRI 3.0. The measured NO is the same as in Figure 5.2.2. The centerline NO mole fractions are plotted in (b).

Alternatively, the computational results can be used to derive a computed fluorescence signal, which can then be compared with the measured fluorescence signal. To this end, the quenching and Boltzmann corrections can be calculated using the temperature and major species output by each of the two numerical simulations. These corrections are then applied to the computed NO mole fraction to determine a computed fluorescence signal. This approach is demonstrated for GRI 2.11 in Figure 5.2.4. Here, the Boltzmann correction is determined based on the temperature result, calculated for the experimental transition being pumped. As was done experimentally (shown in Figure 5.2.1), the quenching correction is determined from the calculated major species using the computational results, utilizing the temperature-dependent quenching cross sections.

Since the quenching and Boltzmann corrections depend on temperature and major species concentrations, it is important to investigate any differences in the corrections obtained using the two kinetic mechanisms. Figure 5.2.5 shows the percent difference in the temperature, Boltzmann and quenching corrections from both mechanisms, relative to the maximum value from GRI 2.11. This calculation is executed for regions where the NO mole fraction is at least 10% of the maximum value to focus on regions where the quenching and Boltzmann corrections will be important. The temperature is found to vary by $< \pm 2\%$, the Boltzmann correction by $< \pm 1.5\%$ and the quenching correction by $< \pm 1\%$ in regions that are not dominated by differences in lift-off height between the two mechanisms. While the overall quenching and Boltzmann corrections are seen to be nearly identical, it is possible that important differences in the two mechanisms could exist that would not appear in these corrections. For example, a decrease in the
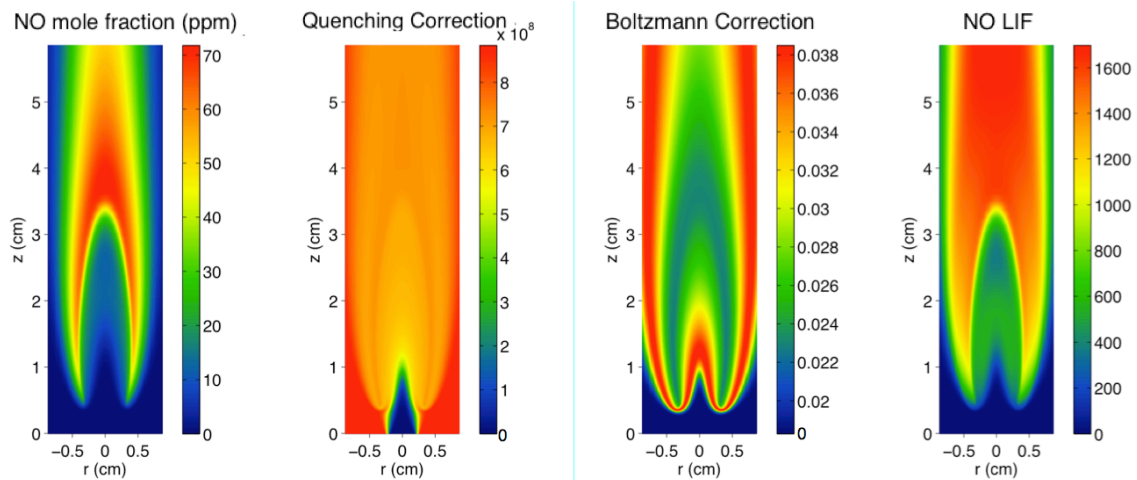
Figure 5.2.4: The computational results from GRI 2.11 are used to derive a computed fluorescence signal. Quenching and Boltzmann corrections are calculated using the temperature and major species output by the numerical simulations.
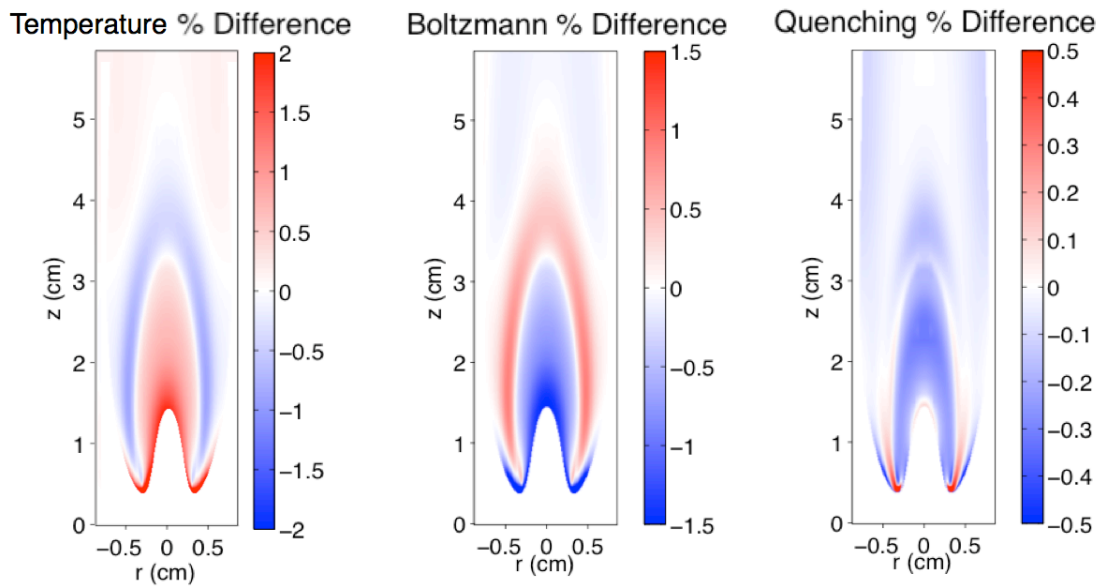
Figure 5.2.5: The percent difference of the temperature, Boltzmann correction and quenching correction between computations using both mechanisms is calculated. The temperature varies $<\pm 2\%$; the Boltzmann correction varies $<\pm 1.5\%$; the quenching correction varies $<\pm 1\%$. Red (positive) indicates where GRI 2.11 is greater; blue (negative) indicates where GRI 3.0 is greater.

concentration of one quenching partner in the computations would lead to an increase in the fluorescence signal, while an increase in the computed temperature could cause a decrease in the fluorescence signal. It is conceivable that these two variations could offset one another in the final result. For this reason, a sensitivity analysis was carried out to determine the dependence of this kind of comparison on variations in different components of the computational results. The same calculation of percent differences between the two mechanisms was implemented for the computed mole fractions of the major species and for the quenching correction for each quenching partner individually (see Figure 5.2.6). Discrepancies between the GRI 2.11 and GRI 3.0 results were found to be $< \pm 3\%$ and $< \pm 0.5\%$, for mole fractions, and individual quenching terms, respectively. These variations are negligible when compared with the 120% difference between the computed mole fractions of NO. Thus, within these limits, the comparison of computed fluorescence signals to the measured signal is anticipated to reflect the ability of each mechanism to predict NO formation.

In many of the percent difference plots in Figures 5.2.5 and 5.2.6 the largest fluctuations occur at the base of the flame. This is attributed to small variations in lift-off height between the two mechanisms. In this region of the flame, near its base, the temperature gradients are quite large causing the appearance of large discrepancies. To illustrate this point, Figure 5.2.7 plots the percent difference in temperature computed with GRI 2.11 and GRI 3.0 (a), as well as the temperature computed with GRI 2.11(b) and GRI 3.0 (c) and the temperature measured with Rayleigh scattering (d). Also shown are the centerline temperatures from GRI 2.11, GRI 3.0, and measurements (e). Neglecting lift-off height variations, fluctuations in Figures 5.2.5 – 5.2.7 would be even
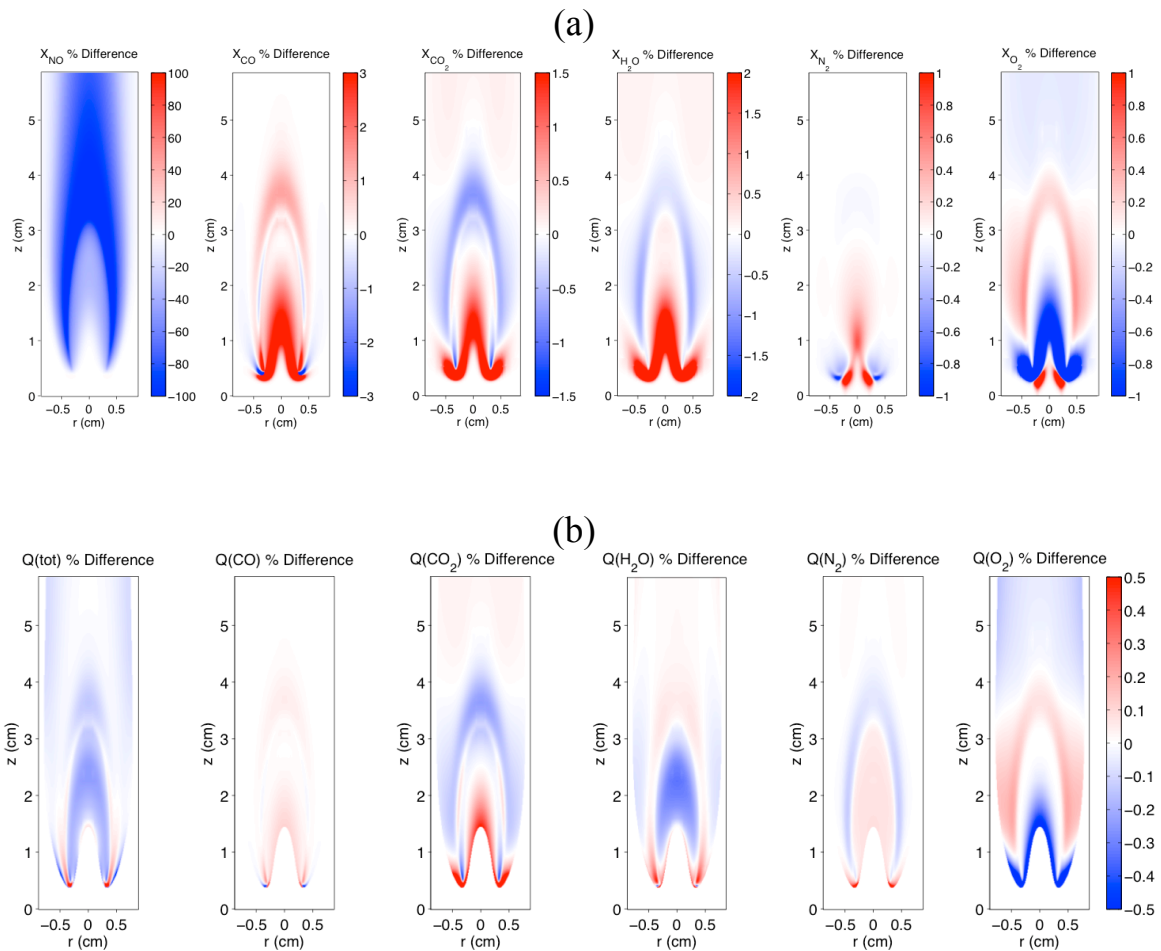
Figure 5.2.6: The percent difference (relative to the maximum values of GRI 2.11) in species mole fractions (a) and in the quenching correction (b) computed with GRI 2.11 and GRI 3.0. The difference is shown for regions where the NO mole fraction is at least 10% of the maximum value. Red (positive) indicates where GRI 2.11 is greater; blue (negative) indicates where GRI 3.0 is greater.
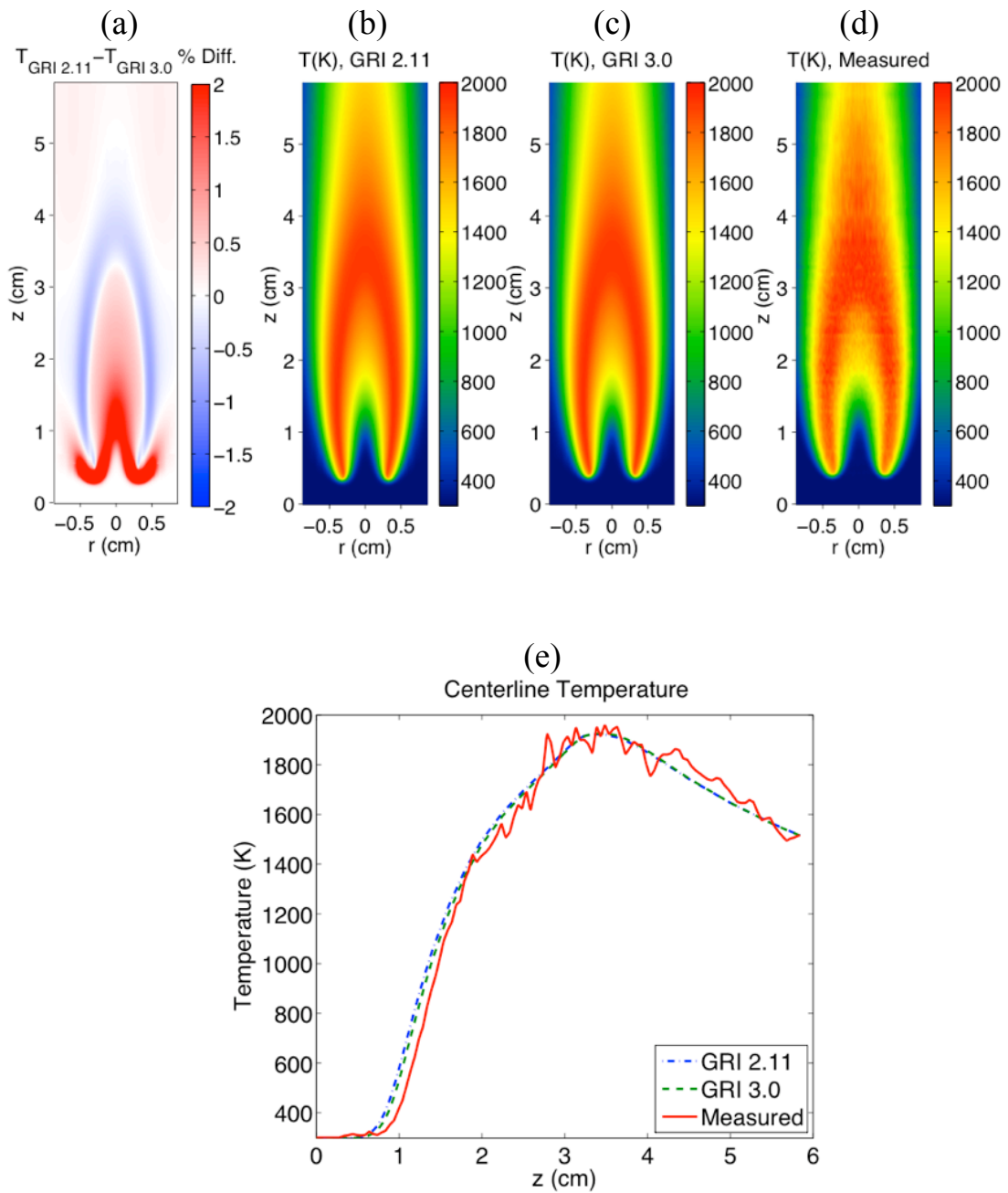
Figure 5.2.7: (a) Percent difference (relative to the maximum values of GRI 2.11) in temperature computed with GRI 2.11 and GRI 3.0. The main cause of differences in temperature is a slight variation in lift-off height calculated using the two different mechanisms. (b) Temperature computed with GRI 2.11. (c) Temperature computed with GRI 3.0. (d) Temperature measured with Rayleigh scattering. (e) Centerline temperatures from GRI 2.11, GRI 3.0, and measurements.

smaller than what is observed here.

The computed NO fluorescence signals are compared with the measured signal in Fig. 5.2.8. A direct comparison can be made between the computed and measured signals using a calibration gas of known composition both experimentally and computationally (46 ppm NO in a balance of N_2 for these experiments). The features that were observed in the mole fraction comparison are evident in the comparison of fluorescence signals, and the same conclusions can be reached. Specifically, the computed fluorescence signal derived from the simulation using GRI 2.11 is consistently less than the measured fluorescence signal, while the computed signal using GRI 3.0 agrees reasonably well on the fuel side of the flame front below 2.5 cm, then increases to levels significantly greater than the measurements in the region above the flame. This approach of comparing the signals, not the mole fractions, has the advantage that the comparison involves data containing less uncertainty (due to both noise and possible systematic errors in the measurements) than the traditional approach, and the comparison can be made with a single measurement of the NO fluorescence.

The results of this analysis are important to note when applying the concept of comparing signals. This approach was applied in Section 3.5 where the relationship of NO and soot was examined by adding NO_x chemistry (GRI 2.11) to the previously studied soot model [Smooke 2005]. The presence of soot in these flames makes many common diagnostic techniques extremely difficult, and makes it impossible to perform the quenching calculations necessary to determine minor species mole fractions from measured LIF signals. In this setting, the concept of comparing computed and measured signals is very valuable and a necessity.
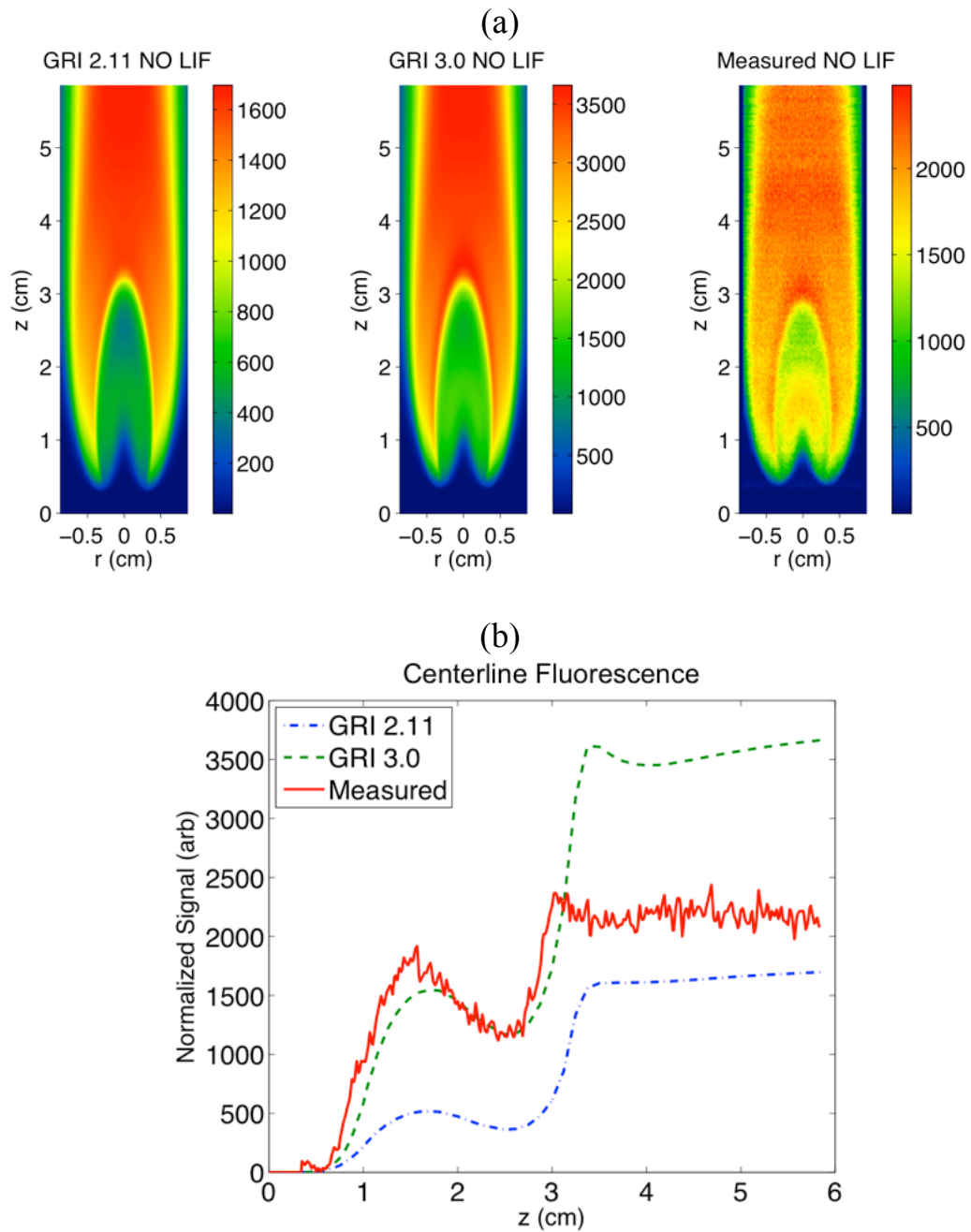
Figure 5.2.8: (a) Comparison of the computed and measured fluorescence signals. The computed signals are derived from the numerical simulations using GRI 2.11 and GRI 3.0, and the measured signal comes from NO LIF. (b) The centerline NO fluorescence signals are plotted on the right.

5.3   Luminosity Images of Two Sooting Laminar Flames

The computational model for the sooting flames examined in Section 3.4.1 includes a soot submodel, as described in Section 3.2.2 and in [Smooke 2005]. Testing the soot submodel in the traditional way involves comparing soot volume fractions – an output of the simulations – with measured soot volume fractions. The latter have been determined via multiple experimental techniques, providing a consistency check and helping improve confidence in each individual measurement. In one experiment (detailed in Section 3.4), laser extinction measurements are coupled with laser-induced incandescence (LII) measurements to obtain calibrated two-dimensional soot volume fraction images [Smooke 2005]. In a separate experiment (detailed in Section 3.3), two-color optical pyrometry [Levendis 1992; Cignoli 2001] using a color digital camera (Nikon D70) is used to determine soot surface temperatures and soot volume fractions. The camera has been calibrated using two independent techniques: characterization of the camera's color filter array (CFA) and a blackbody calibration. The pyrometry measurement technique requires application of a tomographic inversion to the line-of-sight emission images [Dasch 1992], which is known to add error to the radial profile [Walsh 2000b], and then further calibration-dependent calculations, all of which are sources of error. Signal ratios between the separate color images are then taken using the relatively noisy radial profiles to calculate temperatures, further increasing the noise level. Consequently, temperature and soot volume fraction fields determined using pyrometry contain a kind of pixilated noise, which worsens as the flame centerline is approached. Despite this noise, soot pyrometry and LII measurements of peak soot

196

volume fractions, as well as variations in the soot volume fraction across the target

flames, show excellent agreement (see Figure 5.3.1).

To facilitate comparison, the soot volume fraction images from the computations

and LII measurements from Section 3.4.1 are plotted side-by-side for the 40% flame in

Figure 5.3.2a and the 80% flame in Figure 5.3.2b. Observations were made in Section

3.4.1 that for both flames the computed soot region is larger, particularly in the case of

the 40% flame. For the 80% flame, both the computed and measured soot regions peak

on the wings, while the computed soot region extends farther down and the shape at the

flame tip is different. Quantitative comparison between the experiment and computations

for the 80% flame is favorable, as the computed soot volume fraction peak is only

slightly higher. For the 40% flame, the computed soot volume fraction is substantially

higher (by a factor of 2.4) and peaks on the wings, while the measured soot is shown to

peak on the centerline. While these comparisons of soot volume fraction are valuable, it

is possible to come to many of the same conclusions using a much simpler comparison.
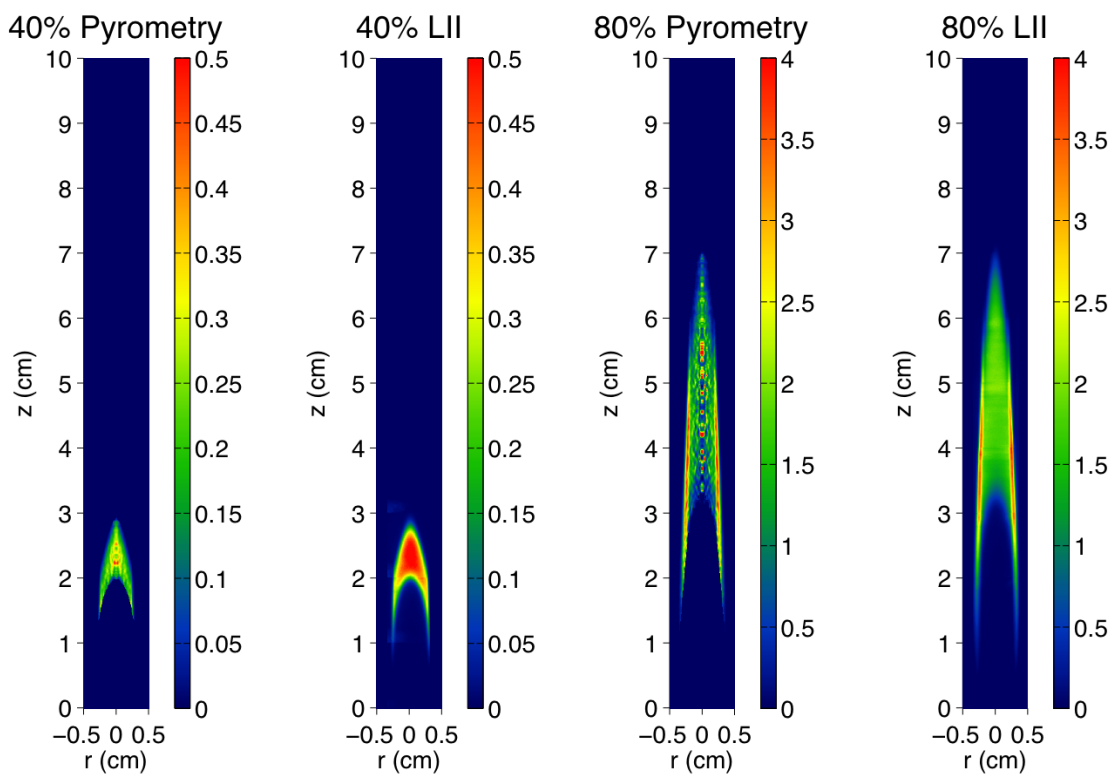
Figure 5.3.1: Soot volume fractions measured using pyrometry and LII from a moderately sooting flame (40% C_2H_4 / 60% N_2) and a more heavily sooting flame (80% C_2H_4 / 20% N_2). Overall agreement is good, but the pyrometry data suffers from considerable noise along the centerline due to the Abel inversion required to transform the line of sight data into a two-dimensional profile. Please note that K_{ext}=8.6 here.
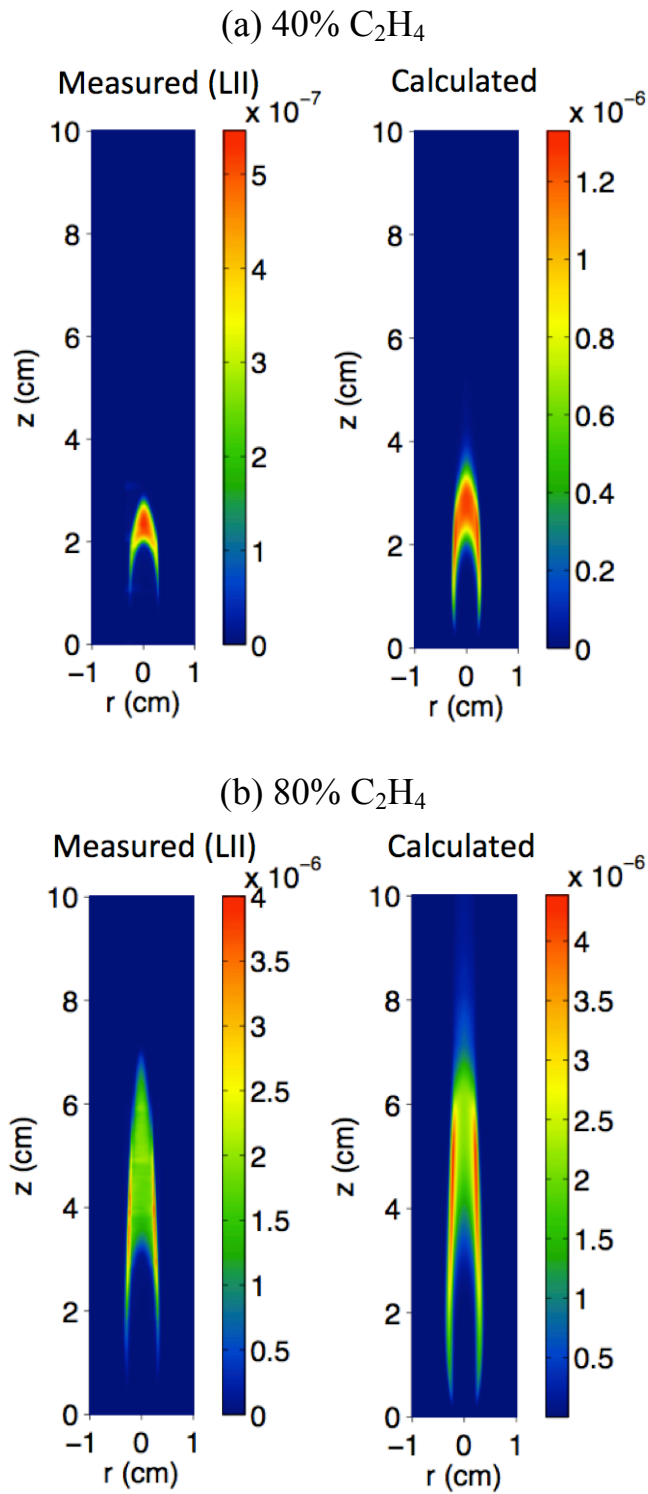
(a) 40% C_2H_4

(b) 80% C_2H_4

Figure 5.3.2: Measured (using LII) and computed soot volume fractions for (a) the 40% C_2H_4 flame and (b) the 80% C_2H_4 flame.

It is possible to compare measurements and computations by using line-of-sight emission as the point of comparison. From the simulations for each flame, the computed flame luminosity can be derived as follows. The computed two-dimensional soot profiles and temperature fields are combined with Planck's law to get an intensity distribution as a function of wavelength (see Figure 5.3.3). This intensity distribution is then convolved with the measured CFA profiles for the red, green, and blue filters used in the digital camera (see Figure 3.3.5). In addition to the soot luminosity, chemiluminescence from CH* is an important contributor to the overall visible flame emission. Since the chemical mechanism used here does not include CH* chemistry, the spatial distribution of CH is used as a surrogate for CH*. While these are entirely different chemical species, it has been shown that, at the base of the flame where the CH* luminosity is greatest, the two species are spatially coincident [Walsh 1998]. Figure 5.3.4a shows the simulated CH* profile.

The integrated two-dimensional intensity distributions are rotated about the symmetry axis to obtain the three-dimensional intensity distribution, as shown in Figure 5.3.4b for the simulated CH*. The three-dimensional intensity distribution is then projected onto the image plane using the geometry of the camera system used to take experimental images. The camera is approximated using a pinhole geometry, with the pinhole at the location of the camera lens. The simulated CH* luminosity is added to the blue image channel using an empirical scaling constant and the computed luminosity images can then be compared with images taken with the digital camera. If the appropriate reactions are added to the computations, CH* can be computed directly, eliminating the need for the arbitrary scale factor.
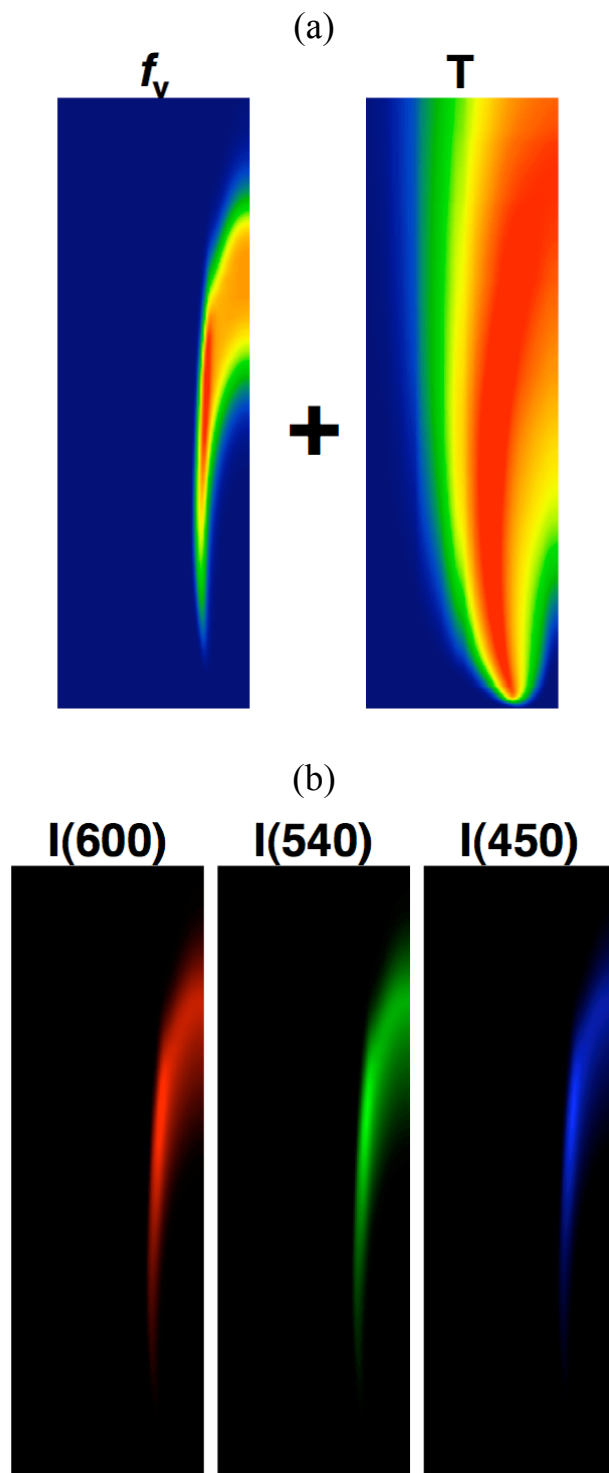
Figure 5.3.3: The (a) computed soot volume fraction and temperature can be used with Planck's Law to (b) calculate the soot luminosity at different wavelengths. The resulting spectrum is convolved with the measured color filter array of the digital camera.

(a)   (b)
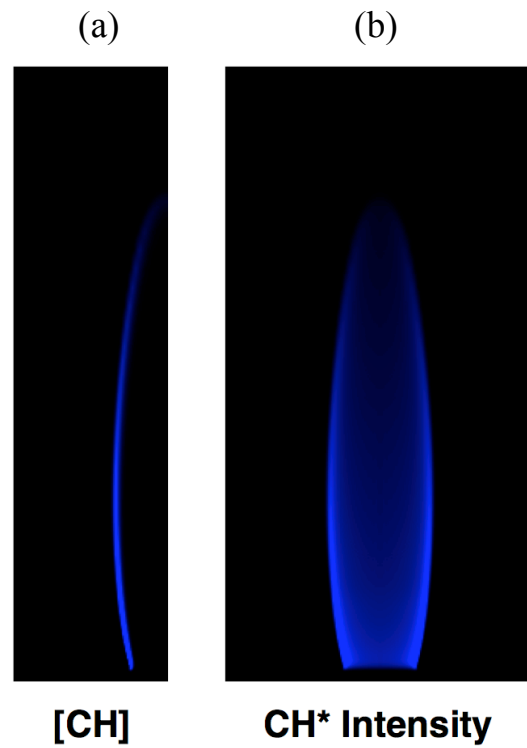
[CH]   **CH* Intensity**

Figure 5.3.4: (a) The calculated spatial distribution of *CH* is used to simulate chemiluminescence from *CH** at the base of the flame. (b) The integrated intensity distributions are rotated about the symmetry axis to obtain the 3D intensity distribution. The 3D intensity distribution is projected onto the image plane using the geometry of the camera.

The above approach can be used to compare luminosity data from the 40% and

80% C_2H_4 flames. Figure 5.3.5a plots the results for the 80% flame. Here the maximum

intensity has been normalized to one. A centerline plot comparing the image intensities is

shown in Figure 5.3.5b for the red, green and blue channels separately. Figure 5.3.6 plots

the same results for the 40% flame, where the intensity has been normalized with respect

to the 80% flame. By comparing the digital camera photos – the output of a very simple

diagnostic technique – with the computed luminosity images, it is already possible to

draw some conclusions. The computed 40% C_2H_4 flame shows a significantly taller area

of soot than the camera image, with the distribution of the most intense regions of

luminosity more heavily located on the wings of the flame. The computed 80% C_2H_4

flame shows a wider area of soot that extends further down than the camera image, with

the more intense regions covering a larger portion of the flame. These are all

observations that have been made above when comparing computed soot volume

fractions with the more complicated LII technique, as well as with pyrometry

measurements. Specifically, the computed soot volume fraction (0.85 maximum) has

been observed to be greater than the measured value (0.36 maximum) for the 40% C_2H_4

flame by a factor of 2.4, with the calculated soot peaking on the wings and the measured

soot peaking on the centerline. Also, the calculated soot region has been observed to

occupy a larger area, with sooting regions extending further down for both the 40% and

80% C_2H_4 flames.
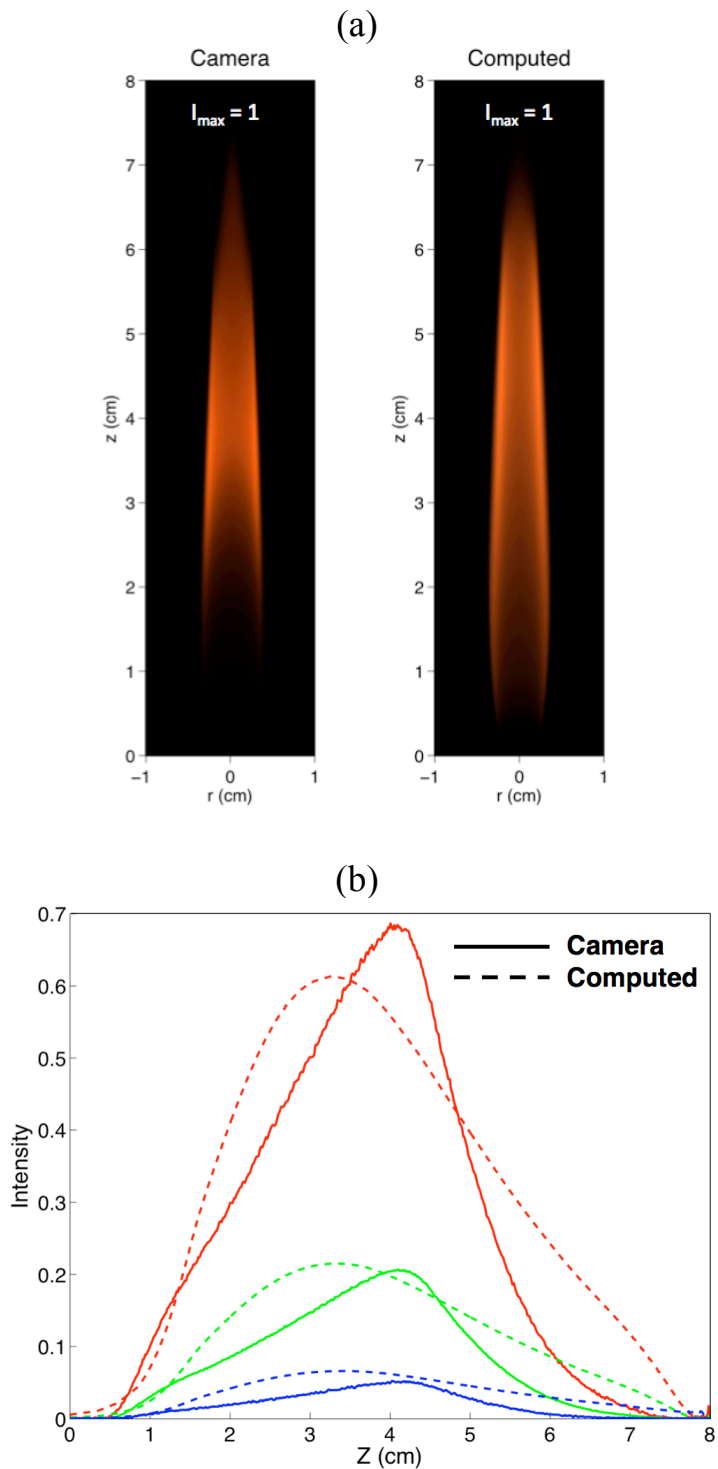
Figure 5.3.5: (a) Comparison of luminosity "images" for the 80% C_2H_4 flame. The intensity scale has been normalized to one for both the camera and computed images. (b) Centerline plot of the luminosity images for the red, green and blue channels.

(a)

(b)
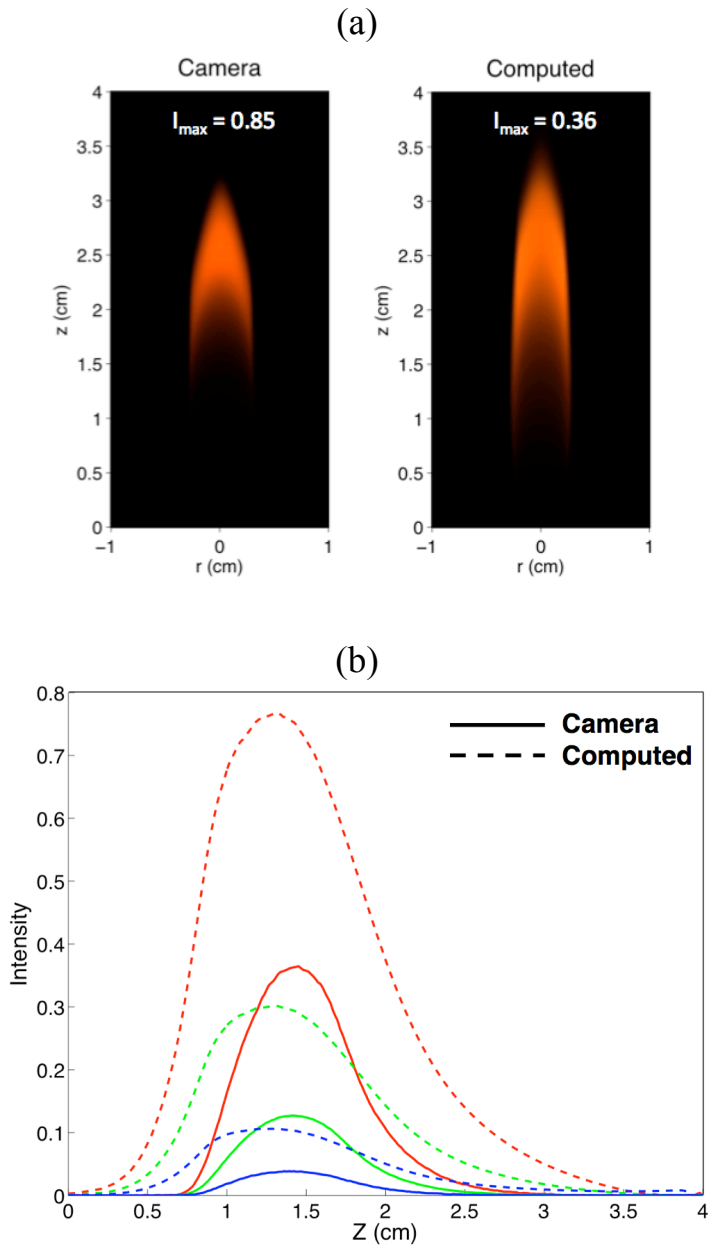
Figure 5.3.6: (a) Comparison of luminosity "images" for the 40% C2H4 flame. The intensity scale has been normalized with respect to the maximum of the 80% flame. (b) Centerline plot of the luminosity images for the red, green and blue channels.

It is apparent that the flame images in Figures 5.3.5 and 5.3.6 do not have the appearance one would expect from a sooting flame. That is because care was taken to not to saturate any of the channels in order to obtain quantitative data. The blackbody spectrum is heavily weighted to the red at flame temperatures. Figure 5.3.7 re-plots the computed and camera flame images with the red and green components partially saturated to look more like standard photographs, which often saturate the most intense parts of an image to simulate human visual response. The comparison of the 40% C_2H_4 flame in the lower left of the figure is even more heavily saturated, resulting in images that more closely resemble what is observed when viewing this flame by eye.

Regardless of whether traditional (e.g., LII or pyrometry) or non-traditional methods of comparison are used, the largest source of error in a majority of techniques used to determine sooting characteristics relates to the optical properties of the soot. As discussed earlier, the values of the soot absorption function, $E(m)$, and the dimensionless extinction coefficient, K_{ext}, are known to vary by as much as 20%. Both quantities are difficult to determine, in part because they depend upon the soot's properties (e.g., primary particle size, aggregate size), which vary with the fuel used and the exact location within each flame. Since it is impractical to measure K_{ext} independently for all flame cross sections, an average value is used to determine the soot volume fraction using both pyrometry and LII, and in the determination of the radiation field in the numerical simulations. Clearly, this constant value of K_{ext} is not entirely accurate, particularly near the burner exit, but it is at the very least consistent across all determinations of sooting characteristics.
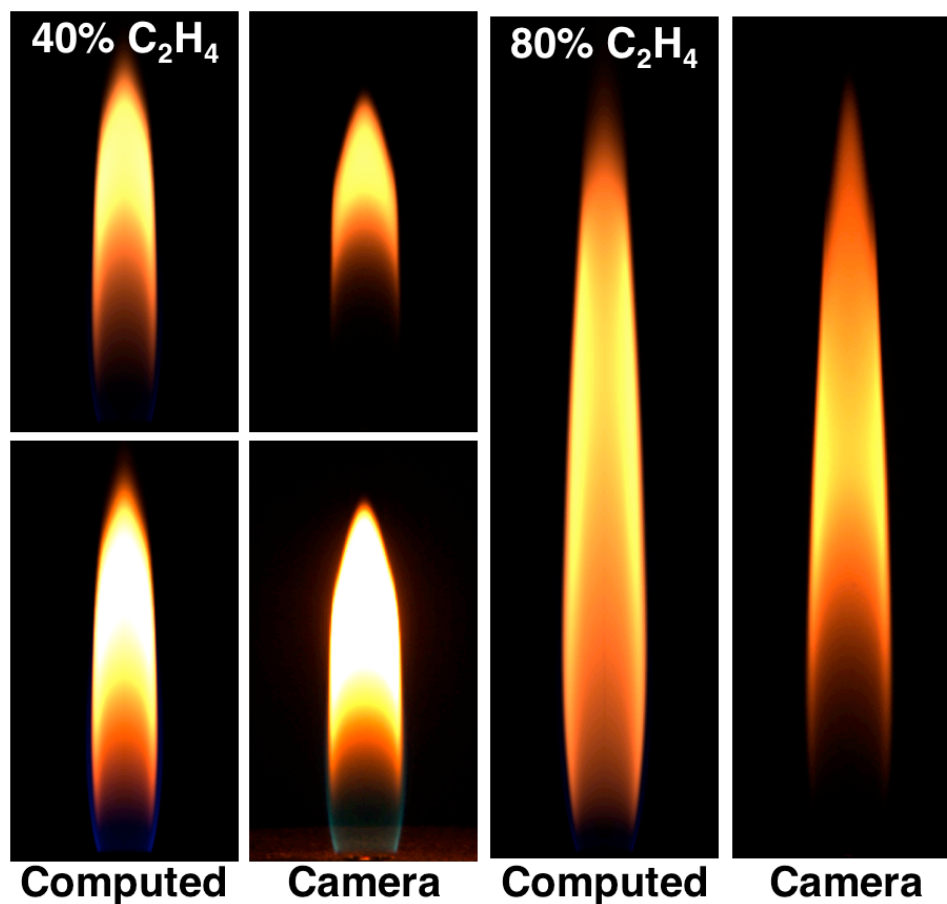
Figure 5.3.7: Comparison of the computed and measured (camera) flame luminosity images for the moderately sooting flame (40% C_2H_4/60% N_2) and the heavily sooting flame (80% C_2H_4/20% N_2). In the upper leftmost and rightmost pairs of images, the red and green components are partially saturated to look more like standard photographs, which often saturate the most intense parts of an image to stimulate the response of the eye. In the lower leftmost pair of images, the red and green components are heavily saturated.

5.4   Improving Computations for Real Fuels

Practical combustion systems generally operate under unsteady and often turbulent conditions and burn complex fuels that are not well understood. As the simplified systems are becoming better understood, research applications are moving towards more complex configurations by increasing the flow complexity and the detail of the chemical model. Chapter 4 presented an investigation where a periodic perturbation was applied to well-characterized steady flames in an effort to study flames that more closely exemplify features that are seen in practical systems. In this study, a better understanding is sought of the combustion of real, more complex fuels such as JP-8 (and its surrogates), gasoline and dodecane. To study this case, computational and experimental approaches need to be adapted to study the larger molecules that can be found in realistic combustion systems. Existing chemical mechanisms will need to be expanded to include a larger set of molecules and improved to provide suitable agreement with experimental efforts. New experimental approaches will need to be developed to quantify the larger molecules that are present in these systems. The investigation presented here is part of a current study involving more realistic (and thus complex) fuels.

5.4.1   Computational Approach

Computations for this study were carried out by Luca Tosatto in Professor Mitchell Smooke's group. The simulations are obtained using a fully implicit parallel Newton solver. A pseudo-time stepping technique is used to aid convergence for an arbitrary initial condition. The large dimension of the mechanism (224 species, 4092 reactions) makes the simulation impossible on one CPU. The total memory requirement

is up to 80 GB to allocate the Jacobian matrix for solution. Extensive parallel computation is required to bring memory requirements and computational time within a reasonable range. A checkerboard decomposition of the grid was used to split the problem among the 64 CPUs utilized. MPI was used to broadcast the necessary information (thermodynamic variables, rate of formation, diffusion coefficients, etc.) during Jacobian assembly. A distributed GMRES algorithm was used to resolve the large linear system in a fast and reliable way.

The implementation of this computational model, which is intended for the simulation of JP-8 and JP-8 surrogate flames, is applied to a series of C_2H_4 laminar diffusion flames. Simulations are performed on flames ranging from nonsooting to sooting. Though the computations do not yet include a soot model, they do consider a wide range of PAH molecules. The computational results are analyzed to determine most prevalent contributions from PAHs to determine which molecules are of the most interest.

5.4.2 Experimental Approach

Detailed experimental investigations into PAH formation are not well developed, particularly those that seek to determine quantitative information on the molecules using species specificity. A novel approach is presented by Aizawa *et al*. [Aizawa 2003; Aizawa 2004; Aizawa 2008], where an Excitation-Emission Matrix (EEM) is defined for PAH molecules. A "rainbow laser" consisting of laser light that is generated using a Raman cell frequency converter that is pumped with a Nd:YAG laser is used to excite the PAH fluorescence and the spectrally-resolved fluorescence is then detected. Both the characteristic emission and excitation wavelengths of PAH molecules with different

numbers of rings are shown to have a wavelength dependence that increases with an increase in the number of rings. Further, data taken in a butane diffusion flame shows an evolution of the emission and excitation wavelengths towards longer wavelengths as the height above the burner is increased, thus indicating that larger molecules are formed as the height above the burner is increased. Similarly, a study by Kobayashi *et al.* [Kobayashi 2008] demonstrates that a correlation exists between the number of carbon atoms in the molecule and the maximum emission wavelength. They show that the location of the peak of the fluorescence signal moves towards longer wavelengths as the height above the burner is increased, indicating a growth in the average size of the molecules.

Using this information, spatially and spectrally-resolved PAH fluorescence data should be able to provide information on PAH location, as well as qualitative information on average PAH size as molecules grow towards soot inception. Combining the information in [Aizawa 2004] and [Kobayashi 2008] with data on PAH fluorescence spectra in [Berlman 1971], a table of emission and excitation ranges for PAH molecules of interest was compiled (see Figure 5.4.1). The data contained in this table can then be used to determine the qualitative location of PAH molecules, as a function of molecule size, for our flames of interest.

5.4.3   Experimental Setup

The experimental setup is shown in Figure 5.4.2. The third and fourth harmonics of a Nd:YAG laser (Continuum PL8010, ~10 ns pulse width at 10 Hz and 355 nm / 266 nm) are used to excite PAH fluorescence in a set of ethylene diffusion flames. A 50 cm focal length quartz lens is used to focus the UV beam across the diffusion flame.
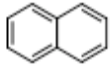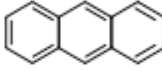
Chemical Compound	Number of Carbons	Number of Rings	Excitation Range	Emission Range	Range Used
Benzene (C_6H_6)	6	1	230 - 270 nm	270 - 320 nm	280 - 300 nm
Naphthalene ($C_{10}H_8$)	10	2	240 - 295 nm	310 - 380 nm	330 - 350 nm
Pyrene ($C_{16}H_{10}$)	16	4	290 - 350 nm	360 - 430 nm	385 - 405 nm
Anthracene ($C_{14}H_{10}$)	14	3	360 - 440 nm	410 - 475 nm	410 - 428 nm
Coronene ($C_{24}H_{12}$)	24	6	360 - 440 nm	425 - 475 nm	440 - 457 nm

Figure 5.4.1: Table of PAH molecules important in the combustion process. The number of carbon atoms, number of rings, excitation range, emission range and the emission range used in this study are tabulated.

211
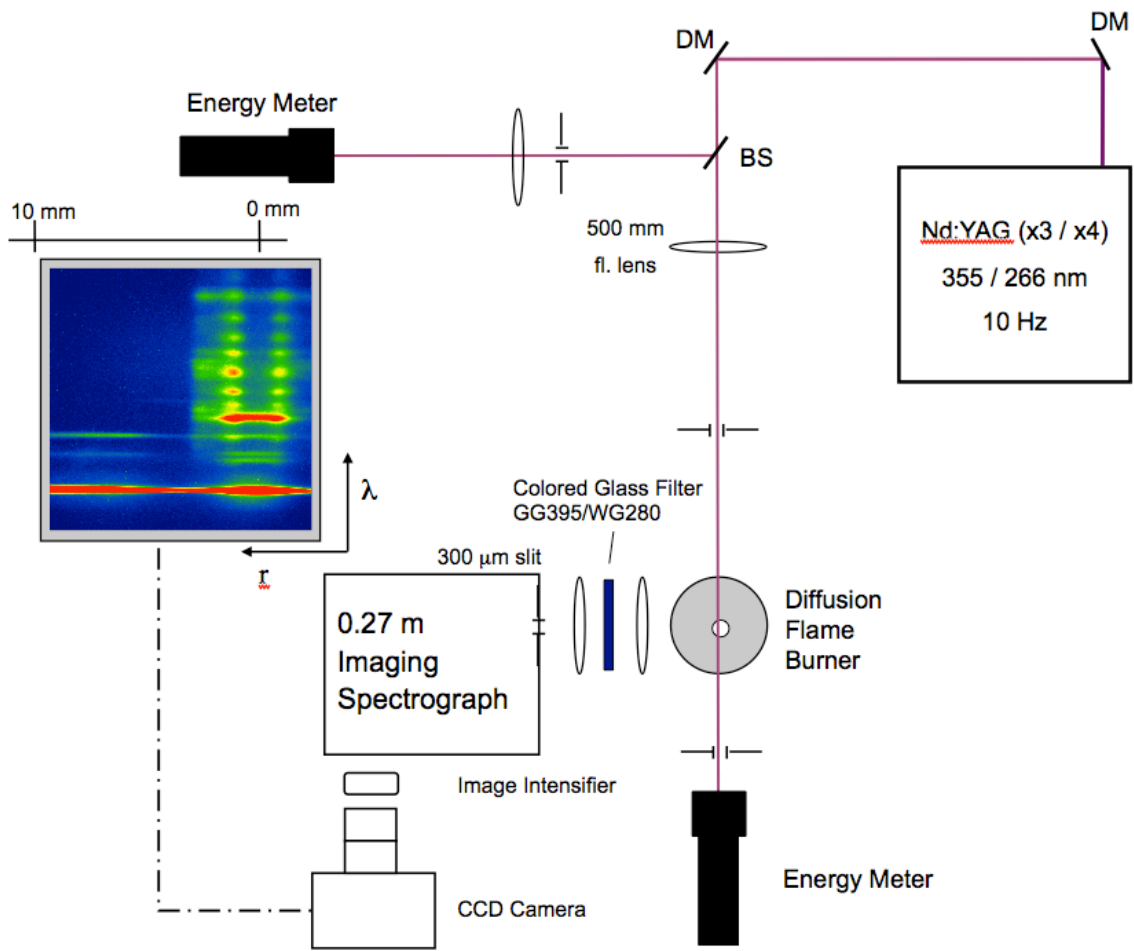
Figure 5.4.2: Experimental layout used to measure PAH fluorescence.

To ensure that the fluorescence is in the linear regime, with no partial saturation, the measurements are made 5 cm before the focus of the UV beam, resulting in a beam diameter of roughly 0.5 mm in the measurement region. The laser energy is monitored both on and off the diffusion flame beam path using a pair of pyroelectric energy meters (LaserProbe RjP-734) connected to a digital oscilloscope. Though the fluorescence never approached the saturation limit, a relatively low laser energy (~135 mJ at 355 nm and ~50 mJ at 266 mJ) had to be used in order to avoid dielectric breakdown of the air and ethylene gases, which would otherwise cause a broadband background interference and flickering of the flame.

PAH fluorescence in the diffusion flame is imaged onto a 300-µm entrance slit of a spectrograph (SPEX 270M) using a UV camera lens (UV-Nikkor 105 mm, f/4.5) and a 10 cm focal length quartz lens. A colored glass filter (Corning GG395 at 355 nm, and WG280 at 266 nm) is placed between the two collection lenses to suppress the Rayleigh scattering by the soot, which would otherwise saturate the detector. The fluorescence is dispersed with a 300 groove/mm grating (250 nm blaze angle) and imaged with an intensified CCD detector (a gated Gen II intensifier optically coupled to a Princeton Instruments TE/CCD-512 CCD). The CCD image contains information in one spatial and one spectral dimension. Spatially, a 10-mm window is imaged radially extending from slightly downstream of the flame centerline, outward upstream of the direction of laser propagation. Spectrally the region from 350 – 480 nm is recorded for 355 nm excitation and from 260 – 480 nm for 266 nm excitation. The spectral region includes Rayleigh scattering, a number of Raman lines, formaldehyde fluorescence (when using 355 nm excitation), soot interferences and PAH fluorescence. The signal is integrated on the

detector for 12.8 seconds (128 laser pulses), chosen to correspond to event sampling on the oscilloscope. The experiment is controlled through a computer, which records synchronized data from the CCD camera and the digital oscilloscope.

The final fluorescence images are obtained by summing the fluorescence intensity over various 20 nm spectral regions, chosen to target a molecule of interest. Two-dimensional images of the fluorescence distributions are created by tiling together a series of spatial/spectral images recorded at 0.25-mm intervals from 1 to 30 mm above the burner. Each image is corrected for detector background, normalized by the recorded laser energy, and corrected for nonuniform detector gain and optical throughput. Figure 5.4.3 plots fluorescence (and interference) images obtained using 266 nm excitation for a series of 5-nm spectral detection windows, centered on the wavelength that is indicated. The wavelength range used to indicate each representative molecule (benzene, naphthalene, pyrene and coronene) is demonstrated by the color-coded legend on the bottom of the figure. The red numbers represent interferences from C_2 (and some C_3) fluorescence [Bengtsson 1990; Bengtsson 1995].

5.4.4 Computational and Experimental Results

This study looked at a range of C_2H_4 flames that ranged from barely sooting to lightly sooting (20%, 24%, 28% and 32% C_2H_4, in a balance of N_2, see Figure 5.4.4 for images of flame luminosity). As the fuel mole fraction was increased the soot loading increased, resulting in more interferences from the soot.

Computed mole fractions of the representative PAH molecules chosen (benzene, naphthalene, pyrene and coronene) are converted to number density for more direct comparison with experimental PAH fluorescence. Unfortunately, fluorescence of PAH
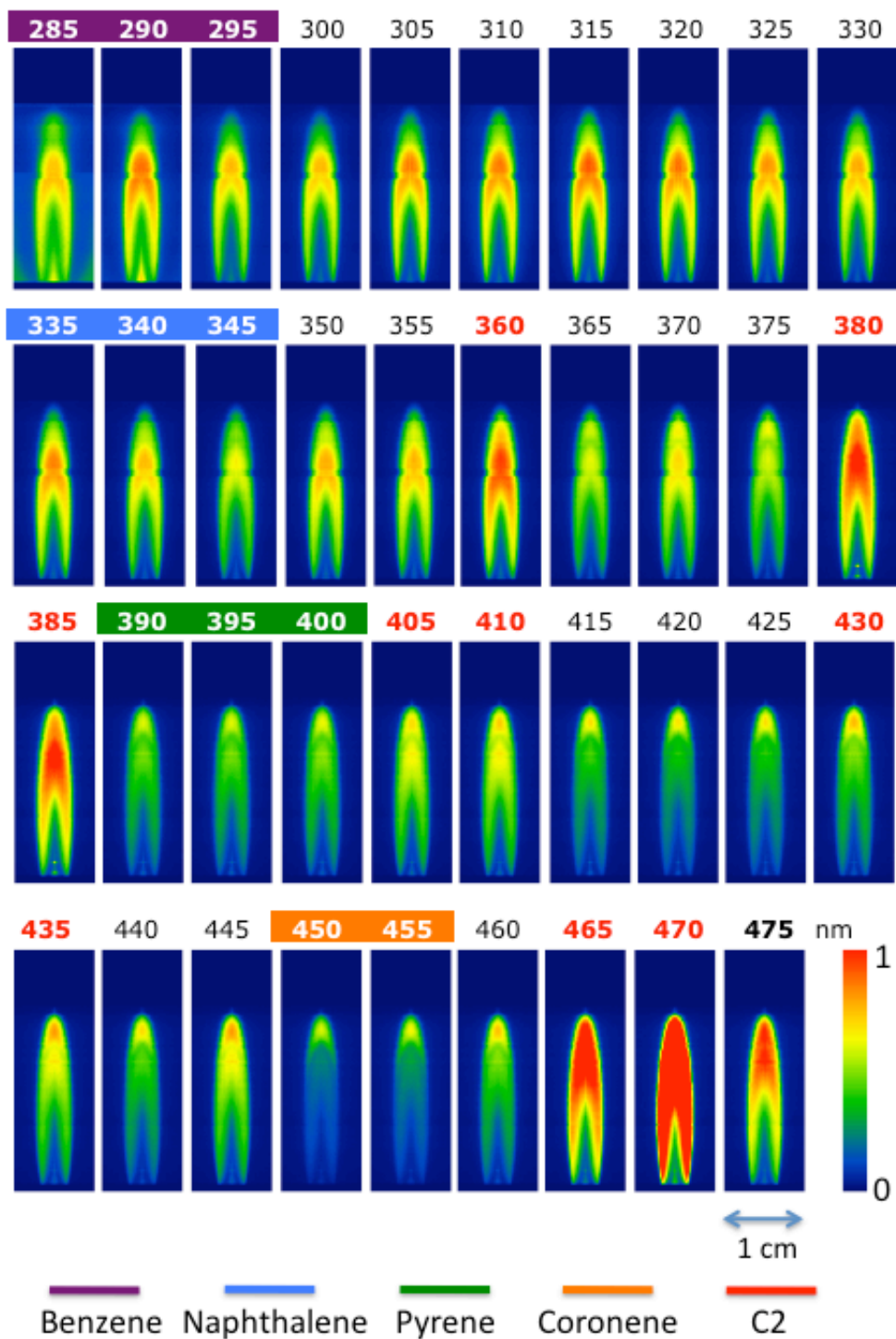
Figure 5.4.3: Detected PAH fluorescence in a 28% C_2H_4 flame. Each panel is integrated over a 5 nm window, centered on the wavelength indicated. The wavelength range used to indicate each representative model is demonstrated by the color-coded legend on the bottom. Red numbers represent interferences from C_2 (as well as some C_3 at the longer wavelengths).

3 cm

20%   24%   28%   32%

Increasing fuel mole fraction and soot loading
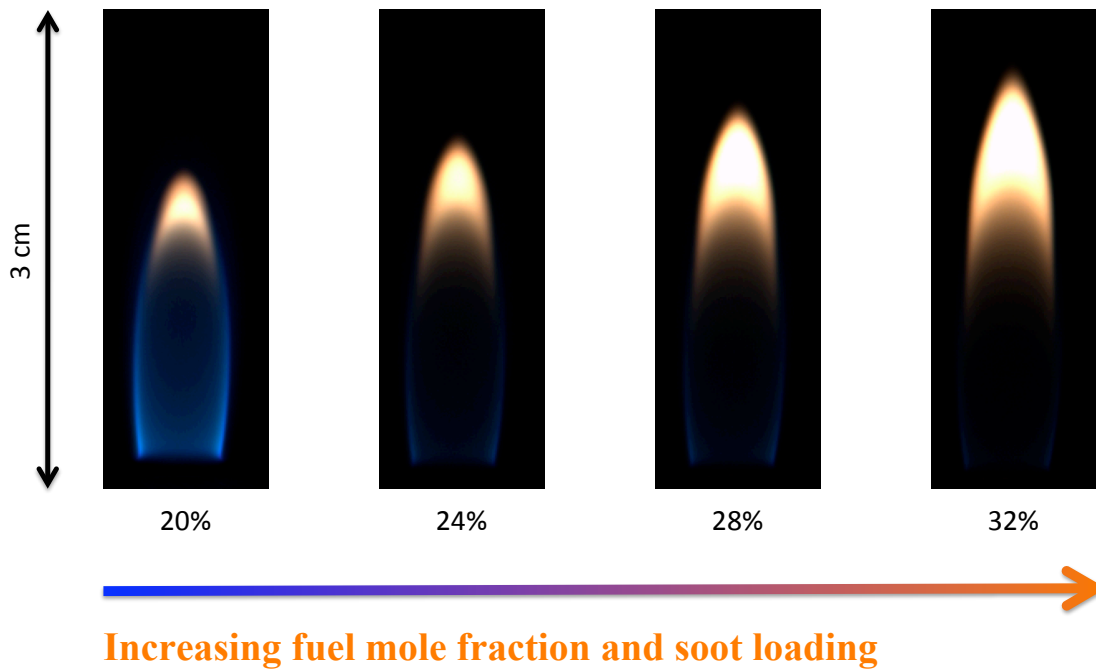
Figure 5.4.4: Digital camera images of flame luminosity for a range of C_2H_4 flames that range from barely sooting to moderately sooting.

molecules is not well understood, as the quenching and Boltzmann corrections necessary to provide quantitative comparisons are not available. The final computed number density and measured fluorescence images are plotted in Figures 5.4.5 – 5.4.8 for the 20%, 24%, 28% and 32% flames, respectively. The panels are arranged so that the molecule size increases as one moves from left to right (benzene to coronene).

Calculations indicate that as PAH size increases, spatial distributions move from the wings to the centerline, with larger PAH species extending farther downstream. This variation in spatial distribution for increasing molecule size becomes more extreme as the fuel mole fraction is increased. The persistence of coronene for regions far downstream is unphysical and can be attributed to the fact that there is no soot model, and that coronene is the largest molecule computed. Experimentally, different spectral bands were integrated to generate fluorescence signals representative of the different size PAH species. The same qualitative features that were observed computationally are also observed experimentally, though the spatial variation for the different spectral bands was not as extreme. A particularly interesting feature of the computational results is the double-peak feature in the pyrene profile on the flame centerline. Initially, this feature seemed as though it was an artifact of the calculations. However, that double-peak feature is repeated in the experimental results, where it occurs in the coronene profile for the 20% flame, the pyrene profile for the 24% flame, the naphthalene profile for the 28% flame and the benzene profile for the 32% flame. Due to interferences from C_2, C_3 and soot, it is difficult to discern whether this feature is in fact due solely from PAH fluorescence, particularly in the case of the 32% flame where soot interferences become overwhelming.
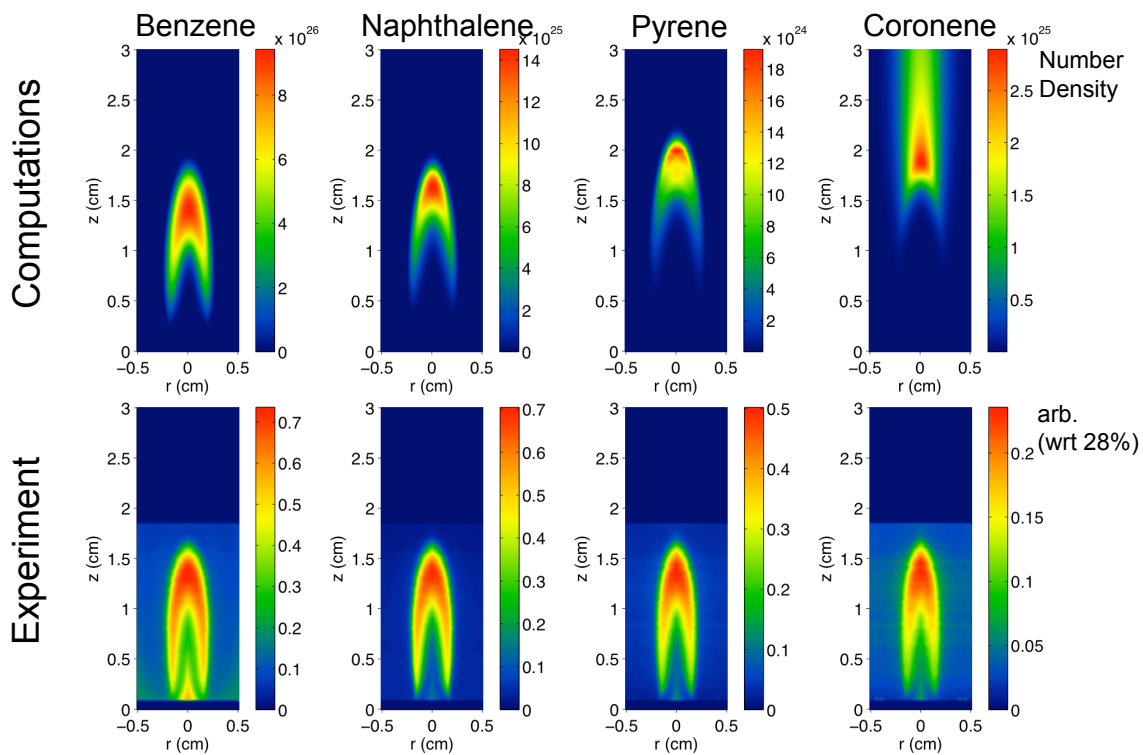
Figure 5.4.5: Computational PAH number density and experimental PAH fluorescence for a 20% C_2H_4 flame. The computational and experimental results are divided into representative molecules (benzene, naphthalene, pyrene and coronene). Each panel in the experimental results is normalized with respect to equivalent panel in the 28% flame.
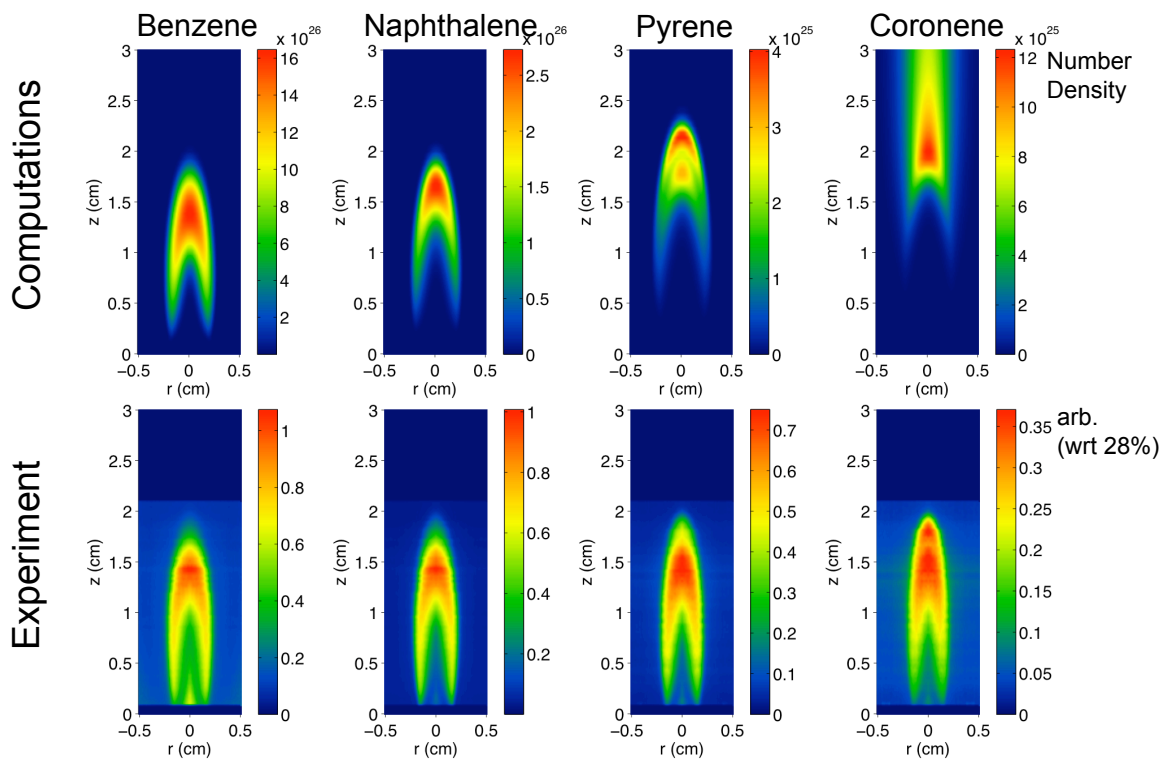
Figure 5.4.6: Computational PAH number density and experimental PAH fluorescence for a 24% C_2H_4 flame. The computational and experimental results are divided into representative molecules (benzene, naphthalene, pyrene and coronene). Each panel in the experimental results is normalized with respect to equivalent panel in the 28% flame.
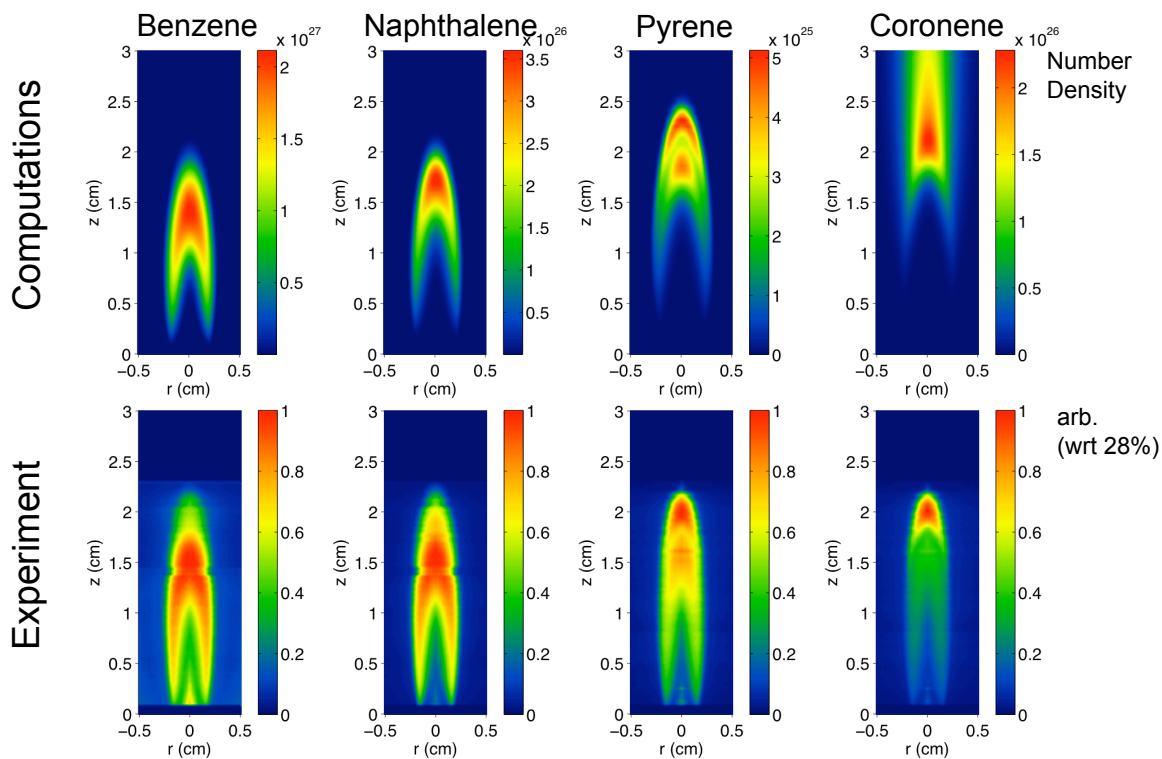
Figure 5.4.7: Computational PAH number density and experimental PAH fluorescence for a 28% C_2H_4 flame. The computational and experimental results are divided into representative molecules (benzene, naphthalene, pyrene and coronene). Each panel in the experimental results is normalized unity.
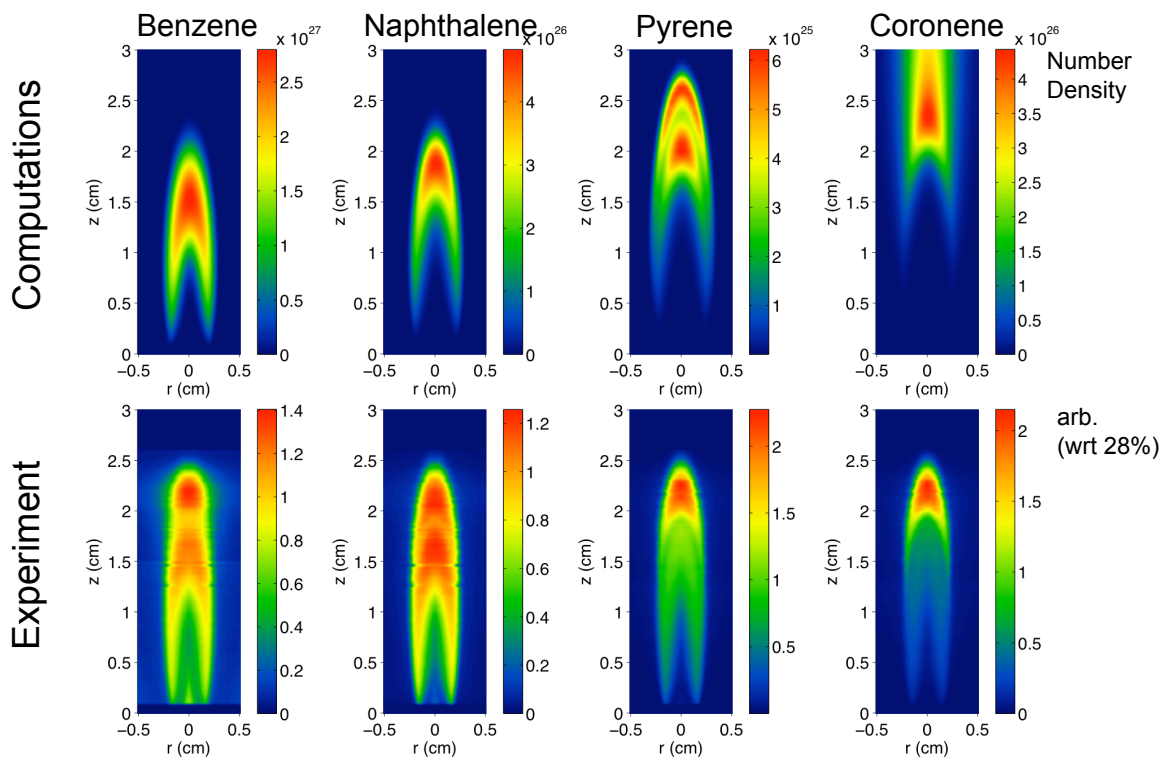
Figure 5.4.8: Computational PAH number density and experimental PAH fluorescence for a 32% C_2H_4 flame. The computational and experimental results are divided into representative molecules (benzene, naphthalene, pyrene and coronene). Each panel in the experimental results is normalized with respect to equivalent panel in the 28% flame.

In the other flames, however, this feature is not represented in the neighboring spectral windows, which would be expected if the source were a broadband interference.

5.4.5   Discussion of Results

Zero order comparisons between measured PAH fluorescence and calculated PAH number density show qualitative agreement, but interferences, particularly from sooting regions, are not accounted for. Further, there is no soot model in the current computations that might otherwise allow for the simulation of these interferences. Consequently, a short-term goal of this study involves incorporating the soot model into the complex chemistry used in these calculations. Currently, computational models include levels of chemical detail that present significant challenges to the diagnostics community. Much more detailed models of the fluorescence and interference will be required for quantitative comparisons in the future. Molecular sampling techniques may be needed to provide calibration data. Still, the available data can be used to fine-tune the appropriate detection bands used to represent various sizes of PAH species and begin to provide feedback for the computational efforts. Currently, a JP8 coflow diffusion flame burner is under construction for future investigations. Use of a more complex fuel will provide the sufficiently large PAH molecules necessary to detect a fluorescence signal, but the fuel concentrations can be modified to provide a nonsooting case for study. Eliminating soot from the problem at this early stage will eliminate uncertainties that are due to soot interferences.

As our need for fuels evolves, it is important to be able to predict the behavior of a wide range of fuels. A primary goal of the computational model is to simulate real fuels interchangeably. The size of the problem requires automated mechanism reduction

depending on input fuels, and the comparison of results from a relatively simple configuration should enable more transparent analysis of approaches to the mechanism reduction. Once refinements are made to the experimental and computational approach, it is anticipated that the results will have a basis for improving future soot formation models and can help improve the understanding of the combustion of real fuels that contain many of the large molecules that are of interest here. Ultimately, a better understanding of these problems can be applied to realistic combustion systems in an effort to minimize pollutants and greenhouse gases and to improve fuel efficiencies even as the fuels themselves become more diverse and complex.

5.5   Conclusions

Three examples of comparing measured and calculated signals have been presented: NO laser-induced fluorescence (LIF) in a non-sooting diffusion flame, luminosity images of sooting diffusion flames, and PAH fluorescence in nonsooting to lightly sooting flames. In all cases, the goal has been to compare computations and experiments by looking at computed and measured signals. This approach lends itself to simpler experiments requiring fewer measurements, resulting in shorter turnaround times for the comparisons. Additionally, the simpler experimental approaches show better signal-to-noise ratios, leading to reduced uncertainties.

The concept of comparing computed and measured signals becomes even more important in sooting flames, because the presence of soot makes many common diagnostic techniques extremely difficult. This approach is also important in turbulent flames, where the simultaneous measurement of a sufficient number of quantities may not be possible, and has the potential to be applied to a number of different measurement

techniques other than those described here, including Rayleigh scattering, Raman scattering, and chemiluminescence images. Experimentalists should take the various experimental issues into account when determining the best way to make a direct comparison with numerical simulations. Specifically, as was demonstrated in Section 5.4, it is essential to possess a detailed understanding of the factors that contribute to signal generation if quantitative results are desired. In many cases, a simpler experiment of comparing measured and computed signals may provide as much information as more complex experiments, with less uncertainty.

CHAPTER 6

6 Conclusions and Direction for Future Work

A coupled experimental and computational study has been presented for a series
of nonsooting and sooting, steady and time-varying, laminar coflow diffusion flames. The
goal of this ongoing investigation is to improve our understanding of combustion
systems, and the specific processes responsible for the production of pollutants such as
soot and NO_x.

Experimental soot volume fractions were determined using two-dimensional
laser-induced incandescence (LII), and by soot pyrometry using a consumer digital
camera. It was seen computationally and experimentally that as the fuel mole fraction
was increased the peak soot migrated from the centerline of the flame to the wings.
Refinements will need to be made to the soot model to improve agreement of trends in
peak soot volume fraction and spatial distribution. Application of a two-color LII
measurement to the studied flames should provide added confidence in the results
presented here.

Measurements of soot particle size distributions were made using two-
dimensional time-resolved LII (TR-LII). The computations were seen predict both larger
particles overall and on the centerline, relative to the wings, suggesting that the artificial
cutoff of surface growth at 25 nm employed in the computations should be revisited.
Improvements to the interpretation of the TR-LII data and to the characterization of the

soot morphology are still required. A complementary laser scattering measurement would prove useful to characterize the aggregation of the soot within the flames. That information could then help to guide the computational effort to include aggregation effects.

Laser-induced fluorescence measurements are made of NO and formaldehyde. For the NO measurements, good qualitative agreement between the computed and measured fluorescence signals was seen, with the computed signal being approximately 30% lower overall than the measured signal. Results indicated that while the dominant route to NO in these flames is due to non-Zeldovich NO (primarily Fenimore), Zeldovich NO is more pronounced in the 80% ethylene flame compared to the 40% ethylene flame. Furthermore, the results indicate that not only does soot and accompanying radiation loss (virtually all from Zeldovich NO) reduce the levels of NO throughout the flame, but for heavier sooting flames, the shape of the NO profile shifts, with NO levels in the wings noticeably higher than centerline levels. To study this problem with sufficient rigor, the Fenimore NO contribution will need to be calculated directly by disabling the coupling reaction that links it to the Zeldovich mechanism.

A preliminary study on sooting, time-varying flames was explored in an effort to approximate better a practical combustion system. In both the experimental and computational results, the peak soot volume fraction transitions between the centerline and wings at different phases of the forcing cycle. Also, the peak soot was seen to transition from the centerline to the wings as a function of phase and the development of pinched oval-shaped soot regions transitioning to hollow shells of unburned fuel are seen in both the experiments and computations. Discrepancies in the relative forcing

amplitudes were seen, where the computational results required roughly twice the forcing level to obtain soot features that are comparable with the experimental results. This will require refinement to the numerical method to avoid damping the spatial features due to using a low-order method to solve the governing equations.

Finally, the approach of comparing measured signals with simulated signals from computational results was examined as an alternative to the traditional approach of comparing fundamental quantities such as temperature and mole fractions. It was seen that quantitative comparisons could be made, and the comparisons benefited from an improvement in the noise level of the comparison. This approach also has the added advantage of enabling the comparison between experiments and computations where perhaps only a signal can be measured experimentally, as is the case in sooting or turbulent environments.

The information presented in this document has attempted to improve the knowledge and understanding of the combustion process, and add to the laser diagnostics community. It should be possible to further expand on this work by making improvements to the computational approach, and by further refining the experimental measurements presented here.

REFERENCES

(2005). Intl. Bunsen Discussion Meeting and Workshop Laser-induced incandescence on Quantitative Interpretation, Modeling, Application, Duisburg, Germany, http://liiscience.org/past_meetings.

(2006). Proc. 2nd International Discussion Meeting on Laser-induced incandescence: Quantitative Interpretation, Modeling, Application, Karlsruhe, Germany, http://liiscience.org/past_meetings.

(2008). Proc. 3rd International Discussion Meeting on Laser-induced incandescence: Quantitative Interpretation, Modeling, Application, Ottawa, Canada, http://liiscience.org/past_meetings.

Aizawa, T., K. Imaichi, H. Kosaka and Y. Matsui (2003). "Measurement of Excitation-Emission Matrix of Shock-heated PAHs using a Multi-wavelength Laser Source," *SAE Transactions*, **112** (4): 906-915.

Aizawa, T. and H. Kosaka (2008). "Investigation of early soot formation process in a diesel spray flame via excitation-emission matrix using a multi-wavelength source," *International Journal of Engine Research*, **9** (1): 79-97.

Aizawa, T., H. Kosaka and Y. Matsui (2004). "Measurement of Excitation-Emission Matrix of PAHs in a Flame using a Multi-Wavelength Source," *The Japan Society of Mechanical Engineers B*, **70** (690): 496-502.

Amantini, G., J.H. Frank, B.A.V. Bennett, M.D. Smooke and A. Gomez (2007a). "Comprehensive study of the evolution of an annular edge flame during extinction and reignition of a counterflow diffusion flame perturbed by vortices," *Combustion and Flame*, **150**: 292-319.

Amantini, G., J.H. Frank, M.D. Smooke and A. Gomez (2006). "Computational and experimental study of standing methane edge flames in the two-dimensional axisymmetric counterflow geometry," *Combustion and Flame*, **147** (1-2): 133-149.

Amantini, G., J.H. Frank, M.D. Smooke and A. Gomez (2007b). "Computational and experimental study of steady axisymmetric non-premixed methane counterflow flames," *Combustion Theory and Modelling*, **11** (1): 47-72.

Anselmitamburini, U., G. Campari, G. Spinolo and P. Lupotto (1995). "A 2-Color Spatial-Scanning Pyrometer for the Determination of Temperature Profiles in Combustion Synthesis Reactions," *Review of Scientific Instruments*, **66** (10): 5006-5014.

Axelsson, B., R. Collin and P.E. Bengtsson (2000). "Laser-induced incandescence for soot particle size measurements in premixed flat flames," *Applied Optics*, **39** (21): 3683-3690.

Axelsson, B., R. Collin and P.E. Bengtsson (2001). "Laser-induced incandescence for soot particle size and volume fraction measurements using on-line extinction calibration," *Applied Physics B-Lasers and Optics*, **72** (3): 367-372.

Bayer, B.E. (1976). *U.S. Patent 391065*.

Bell, J.B., M.S. Day, J.F. Grcar, W.G. Bessler, C. Schulz, P. Glarborg and A.D. Jensen (2003). "Detailed modeling and laser-induced fluorescence imaging of nitric oxide in a NH3-seeded non-premixed methane/air flame," *Proceedings of the Combustion Institute*, **29**: 2195-2202.

Bengtsson, P.E. and M. Alden (1995). "Soot-Visualization Strategies using Laser Techniques - Laser-Induced Fluorescence in C2 from Laser-Vaporized Soot and Laser-Induced Soot Incendescence," *Applied Physics B-Lasers and Optics*, **60** (1): 51-59.

Bengtsson, P.E., M. Alden, S. Kroll and D. Nilsson (1990). "Vibrational CARS Thermometry in Sooty Flames - Quantitative-Evaluation of C2 Absorption Interference," *Combustion and Flame*, **82** (2): 199-210.

Bennett, B.A.V., Z. Cheng, R.W. Pitz and M.D. Smooke (2008a). "Computational and Experimental Study of Oxygen-Enhanced Axisymmetric Laminar Methane Flames," *Combustion Theory and Modelling*, **12**: 497-527.

Bennett, B.A.V. and M.D. Smooke (1998). "Local rectangular refinement with application to axisymmetric laminar flames," *Combustion Theory and Modelling*, **2** (3): 221-258.

Bennett, B.A.V., M.D. Smooke, R.J. Osborne and R.W. Pitz (2008b). "Computational and Experimental Study of Oxy-Fuel Diffusion Flames," *Combustion Theory and Modelling*: in press.

Berlman, I.B. (1971). *Fluorescence spectra of aromatic molecules, 2nd. edition*, Academic Press.

Boslough, M.B. and T.J. Ahrens (1989). "A Sensitive Time-Resolved Radiation Pyrometer for Shock-Temperature Measurements above 1500-K," *Review of Scientific Instruments*, **60** (12): 3711-3716.

Bowman, C.T., R.K. Hanson, D.F. Davidson, W.C. Gardiner Jr., V. Lissianski, G.P. Smith, D.M. Golden, M. Frenklach, H. Wang and M. Goldenberg (1995). GRI-Mech version 2.11. available at <http://www.me.berkeley.edu/gri_mech/>.

Bowman, C.T. and D.V. Seery (1972). *Emissions from Continuous Combustion Systems*, New York, Plenum Press.

Boyce, R.R., J.W. Morton, A.F.P. Houwing, C. Mundt and D.J. Bone (1996). "Computational fluid dynamics validation using multiple interferometric views of a hypersonic flowfield," *Journal of Spacecraft and Rockets*, **33** (3): 319-325.

Bozzelli, J.W. and A.M. Dean (1995). "O+NNH - A Possible New Route for NOx Formation in Flames," *International Journal of Chemical Kinetics*, **27** (11): 1097-1109.

Carter, C.D. and R.S. Barlow (1994). "Simultaneous Measurements of NO, OH, and the Major Species in Turbulent Flames," *Optics Letters*, **19** (4): 299-301.

Chang, L.L. and Y.P. Tan (2004). *IEEE Transactions on Consumer Electronics*, **50**: 355-365.

Cignoli, F., S. Benecchi and G. Zizak (1994). "Time-Delayed Detection of Laser-Induced Incandescence for the 2-Dimensional Visualization of Soot in Flames," *Applied Optics*, **33** (24): 5778-5782.

Cignoli, F., S. De Iuliis, V. Manta and G. Zizak (2001). "Two-dimensional two-wavelength emission technique for soot diagnostics," *Applied Optics*, **40** (30): 5370-5378.

Clouthier, D. and D. Ramsay (1983). "The spectroscopy of formaldehyde and thioformaldehyde," *Annual Review of Physical Chemistry*, **34**: 31-58.

Coffin, D. (2009). "www.cybercom.net/~dcoffin/dcraw/."   Retrieved 1/2009.

Connelly, B.C. (2009a). *Improving the interface between experiments and computations through intelligent experimental design*, Gordon Research Conference on Laser Diagnostics in Combustion, Waterville Valley Resort, NH.

Connelly, B.C., B.A.V. Bennett, M.D. Smooke and M.B. Long (2009b). "A paradigm shift in the interaction of experiments and computations in combustion research," *Proceedings of the Combustion Institute*, **32**: 879-886.

Connelly, B.C., M.B. Long, M.D. Smooke, R.J. Hall and M.B. Colket (2009c). "Computational and Experimental Investigation of the Interaction of Soot and NOx in Coflow Diffusion Flames," *Proceedings of the Combustion Institute*, **32**: 777-784.

Cormack, A.M. (1982). "Computed tomography: some history and recent developments," *Computed Tomography, Proceedings of Symposia in Applied Mathematics*, **27**: 35-42.

Danehy, P.M., P.C. Palma, R.R. Boyce and A.F.P. Houwing (1999). "Numerical simulation of laser-induced fluorescence imaging in shock-layer flows," *Aiaa Journal*, **37** (6): 715-722.

Dankers, S. and A. Leipertz (2004). "Determination of primary particle size distributions from time-resolved laser-induced incandescence measurements," *Applied Optics*, **43** (18): 3726-3731.

Dasch, C.J. (1992). "One-Dimensional Tomography - a Comparison of Abel, Onion-Peeling, and Filtered Backprojection Methods," *Applied Optics*, **31** (8): 1146-1152.

Daun, K.J., B.J. Stagg, F. Liu, G. Smallwood and D.R. Snelling (2007). "Determining aerosol particle size distributions using time-resolved laser-induced incandescence," *Applied Physics B-Lasers and Optics*, **87**: 363-372.

Daun, K.J., K.A. Thomson, F.S. Liu and G.J. Smallwood (2006). "Deconvolution of axisymmetric flame properties using Tikhonov regularization," *Applied Optics*, **45** (19): 4638-4646.

De Iuliis, S., F. Cignoli and G. Zizak (2005). "Two-color laser-induced incandescence (2C-LII) technique for absolute soot volume fraction measurements in flames," *Applied Optics*, **44** (34): 7414-7423.

Dobbins, R.A. and C.M. Megaridis (1987). "Morphology of Flame-Generated Soot as Determined by Thermophoretic Sampling," *Langmuir*, **3** (2): 254-259.

Dockery, D.W., J.H. Ware, B.G. Ferris, F.E. Speizer, N.R. Cook and S.M. Herman (1982). "Change in Pulmonary-Function in Children Associated with Air-Pollution Episodes," *Journal of the Air Pollution Control Association*, **32** (9): 937-942.

Drake, M.C. and R.J. Blint (1991). "Calculations of NOx Formation Pathways in Propagating Laminar, High-Pressure Premixed CH4/Air Flames," *Combustion Science and Technology*, **75** (4-6): 261-285.

Drake, M.C. and J.W. Ratcliffe (1993). "High-Temperature Quenching Cross-Sections for Nitric-Oxide Laser-Induced Fluorescence Measurements," *Journal of Chemical Physics*, **98** (5): 3850-3865.

Dworkin, S.B., B.C. Connelly, A.M. Schaffer, M.B. Long, M.D. Smooke, M.P. Puccio, B. McAndrews and J.H. Miller (2006). "Computational and Experimental Study of a Forced, Time-Dependent, Methane-Air Coflow Diffusion Flame," *Proceedings of the Combustion Institute*, **31**.

Dworkin, S.B., J.A. Cooke, B.A.V. Bennett, B.C. Connelly, M.B. Long, M.D. Smooke, R.J. Hall and M.B. Colket (2009a). "Distributed-memory parallel computation of

a forced, time-dependent, sooting, ethylene/air coflow diffusion flame," *Combustion Theory and Modelling*: DOI: 10.1080/13647830903159293, in press.

Dworkin, S.B., A.M. Schaffer, B.C. Connelly, M.B. Long, M.D. Smooke, M.A. Puccio, B. McAndrew and J.H. Miller (2009b). "Measurements and calculations of formaldehyde concentrations in a methane/N-2/air, non-premixed flame: Implications for heat release rate," *Proceedings of the Combustion Institute*, **32**: 1311-1318.

Eckbreth, A.C. (1977). "Effects of Laser-Modulated Particulate Incandescence on Raman-Scattering Diagnostics," *Journal of Applied Physics*, **48** (11): 4473-4479.

Eckbreth, A.C. (1996). *Laser Diagnostics for Combustion Temperature and Species*, Amsterdam, Overseas Publishers Association.

Engleman Jr., R., P.E. Rouse, H.M. Peek and V.D. Baiamonte (1970). Beta and Gamma Systems of Nitric Oxide. Los Alamos, NM, Los Alamos Scientific Laboratory.

Ern, A. and M.D. Smooke (1993). "Vorticity-Velocity Formulation for 3-Dimensional Steady Compressible Flows," *Journal of Computational Physics*, **105** (1): 58-71.

Gaston, M.J., A.F.P. Houwing, N.R. Mudford, P.M. Danehy and J.S. Fox (2002). "Fluorescence imaging of mixing flowfields and comparisons with computational fluid dynamic simulations," *Shock Waves*, **12** (2): 99-110.

Geitlinger, H., T. Streibel, R. Suntz and H. Bockhorn (1998). "Two-dimensional imaging of soot volume fractions, particle number densities, and particle radii in laminar and turbulent diffusion flames," *Proceedings of the Combustion Institute*, **27**: 1613-1621.

Gelbard, F. and J.H. Seinfeld (1980). "Simulation of Multicomponent Aerosol Dynamics," *Journal of Colloid and Interface Science*, **78** (2): 485-501.

Giovangigli, V. and N. Darabiha (1987). *Vector Computers and Complex Chemistry Combustion*. Proceedings of the Conference of Mathematical Modeling in Combustion. Lyon, France.

Guo, H.S. and G.J. Smallwood (2007). "The Interaction between Soot and NO Formation in a Laminar Axisymmetric Coflow Ethylene/Air Diffusion Flame," *Combustion and Flame*, **149**: 225-233.

Hall, R.J. (1994). "Radiative Dissipation in Planar Gas Soot Mixtures," *Journal of Quantitative Spectroscopy & Radiative Transfer*, **51** (4): 635-644.

Hall, R.J., M.D. Smooke and M.B. Colket (1997). Physical and Chemical Aspects of Combustion: A Tribute to Irvin Glassman. R. F. Sawyer and F. L. Dryer, Gordon and Breach.

Harrington, J.E., C.R. Shaddix and K.C. Smyth (1993a). "Soot in a time-varying flame: are scattering and extinction measurements sufficient?," *Chemical and Physical Processes in Combustion*: 390-393.

Harrington, J.E. and K.C. Smyth (1993b). "Laser-Induced Fluorescence Measurements of Formaldehyde in a Methane Air Diffusion Flame," *Chemical Physics Letters*, **202** (3-4): 196-202.

Harris, S.J. and A.M. Weiner (1983). "Surface Growth of Soot Particles in Premixed Ethylene Air Flames," *Combustion Science and Technology*, **31** (3-4): 155-167.

Hofmann, M., W.G. Bessler, C. Schulz and H. Jander (2003). "Laser-induced incandescence for soot diagnostics at high pressures," *Applied Optics*, **42** (12): 2052-2062.

Hofmann, M., B. Kock and C. Schulz (2007). *A web-based interface for modeling laser-induced incandescence (LIISim)*, Proceedings of the European Combustion Meeting, Kreta, April 11-13, 2007, http://www.liisim.com.

Hottel, H.C. and F.P. Broughton (1932). "Determination of True Temperature and Total Radiation from Luminous Gas Flames
Use of Special Two-Color Optical Pyrometer," *Industrial and Engineering Chemistry*, **4** (2): 166-175.

Hura, H.S. and I. Glassman (1988). *Proceedings of the Combustion Institute*, **22**: 371-378.

Kalt, P.B. and M.B. Long. (2009). "www.oma-x.org."   Retrieved 5/2009.

Keyes, D.E. and M.D. Smooke (1987). "Flame Sheet Starting Estimates for Counterflow Diffusion Flame Problems," *Journal of Computational Physics*, **73**: 267-288.

Kobayashi, Y., T. Furuhata, K. Amagai and M. Arai (2008). "Soot precursor measurements in benzene and hexane diffusion flame," *Combustion and Flame*, **154**: 346-355.

Kock, B.F., C. Kayan, J. Knipping, H.R. Orthner and P. Roth (2005). "Comparison of LII and TEM sizing during synthesis of iron particle chains," *Proceedings of the Combustion Institute*, **30**: 1689-1697.

Kock, B.F., B. Tribalet, C. Schulz and P. Roth (2006). "Two-color time-resolved LII applied to soot particle sizing in the cylinder of a Diesel engine," *Combustion and Flame*, **147** (1-2): 79-92.

Koylu, U.O., C.S. McEnally, D.E. Rosner and L.D. Pfefferle (1997). "Simultaneous measurements of soot volume fraction and particle size/microstructure in flames using a thermophoretic sampling technique," *Combustion and Flame*, **110** (4): 494-507.

Krishnan, S.S., K.C. Lin and G.M. Faeth (2000). "Optical properties in the visible of overfire soot in large buoyant turbulent diffusion flames," *Journal of Heat Transfer-Transactions of the Asme*, **122** (3): 517-524.

Krishnan, S.S., K.C. Lin and G.M. Faeth (2001). "Extinction and scattering properties of soot emitted from buoyant turbulent diffusion flames," *Journal of Heat Transfer-Transactions of the Asme*, **123** (2): 331-339.

Kuhlmann, S.A., J. Schumacher, J. Reimann and S. Will (2004). PARTEC, Nuremburg, Germany.

Kyritsis, D.C., V.S. Santoro and A. Gomez (2004). "The effect of temperature correction on the measured thickness of formaldehyde zones in diffusion flames for 355 nm excitation," *Experiments in Fluids*, **37** (5): 769-772.

Levendis, Y.A., K.R. Estrada and H.C. Hottel (1992). "Development of Multicolor Pyrometers to Monitor the Transient-Response of Burning Carbonaceous Particles," *Review of Scientific Instruments*, **63** (7): 3608-3622.

Liu, F., H.S. Guo, G.J. Smallwood and O.L. Gulder (2002). "Effects of Gas and Soot Radiation on Soot Formation in a Coflow Laminar Ethylene Diffusion Flame," *Journal of Quantitative Spectroscopy & Radiative Transfer*, **73** (409-421).

Liu, F., B.J. Stagg, D.R. Snelling and G.J. SMallwood (2006a). "Effects of primary soot particle size distribution on the temperature of soot particles heated by a nanosecond pulsed laser in an atmospheric laminar diffusion flame," *International Journal of Heat and Mass Transfer*, **49**: 777-788.

Liu, F., M. Yang, F.A. Hill, D.R. Snelling and G.J. Smallwood (2006b). "Influence of polydisperse distributions of both primary particle and aggregate size on soot temperature in low-fluence LII," *Applied Physics B-Lasers and Optics*, **83** (3): 383-395.

Luque, J., J.B. Jeffries, G.P. Smith, D.R. Crosley, K.T. Walsh, M.B. Long and M.D. Smooke (2000). "CH(A-X) and OH(A-X) optical emission in an axisymmetric laminar diffusion flame," *Combustion and Flame*, **122** (1/2): 172-175.

Marran, D.F. (1996). Quantitative Two-Dimensional Laser Diagnostics in Idealized and Practical Combustion Systems. New Haven, CT, Yale University, Ph.D. Thesis.

McCoy, B.J. and C.Y. Cha (1974). "Transport phenomena in the rarefied gas transition regime," *Chemical Engineering Science*, **29**: 381-388.

McEnally, C.S., U.O. Koylu, L.D. Pfefferle and D.E. Rosner (1997). "Soot volume fraction and temperature measurements in laminar nonpremixed flames using thermocouples," *Combustion and Flame*, **109** (4): 701-720.

McEnally, C.S., L.D. Pfefferle, A.M. Schaffer, M.B. Long, R.K. Mohammed, M.D. Smooke and M.B. Colket (2000). "Characterization of a coflowing methane/air non-premixed flame with computer modeling, Rayleigh-Raman imaging, and on-line mass spectrometry," *Proceedings of the Combustion Institute*, **28**: 2063-2070.

McEnally, C.S., A. Schaffer, M.B. Long, L.D. Pfefferle, M.D. Smooke, M.B. Colket and R.J. Hall (1998). "Computational and Experimental Study of Soot Formation in a Coflow, Laminar Ethylene Diffusion Flame," *Proceedings of the Combustion Institute*, **27**: 1497-1505.

Melton, L.A. (1984). "Soot Diagnostics Based on Laser-Heating," *Applied Optics*, **23** (13): 2201-2208.

Menon, S., J. Hansen, L. Nazarenko and Y.F. Luo (2002). "Climate effects of black carbon aerosols in China and India," *Science*, **297** (5590): 2250-2253.

Mewes, B. and J.M. Seitzman (1997). "Soot volume fraction and particle size measurements with laser-induced incandescence," *Applied Optics*, **36** (3): 709-717.

Michelsen, H.A. (2003a). "Understanding and predicting the temporal response of laser-induced incandescence from carbonaceous particles," *Journal of Chemical Physics*, **118** (15): 7012-7045.

Michelsen, H.A. (2006). "Laser-induced incandescence of flame-generated soot on a picosecond time scale," *Applied Physics B-Lasers and Optics*, **83** (3): 443-448.

Michelsen, H.A., F. Liu, B.F. Kock, H. Bladh, A. Boiarciuc, M. Charwath, T. Dreier, R. Hadef, M. Hofmann, J. Reimann, S. Will, P.E. Bengtsson, H. Bockhorn, F. Foucher, K.P. Geigle, C. Mounaim-Rousselle, C. Schulz, R. Stirn, B. Tribalet and R. Suntz (2007). "Modeling laser-induced incandescence of soot: a summary and comparison of LII models," *Applied Physics B-Lasers and Optics*, **87** (3): 503-521.

Michelsen, H.A., P.O. Witze, D. Kayes and S. Hochgreb (2003b). "Time-resolved laser-induced incandescence of soot: the influence of experimental factors and microphysical mechanisms," *Applied Optics*, **42** (27): 5577-5590.

Miller, J.A. and C.T. Bowman (1989). "Mechanism and Modeling of Nitrogen Chemistry in Combustion," *Progress in Energy and Combustion Science*, **15** (4): 287-338.

Mohammed, R.K., M.A. Tanoff, M.D. Smooke, A.M. Schaffer and M.B. Long (1998). "Computational and experimental study of a forced, time-varying, axisymmetric, laminar diffusion flame," *Proceedings of the Combustion Institute*, **27** (Vol. 1): 693-702.

Moreau, C.S., E. Therssen, X. Mercier, J.F. Pauwels and P. Desgroux (2004). "Two-color laser-induced incandescence and cavity ring-down spectroscopy for sensitive and

quantitative imaging of soot and PAHs in flames," *Applied Physics B-Lasers and Optics*, **78** (3-4): 485-492.

Naik, S.V., N.M. Laurendeau, J.A. Cooke and M.D. Smooke (2003a). "A soot map for methane-oxygen counterflow diffusion flames," *Combustion Science and Technology*, **175** (6): 1165-1177.

Naik, S.V., N.M. Laurendeau, J.A. Cooke and M.D. Smooke (2003b). "Effect of radiation on nitric oxide concentration under sooting oxy-fuel conditions," *Combustion and Flame*, **134** (4): 425-431.

Panagiotou, T., Y. Levendis and M. Delichatsios (1996). "Measurements of particle flame temperatures using three-color optical pyrometry," *Combustion and Flame*, **104** (3): 272-287.

Paul, P. and H. Najm (1998). "Planar laser-induced fluorescence imaging of flame heat release rate," *Proceedings of the Combustion Institute*, **27**: 43-50.

Paul, P.H., J.A. Gray, J.L. Durant and J.W. Thoman (1993). "A Model for Temperature-Dependent Collisional Quenching of NO A(2)Sigma+," *Applied Physics B-Photophysics and Laser Chemistry*, **57** (4): 249-259.

Penner, J.E., D.H. Lister, D.J. Griggs, D.J. Dokken and M. McFarland (1999). *Aviation and the Global Atmosphere, A Special Report of IPCC Working Groups I and III*, Cambridge University Press.

Puri, R., T.F. Richardson, R.J. Santoro and R.A. Dobbins (1993). "Aerosol Dynamic Processes of Soot Aggregates in a Laminar Ethene Diffusion Flame," *Combustion and Flame*, **92** (3): 320-333.

Quay, B., T.W. Lee, T. Ni and R.J. Santoro (1994). "Spatially-Resolved Measurements of Soot Volume Fraction Using Laser-Induced Incandescence," *Combustion and Flame*, **97** (3-4): 384-392.

Reimann, J., S.A. Kuhlmann and S. Will (2008). "Improvement in soot concentration measurements by laser-induced incandescence (LII) through a particle size correction," *Combustion and Flame*, **153** (4): 650-654.

Ruyten, W.M., W.D. Williams and F.L. Heltsley (1994). *Computational Flow Imaging for Planar Laser-Induced Fluorescence Applications (CFI-PLIF)*, 18th Aerospace Ground Testing Conference, AIAA Paper 94-2621.

Santoro, R.J., H.G. Semerjian and R.A. Dobbins (1983). "Soot Particle Measurements in Diffusion Flames," *Combustion and Flame*, **51**: 203.

Schaffer, A.M. (2001). *Quantitative Characterization of Species, Temperature, and Particles in Steady and Time-Varying Laminar Flames by Optical Methods*, New Haven, CT, Yale University, Ph.D. Thesis.

Schiessl, R., S. Kaiser, M. Long and U. Mass (2009). "Application of reduced state spaces to laser-based measurements in combustion," *Proceedings of the Combustion Institute*, **32**: 887-894.

Schulz, C. (2006a). "Special issue: Laser-induced incandescence," *Applied Physics B-Lasers and Optics*, **83** (3): 331-331.

Schulz, C., B.F. Kock, M. Hofmann, H. Michelsen, S. Will, B. Bougie, R. Suntz and G. Smallwood (2006b). "Laser-induced incandescence: recent trends and current questions," *Applied Physics B-Lasers and Optics*, **83**: 333-354.

Schumann, U., J. Strom, R. Busen, R. Baumann, K. Gierens, M. Krautstrunk, F.P. Schroder and J. Stingl (1996). "In situ observations of particles in jet aircraft exhausts and contrails for different sulfur-containing fuels," *Journal of Geophysical Research-Atmospheres*, **101** (D3): 6853-6869.

Schwartz, J. (1993). "Particulate Air-Pollution and Chronic Respiratory-Disease," *Environmental Research*, **62** (1): 7-13.

Settersten, T.B., B.D. Patterson and J.A. Gray (2006). "Temperature-and species-dependent quenching of NO A (2)Sigma(+)(v(')=0) probed by two-photon laser-induced fluorescence using a picosecond laser," *Journal of Chemical Physics*, **124** (23).

Shaddix, C.R., J.E. Harrington and K.C. Smyth (1994a). "Enhanced Soot Formation in Flickering Diffusion Flames," *Abstracts of Papers of the American Chemical Society*, **207**: 23-FUEL.

Shaddix, C.R., J.E. Harrington and K.C. Smyth (1994b). "Quantitative Measurements of Enhanced Soot Production in a Flickering Methane Air Diffusion Flame," *Combustion and Flame*, **99** (3-4): 723-732.

Shin, D.I., T. Dreier and J. Wolfrum (2001). "Spatially resolved absolute concentration and fluorescence-lifetime determination of H2CO in atmospheric-pressure CH4/air flames," *Applied Physics B-Lasers and Optics*, **72** (2): 257-261.

Sick, V., F. Hildenbrand and P. Lindstedt (1998). "Quantitative Laser-Based Measurements and Detailed Chemical Kinetic Modeling of Nitric Oxide Concentrations in Methane-Air Counterflow Diffusion Flames," *Proceedings of the Combustion Institute*, **27**: 1401-1409.

Skaggs, R.R. and J.H. Miller (1996). *Tunable Diode Laser Absorption Measurements of Carbon Monoxide and Temperature in a Time-varying, Methane/Air, Non-Premixed Flame*, Twenty-Sixth Symposium (International) on Combustion, The Combustion Institute.

Smallwood, G., D. Clavel, G. D., R.A. Sawchuk, D.R. Snelling, P.O. Witze, B. Axelsson, W.D. Bachalo and O.L. Gulder (2002). "Concurrent Quantitative Laser-Induced

Incandescence and SMPS Measurements of EGR Effects on Particulate Emissions from a TDI Diesel Engine," *SAE Tech Paper Ser. 2002-01-2715*.

Smallwood, G.J., D.R. Snelling, F. Liu and O.L. Gulder (2001). "Clouds over soot evaporation: Errors in modeling laser-induced incandescence of soot," *Journal of Heat Transfer-Transactions of the Asme*, **123** (4): 814-818.

Smith, G.P., D.M. Golden, M. Frenklach, N.W. Moriarty, B. Eiteneer, M. Goldenberg, C.T. Bowman, R.K. Hanson, S. Song, W.C. Gardiner Jr., V.V. Lissianski and Z. Qin GRI-Mech version 3.0. available at <http://www.me.berkeley.edu/gri_mech/>.

Smooke, M.D. (1983). "Error Estimate For The Modified Newton Method With Applications To The Solution Of Non-Linear, 2-Point Boundary-Value-Problems," *Journal of Optimization Theory and Applications*, **39** (4): 489-511.

Smooke, M.D., A. Ern, M.A. Tanoff, B.A. Valdati, R.K. Mohammed, D.F. Marran and M.B. Long (1996). "Computational and Experimental Study of Nitric Oxide in an Axisymmetric Laminar Diffusion Flame," *Proceedings of the Combustion Institute*, **26**: 2161.

Smooke, M.D., R.J. Hall, M.B. Colket, J. Fielding, M.B. Long, C.S. McEnally and L.D. Pfefferle (2004). "Investigation of the transition from lightly sooting towards heavily sooting co-flow ethylene diffusion flames," *Combustion Theory and Modelling*, **8** (3): 593-606.

Smooke, M.D., M.B. Long, B.C. Connelly, M.B. Colket and R.J. Hall (2005). "Soot formation in laminar diffusion flames," *Combustion and Flame*, **143** (4): 613-628.

Smooke, M.D., C.S. McEnally, L.D. Pfefferle, R.J. Hall and M.B. Colket (1999a). "Computational and experimental study of soot formation in a coflow, laminar diffusion flame," *Combustion and Flame*, **117** (1-2): 117-139.

Smooke, M.D., C.S. McEnally, L.D. Pfefferle, R.J. Hall and M.B. Colket (1999b). "Computational and experimental study of soot formation in a coflow, laminar diffusion flame," *Combustion and Flame*, **117** (1/2): 117-139.

Smooke, M.D., R.E. Mitchell and D.E. Keyes (1989). "Numerical-Solution of 2-Dimensional Axisymmetric Laminar Diffusion Flames," *Combustion Science and Technology*, **67** (4-6): 85-122.

Smyth, K.C., J.E. Harrington, E.L. Johnsson and W.M. Pitts (1993a). "Greatly Enhanced Soot Scattering in Flickering CH4/Air Diffusion Flames," *Combustion and Flame*, **95**: 229-239.

Smyth, K.C., J.E. Harrington, E.L. Johnsson and W.M. Pitts (1993b). "Greatly enhanced soot scattering in flickering methane/air diffusion flames," *Combustion and Flame*, **95** (1-2): 229-239.

Smyth, K.C., J.E. Harrington, C.R. Shaddix, W.M. Pitts and E.L. Johnsson (1994). *Flickering Flames as Testing Grounds for Reliable Models of Gas Combustion*, NIST, Gaithersburg, MD.

Smyth, K.C., J.H. Miller, R.C. Dorfman, W.G. Mallard and R.J. Santoro (1985). "Soot Inception in a Methane/Air Diffusion Flame as Characterized by Detailed Species Profiles," *Combustion and Flame*, **62**: 157-181.

Smyth, K.C. and C.R. Shaddix (1996). "The elusive history of (m)over-bar=1.57-0.56i for the refractive index of soot," *Combustion and Flame*, **107** (3): 314-320.

Snelling, D.R., F.S. Liu, G.J. Smallwood and O.L. Gulder (2004). "Determination of the soot absorption function and thermal accommodation coefficient using low-fluence LII in a laminar coflow ethylene diffusion flame," *Combustion and Flame*, **136** (1-2): 180-190.

Snelling, D.R., G.J. Smallwood, F. Liu, O.L. Golder and W.D. Bachalo (2005). "A calibration-independent laser-induced incandescence technique for soot measurement by detecting absolute light intensity," *Applied Optics*, **44** (31): 6773-6785.

Snelling, D.R., K.A. Thomson, G.J. Smallwood and O.L. Gulder (1999). "Two-dimensional imaging of soot volume fraction in laminar diffusion flames," *Applied Optics*, **38** (12): 2478-2485.

Snelling, D.R., K.A. Thomson, G.J. Smallwood, O.L. Gulder, E.J. Weckman and R.A. Fraser (2002). "Spectrally resolved measurement of flame radiation to determine soot temperature and concentration," *Aiaa Journal*, **40** (9): 1789-1795.

Stagg, B.J. (2006). Proc. 2nd International Discussion Meeting on Laser-induced incandescence: Quantitative Interpretation, Modeling, Application, Karlsruhe, Germany.

Stipe, C.B., J.H. Choi, D. Lucas, C.P. Koshland and R.F. Sawyer (2004). "Nanoparticle production by UV irradiation of combustion generated soot particles," *Journal of Nanoparticle Research*, **6**: 467-477.

Sun, C.J., C.J. Sung, H. Wang and C.K. Law (1996). "On the structure of nonsooting counterflow ethylene and acetylene diffusion flames," *Combustion and Flame*, **107** (4): 321-335.

Tait, N.P. and D.A. Greenhalgh (1993). "PLIF Imaging of Fuel Fraction in Practical Devices and LII Imaging of Soot," *Ber. Bunsenges. Phys. Chem.*, **97** (12): 1619-1635.

Vander Wal, R.L., T.M. Ticich and A.B. Stephens (1998). "*Optical and microscopy investigations of soot structures by laser-induced incandescence,*" *Applied Physics B-Lasers and Optics*, **67**: 115.

Vander Wal, R.L., T.M. Ticich and A.B. Stephens (1999). "Can soot primary particle size be determined using laser-induced incandescence?," *Combustion and Flame*, **116** (1-2): 291-296.

Vanderwal, R.L. and K.J. Weiland (1994). "Laser-Induced Incandescence - Development and Characterization Towards a Measurement of Soot-Volume Fraction," *Applied Physics B-Lasers and Optics*, **59** (4): 445-452.

Walsh, K.T. (2000a). *Quantitative Characterizations of Coflow Laminar Diffusion Flames in a Normal Gravity and Microgravity Environment*, New Haven, CT, Yale University, Ph.D. Thesis.

Walsh, K.T., J. Fielding and M.B. Long (2000b). "Effect of light-collection geometry on reconstruction errors in Abel inversions," *Optics Letters*, **25** (7): 457-459.

Walsh, K.T., J. Fielding, M.D. Smooke and M.B. Long (2000c). "Experimental and computational study of temperature, species, and soot in buoyant and non-buoyant coflow laminar diffusion flames," *Proceedings of the Combustion Institute*, **28**: 1973-1979.

Walsh, K.T., M.B. Long, M.A. Tanoff and M.D. Smooke (1998). "Experimental and computational study of CH, CH*, and OH* in an axisymmetric laminar diffusion flame," *Proceedings of the Combustion Institute*, **27** (Vol. 1): 615-623.

Will, S., S. Schraml, K. Bader and A. Leipertz (1998). "Performance characteristics of soot primary particle size measurements by time-resolved laser-induced incandescence," *Applied Optics*, **37** (24): 5647-5658.

Will, S., S. Schraml and A. Leipertz (1995). "2-Dimensional Soot-Particle Sizing by Time-Resolved Laser-Induced Incandescence," *Optics Letters*, **20** (22): 2342-2344.

Williams, T.C., C.R. Shaddix, K.A. Jensen and J.M. Suo-Anttila (2005). *Measurement of the Dimensionless Extinction Coefficient of Soot within Laminar Diffusion Flames*, Joint Meeting of the U.S. Sections of the Combustion Institute.

Zeldovich, Y.B. (1946). *Acta Physicochim USSR*, **21**: 557.

Zhao, H. and N. Ladommatos (1998). "Optical diagnostics for soot and temperature measurement in diesel engines," *Progress in Energy and Combustion Science*, **24** (3): 221-255.

Zhu, X.L. and J.P. Gore (2005). "Radiation effects on combustion and pollutant emissions of high-pressure opposed flow methane/air diffusion flames," *Combustion and Flame*, **141** (1-2): 118-130.